

# **Turbulent Flows over Rough Permeable Beds in Mountain Rivers: Experimental Insights and Modeling**

**Thèse N° 9327**

Présentée le 22 mars 2019

à la Faculté de l'environnement naturel, architectural et construit  
Laboratoire d'hydraulique environnementale  
Programme doctoral en mécanique

pour l'obtention du grade de Docteur ès Sciences

par

**Gauthier Paul Daniel Marie ROUSSEAU**

Acceptée sur proposition du jury

Prof. F. Gallaire, président du jury  
Prof. C. Ancey, directeur de thèse  
Dr Ph. Frey, rapporteur  
Dr E. Lajeunesse, rapporteur  
Dr G. De Cesare, rapporteur

2019



*“Il paraît que l’on n’a pas vu une aussi grosse tempête depuis longtemps à Chézy ! C’est impressionnant de voir les voitures flotter dans les rues inondées, certaines personnes ont été envahies chez elles par une poussée d’eau à hauteur de leur poitrine. Les fortes pluies ont fait déborder le Dolloir, petit Ru qui traverse Chézy entraînant des torrents de boue et toutes sortes de broussailles . En faisant un tour dans le village aujourd’hui, je me suis vraiment rendue compte de l’ampleur de la catastrophe, ponts détruits, voitures dans les cours d’eau, murs et maisons dévastées, chaussées éclatées, le beau village de Chézy et sa population ont souffert dans leur chair, il faudra bien du temps pour redonner à notre village son éclat, et redonner aux habitants qui ont tout perdu le courage de repartir et de retrouver leur joie de vivre.”*

— Une note de Marie rédigée sur son blog personnel *Autour de Chézy-sur-Marne* au lendemain d’une crue extrême dans les bas de l’Aisne, le 14 Juin 2009.

À mes grand mères, Mammy et Mamia  
À mon gran père Bon Papa  
Tous les trois partis pendant mon doctorat  
À la famille et aux amis





## Remerciements

---

Beaucoup de sueur mais aussi beaucoup de rires échangés lors de cette belle aventure humaine. Rien de tout cela n'aurait été possible sans vous.

En premier lieu, je remercie donc la personne qui m'a permis de réaliser ce doctorat, le professeur Christophe Ancey, le père actuel du Laboratoire d'Hydraulique Environnementale : le L-H-E. Son expertise scientifique, son aisance à l'écrit et son esprit critique "franc du collier" ont été pour moi des qualités essentielles qui m'ont permis de mener à bien cette recherche. Merci aussi de m'avoir laissé la liberté d'entreprendre un sujet qui n'était pas tellement prévu au programme.

Autour de Christophe, l'équipe du laboratoire se réunit traditionnellement au déjeuner de 11h30 au Parmentier. On y parle de sujets captivants tels que les radars sur l'autoroute ou encore du cours de la bourse et de son prochain effondrement. A droite, Bob de Graffenried qui a toujours eu la motivation et les idées pour répondre à nos besoins expérimentaux et sans qui on ne mesurerait pas grand chose. En face, Barbara Tinguely qui gère les tâches administratives et qui apporte aussi la douceur bien nécessaire à notre équilibre. Sur une table un peu plus loin, il y a l'équipe de l'Atelier autour de Michel Teusher qui confectionne et perfectionne les différents outils et canaux qu'on leur commande (même parfois en urgence!). Et puis à gauche de Christophe, il y a les graveleux, toute l'équipe des doctorants bruyants avec leurs tupperwares : Zhenzhu a cuisiné de bon petits raviolis communistes chinois, Blaise prépare les cocktails pour la Terrasse GC de ce soir ; Daniel nous a confectionné des spécialités... Argentines ? Italiennes ? ou Camerounaises ? Ivan revient de sa petite promenade de 40 km en ski de fond ; tandis que Tomás nous raconte le Chili et nous fait goûter de succulentes empanadas. Toute cette équipe se retrouvera plus tard autour d'un baby à Sat ou une bière à Zelig ! Merci donc à toutes ces têtes que j'ai vu quotidiennement à l'EPFL et qui font que l'on se sent bien ici. Merci aussi au personnel de ménage que j'ai souvent croisé à des heures tardives.

Et parfois, on aperçoit des têtes d'anciens : Bertil va sûrement faire une thèse sur les avalanches, on croise les doigts ; François Mettra a maintenant sa serre dans le potager d'Unipoly ; Kasper me raconte comment faire les mélanges iso-indice ; Nicolas Andreini me fournit encore quelques derniers conseils pour la PIV et Joris m'explique que ce serait bien de faire une expérience de transport solide en isoindice. Oui, c'est aussi grâce à toutes ces personnes que j'ai trouvé mon inspiration pour finalement aboutir, cahin-caha, à mon sujet final de thèse : l'écoulement sur des cailloux qui ne bougent pas !

Et puis, il y a ceux qui son venu dans notre labo faire des stages ou des projets de semestres en pensant se dorer la pilule dans des torrents en pleine nature. Pas de bol... les expériences se passeront dans une cave sans lumière ou une cabane en bois (construite avec Bob, Sasan et Daniel en Aout 2015 !) ou bien dans un laboratoire aseptisé avec des lasers verts puissants et dangereux. On traitera ensuite les données devant un écran 90 % du temps. Grâce à vous donc, Philippe, Anthony, Elizam, Victoire, Angeliki, Basile, Nicola, Vincent, Hugo, Nicolas et Mohamed, j'ai appris à transmettre mais aussi à, petit à petit, aboutir à mon sujet final.

## Remerciements

---

Ensuite, il y a ceux qui sont un peu plus loin, avec qui on échange des conseils et qui viennent parfois profiter du soleil matinal dans mon bureau. Les doctorants du Laboratoire de Construction Hydraulique (LCH) ou encore ceux du Laboratoire de Mécanique des Sols (LMS). Je pense surtout à Étienne avec qui j'ai partagé, à quelques jours près, la même aventure de thèse avec un rush final pas facile facile. Mais tellement de rires échangés avec Daniel, Blaise et Bernard. Heureusement que vous étiez par là :) Tient bon ! Merci aussi à Alessandro, probablement le futur professeur du LMS ! et Severin ! le futur professeur du LCH ! Je pense aussi à Darko et à son raki, Dimitrios et son Mikonos... et j'en oublie !

Dans d'autres écoles doctorales aussi on se fait des amis. on n'est pas sectaire. En Chimie, Franck, Coralie et Anto ! En neurosciences Xander ! Et puis le soir on rentre à la maison et on retrouve les colocos. Au début de mon séjour à Lausanne je résidais à l'avenue de France avec Magaly et Marius, puis après un petit séjour à Renens Village chez les Lamentins où je me suis mis au vert me voici maintenant chez le romain Andrea. A quelques moments on fait aussi du bénévolat où là aussi on rencontre des gens magnifiques, au cinéma City Club de Pully ou bien à Unipoly. C'est très réconfortant d'avoir des gens à son écoute pour préparer de futurs projets et résoudre les petits problèmes du quotidiens.

Je remercie aussi particulièrement mon jury de thèse avec qui j'ai eu aussi la possibilité d'échanger au cours de ma thèse. Ce sont François Gallaire le président du Jury, Philippe Frey pour sa relecture très attentive, Eric Lajeunesse pour ses conseils de physicien et Giovanni De Cesare pour son sens pratique de l'hydraulique.

Je remercie également les scientifiques avec qui j'ai échangés pendant mon doctorat et qui m'ont soutenu et/ou conseillé sur mon sujet : Hervé Capart, Patricio Bohorquez, Julien Chauchat, Guillaume Dramais, Johan Gaume, Jeff Prancevic, Joey Voermans, Vladimir Nikora, Koen Blanckaert, Mario Franca, Raphaël Maurin, James Best, Florence Bertails-Descoubes, Valérie Vidal, Philippe Ung... Ce sont parfois des échanges skype ou bien seulement quelques mots devant un poster mais qui ont fait toute la différence sur mon parcours de thèse.

Et puis il y a tous les amis, la team HH du master Hydrologie-Hydrogéologie (Lila, Camille, les Pierres, Benjy, Cyril, etc.). Je pensais un moment quitter les rivières pour aller vers la Physique et finalement le destin m'a ramené à la raison vers vous pour travailler à l'interface entre ces deux domaines. C'est une évidence mais je dois aussi beaucoup à mes profs de Lycée, de Licence et de Master que je ne peux pas citer ici tellement la liste serait longue. Merci aussi aux vieux potes sur lesquels on peut toujours compter, (en tous cas pour boire des bières !) je pense à Matthias, Mathieu, Marta, Pierre, Helmy,... (et j'en oublie plein !)

Bien sûr je remercie toute ma famille et en particulier ma mère, mon père et ma sœur Jeanne ainsi que son mari Hubert et leurs enfants Louise et Auguste. C'est avec vous que je me ressource dans ma Picardie natale à Chézy-sur-Marne. Et contre toute vraisemblance Chézy n'est pas le village natal de l'hydraulicien Antoine Chézy ! En revanche, c'est bien là bas que j'ai passé mes après midis d'enfance à barboter dans l'eau. Merci aussi à Adélia qui m'a supporté pendant cette dernière année de thèse en apportant tendresse, raison mais aussi parfois... de nécessaires déraisons.

Je remercie aussi spécialement mon ami anglais, Julius Hogben qui a lu et relu de nombreux bouts de thèse pour y apporter d'innombrables corrections. Karl Embleton a aussi été d'une précieuse aide. C'est grâce à ces deux anglophones que cette thèse a été appréciée à la première lecture par mon Jury.

Et comme des remerciements ne sont jamais exhaustifs, je remercie tous les membres de ma famille, collègues et amis que j'ai oublié de citer ici mais qui comptent tout autant.

*Lausanne, 7 Mars 2019*

G. R.

# Abstract

---

Steep mountain streams exhibit shallow waters with roughness elements such as stones and pebbles that are comparable in size to flow depth. Owing to the difficulty in measuring fluid velocities at the interface, i.e., from the rough permeable bed to the free surface, experimental results are rare although they are essential to improve models. Using a novel experimental procedure, this thesis attempts to improve predictions of the vertical structure of turbulent flows over rough permeable beds.

To explore flows at the bed interface, I devised an experimental set-up where a fluid flowed over glass spheres ( $8 \text{ mm} < d_p < 14 \text{ mm}$ ) in a narrow flume ( $W = 6 \text{ cm}$ ) with slopes varying from 0.5% to 8%. The *Refractive Index Matching* (RIM) technique has been employed. This involves matching the refractive index of the fluid with that of the glass spheres, thereby allowing the interior of the medium to be examined and velocities to be measured by *Particle Image Velocimetry* (PIV). Vertical profiles are retrieved by employing the spatiotemporal *double averaging* method.

In the course of this manuscript, flow processes are studied at the mesoscopic scale, i.e., by averaging quantities over distances ranging from 5 to 10 grain diameters. For open-channel flows over rough permeable beds, the spatial averaging procedure yields a *continuous porosity profile*. When applied to the Navier-Stokes equations, it produces a momentum equation with several terms including *drag forces* and three stresses: the *turbulent*, *dispersive*, and *viscous stresses*. The momentum equation was employed to devise a one dimensional (1D) model describing the vertical structure of a unidirectional turbulent flow.

A turbulent boundary layer over the rough bed was observed while experiments were performed at intermediate Reynolds numbers, i.e.,  $Re = O(1000)$ . In such conditions, viscosity plays a critical role through the *van Driest damping effect*. To model vertical profiles, the *Darcy-Ergün* equation is well suited to the prediction of friction forces in the permeable bed, i.e., in roughness and subsurface layers. Based on the *Prandtl mixing length theory*, turbulent stress is predicted from a mixing length distribution that considers dispersive effects and assumes a continuous porosity profile. This alternative contrasts with most existing boundary layer models which postulate a discontinuous porosity profile for permeable or impermeable walls.

Finally, hydraulic conditions collected by a Unmanned Aerial Vehicle (UAV) and classical flow resistance equations (*Chézy*, *Keulegan*, ...) were compared with profile simulations and demonstrate a good agreement between predictions and observations. It reveals the crucial role of fluid depth definition in equations in small submergence conditions. Furthermore, incipient sediment motion conditions have been estimated and compared to empirical results showing the importance of turbulence and lift force for grain entrainment.

With regard to fluid dynamics, mountain streams are a case study of the larger scientific family of turbulent flows interacting with porous structures. Insights and developments acquired in the course of this thesis are likely to be transferable to other domains working with these phenomena such as flows over buildings, vegetal canopies or rough wings.



# Résumé

---

Dans les rivières de montagne, l'écoulement a la particularité d'être peu profond avec des éléments rugueux de taille comparable à la hauteur d'eau. Comme il est difficile de mesurer les vitesses du fluide à l'interface, c'est-à-dire, du lit perméable à la surface libre, les résultats expérimentaux sont rares bien qu'ils soient requis pour concevoir les modèles. C'est dans ce contexte qu'une procédure expérimentale novatrice a été élaborée afin de prédire la structure verticale d'un écoulement turbulent sur un lit rugueux perméable.

Pour mesurer l'écoulement à l'interface, le dispositif expérimental consiste à laisser s'écouler un fluide sur des billes de verre ( $8 \text{ mm} < d_p < 14 \text{ mm}$ ), dans un canal étroit ( $W = 6 \text{ cm}$ ) à pente variable (0.5% à 8%). La technique d' *adaptation d'indice de réfraction* a été utilisée. Elle consiste à égaliser l'indice de réfraction du fluide avec les billes de verre solides pour observer l'écoulement entre les grains et mesurer les vitesses par vélocimétrie laser (PIV). Les profils verticaux sont obtenus par *double moyenne* temporelle et spatiale.

Une couche limite turbulente au dessus du lit perméable rugueux a été observée pour des nombres de Reynolds intermédiaires,  $Re = O(1000)$ . Dans ces conditions, la viscosité joue un rôle à travers l'effet d'atténuation de Van Driest. Pour modéliser les profils verticaux, l'équation de type *Darcy-Ergün* permet de prédire les forces de frottement dans le lit perméable, c'est à dire dans la couche rugueuse et de subsurface. Élaboré à l'aide de la *théorie de Prandtl*, une contrainte turbulente a été conçu tenant compte de la dispersion et considérant un profil de porosité continu. Cette approche alternative contraste avec les modèles traditionnels de couche limite sur lit perméable ou imperméable qui postulent un profil de porosité discontinu.

Pour finir, des mesures hydrauliques de terrain collectés par drone ainsi que des lois de résistance à l'écoulement (*Chézy, Keulegan,...*) ont été comparé à des simulations. Les conditions hydrauliques pour atteindre le seuil de mise en mouvement du grain ont été estimées et comparées à des résultats empiriques. Ces comparaisons permettent d'attester du bon accord entre les prédictions et les observations et dévoilent l'importance de la définition de la hauteur de fluide ainsi que le rôle de la turbulence et de la portance pour prédire l'entraînement d'un grain.

With regard to fluidity, turbulent streams are a case study of the larger scientific family of turbulent flows interacting with porous structures. Insights and developments acquired in the course of this thesis are likely to be transferable to other domains working with these phenomena such as building/wind or air/wings interactions.

En ce qui concerne la dynamique du fluide, les rivières constituent un cas particulier de la grande famille scientifique des écoulements turbulents en interaction avec des structures poreuses. Les connaissances et les développements acquis au cours de cette thèse sont susceptibles d'être transférés à d'autres domaines travaillant avec ces phénomènes tels que l'écoulement de l'air sur des bâtiments, une canopée végétale ou encore des ailes.



# Contents

---

<b>Remerciements</b>	<b>v</b>
<b>Abstract</b>	<b>vii</b>
<b>Résumé</b>	<b>ix</b>
<b>List of figures</b>	<b>xv</b>
<b>List of tables</b>	<b>xx</b>
<b>Notation</b>	<b>xxiii</b>
<b>1 Introduction</b>	<b>1</b>
1 Preliminary field observations . . . . .	1
2 Hydrodynamic problems in gravel-bed rivers . . . . .	2
2.1 Flow resistance . . . . .	2
2.2 Hyporheic exchanges . . . . .	4
2.3 Incipient motion . . . . .	4
2.4 Sediment-fluid interface modeling: a recurrent issue . . . . .	5
3 Double-averaging methodology . . . . .	5
3.1 Concept . . . . .	5
3.2 Crucial role of the vertical porosity structure . . . . .	6
3.3 Double-averaged momentum equation . . . . .	7
4 Main motivations and contribution . . . . .	7
5 Outline of the dissertation . . . . .	9
<b>I Theory</b>	<b>11</b>
<b>2 Fluvial flows and porous media</b>	<b>13</b>
1 Turbulent open-channel flows . . . . .	13
1.1 River flow and friction laws: an historical review . . . . .	13
1.2 Vertical velocity structure of turbulent open-channel flows . . . . .	17
1.2.1 Non dimensional numbers . . . . .	17
1.2.2 Log-law of the wall . . . . .	18
1.2.3 Buffer layer and damping effect . . . . .	20
	xi

## Contents

---

1.2.4	The velocity defect-law . . . . .	21
1.3	Reassessments . . . . .	22
2	Flows in a porous media . . . . .	22
2.1	Darcy based laws . . . . .	22
2.1.1	Darcy law . . . . .	22
2.1.2	Darcy-Forchheimer law: the Ergün equation . . . . .	23
2.1.3	Scaling in a porous media . . . . .	24
2.2	Drag force based laws . . . . .	25
2.3	Comparison between drag force based law and porous media laws . . . . .	26
2.4	Porous media interactions: up-scaling approaches . . . . .	26
2.4.1	Classical approaches . . . . .	26
2.4.2	Homogenization and spatial averaging concepts . . . . .	26
2.4.3	Discussion . . . . .	28
3	Flow-porous structure interactions . . . . .	28
3.1	Pioneering investigations . . . . .	28
3.2	Hyporheic exchanges and flux across the water-sediment interface . . . . .	29
3.3	Modeling issues . . . . .	30
4	Conclusion on the theoretical background . . . . .	30
<b>3</b>	<b>Theoretical developments</b>	<b>31</b>
1	Unidirectional equation of motion . . . . .	32
2	Closure problem . . . . .	33
2.1	Drag forces in the porous bed - $f_{p,x} + f_{v,x}$ . . . . .	33
2.1.1	Closure choice . . . . .	33
2.1.2	Discussion on the closure choice . . . . .	34
2.2	Dispersive stress - $\tau_d$ . . . . .	35
2.2.1	Preamble . . . . .	35
2.2.2	Dispersive stress closure on a regular packed bed . . . . .	35
2.2.2.1	Bed geometry and porosity . . . . .	37
2.2.3	Final expression and simplifications . . . . .	38
2.3	Viscous stress - $\tau_v$ . . . . .	39
2.4	Turbulent stress - $\tau_t$ . . . . .	40
2.4.1	Mixing length theory and open channel flows . . . . .	40
2.4.2	Experimental scatters in the Von Kármán determination with the fitting procedure . . . . .	41
2.4.3	Mixing length distribution and damping effect: from idealized smooth surfaces to rough permeable beds . . . . .	42
2.4.4	How negligible is the turbulent mixing in the subsurface layer ( $z < z_t$ ) ? . . . . .	43
2.4.5	Closure choice and adaptation to a continuous interface . . . . .	45
2.5	Summary . . . . .	47
3	Numerical simulations . . . . .	48
3.1	Porosity profile . . . . .	48
3.2	Real case scenarios . . . . .	48
3.2.1	Hydraulic conditions . . . . .	48
3.2.2	Figures details . . . . .	50
3.2.3	Comments on the three scenarios . . . . .	51
3.3	Velocity structure and flow characteristics . . . . .	52



3.3.1	Flow depth . . . . .	52
3.3.2	Slope . . . . .	53
3.3.3	Grain size . . . . .	54
3.3.4	Continuous porosity profile . . . . .	55
3.4	Gibilaro-DiFelice and Ergün equations . . . . .	56
4	Summary of the theoretical development . . . . .	58
<b>II Experimental work</b>		<b>59</b>
<b>4</b>	<b>Experimental procedure</b>	<b>61</b>
1	Experimental setup . . . . .	61
1.1	Flume and materials . . . . .	61
1.2	Optics . . . . .	63
1.3	Coupling between PIV and RIM for measuring interstitial flow in previous contributions . . . . .	63
1.4	Transverse scanning and mean porosity profiles . . . . .	64
2	Velocimetry and transverse scans . . . . .	65
2.1	Image velocimetry processing . . . . .	65
2.2	Quantities of interest within the double-averaging framework . . . . .	65
2.3	Constraints on the laser sheet displacement when measuring by scanning . . . . .	66
2.4	Scanning and averaging procedure . . . . .	67
2.5	Evaluation of the scanning methodology . . . . .	68
2.5.1	Flow characteristics and evaluation procedure . . . . .	68
2.5.2	Temporal and spatial averaging measurements with the fixed laser sheet . . . . .	68
2.5.3	Turbulence statistics . . . . .	72
2.5.4	Results of the evaluation . . . . .	74
2.6	Preliminary results from the PIV-RIMS method . . . . .	75
2.6.1	3D vizualisation and the side-wall effect on the flow . . . . .	75
2.6.2	PIV-RIMS procedure and double-averaged profiles . . . . .	76
3	Repeatability and uniformity . . . . .	78
3.1	Repeatability: the crucial role of bed arrangement . . . . .	78
3.1.1	Repeatability at the mesoscopic scale . . . . .	78
3.1.2	Inter-comparisons: the vertical origin definition . . . . .	79
3.1.3	Scatters in the porosity and the velocity profiles . . . . .	80
3.2	Uniformity: the permeable grid influence . . . . .	80
3.2.1	Influence of the permeable grid on the subsurface flow . . . . .	81
3.2.2	Verification of the nearly uniform conditions . . . . .	81
4	Summary of the experimental procedure . . . . .	83
<b>5</b>	<b>Experimental results</b>	<b>85</b>
1	Characteristics of the vertical profiles . . . . .	85
1.1	Porosity profiles . . . . .	87
1.2	Velocity . . . . .	88
1.3	Turbulent, dispersive and viscous stresses . . . . .	88
2	Voermans <i>et al.</i> 's (2017) measurements and findings . . . . .	90
3	Vertical structures . . . . .	91

## Contents

---

3.1	Mean velocity structure . . . . .	91
3.2	Measured subsurface velocities and Ergün equation . . . . .	94
3.3	Turbulence structure . . . . .	94
3.4	Disturbance and dispersive stress . . . . .	99
3.5	Dispersive stress: parametrization and experimental profiles . . . . .	99
3.5.1	Comparison between the closure and experimental dispersive stress profiles . . . . .	99
3.6	Complete and approximated formulae . . . . .	99
3.7	Mixing length distribution . . . . .	100
3.7.1	Methodology to compute the mixing length distribution . . . . .	100
3.7.2	Surface layer and mixing length . . . . .	101
3.7.3	Roughness layer and mixing length . . . . .	104
4	Numerical 1D model and experimental results . . . . .	104
4.1	Reference parametrisation . . . . .	105
4.2	Damping effect influence . . . . .	105
5	Summary of the experimental results . . . . .	108
<b>6</b>	<b>Real case scenario and mountain river monitoring</b>	<b>109</b>
1	From surface velocity to flow depth . . . . .	111
1.1	Site, slope and grain size distribution . . . . .	111
1.2	Velocities . . . . .	111
1.3	Depth and relative submergence estimation . . . . .	111
1.4	Simulation of velocity profiles . . . . .	113
2	Depth and flow resistance formulas . . . . .	115
3	Consequences for the critical Shields stress . . . . .	119
3.1	Preamble . . . . .	119
3.2	Mechanistic model and methodology . . . . .	119
3.3	Simulations and critical shear stress estimations . . . . .	121
3.3.1	Without lift force and without turbulence . . . . .	122
3.3.2	With lift force and without turbulence . . . . .	122
3.3.3	With turbulence and Without lift force . . . . .	124
3.3.4	With turbulence and lift force . . . . .	125
4	Conclusions on mountain river monitoring . . . . .	126
<b>7</b>	<b>Conclusion and outlook</b>	<b>127</b>
<b>III</b>	<b>Appendix</b>	<b>131</b>
<b>A</b>	<b>Double-averaging methodology</b>	<b>133</b>
1	Definitions . . . . .	133
1.1	Time averaging . . . . .	133
1.2	Space averaging . . . . .	133
1.3	Spatial averaging theorem . . . . .	134
2	Double-averaged Navier-Stoke equations . . . . .	135
2.1	Continuity equation . . . . .	135
2.2	Double-averaged momentum equation . . . . .	135
2.3	Simplifications for gravity driven open channel flows with uniform conditions	136
2.4	Lemma on porosity and the gradient of the intrinsic velocity . . . . .	136

3	Spatial averaging and homogeneous porous media laws . . . . .	136
4	Viscous shear stress and spatial averaging . . . . .	137
4.1	Spatial averaging of the viscous shear stress . . . . .	138
4.2	Spatial averaging for dilute spherical particles in a pure straining flow: Einstein correction . . . . .	138
4.3	Spatial averaging for a unidirectional flow in a porous medium with a porosity gradient . . . . .	139
<b>B Numerical resolution of the 1D model</b>		<b>141</b>
<b>C Image velocimetry processing</b>		<b>143</b>
1	Pre-processing . . . . .	144
2	Velocimetry processing . . . . .	144
3	Post processing and interpolation scheme . . . . .	145
4	Test on the 4th PIV challenge - Case A . . . . .	146
<b>D Complements for the experimental procedure</b>		<b>149</b>
1	Benzyl Alcohol/Ethanol mixture . . . . .	150
2	Calibration curve of the constant head tank system . . . . .	151
3	Influence the permeable grid distance from the measure estimated with Darcy law	151
<b>E Vertical structure: experimental measurements and modeling</b>		<b>153</b>
<b>F Free surface velocity, slope, and grain size measurements in a gravel-bed river</b>		<b>159</b>
1	Image-based velocimetry measurement of free surface flow in a gravel bed river: methodology and testing . . . . .	159
1.1	Site and region of interest . . . . .	159
1.2	Discharge definition . . . . .	161
1.3	Methodology . . . . .	162
1.3.1	Image velocimetry algorithm . . . . .	162
1.3.2	Displacement constraint . . . . .	162
1.4	Results . . . . .	162
1.4.1	Instantaneous measurement . . . . .	162
1.4.2	Fluctuations and estimation of the accuracy . . . . .	162
1.4.3	Measurements from the gauging station . . . . .	165
1.4.4	Measurements on transverse sections upstream of the gauging station . . . . .	165
1.4.5	From the surface velocity to the depth-averaged velocity . . . . .	167
1.5	Conclusions on the evaluation . . . . .	168
2	Estimation of local slopes . . . . .	168
3	Grain-size distribution and median grain diameter . . . . .	170
<b>Bibliography</b>		<b>180</b>



## List of Figures

---

1.1	The Navizence River at Zinal . . . . .	1
1.2	Spatial scales in a gravel-bed river from aerial photographs . . . . .	3
1.3	Grain-scale processes of a turbulent flow over a rough permeable bed . . . . .	6
1.4	Refractive index matchnig and particle image velocitmetry . . . . .	8
2.1	Open-channel flow over an inclined bed . . . . .	14
2.2	Pioneering contribution of Chézy . . . . .	15
2.3	Flow over a rough impermeable bed . . . . .	18
2.4	Uniform gravity driven flow in a confined porous medium . . . . .	22
2.5	Drag approach and Darcy approach . . . . .	27
3.1	Scheme of a gravity driven turbulent flow over a permeable medium . . . . .	32
3.2	A schematic illustration of a bead lying on a packed bed of beads, side view. . .	36
3.3	A schematic illustration of a bead lying on a packed bed of beads, top view. . .	36
3.4	Evolution of the theoretical non-dimensional dispersive stress for a regular packed bed ( $\epsilon_b = 0.4$ ). . . . .	39
3.5	Slope/diameter diagram characterizing the turbulent penetration under the <i>roughness</i> <i>layer</i> . . . . .	44
3.6	Slope/diameter diagram characterizing the turbulent penetration under the roughness crest . . . . .	45
3.7	Case $\mathcal{P}$ low relative submergence flow on coarse sand . . . . .	49
3.8	Scenario $\mathcal{Q}$ , typical of a gravel-bedded river . . . . .	50
3.9	The reference case $\mathcal{R}$ , the hydraulics condition used in our laboratory . . . . .	51
3.10	Velocity profiles for four fluid depths . . . . .	52
3.11	Slope influence on the non dimensional velocity profiles . . . . .	53
3.12	Grain size influence on the non dimensional velocity profiles. . . . .	55
3.13	Porosity structure and bulk porosity influence . . . . .	56
3.14	Porous medium law influence . . . . .	57
4.1	Experimental set-up . . . . .	62
4.2	Porosity measurement with RIMS . . . . .	64
4.3	Scheme of the transverse continuous scan methodology . . . . .	67
4.4	From instantaneous to <i>double-averaged</i> quantities . . . . .	71
4.5	Points of interest surrounding a bead at the top of the permeable bed and turbulence statitstics . . . . .	72

## List of Figures

---

4.6	Temporal fluctuations for 8 measurement points as shown in Figure 4.5–(a). . .	73
4.7	Comparison of estimated profiles . . . . .	74
4.8	3D visualization of the horizontal velocity . . . . .	76
4.9	Side wall effect . . . . .	76
4.10	Comparison of the dispersive and turbulent stresses obtained with the fixed laser sheet . . . . .	77
4.11	Comparison between two replicates using the PIV-RIMS procedure . . . . .	78
4.12	Reproducibility evaluation with different bed structures . . . . .	79
4.13	Permeable outlet condition to ensure a subsurface flow . . . . .	81
4.14	Velocity profiles for various $\delta_g$ to evaluate the flow uniformity in the channel . .	82
5.1	Vertical profiles for the runs A1 ( $i = 0.5\%$ ) and A3 ( $i = 2\%$ ) . . . . .	87
5.2	Comparison of vertical velocity structures between Voermans <i>et al.</i> (2017) and the PIV-RIMS profiles (this study). . . . .	91
5.3	Velocity profiles and porosity profiles for the B runs . . . . .	92
5.4	Mean velocity structures for the nine experimental cases . . . . .	93
5.5	Measured subsurface velocities in a bi-disperse media $D = 7 - 9$ mm for 17 runs	95
5.6	Measured subsurface velocities in a bi-disperse media ( $D = 13/15$ ) mm for 11 runs	96
5.7	Bulk temporal and spatial statistics for A runs . . . . .	97
5.8	The turbulent stress structures for two different shear stress definitions and a comparison with Voermans <i>et al.</i> (2017) data . . . . .	98
5.9	Experimental dispersive stress distributions in comparison with the closure Equation 5.5 . . . . .	100
5.10	Measured vertical dispersive stress profiles from the closure Equation 5.5 in comparison with the simplified closure Equation 5.6 . . . . .	101
5.11	Depth-normalized distribution of the mixing-length evaluated from Equation 5.7. [Left] A runs ( $d_p = 8$ mm); [Right] B runs ( $d_p = 14$ mm). . . . .	102
5.12	Mixing-length distribution in the roughness layer . . . . .	103
5.13	Simulations with damping effect and experimental profiles for the run A3 . . . .	106
5.14	Simulations without damping effect and experimental profiles for the run A3 . .	107
6.1	Location of the region of interest on the Navizence River . . . . .	110
6.2	Free surface velocity field and velocity profiles on the transects . . . . .	112
6.3	Profile simulation for the upstream condition . . . . .	114
6.4	Profile simulation for the downstream conditions . . . . .	115
6.5	Simulations from the 1D model in terms of the non-dimensional Chézy coefficient	118
6.6	Force balance on a grain situated at the top of the permeable bed. $F_D$ , $F_M$ , $P$ , $F_B$ and $\mu N$ are the forces due to drag, lift, weight, buoyancy and friction, respectively. $\mathbf{V}$ is the instantaneous velocity vector, and $u_x = U_x + u'_x$ the instantaneous magnitude along $x$ . . . . .	120
6.7	Critical Shields number versus slope simulated from the hydraulic conditions of Prancevic & Lamb (2015) (see Table 6.2). Without turbulence and without lift forces ( $F_M = 0$ and $u_x = U_x$ ). . . . .	123
6.8	Critical Shields number versus slope simulated from the hydraulic conditions of Prancevic & Lamb (2015) (see Table 6.2). Without turbulence and with lift force ( $F_M$ given by 6.7 and $u_x = U_x$ ) . . . . .	123

6.9	Critical Shields number versus slope simulated from the hydraulic conditions of Prancevic & Lamb (2015) (see Table 6.2). With turbulence and without lift force ( $F_M$ given by 6.7 and $u_x = U_x$ ) . . . . .	124
6.10	Critical Shields number versus slope simulated from the hydraulic conditions of Prancevic & Lamb (2015) (see Table 6.2). With turbulence $u_x = U_x + 3 u_*$ and lift force ( $F_M$ given by 6.7 and $u_x = U_x$ ). Note that compared to the above Figure 6.8, the limits for the $\Theta_{th}$ axis have been changed . . . . .	125
C.1	Graphical overview of the workflow: from the raw image to the velocity field. . .	143
C.2	Displacement measured on the 4th PIV Challenge . Case A (e.g. Kähler <i>et al.</i> (2016)) . . . . .	146
C.3	Histogram of the vertical and horizontal displacement measured on the 4th PIV Challenge . Case A (e.g. Kähler <i>et al.</i> (2016)) . . . . .	147
C.4	Root mean square of the displacements measured on the 4th PIV Challenge . Case A (e.g. Kähler <i>et al.</i> (2016)) . . . . .	147
D.1	Measure of the refractive index of the Benzyl-Alcohol/Ethanol mixture . . . . .	150
D.2	Measure of viscosity and density of the 40/60 Benzyl-Alcohol/Ethanol mixture .	150
D.3	Calibration curve of the flow discharge $q_f$ at the inlet of the flume . . . . .	151
E.1	Run A1 - Simulated and measured profiles . . . . .	154
E.2	Run A2 - simulated and measured profiles . . . . .	154
E.3	Run A4 - Simulated and measured profiles . . . . .	155
E.4	Run B1 - Simulated and measured profiles . . . . .	155
E.5	Run B2 - Simulated and measured profiles . . . . .	156
E.6	Run B3 - Simulated and measured profiles . . . . .	156
E.7	Run B4 - Simulated and measured profiles . . . . .	157
E.8	Run B5 - Simulated and measured profiles . . . . .	157
F.1	Location of the gauging station . . . . .	160
F.2	The region of interest upstream of the stream gauge station . . . . .	160
F.3	Raw image of the region of interest showing the scale $14.6\text{m} \approx 700 \text{ px}$ . . . . .	161
F.4	Instantaneous free surface velocity measurement performed using the image velocimetry algorithm. The instantaneous velocity is measured from two consecutive frames spaced of $\Delta T = \frac{1}{f_p} = 83 \text{ ms}$ . . . . .	163
F.5	Standard deviation of the velocity magnitude calculated from the surface over a video of 9 seconds (111 pairs of images). . . . .	163
F.6	Temporal evolution and Probability Density Function of the velocities . . . . .	164
F.7	Estimated standard deviation of the empirical error as a function of the sampling time interval. . . . .	164
F.8	Discharge and water depth evolution on 20th of June 2018. . . . .	165
F.9	Time averaged velocity field and position of the transverse section upstream of the gauging station. . . . .	166
F.10	Time averaged velocities at the transverse section upstream of the gauging station. 166	
F.11	Averaged surface velocities on the transects shown in Figure F.9. . . . .	167
F.12	Measurement of the local slope using the Pix4D mapping software . . . . .	169
F.13	Estimates of 3 local slopes by employing the Pix4D mapping software . . . . .	170

**List of Figures**

---

F.14 The region of interest in which the river bed grain sizes were measured was located in the dead arm. The red disks represent the area covered by the selected individual measured stones. . . . . 171

F.15 Particle size distribution in the dead arm and mass median grain diameter estimated at  $D_{50} = 0.58$  m. . . . . 171



## List of Tables

---

3.1	Summary of the closure choices for the governing Equation 3.23. . . . .	47
3.2	Reference parameters of the model . . . . .	50
3.3	Characteristics of the scenarios . . . . .	52
3.4	Characteristics of the different grain size scenarios . . . . .	54
4.1	Experimental conditions for the test of the PIV-RIMS methodology . . . . .	68
4.2	Experimental conditions for the Fixed Laser Sheet and the Moving Laser Sheet. . . . .	68
5.1	Hydraulic parameters for the nine runs . . . . .	86
5.2	Hydrodynamic properties of Voermans <i>et al.</i> (2017) . . . . .	90
5.3	Summary of the different length scales associated with the subsurface layer and the surface layer . . . . .	93
6.1	Hydraulic properties in the 3 transects . . . . .	113
6.2	Hydraulic conditions of the Prancevic & Lamb (2015) runs . . . . .	122



## Notation

---

### Parameters

$h_f$	Flow depth	[m]
$d_p$	Grain size	[m]
$\rho_f$	Fluid density	[kg/m <sup>3</sup> ]
$\nu_f$	Kinematic viscosity	[m <sup>2</sup> /s]
$\rho_s$	Sediment density	[kg/m <sup>3</sup> ]
$\mu$	friction factor	[-]
$g$	Gravity	[m s <sup>-2</sup> ]
$i$	Inclination	[%]
$\zeta$	Bed angle	[radian]
$\tau_b$	Bed shear stress	[kg m <sup>-1</sup> s <sup>-2</sup> ]
$\Theta$	Shields stress	[-]
$p$	Pressure	[Pa]
$W$	Channel width	[m]
$R_h$	Hydraulic radius	[m]
$Q_f$	Discharge	[m <sup>3</sup> /s]
$q_f$	Discharge per unit width	[m <sup>2</sup> /s]
$z_{rc}$	Elevation of the roughness crest	[m]
$z_t$	Elevation of the roughness troughs	[m]
$z_{surf}$	Elevation of the free surface	[m]
$\epsilon(z)$	Porosity profile	[m]
$\epsilon_b$	Bulk porosity	[m]
$K$	Permeability	[m <sup>2</sup> ]
$l_p$	Pore length scale	[m]
$T$	Temperature	[°K]
$n_f$	Fluid refractive index	[-]
$\sigma_f$	Fluid surface tension	[N · m <sup>-1</sup> ]
$\chi$	Dimensional Chézy coefficient	[m <sup>1/2</sup> /s]
$C$	Non-dimensional Chézy coefficient	[-]
$\kappa$	von Kármán ‘constant’	[-]
$\phi_{Eth}$	Volume fraction of Ethanol	[-]

**Velocity, averages and double-averaged stresses**

$\mathbf{V}$	Instantaneous velocity vector	[m/s]
$u_x$	Instantaneous velocity along $x$	[m/s]
$\bar{u}_x$	Time averaged velocity along $x$	[m/s]
$\langle \bullet \rangle_s$	Superficial spatial averaging	
$\langle \bullet \rangle$	Intrinsic spatial averaging	
$\langle u_x \rangle$	Spatially averaged velocity along $x$	[m/s]
$\tilde{u}_x$	dispersive velocity component or disturbance	[m/s]
$U_x = \langle \bar{u}_x \rangle$	Double-averaged velocity along $x$	[m/s]
$U_b$	bulk velocity	[m/s]
$u_*$	shear velocity	[m/s]
$\tau_d = -\rho_f \epsilon \langle \tilde{u}_x \tilde{u}_z \rangle$	Dispersive stress	[kg m <sup>-1</sup> s <sup>-2</sup> ]
$\tau_t = -\rho_f \epsilon \langle u'_x u'_z \rangle$	Turbulent stress	[kg m <sup>-1</sup> s <sup>-2</sup> ]
$\tau_v$	Viscous stress	[kg m <sup>-1</sup> s <sup>-2</sup> ]

**Non-dimensional numbers**

$Re_b$	Bulk Reynolds number	[-]
$Re_{surf}$	Surface Reynolds number	[-]
$h_+$	friction Reynolds number	[-]
$Re_K$	Permeability Reynolds number	[-]
$Fr$	Froude number	[-]

**Closure parameters**

$f_v$	Volume averaged viscous drag force	[N m <sup>-3</sup> ]
$f_p$	Volume averaged pressure drag force	[N m <sup>-3</sup> ]
$\lambda_+$	Dispersive stress parameter	[-]
$A_E$	Constant of the linear term of the Ergün equation	[-]
$B_E$	Constant of the quadratic term of the Ergün equation	[-]
$l_m$	Mixing length distribution	[m]
$Z_{vD}$	Mixing length - vertical distance	[m]
$Re_{vD}$	van Driest Reynolds number	[-]
$C_{vD}$	Mixing length - additional term	[-]
$C_p$	Roughness layer constant	[-]

**Abbreviations**

PIV	Particle Image Velocitmetry
RIMS	Refractive Index Matched Scanning
ROI	Region Of Interest
UAV	Unmanned Aerial Vehicle
DTM	Digital Terrain Model

# 1

## Introduction

---

Among the diverse flow processes found on Earth, flow in rivers is likely to be the most scrutinized. Rivers form remarkable valleys and provide valuable resources, services, and ecosystems. Usually, these coupled earth/water systems evolve gently, but sporadic heavy rainfall may abruptly change the water level and the material-at-rest equilibrium, triggering floods and massive sediment transport events with devastating consequences. Predicting such flows is a central concern of fluvial hydraulics and involves many physical aspects such as hydrodynamic forces, turbulence, and granular media processes.



Figure 1.1 – The Navizence River at Zinal (Wallis - Switzerland). Credit: Bob de Graffenried

## 1 Preliminary field observations

In mountainous environments, rivers exhibit shallow waters with roughness elements such as stones and pebbles that are comparable in size to water depth. This feature is typical of a gravel-bed rivers, the systems examined in the course of this dissertation. In such environments,

interactions between surface water, subsurface water, and sediments are expected to be intricate. Indeed, these streams are far distinct from alluvial rivers, where most of the sediment transport and flow resistance laws have been established. A quick look at the photograph shown in Figure 2.1 reveals some of the specificities of this system: Running water may seep between coarse elements to reappear several meters further on, and a large quantity of gravel and boulders with young vegetation may emerge. In braided rivers, for example, there may be only a small percentage of the bed surface that is usually covered by water. Seepage observation reveals that a riverbed is permeable, and sometimes highly permeable. Dry areas between riverbanks substantiate the hypothesis that in the course of an extreme episode, hydraulic conditions may deviate considerably from the ordinary state.

A diverse range of bedforms can be observed in the aerial views presented in Figure 1.2. These bedforms are termed *alternate bars*, *riffles*, or *antidunes*, and result from diverse entrainment and deposition processes. In turn, these bedforms control the flow path and impose large spatial variabilities on the system. At the grain scale, the flow path is disturbed by the presence of protuberances affecting both the turbulence behavior and the fluid surface.

Based on these observation and focusing on the gravel-bed river at the grain scale, this thesis investigates steep open channel flow over rough permeable beds involving relatively small submergence. Comparisons between the roughness size and flow depth reveal the relative submergence to be a key concept for this flow type.

## 2 Hydrodynamic problems in gravel-bed rivers

With knowledge of the flow discharge, hydraulicians and hydro geomorphologists usually predict the expected flow depth, velocities, and sediment transport rates for various natural or anthropogenic geometries (e.g. bed slope, bank width, roughness height). These predictions are essential for river management such as bedform or ecosystem classification and restoration, and are crucial for the building of bridges, dikes, and dams, where failures may incur important costs.

### 2.1 Flow resistance

Considerable efforts have been made to study flow resistance in open channels, i.e., to link mean velocity to slope and depth. For flows over a surface with small-scale roughness, these predictions can be successfully obtained by the Prandtl boundary layer theory. This produces logarithmic profiles that accurately predict most open-channel flow measurements in large relative submergence conditions. Encouraged by the success of this approach, researchers have been extensively applying it to steeper open channel flows with smaller relative submergences, such as gravel-bed streams (Hey, 1979; Griffiths, 1981; Bathurst, 1985). Although the assumptions required to provide the log-law of the wall are not verified in these conditions, the authors overcome this issue by providing case-by-case parametrization. However, recent studies have demonstrated the large bias produced with the log-law framework, and have suggested a more appropriate power law calibrated on field data (Ferguson, 2007; Rickenmann & Recking, 2011). This alternative approach improves flow resistance predictions, although another important issue is brought to light: the physics underlying the turbulent boundary layer fail to provide reliable predictions of flows showing a small relative submergence.

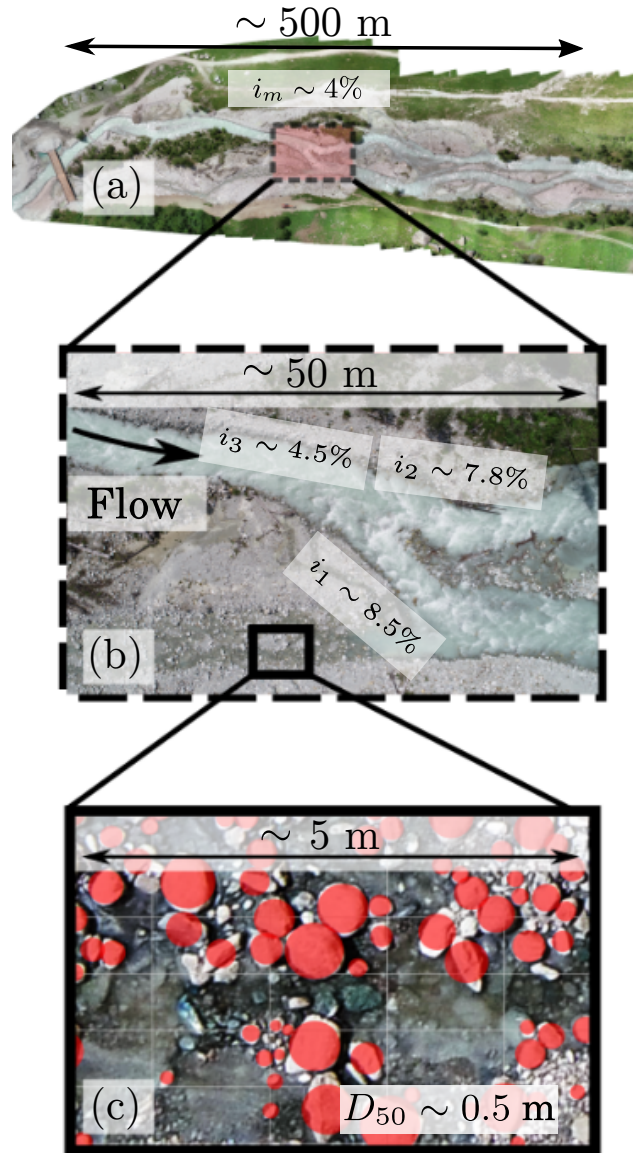


Figure 1.2 – Spatial scales in a gravel-bed river from aerial photographs: the Navizence River (Wallis - Switzerland).

(a) At the kilometer scale, a braided river is observed with a succession of bed forms. The average slope is measured at  $i = 4\%$  where  $i$  is the slope.

(b) At the bed form scale, the slope can vary locally from  $i = 4\%$  to  $i = 10\%$ . The main channel is separated into two channels downstream.

(c) At the grain scale, the size distribution of the bed can be estimated in a dead arm. The red disks represent the measured equivalent surface of the stones.

In addition, owing to the complications in defining flow depth with a large roughness size, inconsistencies are observed between field campaign measurements and predictions. Consequently, specialists are keen to work directly on flow discharge, which is better defined in these conditions, and thus more accurately monitored.

### 2.2 Hyporheic exchanges

In addition to flow resistance, water exchanges between the free surface and groundwater play a critical role in regulating fluvial ecosystems. These exchanges are termed hyporheic flows, an adjective combining the Greek prefix ‘hypos’ and the root word ‘rheos’, meaning ‘under the flow’. In these zones, diffusive processes transport waters from different origins, catalyzing reactions, supplying nutriment to microorganisms and plants, and with a domino effect, delivering food to the entire aquatic macrofauna.

An outstanding effort to summarize the hyporheic exchange issues was made by Boano *et al.* (2014). While the chemical aspects of this work are out of the scope of this dissertation, a glance at this review reveals a poor understanding of the hydrodynamics at the grain scale. Convective and diffusive components transporting solutes in rivers are generally considered at a larger scale. The exchange models involve bedforms such as dunes and meanders, which can act as obstacles creating dead zones or forcing the gain or loss of water (Bencala & Walters, 1983; Elliott & Brooks, 1997; Fox *et al.*, 2014). For uniform flows, as emphasized by Blois *et al.* (2014), numerical models typically treat the surface and the subsurface flow as two divided layers, assuming turbulent flows above the bed and Darcian flows beneath. Coupling both flows is then obtained with step conditions forcing the continuity. Little is known about local exchanges at the interface between the ground water flows and the surface flows where the *roughness layer* might play an crucial role.

### 2.3 Incipient motion

Solid materials in steep rivers are transported downstream by sliding, rolling or saltating over the movable bed. This is the so-called bed load transport process. The bed is traditionally assumed to become mobile when hydrodynamic forces on the grains, evaluated through the bed shear stress, cross a defined threshold.

In turbulent flow conditions, low sediment transport rates fluctuates and a fixed threshold is not observed (Buffington & Montgomery, 1997). Nevertheless, a transition from low sediment transport rates to a rapid growth in these rates when the bed shear stress increases is observed. This transition allows to define a non dimensional bed shear stress threshold, also called critical Shields number.

The slope influence on incipient motion has fertilized many debates in the last two decades, since well-documented experiments have reflected an unexpected behavior, i.e., an increment in the non dimensional bed shear stress required to mobilize grains when the slope increases, whereas the gravitational contribution should rationally reduce it. This behavior is only observable with steep streams, i.e., conditions that are inevitably of low relative submergence. Consequently, classical river transport formulae often predict higher sediment transport rates than observed in steep rivers. Some authors explained this feature in term of force balance on individual grains



(Lamb *et al.*, 2008; Recking, 2009) while Ferguson (2012) explained it based on bulk-flow terms. These different approaches reveal the limit of the traditional frameworks employed for river flows. Although the bed shear stress is probably the most popular term in environmental hydraulics, it is still roughly defined in low submergence conditions where a non negligible part of the flow seep through the bed layers (Nikora *et al.*, 2007).

#### 2.4 Sediment-fluid interface modeling: a recurrent issue

As highlighted above, the lack of understanding of the hydrodynamic processes of the interface between the permeable bed and the fluid surface has been raised as the most recurrent and fundamental issue. A major reason behind is the difficulty in obtaining accurate measurements across this interface. Without detailed experiments to characterize the complexity of the flow at the interface, the common approach is to use models built from measurements on deep flows over impervious rough beds. When the conditions under which these mechanistic models are applied are examined, their transfer to shallow flows over rough permeable beds reveals important inconsistencies:

- The transition from the permeable bed to the surface flow is usually considered as a step boundary problem, while the properties of the permeable bed evolve continuously across the interface via the *roughness layer*.
- The traditional log-law framework is generally applied, although it is unable to describe the various mechanisms involved at the interface. In addition, the conditions required to obtain the logarithmic function from the governing equations are not fulfilled.
- As the interface is not well defined, there are difficulties in defining flow depth. This causes discrepancies in the definition of the bed shear stress, as well as the determination of a reference. As a result, flow resistance and incipient motion predictions that rely on these definitions are subject to large uncertainties.

To obtain a more comprehensive picture of the flow across the interface, the *double-averaging* concept is essential. This allows the problem to be treated continuously.

## 3 Double-averaging methodology

### 3.1 Concept

At the grain scale, flows over rough permeable beds involve the development of turbulent boundary layers with large spatial heterogeneity as shown in Figure 1.3. Protuberances act as obstacles to the flow, creating local wakes and producing different classes of velocity profile (Mignot *et al.*, 2009a). Moreover, the flow paths in the roughness layer and the interior of the porous media are tortuous.

A local description of flow around grains has the potential to improve models resolving time-dependent structure such as *Large Eddy Simulations* (LES) or *Direct Numerical Simulations* (DNS). However, the fluvial fluid mechanics involve complex forcing, and the classical assumptions

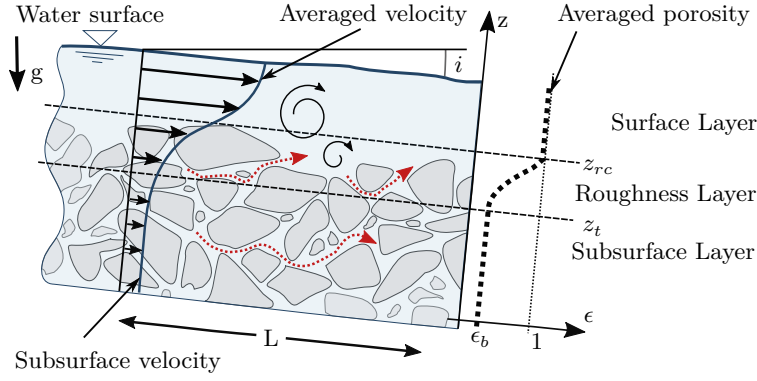


Figure 1.3 – Grain-scale processes of a turbulent flow over a rough permeable bed. The porosity  $\epsilon$  and velocity profiles are averaged over a thin layer parallel to the flow on the mesoscopic longitudinal distance  $L$ , as prescribed by the *double-averaging* concept. The flow is subdivided into three specific regions: the *surface layer*, the *roughness layer*, and the *subsurface layer*. The roughness crest  $z_{rc}$  above which the averaged porosity is 1, and the troughs of the roughness elements  $z_t$  where the bulk porosity  $\epsilon_b$  is reached, delimit the *roughness layer*. The red dotted arrows represent streamlines in the *roughness* and *subsurface layers* both forming the *permeable bed*.

involved in modeling turbulence in these approaches are commonly violated (Keylock, 2015). Furthermore, *Computational Fluid Dynamic* tools that can model the flow between grains and provide very detailed descriptions of the flow are computationally expensive, and are not realistically useful for modelling flows at river scales.

Instead, it is more appropriate to model processes at the mesoscopic scale by spatially averaging them over a larger volume. For homogeneous porous media, it is common to upscale the hydrodynamic processes from the pore to the mesoscopic scale to explain empirical laws such as the Darcy law (Whitaker, 1986). For water flows over rough permeable beds, these quantities fluctuate in time, i.e., they involve turbulence. Thus, averaging must first be performed over the temporal scale, to produce time-averaged quantities, and then averaging can be performed over the spatial scale of a thin layer parallel to the mean bed. This global averaging procedure in time and space is termed the *double-averaging* methodology (Nikora *et al.*, 2001, 2007). It can produce the averaged velocity profile, as well as the mean porosity profile. The averaged porosity profile allows the flow to be subdivided into three different layers, the *surface*, *roughness* and *subsurface* layers, as observed in Figure 1.3.

### 3.2 Crucial role of the vertical porosity structure

The spatial averaging methodology applied to rough beds produces a continuous porosity profile that contains information describing the interface. As observed in Figure 1.3, the distance  $z_{rc} - z_t$  defines the *roughness layer* thickness, whilst if  $\epsilon_b = 0$ , the bed is impermeable at  $z = z_t$ . This characterization of the bed interface as a continuum contrasts with most previous theoretical investigations. Indeed, the problem of flows adjacent to a permeable wall is commonly treated by introducing a step boundary condition between the two regions (Beavers & Joseph, 1967; Mendoza & Zhou, 1992; Breugem *et al.*, 2006; Tilton & Cortezzi, 2008; Rosti *et al.*, 2015; Zampogna &

Bottaro, 2016). This condition involves a complex procedure to include the momentum transfer at the boundary as described by Ochoa-Tapia & Whitaker (1995). Also, for simplification reasons, an empirical Brinkman condition that imposes penetration of the momentum for an arbitrary distance is generally introduced (Brinkman, 1949). This method is regularly questioned since the inertial effect is expected to penetrate into the porous medium when turbulence is observed in the surface layer (see the discussions on this problem of Tilton & Cortelezzi (2008) or Zampogna & Bottaro (2016) for examples).

A continuous description within the *double averaging* framework offers an alternative method to describe flows over permeable or impermeable rough walls. The roughness thickness is therefore revisited as a thin permeable medium with a varying porosity, where closures can be adapted according to experimental results. In general, I argue that the continuous porosity offers a relatively unexploited and practical approach to describe diverse types of rough interfaces where the roughness layer plays an active role.

### 3.3 Double-averaged momentum equation

*Double-averaging* of the Navier-Stokes equations provides the *double-averaged momentum equations*. Five distinct terms result from the procedure. The classical *viscous stress* and *turbulent stress* are generated from the time averaged procedure, and three additional terms are produced with the spatial averaging procedure: the *viscous drag*, the *pressure drag*, and the *dispersive stress* (also termed *form induced stress*).

The *dispersive stress* and *turbulent stress* are algebraically defined and can be conveniently captured from experimental or *computational fluid dynamic* model outputs. *Dispersive stress* has recently received particular attention; it is a measurable stress associated with the spatial variability of the velocities. Studies have revealed that this stress has a non-negligible role, with a maximum being observed just below the roughness crest (Voermans *et al.*, 2017; Fang *et al.*, 2018).

## 4 Main motivations and contribution

Predictions of flow resistance and incipient motion remain inaccurate for small relative submergence flows in gravel-bed rivers. This inaccuracy is due to the extensive use of incomplete tools for monitoring this flow types. Regarding these lack of consensus and understanding, the work covered in this study aims to provide a 1D model to predict the vertical structure of flows over rough permeable beds under turbulent conditions.

The spatial averaging procedure, which is performed subsequent to the time-averaging procedure, is now considered as the most suitable approach to describe open channel flows with small relative submergence. With this approach, the resulting *double-averaged momentum equation* provide terms that need closures.

For this purpose, comparison of predictions to reliable measurements forms the principle obstacle. Velocity measurements in the permeable bed, i.e. in the *roughness* and the *subsurface layers*, cannot be performed with most available equipment. Invasive methods dramatically affect the flow, and non-invasive methods such as *Particle Image Velocimetry* (PIV) or *Laser Doppler*

## Chapter 1. Introduction

*Velocimetry* (LDV) are limited by the opacity of the permeable bed (Pokrajac *et al.*, 2007; Mignot *et al.*, 2009a; Cameron *et al.*, 2017). To overcome these issues, I employed the *Refractive Index Matched Scanning* (RIMS) method coupled with a PIV technique for measuring velocities across the interface. RIMS is an alternative approach to examine the interior of the permeable bed that involves adjusting the refractive index of a fluid mixture to match the refractive index of a transparent solid material, as illustrated in Figure 1.4. The velocities are thus continuously collected in the three-dimensional space while a laser sheet is moving. Using an idealized approach, the fluid mixture flows over glass beads in a rectilinear flume and provides velocity profiles for a unidirectional flow condition.

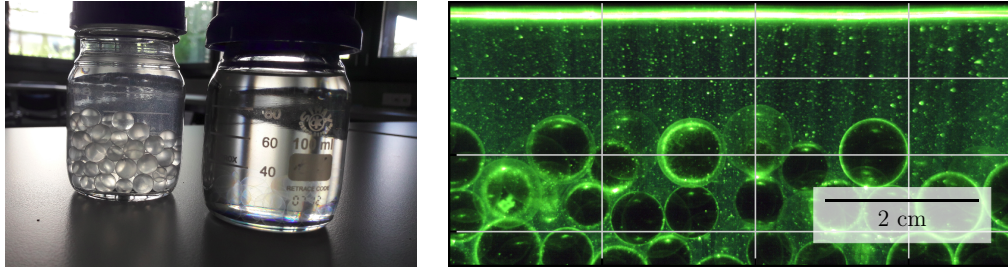


Figure 1.4 – [Left] - Two bottles containing glass beads in equal quantities. The left bottle also contains water, while the right bottle also contains a fluid that exactly matches the refractive index of the solid glass beads. In the bottle with water, the refractive index difference between the solid and liquid permits the differentiation of the beads. In the bottle on the right, the beads are invisible, and the interstitial fluid is accessible for measurements. [Right] - Photograph of a gravity-driven flow ( $i = 0.5\%$ ) over a rough permeable bed composed of glass beads. The *refractive index matching* technique allows for examination of the interior of the *roughness layer* and the *subsurface layer*. The black disks are glass beads crossed by the laser sheet, while the small dots are tracers. By using two consecutive images, the displacement of the tracers can be measured via a PIV technique, yielding instantaneous 2D measurements of the velocity field.

These experimental results permit to establish the critical role of the *damping effect* (van Driest, 1956) and the *velocity defect-law* (Coles, 1956) for small relative submergence flows.

In addition, these experimental results describing the vertical structure of the flow helped to devise a 1D model based on the double-averaging concept. A mechanistic closure for the dispersive stress has been developed. The other terms of the unidirectional *double-averaged momentum equation* have been parametrized according to existing contributions and adapted to the continuous porosity approach. The 1D model is then able to predict the vertical structure of the flow for various hydraulic condition and without the introduction of a vertical origin. This model is fundamentally dependent on the continuous description of the bed roughness via averaged porosity profiles at the mesoscopic scale, an approach that contrasts with most previous studies on flow/porous structure interactions.

Finally, this 1D model is compared with the main empirical laws employed in gravel-bedded rivers to predict flow resistance and incipient motion calibrated on field datas.

This work provides novel results concerning turbulent flows over permeable rough beds, with potential applications for gravel-bed flows. However, the scope of this study goes beyond the

framework of fluvial hydraulics; insights and developments acquired in the course of this thesis are likely to be transferable to other domains where a turbulent fluid flows over a rough permeable medium.

From a mechanistic point of view, a mountain stream is a liquid flowing on a permeable polydispersed granular medium with a small relative submergence. With regard to fluidity, this system is a case study of the larger scientific family of flows over rough porous media. This family includes diverse processes, including atmospheric boundary layer modeling such as wind/forest (Novak *et al.*, 2000) and wind/building (Roth, 2000) interactions, and flow over submerged aquatic canopies (Ghisalberti & Nepf, 2009)).

## 5 Outline of the dissertation

Including the introduction, this dissertation contains seven chapters:

- Chapter 2 provides an overview of the current position on open-channel flows and porous media flows. These two domains are generally disconnected, even though they are both essential to describe the problem. This chapter closes with a presentation of the previously documented investigations on fluid/porous structure interactions that inspired this thesis.
- Chapter 3 covers the theoretical developments leading to the 1D model to describe flows over rough permeable beds. While this theoretical development owes a great deal to the experimental insights presented in Chapters 4 and 5, a description of the fundamentals of the *double-averaging* framework is essential to understand what the experimental procedure involves.
- Chapter 4 is devoted to description of the experimental set-up, the materials, and the transverse scanning methodology. This chapter closes with an examination of flow uniformity and steadiness conditions in the flume.
- Chapter 5 presents the experimental results. The experimental vertical profile is discussed and compared with the existing theories on open-channel flows. The second part of this chapter is devoted to a comparison of the experimentally obtained vertical profiles with the model developed in Chapter 3.
- Chapter 6 illustrates a real case scenario and shows why the definitions of flow depth in the fluvial hydraulics are critical. Flow resistance and incipient motion predicted by the 1D model are compared with existing formulae in the literature.
- Chapter 7 concludes this dissertation with a discussion on the experimental results and the findings provided by the model. Guide-lines for monitoring gravel-bed streams are suggested.



# Theory **Part I**





# 2

## Fluvial flows and porous media

---

This chapter provides the essential scientific background for the understanding of my research. In parallel, the mathematical notations and the definitions employed in the course of this dissertation are presented. In the first section of this chapter, a brief historical overview which traces the origins of the contemporary tools in fluvial hydraulics is presented. Modern concepts from the boundary layer theory such as the *van Driest damping effect* as well as the *velocity-defect law* play a key role in describing the experimental results of this manuscript. The current limitations of open-channel flow models when applied to rough beds with a small relative submergence are highlighted. Moreover, as explained in the introduction, the permeable bed is regarded as a porous media continuum where the mean porosity profile varies sharply in the *roughness layer* between the *surface layer* and *subsurface layer*. In addition to questions of hydraulics, porous media processes are therefore presented in the second section. The duality between drag force based law and porous media law to relate solid/fluid interactions is introduced. In the last section, the pioneering contributions and the recent advances concerning flows adjacent to a porous structure that inspired my research are reviewed.

### 1 Turbulent open-channel flows

#### 1.1 River flow and friction laws: an historical review

This section chronologically reviews the outstanding investigations over the past three centuries which have influenced the river science community.

Quantitative fluvial hydraulics in the western world trace their origins back to the XVIII c. Savants, inspired by the well established Newton laws and Euler's derivations around 1750, explained the velocity steadiness in open-channel flows by a bed friction force on the bed surface that exactly compensates for the gravitational interaction on the water:

$$\underbrace{P\delta_x \tau_b \cdot e_x}_{\text{friction}} = \underbrace{M \cdot e_x}_{\text{gravity}} = V_f \rho_f g \sin \zeta \quad (2.1)$$

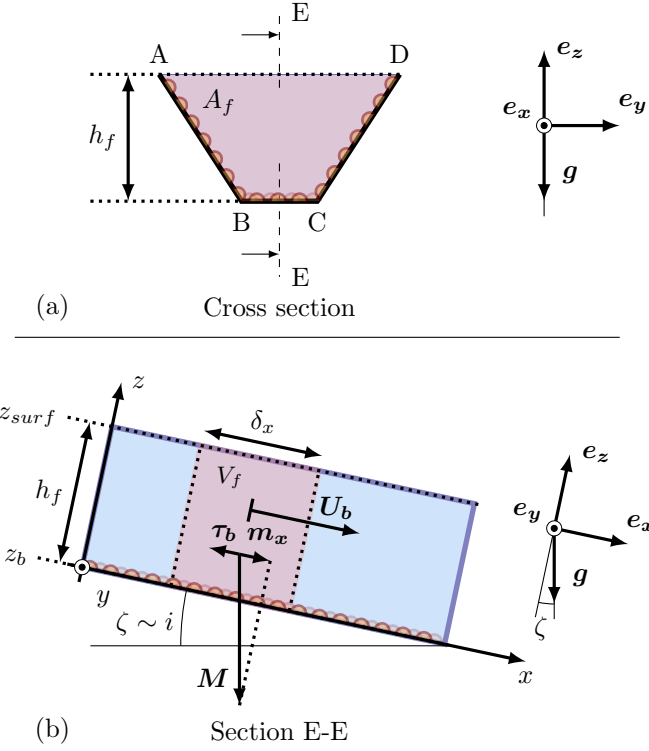


Figure 2.1 – Open-channel flow over an inclined bed

$\mathbf{M} = \rho_f V_f \mathbf{g}$  is the weight of an inclined column of fluid of volume  $V_f = \delta_x A_f$ , where  $A_f$  is the cross sectional area on Figure 2.1-(a). The friction force on the total bed area  $\delta_x P$  balances the projected mass on the streamwise direction, where  $P$  is the wetted perimeter [ABCD] on the Figure 2.1-(a).  $\tau_b$  is a force per unit bed area,  $g$  is the gravity constant,  $\rho_f$  is the fluid density in kilogram per cubic meter and  $\zeta$  the bed angle in radian. From mountainous to low land environments, fluvial channels are slightly inclined (the slope  $i$  rarely exceeds 20%) and the small-angle approximation is generally assumed:  $i = \tan \zeta \sim \sin \zeta \sim \zeta$ .

By defining the hydraulic radius  $R_h = \frac{A_f}{P}$ , Equation 2.1 becomes :

$$\tau_b = m_x = \rho_f g R_h i \quad (2.2)$$

Note that the flow depth  $h_f$  is equivalent to the hydraulic radius when the channel is wide enough. To obtain the relation between the slope, the hydraulic radius and the velocity, a closure that relates the friction  $\tau_b$  to the mean velocity is required. In 1757, the German scientist Albert Brahms introduced the idea that this action in uniform flow should be proportional to the square of the velocity (Brahms, 1757). While Brahms provided measurement of depth, velocity and slopes of rivers to verify his statements, he never published a formula (Herschel, 1897).

Shortly after, Antoine Chézy, engineer from the new École National des Ponts et Chaussées, was tasked in 1768 with designing the cross section of a channel to bring fresh water to Paris from the Yvette river. It is a critical engineering challenge, since the width and the slope of the channel must be scaled to provide the desired flow discharge. Chézy found nothing relevant in the literature that addressed the issue and started his own measurements, on the Seine river and other waterways, devising the most lasting formula to describe open-channel flows in 1775:

$$U_b = \chi \sqrt{R_h i} \implies \tau_b = \rho_f g \frac{U_b^2}{\chi^2} \quad (2.3)$$

where  $\chi$  is the dimensional Chézy coefficient that depends on the properties of the channel.  $U_b = \langle U_x \rangle_{V_f}$  is the volume-averaged velocity<sup>1</sup>. Interestingly, in his original manuscript, Chézy admitted that his formula is not adequate as a general theory but must be determined from one channel configuration to another<sup>2</sup>.

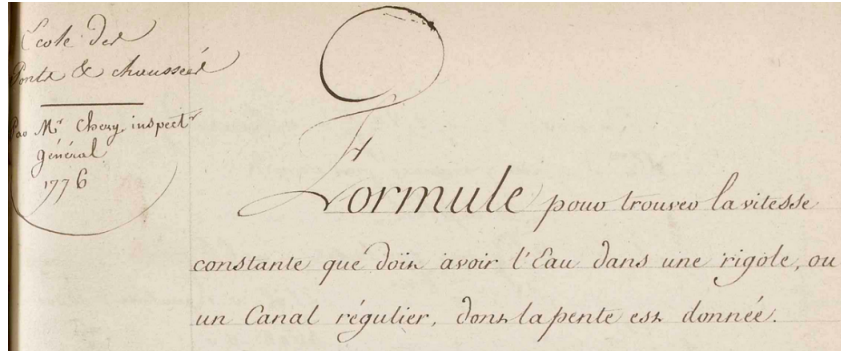


Figure 2.2 – Few traces survive of the pioneering contribution of Chézy. Here is a copy of the second manuscript of Chézy from 1776 describing the formula (from the library of Ecole National des Ponts et Chaussées)

His successors, Pierre Du Buat, Pierre-Simon Girard and Gaspard de Prony, acknowledged the pioneering efforts of Chézy but found it more appropriate to work on a binomial form:

$$\tau_b = K_1 U_b + K_2 U_b^2 \quad (2.4)$$

These scientists were focused on Equation 2.4 to conclude with a general theory that included viscous effects through the additional linear term (de Prony, 1804). Although this resolution has been fruitful in producing the future Darcy-Weisbach and the Navier-Stokes derivations, it has been a source of confusion for hydraulic engineering issues. Indeed, it is now well established that viscosity plays a negligible role in fluvial flows. Nevertheless, Girard used the binomial formulation to devise the Ourcq canal that opened to navigation in 1822. After that, the binomial

<sup>1</sup> $\langle U_x \rangle_{V_f} = \frac{1}{V_f} \iiint_{V_f} U_x(z) dV$  is the mean velocity, where  $U_x(z)$  is the velocity at the altitude  $z$

<sup>2</sup>According to Herschel (1897), Chézy's contribution has not been fairly recognized by his peers. De Prony, the director of the "Ecole des ponts et chaussées" and Chézy's friend wrote : "Chézy died poor, [...] the period from 1745 to 1798 [...] was not favourable for modest engineers" (An excerpt from a notice written by Helmina von Chézy, Chézy's daughter-in-law (von Chézy, 1834)). During this "Age of Enlightenment", the Yvette canal was canceled and the French Revolution broke out in France.

formulation was progressively depreciated for open-channel flows predictions.

During the XIX c, various formulations similar to the Equation 2.3 were developed in Europe. For instance, Eytelwein developed what is still known as the Chézy-Eytelwein law in Germany. From Italy, the Tadini formula, identical to the Chézy formula, became one of the most popular open channel equation in Europe. After years of calibration, most engineers established that the constant  $\chi \approx 50 \text{ m s}^{-1/2}$  must be adopted.

Continuing Du Buat's, Prony's and Girard's achievements, Henry Darcy (1803-1858) and Julius Weisbach (1806 - 1871), developed an equation that significantly impacted on the fluvial engineering community. Whilst their contribution was more intended to predict pipe flows than river flows, the non dimensional Darcy-Weisbach coefficient  $f$  gained popularity because of its convenience for transferring the equations from one metric system to another (Brown, 2003). The relation is given by :

$$\tau_b = f \rho_f \frac{U_b^2}{8} \implies U_b = \sqrt{\frac{8}{f}} \sqrt{g R_h i} \quad (2.5)$$

Later, outstanding efforts were made by Phillipe Gauckler(1826-1905), Robert Manning (1816-1897) and Albert Strickler (1887 - 1963) in calibrating a more rigorous empirical formula. They established that the bulk velocity is better described by :

$$U_b = \chi \sqrt{R_h i} = \frac{1}{n} R_h^{2/3} i^{1/2} \quad (2.6)$$

where  $n$  is the Manning coefficient that must be calibrated for various bed surfaces. For instance, Stickler suggested  $n = d_p^{1/6}/24$ . The Chézy coefficient is thus parametrized by  $\chi = \frac{R_h^{1/6}}{n} = 24 \frac{R_h^{1/6}}{d_p}$ .

Chézy, Darcy-Weisbach or Manning-Strickler formulae are nowadays widely employed by water engineers since they allow prediction of depth in rivers with various discharges, slopes, and roughness. These predictions are essential for navigation channels where boats need a certain depth to navigate. They become crucial for forecast issues, i.e., predictions of extreme floods where existing bridges, dikes, dams or other infrastructures are involved, or are being constructed.

Most of these formulae were calibrated for low gradient rivers ( $i < 1\%$ ). More than a century later, studies reveal that significant uncertainties persist for steep streams ( $i > 1\%$ ) such as gravel-bed rivers (Bathurst, 1985; Ferguson, 2007; Rickenmann & Recking, 2011).

The observed uncertainties on empirical relations depend largely on a lack of consensus on operational definitions such as the flow depth, the mean velocity or the grain-size length scale (Ferguson, 2007). This problem becomes particularly significant when flow depth has the same order of magnitude as the roughness height, i.e., with small relative submergence quantitatively defined by  $S_m = h_f/d_p$ , where  $d_p$  is the grain size length scale.

Despite the basic need to predict flow depth, gaps remain in the understanding of flow processes in mountain rivers.

Thus, a better understanding of the underlying physics is required to improve both predictions and operational definitions. This goal has already stimulated vigorous debates in the community, and the cornerstone lies in modeling the vertical structure where turbulence is critical.

## 1.2 Vertical velocity structure of turbulent open-channel flows

### 1.2.1 Non dimensional numbers

In 1883, Osborne Reynolds reported experiments in pipe flows, making a distinction between laminar or turbulent flow regimes. He developed non dimensional numbers now called Reynolds numbers that relate the inertial forces to viscous forces, to differentiate these regimes. To characterize an open-channel flow three different Reynolds numbers are generally given:

$$Re_b = \frac{U_b h_f}{\nu} \quad (2.7)$$

$$Re_{surf} = \frac{U_{surf} h_f}{\nu} \quad (2.8)$$

$$h_+ = \frac{u_* h_f}{\nu} \quad (2.9)$$

$Re_b$  is the bulk Reynolds number,  $Re_{surf}$  is the surface Reynolds number (where  $U_{surf}$  is free surface velocity) and  $h_+$  is the friction Reynolds number (where  $u^* = \sqrt{g h_f i}$  is termed the shear velocity).

The dimensionless Froude number developed by William Froude (1810-1879) also plays a critical role in open-channel flows:

$$Fr = \frac{U_{surf}}{\sqrt{g h_f \cos \zeta}} \sim \frac{U_{surf}}{\sqrt{g h_f}} \quad (2.10)$$

where  $U_{surf}$  is the surface velocity. The Froude number relates inertial to gravitational forces, and is also the ratio between surface velocity and the wave speed  $c = \sqrt{g h_f \cos \zeta}$ . It characterizes the development of various flow features in open channel flows from a low to a large Reynolds number.

For instance, an hydraulic jump is observed when a torrential flow ( $Fr > 1$ , also called supercritical flow) slows down and switches abruptly to a fluvial regime ( $Fr < 1$ , also called subcritical flow). Indeed, at  $Fr = 1$ , the situation is singular, since the velocity of the water is equal to the wave speed.

While the Froude number does not appear as essential for uniform flow, it plays a critical role in describing instabilities when a periodic perturbation is imposed on the surface along the streamwise direction. For instance, the growth of instabilities resulting in Kapitza waves in viscous regime or roll waves in turbulent regime can be forecasted (e.g. Charru (2011); Richard &

Gavrilyuk (2012)). In turn, these instabilities generate internal coherent structures and turbulence, influencing the vertical transfer of momentum.

If instabilities of free surface flow over inclined beds appear at very low bulk Reynolds numbers  $Re_b$ <sup>3</sup>, it is usually admitted that a fully turbulent flow over smooth bed is obtained at  $Re_b > 1800$  and without ambiguity for  $Re_b > 3000$  (Pope, 2001).

### 1.2.2 Log-law of the wall

Turbulent streams exhibit 3D complex structures but the 2D approximation is usually assumed to describe the first order dynamics (see Figure 2.3). Here, the time-averaged velocity is oriented on the  $x$  direction  $\overline{\mathbf{V}}(z, t) = U_x(z)\mathbf{e}_x$ , but turbulence occurs in the  $x$  and  $z$  direction.

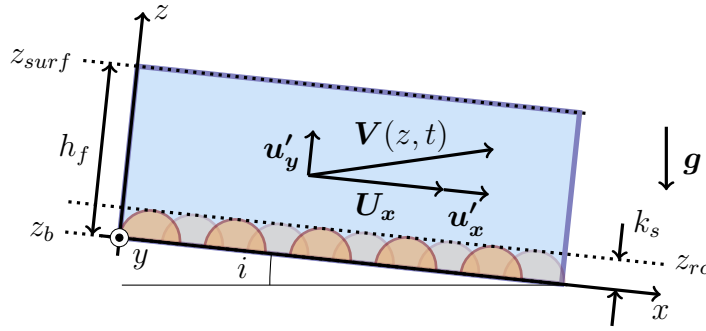


Figure 2.3 – Flow over a rough impermeable bed: velocity decomposition and roughness length  $k_s$ .

The decomposition of the instantaneous velocity  $\mathbf{V}(z, t)$  into its mean  $U_x$  and the temporal fluctuations in the 3 directions of the space is referred to as the *Reynolds decomposition*:

$$\mathbf{V}(z, t) = (U_x(z) + u'_x(z, t)) \mathbf{e}_x + u'_y(z, t) \mathbf{e}_y + u'_z(z, t) \mathbf{e}_z \quad (2.11)$$

In the early XXc, Ludwig Prandtl (1875-1953) discovered that turbulence plays a key role by transferring the momentum vertically, and he developed what is known as the Prandtl boundary layer theory. Later, his students Theodor Von K  rm  n (1881 - 1979), Paul Blasius (1883 - 1970) and Johann Nikuradse (1894 - 1979) attempted to provide analytical predictions of the friction laws on pipe and open-channel flows.

The vertical velocity profiles are derived by solving the steady unidirectional *Reynolds*

<sup>3</sup>according to Charru (2011) Kapitza instabilities appears for  $i \approx 1\%$  at  $h^+ \approx 10$ , interestingly for pure viscous open-channel flows  $Re_b = h^+{}^2$ .

equation:

$$0 = \frac{d\tau_v}{dz} + \frac{d\tau_t}{dz} + \rho_f g i \quad (2.12)$$

$\tau_v = \rho_f \nu \frac{du_x}{dz}$  is the viscous stress (where  $\nu$  is the kinematic viscosity in  $\text{m}^2/\text{s}$ ) and  $\tau_t = -\rho_f \overline{u'_x u'_z}$  is the turbulent stress. Equation 2.12 can be integrated from the free surface altitude where  $\tau_v + \tau_t$  is assumed to be zero to obtain:

$$-\overline{u'_x u'_z} + \nu \frac{du_x}{dz} = g i (z_{surf} - z) = u_*^2 \left( 1 - \frac{z - z_b}{h_f} \right) \quad (2.13)$$

The right hand expression introduces the bed position  $z_b$  defining  $h_f = z_{surf} - z_b$ .

The classical Prandtl mixing length assumption is ordinarily employed as a closure equation for turbulent stress:

$$\tau_{xz} = -\rho_f \overline{u'_x u'_z} = \rho_f l_m^2 \frac{dU_x}{dz} \left| \frac{dU_x}{dz} \right| \quad (2.14)$$

Prandtl proposed the well-known relation  $l_m = \kappa(z - z_b)$ , where  $\kappa$  is termed the Von Kármán empirical constant. The syntheses by Garbis H. Keulegan (1890–1989) of previous theoretical and experimental works, has been essential to describe flows in rough channels (Keulegan, 1938).

The vertical structure of a regular open-channel flow may be subdivided into three layers : the viscous sublayer, the log-law region and the outer region.

For  $z - z_b \sim 0$ , the laminar sublayer is reached, the viscous effect dominates. For  $z - z_b > 0.2 h_f$ , the outer layer is reached. When  $z - z_b$  is in between, i.e., sufficiently far from both the solid wall and the free surface ( $z - z_b \ll h_f$ ) the Equation 2.13 with the closure Equation 2.14 can be solved to obtain the Kármán law of velocity distribution known as the log-law of the wall:

$$\frac{U_x(z)}{u_*} = \underbrace{\frac{1}{\kappa} \ln \left( \frac{(z - z_b) u_*}{\nu} \right)}_1 + A_r = \underbrace{\frac{1}{\kappa} \ln \left( \frac{(z - z_b)}{k_s} \right)}_2 + B_r = \underbrace{\frac{1}{\kappa} \ln \left( \frac{z - z_b}{z_0} \right)}_3 \quad (2.15)$$

Here in one line are the three common forms of the log law of the wall found in the literature.  $A_r$  and  $B_r$  are integration constants from the viscosity/roughness-affected region close to the bed. In the first form Equation 2.15-1, the logarithmic law depends on the viscosity. According to Keulegan (1938), when the roughness length  $k_s < \frac{3.3\nu}{u_*}$ , the surface behaves as if it were smooth.  $A_r$  is a constant that has been empirically calibrated at 5.5 by Nikuradse (1933). For higher values of  $k_s$ ,  $A_r$  can be expressed by:

$$A_r = 8.5 - \frac{1}{\kappa} \ln \left( \frac{k_s u_*}{\nu} \right) \quad (2.16)$$

With this expression, Equation 2.15-2 becomes more convenient since  $B_r$  is a constant equal to 8.5.

The last formulation, Equation 2.15-3, is generally given to simplify the developments and  $z_0 = k_s / \exp(\kappa B_r)$ . It should be emphasized that  $z_0 = k_s / \exp(\kappa B_r) \sim k_s / 30$ . Thus, the conventional 30 factor between  $z_0$  and  $k_s$  (as well as the 12 factor in the right hand term of Equation 2.17) are deduced from the Nikuradse experimental results with Equation 2.16.

Integration of a logarithmic law of the wall, Equation 2.15, between  $z_b + k_s$  to  $z_{surf}$  yields an approximation of the bulk velocity  $U_b$ , and by deduction a physically based friction law.

$$C = \frac{U_b}{u_*} \approx \frac{1}{\kappa} \left( \ln \left( \frac{h_f}{z_0} \right) - 1 \right) = \frac{1}{\kappa} \ln \left( \frac{h_f}{e z_0} \right) = \frac{1}{\kappa} \ln \left( \frac{12 h_f}{k_s} \right) \quad (2.17)$$

$C$  is the non dimensional Chézy coefficient (also termed non-dimensional conductance) and relate bulk velocity  $U_b$  to the friction velocity  $u_*$ . This terminology is regularly employed in fluvial hydraulics (Aguirre-Pe & Fuentes, 1990; Colombini & Stocchino, 2012). Note that this coefficient is linked to the traditional dimensional Chézy coefficient  $\chi$  and the Darcy-Weisbach friction factor by :

$$C = \frac{\chi}{\sqrt{g}} = \sqrt{\frac{8}{f}}$$

Until now, the log-law of the wall and its derivations of resistance formula have been primarily responsible for shaping laws from pipes to mountain rivers.

There has been a corpus of studies developing parameterizations to explain the different behaviors of deep turbulent flow over smooth or rough walls. A summary of this work has been made by Nezu (2005). Two important features must be addressed because of their fundamental role in understanding the hydrodynamic processes in open-channel flows: the *damping effect* and the *velocity defect-law*. They play a crucial role in interpreting my measurements.

### 1.2.3 Buffer layer and damping effect

To describe flows over a smooth wall, different corrections of the mixing length function have been suggested. Since the role of the damping effect has been essential for subsequent developments, the concept is briefly presented here. The most famous formulation is due to van Driest (1956).

It involves an exponential decay damping the turbulence near the wall by the presence of the viscous effect. E. R. van Driest proposed the following specification:

$$l_{m,vD} = \kappa(z - z_{sm}) \Gamma; \quad \Gamma = \left( 1 - \exp \left( -\frac{1}{Re_{vD}} \frac{(z - z_b)u_*}{\nu} \right) \right), \quad (2.18)$$

with  $\Gamma(z)$  the damping function which tends toward zero at the bed interface  $z_b$  and increase to reach one when viscous effect are negligible, i.e.,  $\frac{(z - z_b)u_*}{\nu} \gg Re_{vD}$ . When the local Reynolds number in the viscous sub layer (where the velocity profile is linear, i.e.  $U_x(z) = (z - z_b) u_*^2 / \nu$ ) exceeds the non dimensional number  $Re_{vD}$ , the turbulence becomes the dominant factor in



diffusing the momentum (the van Driest Reynolds number is originally given at 26).

If the damping effect is not introduced in the equations, the mean velocity in the outer layer can be largely under-estimated. Indeed, the damping effect occurs in a small layer close to the wall and reduces the apparent turbulent viscosity. Since the velocity gradient is important in this region, this significantly affects the entire vertical profile.

The importance of this damping effect has been largely unconsidered for turbulent flows over rough wall, the boundary conditions being expected to be fully turbulent.

#### 1.2.4 The velocity defect-law

In the outer region ( $z - z_b > 0.2 h_f$ ), a significant deviation from the log-law predictions has been observed, such that the log law of the wall must be modified:

$$\frac{U_x(z)}{u_*} = \frac{1}{\kappa} \ln \left( \frac{(z - z_b)u_*}{\nu} \right) + A_r + w((z - z_b)/h_f) \quad (2.19)$$

where  $w((z - z_b)/h_f) = \frac{2\Pi}{\kappa} \sin^2 \left( \frac{\pi}{2} (z - z_b)/h_f \right)$ , is an empirical wake function.  $\Pi$  is called the wake strength parameter.

This correction was first introduced by Coles (1956) for boundary layers. It was only 25 years after that scientists recognized its relevance for open-channel flows (Coleman, 1981; Zippe & Graf, 1983; Nezu & Rodi, 1986).

With these considerations, a mixing length expression may be deduced from Eqs. 2.13, 2.14, and 2.19, giving the following mixing length distribution:

$$l_m = h_f \kappa \sqrt{1 - z'_{\epsilon=0.8}/h_f} \left[ \frac{h_f}{z'_{\epsilon=0.8}} + \pi \Pi \sin \left( \pi \frac{z'_{\epsilon=0.8}}{h_f} \right) \right] \Gamma(z) \quad (2.20)$$

with  $\Gamma(z)$  the damping function introduced in Section 1.2.3. This mixing length distribution has been largely tested for low gradient flows. As far as I know, it has never been tested for high gradient open-channel flows ( $i > 0.5\%$ ). The following experimental results illustrates how the Cole modification is essential in describing vertical mixing length distribution in a steep stream.

It must be emphasized that the strategy of the previous studies has been to produce a mixing length distribution from the modification of the velocity profile through an empirical wake function. This strategy is more convenient since it permits a conclusion with an analytical log functional with an additional term.

As noted by Nezu (2005), other empirical wake function have been proposed, but Cole's wake function appears to be the simplest and the most acceptable extension of the log law.

In general, large scatters in the log-law of the wall with the fitting processes might be

due to non-consideration of both the *damping effect* and the *velocity defect-law*, especially in small relative submergence conditions. The theoretical arguments are developed in the following chapters.

### 1.3 Reassessments

If the log law of the wall is retrieved for deep flows, i.e., with a roughness length small compared to the flow depth, the problem is more intricate when a non negligible part of the flow seeps through the permeable rough bed. Engineers also tend to use this log law for steep mountain streams, but the arguments for retrieving a log profile fail, since the layer thickness  $z - z_b$  has both the order of magnitude of  $d_p$  and  $h_f$ . In my opinion, matching an analytical log-law for shallow and rough flows is a hazardous task. A full vertical resolution of the equation is preferable, but no analytical solution is for the moment available.

Another problem is posed within the roughness layer. The complex 3D geometry of the roughnesses influences the turbulence statistics in a manner such that Prandtl assumptions are not valid in this region, where drag forces on protuberance and wake structures are more likely to influence the average flow. However, many articles use the log-law to characterize the roughness properties, even for low submergence flows which are complicated and subject to experimental uncertainties.

In this dissertation, the roughness layer is revisited as a porous media transition. Indeed, the porosity varies from the bulk velocity in the bed to a porosity of one in the free surface flow. I argue that this point of view is convenient because it characterizes the dependence with the porosity (and implicitly the elevation) of the drag force in the roughness layer. The advantages of this description will be developed mainly in the next chapter. In the following section, the different ways of modeling solid/fluid interactions are depicted.

## 2 Flows in a porous media

### 2.1 Darcy based laws

#### 2.1.1 Darcy law

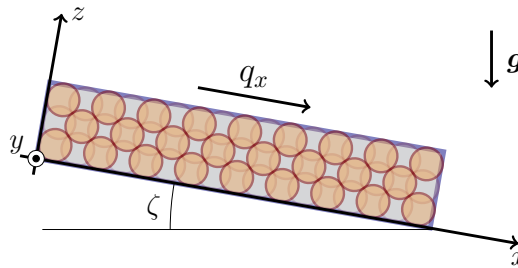


Figure 2.4 – Uniform gravity driven flow in a confined porous medium

The first empirical law for steady creeping flow inside a porous medium has been derived by Darcy (1856) and may be written, in its simplest form, along the  $x$  axis, by:

$$\langle u_x \rangle_s = \frac{K}{\rho_f \nu \epsilon} f_{ext}, \quad (2.21)$$

where  $\epsilon$  denotes the porosity,  $\langle u_x \rangle_s$  is the superficial velocity (i.e. averaged over the entire volume), it is also called the seepage or the darcian velocity depending on the scientific field.  $K$  the permeability,  $f_{ext}$  is the volume averaged external force density exerted on the fluid. In pressure driven flow  $f_{ext}$  is equal to  $-\epsilon \frac{dP}{dx}$ , the pressure gradient, whilst in gravity driven flow  $f_{ext} = \epsilon \rho_f g i$ .

Because porous media contain voids forming the flow path, the intrinsic velocity or interstitial velocity  $U_x$  is higher than the superficial velocity  $\langle u_x \rangle_s$ .

$$U_x = \frac{\langle u_x \rangle_s}{\epsilon}, \quad (2.22)$$

In its linear and empirical form, Darcy law has been used in many domains such as groundwater sciences (de Marsily, 1986) or the fossil resource industry (Muskat & Meres, 1936). One realm has been particularly active in exploring porous media: chemical engineering. Indeed, to design chemical reactors or filters using various gases or liquids in a viscous or turbulent regime, the chemical industry has widely studied the theoretical background of the Darcy law and its limitations.

### 2.1.2 Darcy-Forchheimer law: the Ergün equation

To take into account non-linear effects in the porous medium when velocity increases, the most documented law has been developed by Ergun (1952):

$$f_{ext} = A_E \frac{(1 - \epsilon)^2 \rho_f \nu}{\epsilon d_p^2} U_x + B_E \frac{(1 - \epsilon) \rho_f}{d_p} U_x^2 \quad (2.23)$$

$$= \underbrace{\frac{\rho_f \nu \epsilon^2}{K(U_x)} U_x}_{\text{Darcy approach}} \quad (2.24)$$

where  $A_E$  and  $B_E$  are the Ergün empirical constants. Non-linear forms of the Darcy equation are classically called the Darcy-Forchheimer form, and theoretical forms such as Equation 2.23 are called Darcy-Ergün equations (Nield & Bejan, 2006). The formulation of the force exerted by the fluid depend on the mean grain size  $d_p$  and the porosity  $\epsilon$ .

When the quadratic term is negligible, we end up with the relation known as the *Carman-Kozeny relation*:

$$f_{ext} = A_E \frac{(1 - \epsilon)^2 \rho_f \nu}{\epsilon d_p^2} U_x \quad (2.25)$$

### 2.1.3 Scaling in a porous media

The diameter of the particles is the principal component to describe a flow for a packed bed, and the particle Reynolds number is defined by:

$$Re_p = \frac{d_p U_x}{\nu} \quad (2.26)$$

The porosity also plays a critical role in the flow process in a porous medium, while it is usually not considered in the non dimensional numbers (mainly because  $\epsilon$  is generally a constant between experiments performed on packed beds,  $\epsilon_b = 0.4$ ).

However, Equation 2.23 may be rewritten to relate underlying principles of fluid flow by performing a dimensional analysis.

$$f_{ext} = \Gamma(\rho_f, \nu, U_x, l_p, g, \epsilon), \quad (2.27)$$

where  $\Gamma$  denotes a functional relationship and  $l_p$  the *pore length scale*: Naively,  $l_p$  is often scaled by  $d_p$ . However, the diameter of the grains is inadequate to characterize the mean diameter of the pores. As was elegantly explained by Niven (2002), a better choice is the ratio of the volume of voids  $V_v$  to their surface area  $A_v$ .

$$l_p(d_p, \epsilon) = \frac{V_v}{A_v} = \frac{\epsilon d_p}{6(1 - \epsilon)}, \quad (2.28)$$

This length scaling argument is similar to the one used for hydraulic radius scaling  $R_h = \frac{A_f}{P}$  introduced above for fluvial hydraulics. Indeed, in rivers, skin friction occurs on the entire bed limit as the skin friction in the porous bed occurs on the surfaces of the solid grains. Dimensional analysis yields:

$$\frac{f_{ext}}{\rho_f g} = i = \Gamma \left( Re_l = \frac{l_p U_x}{\nu}, Fr_p = \frac{U_x}{\sqrt{g l_p}}, \epsilon \right), \quad (2.29)$$

$Re_l$  is the pore Reynolds number and  $Fr_l$  is the pore Froude number. The Ergün equation becomes :

$$i = \epsilon \frac{Fr_l^2}{Re_l^2} \left[ A Re_l + B Re_l^2 \right], \quad (2.30)$$

Chemical engineers have constructed another useful non-dimensional number : the Galileo number, independent from fluid velocity.

$$Ga_p = \frac{Re_l^2}{Fr_p^2} = \frac{l_p^3 g}{\nu^2} = \frac{\epsilon^3 d_p^3 g}{\nu^2 (1 - \epsilon)^3} \quad (2.31)$$

$$i = \epsilon \frac{1}{Ga_p} \left[ ARe_l + BRe_l^2 \right], \quad (2.32)$$

The physical basis of the Ergün equation is discussed in Niven (2002), and an interesting response on the origin of the non linear term of the Ergün equation to this article is given by Stevenson (2003). The debate is still active on the origin of the transition from linear to non-linear form. Some authors attributed this transition from laminar to turbulent flows (Leva, 1959) whilst others more carefully refer to inertial effects. Indeed, local inertial losses and fluid turbulence produce variations in the same quadratic term of Equation 2.23.

## 2.2 Drag force based laws

Chemical engineers have also widely explored sedimentation and fluidization processes (Richardson, 1954). The strategy adopted to describe these system diverges from the fixed bed point of view, since resistance to the flow is constructed with the drag force on individual grains. Consider a single grain in an homogeneous fluid with a velocity  $U_x$ . The force on the grain is given by:

$$F_d = C_d(U_x) \frac{\rho_f U_x^2 \pi d^2}{2} \quad (2.33)$$

where  $C_d(U_x)$  is the drag coefficient on a single sphere and can be given, for instance, by the expression of Dallavalle (1943):  $C_D = 24.4/Re_p + 0.4 = 24.4\nu/(U_x d_p) + 0.4$ .

Because the volume of grain present in the system is  $N_g V_g = (1 - \epsilon) V_{tot} = N_g \frac{1}{6} \pi d_p^3$ , where  $N_g$  is the total number of grain. The force per unit of volume is given by:

$$f_{ext} = \frac{N_g F_d}{V_{tot}} = \frac{3}{4} \frac{(1 - \epsilon) \rho_f}{d} \underbrace{C_D^*(\langle u_x \rangle_s, \epsilon) \langle u_x \rangle_s^2}_{\text{Drag approach}} \quad (2.34)$$

where  $C_D^*(\langle u_x \rangle_s, \epsilon) = C_D(\langle u_x \rangle_s) f(\epsilon)$  is a modified drag coefficient. The factor  $f(\epsilon)$  is the voidage function, to take in consideration the hindrance effect due to porosity. The different expressions based on the drag force based laws are conventionally expressed in terms of the superficial velocity  $\langle u_x \rangle_s$  (and not the intrinsic velocity  $U_x$ ). It is a detail, but might be a source of mistakes in different scientific contributions. A usual choice for this function is  $f(\epsilon) = \epsilon^\beta = \epsilon^{-3.8}$  which empirically explains the reduction of the drag coefficient when porosity increases.

This correction is owed to Richardson (1954) and has been tested on highly concentrated sedimentation processes. This interaction formulation has been used in Jenkins & Hanes (1998); Revil-Baudard & Chauchat (2013) for sheet flows and more recently used for bed load transport simulations by Maurin *et al.* (2018). The main advantage of the drag force formulation resides in the  $\epsilon = 1$  limit for which the classical drag force is retrieved.

## 2.3 Comparison between drag force based law and porous media laws

It is possible to express the drag force based law Equation 2.35 in term of the intrinsic velocity and compare it to a porous media law given by the Ergün Equation ??:

$$f_{ext} = A \frac{(1-\epsilon)^2 \rho_f \nu}{\epsilon d^2} U_x + B \frac{(1-\epsilon) \rho_f}{d} U_x^2 = \underbrace{\frac{\rho_f \nu \epsilon^2}{K(U_x)} U_x}_{\text{Darcy approach}} = \underbrace{\frac{3}{4} \frac{(1-\epsilon) \epsilon^2 \rho_f}{d} C_D(U_x) U_x^2}_{\text{Drag approach}} \quad (2.35)$$

By providing the equivalent drag coefficient  $C_d$  for the Ergün formulae, we can compare the Darcian and the Drag point of view on the Figure 2.5. The two points of view are close for the packed beds porosity, i.e.  $\epsilon \sim 0.4$ . For large and low porosities, divergences are observed. Since the Ergün equation was intended only to estimate flows for homogeneous packed beds with a porosity varying from  $\epsilon \sim 0.3$  to  $\epsilon \sim 0.6$  the shifts at higher porosities is expected.

An attempt to obtain a generalized approach to treat both fluidization and fixed beds with various porosities has been devised by Gibilaro *et al.* (1985) and later by Di Felice (1994).

The Gibilaro - Di Felice (1985) correction aims to modify the drag curve to collapse with the Ergün equation for  $\epsilon = 0.4$ . The force exerted by the fluid/solid medium is given by :

$$f_{ext} = \left( \frac{17.3\nu}{\epsilon d_p} + 0.336 U_x \right) \frac{\epsilon^{-1.8}(1-\epsilon)}{d} U_x \quad (2.36)$$

## 2.4 Porous media interactions: up-scaling approaches

Several attempts to explain porous media flows from the grain scale hydrodynamics have been provided. The classical approach simplifies the tortuous path in the pores with tubes, whilst the upscaling methodologies interpret the macroscopic behavior from the pore scale hydrodynamics.

### 2.4.1 Classical approaches

In fluid mechanics textbooks, the behavior of the Darcy law is commonly provided by a comparison with the Poiseuille law which states a linear relation between the pressure gradient and the mean velocity. In that sense, if the porous medium is represented by an array of tubes, the linear Darcy trend is retrieved. We can also describe the local pore-sizes variations by a simplified model of tubes having alternating sizes of section. Using this approach, Niven (2002) concludes with a quadratic non linear trend for high velocities. This non linear deviation can either find its origin from the inertial loss in the local variation of the sections or from the turbulence transition.

### 2.4.2 Homogenization and spatial averaging concepts

From a different perspective, strategies have been developed to explain the macroscopic Darcian behavior from the local description of the flow. These are the upscaling methods including

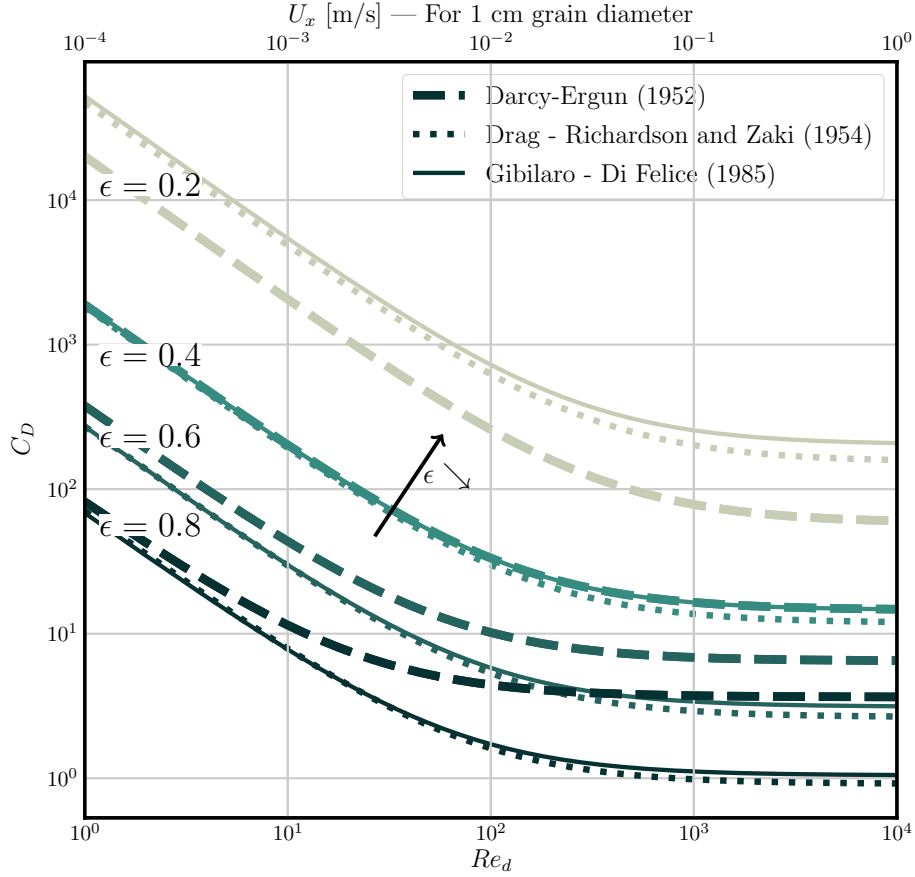


Figure 2.5 – Comparison between Drag approach and Darcy approach for volume averaged non-linear flow laws in fluid/particle interactions. These formulae provide a similar order of magnitude. The velocities on the top are given for  $d_p = 1$  cm, the order of magnitude of the bead size employed later for the experiments

the *homogenization theory* and the *volume averaging methodology*.

The *homogenization theory* applied to porous structure has been popularized by Mei & Auriault (1991). The principle is to consider the Navier-Stokes equation valid at the pore scale. An expansion is done on the variables to obtain a set of equations valid at various scales. This is the multi-scale analysis. With this technique, it is possible to retrieve, at the first order, a Stokes problem at low Reynolds numbers enforced by a no-slip condition on the surface of the solid. By averaging the solution we obtain a Darcy law. By expanding at higher orders for a low Reynolds number, Mei & Auriault (1991) found a cubic correction instead of the usual quadratic term in the Forchheimer law.

The *volume averaging methodology* has also been widely employed in the porous media community (e.g. Whitaker (1986)) and contains likenesses to the *homogenization theory*. It consists in spatially averaging the Navier-Stokes equations. The *volume averaging theorem* allows to isolate from the viscous stress and the pressure contribution the total stress acting on the

surfaces of the solid bodies inside the volume. The volume on which the averaging must be performed is large enough to consider an homogeneous porous medium. With an appropriate closure on the relation between the volume averaged forces acting on the solid walls and the mean flow, it is possible to retrieve the Darcy or the Forchheimer laws (Whitaker, 1996).

Importantly, a singular term also appears from this procedure: it is the *dispersive stress* (also called the *form-induced stress*). It is the equivalent of the turbulent stress when the average of the Navier-Stokes Equations is performed over time. The dispersive stress involves the local deviation of the velocity. For the  $x$  component it is defined by:

$$u_x(\mathbf{X}) = \langle \overline{u_x} \rangle + \tilde{u}_x(\mathbf{X}) \quad (2.37)$$

where  $u_x(\mathbf{X})$  is the local velocity and  $\mathbf{X}$  is the spatial position in the in fluid region.  $\langle \overline{u_x} \rangle$  is space averaged velocity and  $\tilde{u}_x(\mathbf{X})$  the local deviation of the velocity. In an unidirectional flow, the volume size is normally chosen such that  $\langle \overline{u_x} \rangle = U_x$  does not vary with  $\mathbf{X}$ . Interestingly,  $\tilde{u}_x(\mathbf{X})$  corresponds to the first order expansion in the homogenization theory.

If the variation of the velocity only occurs in the  $z$  direction, the dispersive shear stress in the  $x$  direction is thus expressed as:

$$\tau_d = -\rho_f \frac{d\langle \tilde{u}_x \tilde{u}_z \rangle}{dz} \quad (2.38)$$

### 2.4.3 Discussion

While the *homogenization theory* gained popularity in the last decade in studying flows adjacent to porous structures, I did not find any outstanding contribution in which it provides an equivalent of the *dispersive stress*. In the following developments, the dispersive stress plays an important role, since it has been measured in various experimental and numerical cases. Moreover, the volume averaging framework is the cornerstone of the *double-averaging* methodology thoroughly explored within the hydraulic framework by Nikora *et al.* (2007) and later by many experimentalists and theoreticians. It is why I decided to develop the theoretical arguments and the experimental procedures within the volume averaging framework.

## 3 Flow-porous structure interactions

### 3.1 Pioneering investigations

Beavers & Joseph (1967) is the first significant study of a flow adjacent to a permeable wall. Focusing on viscous flows, they conclude with an intrusion of the flow inside the bed at the vicinity of the interface. They report a penetration length scaling with  $\sqrt{K}$ . Pioneering works on the interaction between a highly porous foam and turbulent air flow were performed at the Massachusetts Institute of Technology from 1968 to 1972 (Munoz G. & Gelhar, 1968; Ho & Gelhar, 1973). They found that the log-law can be verified if the von Kármán constant takes values between 0.26 and 0.29. Calibrating log-laws on the profiles, the fictive wall has been



found to be inside the porous medium. They also admitted the importance of the exchange of momentum between laminar flows in the porous region and turbulent flow above, and finally they measured an increase of the friction factor. More recent studies (Mendoza & Zhou, 1992) investigated turbulent water flow over a pervious bed and concluded with similar observations.

## 3.2 Hyporheic exchanges and flux across the water-sediment interface

Hyporheic exchanges have particularly concerned water resources research over the last two decades. The principal issue remains the understanding of biogeochemical and ecological processes due to exchanges across the bed interface (Boano *et al.*, 2014; Blois *et al.*, 2014). This zone is the theatre of exchanges of water from different origins, conditions that are particularly favorable to feed or to trigger chemical reactions. The metabolic activity of microorganisms may catalyze these chemical reactions and participate in the transformation or the precipitation of different chemical species. In turn, precipitations and growth of bacterial communities may modify the flow characteristics, by reducing the permeabilities or by changing the boundary layer conditions. These bacterial formations are also ideal for plants and macroinvertebrates and, by domino effect, is a fundamental activator of the entire river ecosystem, supplying food to macro freshwater fauna such as fish and for the rest of the food chain.

Theoretical analysis has been done to predict flux exchange in the presence of bedforms (Elliott & Brooks, 1997), and with the presence of gaining or losing condition in the bed (Fox *et al.*, 2014).

As explained in the introduction, little is known about the local exchange with the macro rough permeable bed and its eventual role for the transport of solute. These hyporheic models need a better understanding of the hydrodynamics at the grain scale.

A review of scientific studies on turbulent flow over porous media reveals poor experimental investigations of the full vertical structure of the flow, especially when the inertial effect is non-negligible. Recently, Voermans *et al.* (2017) studied in detail flows over a permeable bed composed of beads of different diameter. In this study, the index matching method is used to follow the interfacial hydrodynamics. By employing the *double-averaging* framework (Nikora *et al.*, 2007), the authors were able to deduce the quantity of interest such as the turbulent stress and the dispersive stress; quantities that are of primary importance for mass flux transfer at the water/sediment interface in rivers (Voermans *et al.*, 2018). These authors argue that through the permeability number  $Re_K = \frac{\sqrt{K}u_*}{\nu}$ , it is possible to identify a different regime of diffusivity from impermeable boundary as  $Re_K \rightarrow 0$  to highly permeable boundary  $Re_K \rightarrow \infty$ . At  $Re_K \approx 1 - 2$  they identified an important threshold, above which the diffusive stress starts to dominate the fluid shear stress at the sediment-fluid interface.

These contributions inspired our experimental procedure as well as the strategy to interpret the data. They are a step forward for understanding the vertical structure of the flow. However, they focused on low gradient channels where subsurface velocities are negligible. Furthermore, no model has been developed yet to understand the different components in the hydrodynamics at this interface.

### 3.3 Modeling issues

In the latest numerical works on the flow/porous structure interactions (Tilton & Cortelezzi, 2008; Rosti *et al.*, 2015), the authors grant that there are few or no published data on the inertial exchange between turbulent flow and porous flow. Consequently, they restrict their analysis to flows for which the inertial effect can be ignored in the porous region. Recent numerical contributions also revealed inconsistency in the way the interface condition is considered. The contribution of Zampogna & Bottaro (2016) was to attempt to include the inertial exchange. The authors compared *direct numerical simulations* to a description employing the *homogenization theory*. Within this framework, they were able to develop an analytical model that reproduces well experimental vertical profiles of turbulent flows over a canopy (measurements are presented in Ghisalberti & Nepf (2004)). However, it was realized with a parametrization of the *turbulent stress* that is empirically adjusted on the velocity profiles. Working with linear Darcy law, they revealed a necessary decrease of the permeability with the Reynolds number leading with inconsistency with the usual theoretical assumptions done at the interface, which states that the penetration length is proportional to the permeability (Beavers & Joseph, 1967).

In general, most of the approaches using an Euler description of the interface use a jump condition. A jump condition involves a non-local form of the volume averaged momentum equation as described by Ochoa-Tapia & Whitaker (1995). These authors derived momentum transfer conditions correcting the error. When inertia is not negligible, these conditions are quite complex. There is still a need for a unified approach to clarify the transition of flows with a jump condition.

In the following work, the approach is different. To describe the interface I use a sharp but continuous variation of the porosity at the interface. This continuous description is practical because there is no need to introduce a jump condition. It is also a realistic approach since the space averaged porosity physically decreases smoothly in natural interfaces.

To conclude with the numerical aspects, the dispersive stress is generally neglected or simply omitted in most of the simulations, whereas recent *large eddy scale* simulations revealed its crucial role for flows over a permeable medium (Fang *et al.*, 2018). It is the second aspect of this contribution that deals with dispersive effects in the roughness layer, as will be seen in the next chapter.

## 4 Conclusion on the theoretical background

In this chapter, the essential state of research has been presented in order to understand the following chapters. The historical evolution of the free surface flows is essential to explain the classical approach. These tools are inadequate to describe open-channel flows with small relative submergence. Porous media knowledge is also essential to describe the flow in the *roughness* and the *subsurface layers*. It has been briefly introduced with the duality between Darcy based laws and drag force based laws. To model the interface, in contrast with previous models that used a jump condition, the interface will be treated as a continuous porous medium.

# 3

## Theoretical developments

---

This chapter regards the modeling of a turbulent open channel flow over a rough permeable bed with the application of the *double-averaging* concept. It consists of spatially averaging the time-averaged Navier-Stokes equations, known as Reynolds equations, in a thin layer parallel to the bed. This process results in obtaining the *double-averaged momentum equation*. Initially developed for atmospheric boundary layers and canopy flows (Wilson & Shaw, 1977), this method has been re-examined within the framework of fluvial hydraulics by Nikora *et al.* (2001, 2007). This approach results in the following principle advantages:

1. The turbulent open-channel flow layers are treated continuously from the *surface layer* to the *permeable bed*.
2. The mean porosity profile is continuous and the region where porosity varies sharply defines the *roughness layer*. This continuous approach is particularly advantageous for steep shallow flow where a consequent part of the flow seeps through the *roughness layer* as well as in the *subsurface layer* (see Figure 3.1).
3. The phenomenology can be up-scaled at the desired mesoscopic length-scale for modeling purposes. Closures can be developed in an adequate manner.
4. Quantities involved in the momentum equation are algebraically defined, and may be conveniently captured from experimental outputs for data interpretation and numerical tests.

In comparison to the Reynolds equations, the *double-averaged momentum equation* contains three additional terms: the *dispersive stress* (also called *form induced stress*), the *viscous drag* and the *pressure drag*. I suggest or adapt closures for all these terms as well as for the classical *turbulent stress* and *viscous stress*.

The viscous drag and the pressure drag in the permeable bed are identified with a Darcy-Forchheimer law known as the Ergün equation. These two terms play a critical role in damping the velocities in the *subsurface layer* as well as in the *roughness layer*. Secondly, I suggest a closure for the dispersive stress based on a mechanistic approach. Thirdly, the classical *viscous shear stress* is depicted with a particular attention to the choices found in the literature. Lastly, the turbulent stress is revisited through the Van Driest approach to take into account the so-called

damping effect. With these closures, the main features of a uniform open channel flow are represented together and permit the building of a 1D model.

The 1D model is then numerically solved. By varying the hydraulic conditions (grain size, relative submergence, slopes and porosity profiles), the model outputs are depicted. The important role of the van Driest damping effect is highlighted.

This model is the result of synergies with the experimental observations presented in Chapter 5 (with experimental procedure presented in Chapter 4). The theoretical background and the definitions for the *double-averaging* concept, as well as the assumptions behind the governing equation for uniform, steady and unidirectional flows, are introduced in Appendix A.

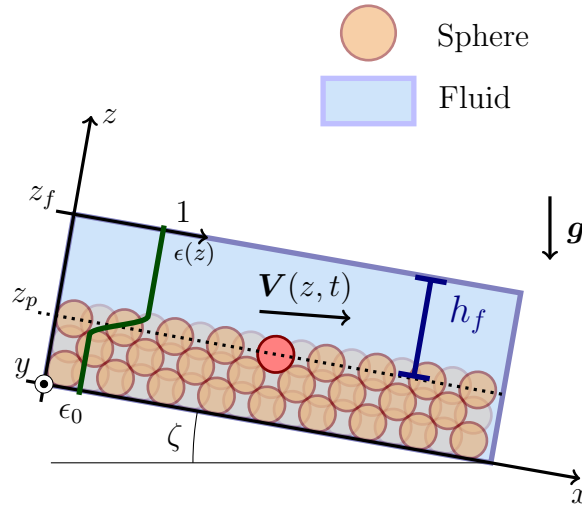


Figure 3.1 – Scheme of a gravity driven turbulent flow over a permeable medium with a small relative submergence.  $\mathbf{V}(\mathbf{x}, \mathbf{y}, \mathbf{z}, \mathbf{t})$  is the local instantaneous velocity vector in the three directions with the components developed in Equation 3.1.  $U_x$  is the *double-averaged* velocity and  $\epsilon(z)$  the spatially averaged porosity.  $z_{rc}$  the roughness crest level and  $z_t$  the altitude where the bulk porosity  $\epsilon_b$  is reached (the troughs of the roughness elements). The *roughness layer* is bounded by the altitudes  $z_{rc}$  and  $z_t$ , while the subsurface layer is below  $z_t$ . The surface layer is above  $z_{rc}$ , in this region  $\epsilon = 1$ .

### 1 Unidirectional equation of motion

In this study, a uniform and steady flow is considered where the quantities are spatially averaged over mesoscopic distances. Similarly to the *Reynolds decomposition*, the local instantaneous velocity is decomposed into the time-space averaged value  $\langle \bar{u}_x \rangle$ , the local disturbance  $\tilde{u}_k$  and the temporal fluctuations  $u'_k$  in the three direction of the space (the index  $k$  denotes  $x$ ,  $y$  and  $z$ ). Assuming a 2-D open channel flow, the *double-averaged decomposition* gives:

$$\mathbf{V}(\mathbf{x}, \mathbf{y}, z, t) = \begin{bmatrix} u_x \\ u_y \\ u_z \end{bmatrix} = \begin{bmatrix} \langle \overline{u_x} \rangle + \tilde{u}_x + u'_x \\ \tilde{u}_y + u'_y \\ \tilde{u}_z + u'_z \end{bmatrix} \quad (3.1)$$

The subscript ‘ $\overline{\phantom{x}}$ ’ denotes the time averaging, the brackets ‘ $\langle \bullet \rangle$ ’ the intrinsic space averaging (i.e. over the fluid phase only) and the tilde subscript ‘ $\tilde{\phantom{x}}$ ’ the local spatial disturbance. The dimensions of the layer along  $x$  and  $y$  are considered sufficiently large to assume  $\langle \tilde{u}_x \rangle \sim 0$ ,  $\langle \tilde{u}_y \rangle \sim 0$ , and  $\langle \tilde{u}_z \rangle \sim 0$ . To simplify the notations, the *double-averaging* intrinsic velocity along the  $x$  direction is written  $\langle \overline{u_x} \rangle = U_x$ .

The *double-averaging* methodology applied to the Navier-Stokes equation for a gravity driven unidirectional Newtonian incompressible flow in the simplified two-dimensional case gives:

$$\langle gi \rangle_s = -\langle u_z \frac{d\overline{u_x}}{dz} \rangle_s + \langle \overline{\nu \frac{d^2 u_x}{dz^2}} \rangle_s \quad (3.2)$$

where  $\langle \bullet \rangle_s$  is the *superficial* spatial averaging (i.e over the entire volume)<sup>1</sup> and the following relation may be deduced  $\langle \bullet \rangle_s = \epsilon \langle \bullet \rangle$ .

After manipulations detailed in the Appendix A, the Equation 3.2 can be transformed in the *double-averaged momentum equation*:

$$0 = \epsilon \rho_f g i + \frac{d\tau_d}{dz} + \frac{d\tau_t}{dz} + \frac{d\tau_v}{dz} + f_{p,x} + f_{v,x}, \quad (3.3)$$

where  $\tau_d = -\rho_f \epsilon \langle \tilde{u}_x \tilde{u}_z \rangle$  and  $\tau_t = -\rho_f \epsilon \langle \overline{u'_x u'_z} \rangle$  are respectively the *dispersive* and *turbulent stresses*;  $f_{p,x}$  and  $f_{v,x}$  are the *pressure drag* and *viscous drag* on the surfaces of the solid elements; and  $\tau_v$  is the viscous stress. Different relations are possible for these terms. The objective of the following section is to suggest convenient closures.

## 2 Closure problem

### 2.1 Drag forces in the porous bed - $f_{p,x} + f_{v,x}$

#### 2.1.1 Closure choice

Following Whitaker (1996), in a homogeneous porous medium, the pressure and viscous drag term from the spatial averaging procedure may be identified by a Darcy-Forchheimer law. Studying a non-mobile permeable bed, I choose the Ergun (1952) equation devised for flows

---

<sup>1</sup>The terminology ‘*superficial*’ is traditionally employed while the average is performed on a volume.

through packed beds.

$$f_{v,x} + f_{p,x} = -A_E \frac{(1-\epsilon)^2 \nu \rho_f}{\epsilon d_p^2} U_x - B_E \frac{(1-\epsilon)}{d_p} \rho_f U_x^2 \quad (3.4)$$

where  $d_p$  denotes the diameter of the grains.  $A_E$  and  $B_E$  are empirical constants. This term is constant in the *subsurface layer* and decreases in the *roughness layer*, whereas the porosity increases. It is equal to zero for  $\epsilon = 1$  above the roughness crest  $z_{rc}$  because  $\epsilon(z > z_t) = 1$ . As suggested by Nikora *et al.* (2007), the viscous drag  $f_{v,x}$  is considered as the linear term of the equation and the pressure drag  $f_{p,x}$  as the quadratic term. The Ergün equation was intended only to estimate flows for homogeneous packed beds with a porosity close to  $\epsilon \approx 0.4$ . Because porosity reaches  $\epsilon = 1$  at the roughness crest, there is a layer where the validity of the Ergün closure is subject to controversy.

### 2.1.2 Discussion on the closure choice

A similar scientific field is particularly affected to provide an estimate of the drag terms: the numerical simulation of sediment transport. For instance, Jenkins & Hanes (1998); Maurin *et al.* (2016) use an averaged drag force law based on the Richardson (1954) formulation. This law, devised for sedimentation problems, is adequate for low solid concentration ( $\epsilon \sim 1$ ) in the sediment transport layer. Indeed, the force tends to the expected classical drag force for individual particles in these conditions through the voidage function (as explained in Chapter 2 - Section 2). However, beneath this sediment transport layer, the porosity decreases sharply and the deployment of equations for high solid concentration is questioned. Concerned by this aspect, some authors use the Equation 3.4 for small values of  $\epsilon$ , and use a drag force law that behaves correctly for larger values of  $\epsilon$  (Jackson, 2000). For instance, Cheng *et al.* (2018) chose to separate the parametrization of the pressure and viscous drag in two porous domains: for  $\epsilon < \epsilon_c$ , they consider a porous bed and employ a Ergün equation; for  $\epsilon > \epsilon_c$ , they consider a fluid-particle flow and employ a drag force based law. They fix a threshold of porosity at  $\epsilon_c = 0.8$ . Although different arguments encourage this combination, it results in a discontinuity at the altitude where  $\epsilon = \epsilon_c$ . Moreover, as far as I know, no report furnishes theoretical arguments to fix  $\epsilon_c$ . Regarding these aspects, it is advisable to select one law to address this issue.

In my opinion, Ergün equation can be considered as the most reasonable choice for a fixed bed. The trends and the orders of magnitude are consistent with the phenomenology, i.e. a reduction of the pressure and viscous drag with an increase of the porosity reaching zero for  $\epsilon = 1$  above  $z_{rc}$ . Other considerations support this choice. Equation 3.4 relies on mechanistic arguments (Whitaker, 1996; Niven, 2002) and may provide insights on the underlying physics in the roughness layer. Also, many studies calibrate the coefficient  $A_E$  and  $B_E$  of the Ergün equation for highly permeable natural materials that are likely to be transferable to river bed material characteristics.

The equation proposed by Gibilaro *et al.* (1985) and introduced in Chapter 2 (Equation 2.36) was also examined. This equation has been elaborated to model flow from dense to sparse porous media. It is therefore ideal for rough permeable beds where porosity is close to the unity at the roughness crest. However, the advantage of this approach seems reduced by the rarity of studies deploying this equation for testing experimental data sets.

## 2.2 Dispersive stress - $\tau_d$

### 2.2.1 Preamble

In the last decade, numerous studies have investigated this quantity through the *double-averaging* methodology for hydraulically rough beds (Mignot *et al.*, 2009a; Detert *et al.*, 2010; Dey & Das, 2012; Voermans *et al.*, 2017) and more recently, *large eddy scale* simulations have been performed for a similar purpose in idealized configurations (turbulent flow over sphere packing geometries) (Fang *et al.*, 2018). Experimental and numerical results yield similar observations: the dispersive stress is ubiquitous in the roughness layer with a maximum observed just below the roughness crest ( $z_{rc}$ ) where few protuberances rapidly damp the velocity. The order of magnitude of this stress is generally lower than the turbulent stress at this altitude. In the numerical simulations of Fang *et al.* (2018), the results suggest that the geometry of the bed has an intricate influence on the structure of the flow above the roughness crest. In some cases stable recirculation and secondary currents appear, inducing a time-averaged flow periodicity in space. This re-circulation contributes significantly to the total dispersive stress. This numerical observation has been done for idealized periodic beds, whereas the effect seems less clear for irregular bed topography from real scenarios.

The dispersive stress might represent a non-negligible part of the momentum budget in the roughness layer compared to other quantities such as the turbulent stress or the form drag. Moreover, it is a measurable quantity, and an opportunity to suggest and test a closure that relies on physical arguments.

### 2.2.2 Dispersive stress closure on a regular packed bed

An explanation follows of why the dispersive stress on a regular packed bed is not expected to be zero. Consider a shear flow on a rough porous bed where the mean velocity shear  $\frac{d\langle \bar{u}_x \rangle}{dz}$  is positive as shown in Figure 3.2.

In the experimental observations performed during the experimental procedure presented in Chapter 4 (see Section 2.5.2), it has been observed that the main contribution for the dispersive stress is localized behind the protuberance where the velocities are significantly lower than the averaged velocity. As a consequence the disturbance in the  $x$  direction  $\tilde{u}_x$  is negative due to the *velocity deficit*. In the *velocity deficit* zones the upward velocities are dominant and the product  $\tilde{u}_x \tilde{u}_z$  is negative (and the dispersive stress positive).

To explain the vertical structure of the dispersive stress, consider two areas at the altitude  $z$ :  $A_+$  is the *velocity deficit* area behind the obstacle and  $A_0$  is the area where the contribution for the dispersive stress is neutral. Mathematically, it means that  $\langle \tilde{u}_x \tilde{u}_z \rangle_{A_+} > 0$  and  $\langle \tilde{u}_x \tilde{u}_z \rangle_{A_0} = 0$  in  $A_0$  but locally  $\tilde{u}_x$  and  $\tilde{u}_z$  may have positive or negative values.

$A_f = A_0 + A_+$  is the total area of fluid such that  $\lambda_+ = A_+/A_f$  and  $\frac{A_f}{A_{tot}} = \epsilon$ ;  $\bar{u}_{+,x} = \mathbf{u}_+ \cdot \mathbf{e}_x$  and  $\bar{u}_{+,z} = \mathbf{u}_+ \cdot \mathbf{e}_z$ .

Secondly, in the interaction region  $\{+\}$ , the local mean velocity is assumed to be influenced by the inclined surface of the bead. The geometry is simplified in such a manner that in the area  $A_+$ , the angle of contact is the same while the spherical shape would produce an orientation in the 3 directions of the space. In other words, the sphere is considered as a cylinder in this region.

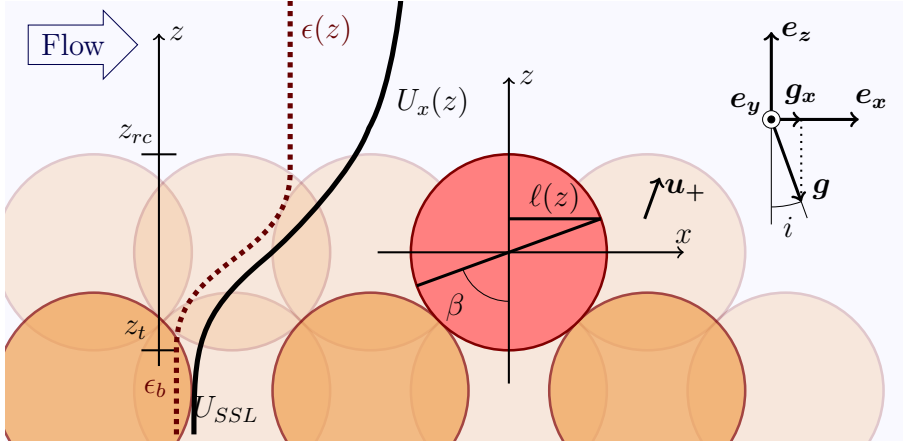


Figure 3.2 – A schematic illustration of a bead lying on a packed bed of beads, side view.

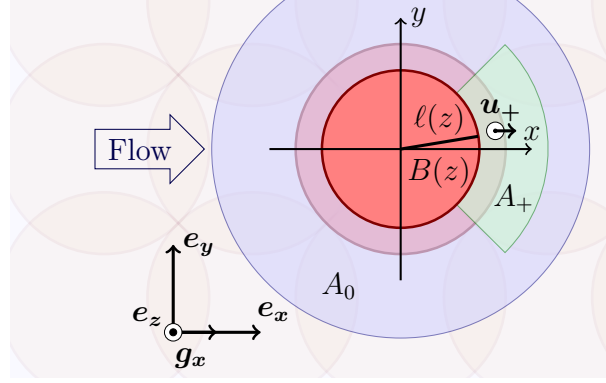


Figure 3.3 – A schematic illustration of a bead lying on a packed bed of beads, top view.

This simplified approach aims to avoid complex integration procedures on the sphere that would not in the end significantly improve either the model, or the interpretation of the phenomenology.

The velocity deficit at the altitude where the angle is  $\beta$  is given by:

$$\bar{u}_{+,x}(z) = \cos \beta U_x(z) \quad (3.5)$$

The spatial decomposition of the velocity gives :

$$\tilde{u}_{+,x}(z) = \bar{u}_{+,x}(z) - U_x = U_x(\cos \beta - 1) \quad (3.6)$$

Similarly, in the  $z$  direction, because  $\langle \bar{u}_z \rangle = \langle \tilde{u}_z \rangle = 0$  we obtain

$$\tilde{u}_{+,z}(z) = \bar{u}_{+,z}(z) = \sin \beta U_x(z) \quad (3.7)$$



and then,

$$\begin{aligned}\tau_d &= -\rho_f \epsilon \tilde{u}_x \tilde{u}_z = -\rho_f \epsilon \lambda_+ \tilde{u}_{+,z}(z) \tilde{u}_{+,x}(z) \\ &= -\rho_f \epsilon \lambda_+ \sin \beta U_x^2 (\cos \beta - 1)\end{aligned}\tag{3.8}$$

This equation relies on the local geometry through a conceptual angle  $\beta$ , but it is not applicable if this angle is not linked to the altitude  $z$ . We must provide arguments that link the surface angle to the averaged porosity profile.

### 2.2.2.1 Bed geometry and porosity

Geometrically, for a regular bed, we may define angles and distances at the interface, i.e. in the roughness layer, in the following manner:

$$\sin \beta = \frac{\ell(z)}{d_p/2},$$

and

$$\cos \beta = \frac{\sqrt{d_p^2/4 - \ell(z)^2}}{d_p/2},$$

where  $\ell(z)$  is the radius of the section of the sphere at the altitude  $z$  (see Figure 3.2).

There is an intrinsic relation between  $\ell(z)$  and the solid fraction  $1 - \epsilon(z) = A(z)/A_{tot}$  at an altitude  $z$ .  $B(z)$  is the area occupied by the solid over the total area. For instance, a bead packing arranged in a Face-Centered-Cubic-Structure (FCCS), the solid fraction verifies  $1 - \epsilon(z) = B(z)/A_{tot} = \pi \ell(z)^2/d_p^2$ . The maximum is reached when  $\ell(z) = R_p = d_p/2$  and the minimum  $\epsilon_{FCCS,min} = 0.31$  is obtained at  $z = z_p$  a value which is slightly higher than the bulk porosity for this idealized structure, i.e.  $\epsilon_{b,FCCS} = 0.36$ . For natural beds or beads in a laboratory flume, the structure is not exactly arranged as FCCS, but similarities are observed: the porous medium is dense and the bulk porosity is generally measured around  $0.3 - 0.5$ . If the porous medium has a narrow distribution in sediment size around  $d_p$ , we can postulate that the minimum of the porosity is reached where  $z = z_t$ .

$$1 - \epsilon(z_t) = \frac{\pi d_p^2}{A_{tot}} \approx 1 - \epsilon_b$$

The following expressions are obtained for  $\ell(z)$ ,  $\sin \beta$ ,  $\cos \beta$  as function of  $\epsilon$ :

$$\ell(z) \approx \frac{d_p}{2} \sqrt{\frac{1 - \epsilon(z)}{1 - \epsilon_b}}\tag{3.9}$$

$$\sin \beta = \frac{\ell(z)}{d_p/2} \approx \sqrt{\frac{1 - \epsilon(z)}{1 - \epsilon_b}}\tag{3.10}$$

$$\cos \beta = \frac{\sqrt{d_p^2/4 - \ell(z)^2}}{d_p/2} \approx \sqrt{1 - \frac{1 - \epsilon(z)}{1 - \epsilon_b}} \quad (3.11)$$

### 2.2.3 Final expression and simplifications

By replacing the expressions of  $\cos \beta$  and  $\sin \beta$  in the Equation 3.8, I arrived at an expression of the dispersive stress as a function of  $\epsilon(z)$ .

$$\tau_d = \rho_f \epsilon \sqrt{\frac{1 - \epsilon(z)}{1 - \epsilon_b}} \lambda_+ \left( 1 - \sqrt{1 - \frac{1 - \epsilon(z)}{1 - \epsilon_b}} \right) U_x^2 \quad (3.12)$$

In some conditions it may be useful to give a simpler form of Equation 3.12, when  $\epsilon(z) = O(1)$  at the roughness crest for instance, or in a porous medium where the porosity is high. By performing the Taylor expansion at the first order  $\sqrt{1 - \frac{1 - \epsilon(z)}{1 - \epsilon_b}} = 1 - \frac{1}{2} \frac{1 - \epsilon(z)}{1 - \epsilon_b}$ , dispersive stress may be given by:

$$\tau_d \sim 1/2 \rho_f \epsilon \lambda_+ \left( \frac{1 - \epsilon(z)}{1 - \epsilon_b} \right)^{3/2} U_x^2(z) \quad (3.13)$$

We define the local non dimensional dispersive stress by  $\check{\tau}_{fi} = \frac{\tau_d}{\rho_f U_x^2(z)}$  and plot the behavior of the expressions (3.12) and (3.13) for different  $\lambda_+$ , in the Figure 3.4. It is shown that in both relations, the non-dimensional local dispersive stress tends to its maximum when  $\epsilon = \epsilon_b$ .

Little is known about the dispersive stress, but this theoretical analysis could explain some mechanisms responsible for momentum diffusivity inside porous media. In the porous bed, the transfer of momentum by diffusive processes is neutral owing to the absence of velocity gradients (at the spatial averaging scale). However, other quantities such as the concentration of chemical elements or pollutant may vary. An estimation of the dispersive stress as well as an estimation of the local velocity disturbance may provide insights into the dynamic of the diffusion in porous media (e.g. Voermans *et al.* (2017, 2018) for a thorough discussion of this problem).

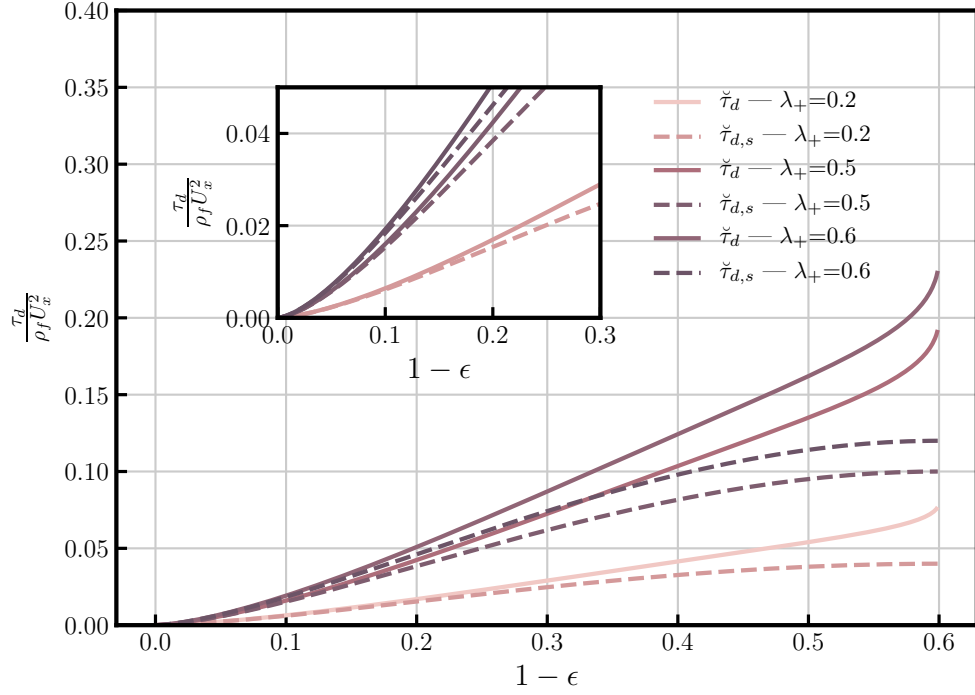


Figure 3.4 – Evolution of the theoretical non-dimensional dispersive stress for a regular packed bed ( $\epsilon_b = 0.4$ ).

### 2.3 Viscous stress - $\tau_v$

While the temptation is strong to neglect the viscous effects for water in the *surface layer*, things appear less simple for the *permeable bed*. Indeed, in real conditions, i.e. with typical values of gravel bed characteristics under water ( $i \sim 1\%$ ,  $d_p \sim 1$  cm,  $\epsilon_b \sim 0.4$ ) it is the viscous drag  $f_{v,x}$  regime that dominates in the subsurface layer when solving Ergün Equation 3.4. Above, the viscous forces do not vanish in the roughness layer where velocities are much lower than the velocities in the surface layer. With this continuous transition, it is unclear in which conditions the diffusion of momentum by viscosity is negligible at the interface. Without expecting any general behavior, the viscous term is added in the model to investigate after the domains of application where viscosity plays a negligible role.

There is a wide variety of theoretical arguments to close the viscous stress for diphasic solid/liquid systems. For the present study, this closure choice has been subject to a dilemma. Recent papers in the bedload transport domain were also confronted with similar circumstances without making extensive comments (Ouriemi *et al.*, 2009; Maurin *et al.*, 2016). The gaps in the theory are explored in Appendix A.4 to guide eventual future investigations but remains inessential for the understanding of this thesis. In Appendix A.4, an expression of the viscous shear including the Brinkman correction and the additional terms from the spatial averaging procedure has been derived. The Einstein correction on the viscosity has been omitted, since no clear experimental or theoretical work justifies its adoption for the present problem. Thus, the

viscous shear stress is given by:

$$\frac{d\tau_v}{dz} = \underbrace{\rho_f \nu \epsilon \frac{d^2 U_x}{dz^2}}_{\text{Brinkman term}} + \underbrace{\rho_f \nu \frac{d\epsilon}{dz} \frac{dU_x}{dz} + \rho_f \nu U_x \frac{d^2 \epsilon}{dz^2}}_{\text{Additional terms}} \quad (3.14)$$

### 2.4 Turbulent stress - $\tau_t$

Contrary to the viscous stress, the turbulent stress closure requires a comprehensive discussion for the subsequent results of this thesis. Prandtl boundary layer theory remains a natural basis to model turbulent stress but the traditional approach requires an origin of the bed to obtain the log-law of the wall. Numerous experimental studies reveal the weaknesses of this approach when applied to small submergence flows. They are briefly reviewed in this section. Herein, I argue that this origin determination is not appropriate for the present problem. An alternative relying on the continuous porosity profile in the roughness layer is suggested. Furthermore, according to my experimental results, the damping effect has been identified as an essential feature. As van Driest suggested, the damping effect depends on the local Reynolds number. Again, the introduction of this effect in the closure must be adapted to the continuous approach of the interface, where subsurface velocities play a key role for predicting the mixing length distribution. Part of the following developments on the van Driest approach applied to rough permeable bed were inspired by the work of Durán *et al.* (2012), where a continuous closure including the van Driest damping for modeling hydrodynamics in bed-load transport conditions has been developed.

#### 2.4.1 Mixing length theory and open channel flows

Mixing length theory is applied to close the turbulent stress term<sup>2</sup>.

$$\tau_t = \rho_f \epsilon \langle l_m^2 \left( \frac{d\bar{u}_x}{dz} \right)^2 \rangle \quad (3.15)$$

For rough surfaces, the *double-averaged* mixing length is generally given by a classical mixing length for regular flat beds and Equation 3.15 becomes:

$$\tau_t = \rho_f \epsilon \langle l_{m,t}^2 \left( \frac{d\bar{u}_x}{dz} \right)^2 \rangle \sim \rho_f \epsilon l_{m,t}^{*2} \left( \frac{dU_x}{dz} \right)^2 \quad (3.16)$$

with  $l_{m,t}^*$ , a space averaged equivalent mixing length. The porous wall has a large number of geometry-dependent variables (roughness layer height, subsurface layer permeability, roughness size). Although the *double-averaging* concept is able to provide insights from the fundamentals of the mixing length theory, the strategies found in the literature to close the mixing length term  $l_m^*$  for rough surfaces are purely empirical. The most common methodology is a case-by-case adaptation of the classical Von Kármán closure given by  $l_{m,vK}^* = \kappa(z - z_b)$ . This closure was

---

<sup>2</sup>A positive gradient of the velocity is considered and  $\frac{d\bar{u}_x}{dz} \left| \frac{d\bar{u}_x}{dz} \right| = \left( \frac{d\bar{u}_x}{dz} \right)^2$

originally developed for deep flows and  $z_b$  is the zero displacement height which is the bed position for smooth walls. It leads to the well-known log-law of the wall for deep flows. In practice, because the surface is rough and porous,  $z_b$  is not well defined and is determined, *a posteriori*, by fitting operations onto the velocity profile or its derivative (See Dey & Das (2012) or Koll (2006) for different practical examples). This procedure gives at the same time an estimate of  $\kappa$ .

For *deep flows*, this assumption is generally justified. The eventual change in level of the curve due to the complex rough boundary conditions at the interface is masked by the fitting procedure. In deep cases, the Von Kármán “constant”  $\kappa = 0.4$  is retrieved. The vertical structure being less dependent on the variety of bed geometries, a given roughness parameter can reproduce the profiles with a good agreement. The Keulegan law presented in Chapter 2 is probably the most lasting expression resulting from this approach for rough-bed flows.

For *small relative submergence conditions*, things are more complex. The damping effect as well as the roughness drag disturbs the momentum diffusion by turbulence in various ways and plays a key role on the vertical velocity structure (Nezu, 2005).

In general, I argue that the fitting procedure with a small relative submergence is not justified. It results in two estimated parameters ( $z_b$  and  $\kappa$ ) in the limited framework of the log-law of the wall, whereas the hydraulic conditions are not fulfilled to produce a well developed log profile. In support of this opinion, a thorough review of the literature reveals that this procedure produces large scatters in the determination of the Von Kármán “constant” when  $h_f \sim d_p$ .

#### 2.4.2 Experimental scatters in the Von Kármán determination with the fitting procedure

Koll (2006) analyzed numerous velocity profiles in small relative submergence conditions ( $S_m \approx 2-10$ ). The study reveals a substantial dispersion in the determination of the Von-Kármán “constant”, producing lower  $\kappa$  values than expected. Interested by these aspects, Gaudio *et al.* (2010) compiled the data of K. Koll and his co-authors with other experimental investigations to point out a *Non-universality of the Von-Kármán  $\kappa$  in fluvial streams*. Ranging from 0.2 to 0.4,  $\kappa$  is lower than expected, and the value increases with  $S_m$  to reach the conventional  $\kappa = 0.4$  for  $S_m \gg 1$ .

Inconsistently, other experiments on synthetic rough beds revealed an increase of the von Kármán “constant” with  $S_m$ . Bayazit (1976) documented an estimate of  $\kappa \sim 1.6$  for  $S_m \sim 1$ . After a detailed analysis of the fitting procedure, Pokrajac *et al.* (2006) estimated that the Von Kármán “constant” found by Bayazit (1976) can be reduced to  $\kappa \sim 1$ . This a value smaller than the original one, but still larger than the Von Kármán “constant”.

The reasons for these various trends remain not clearly explained, but these systematic shifts cannot be attributed to experimental mistakes only. They are more likely to be related to the complex behavior of the vertical structure of the flow in these conditions. Slight differences in the fitting procedure may produce various Von Kármán constants. Moreover, the authors who suggested the existence of the Von Kármán “constant” have never pretended to explain flows over rough beds with low submergence conditions.

Thus, to predict the mixing length behavior, we must consider its evolution across the entire flow depth in a continuous way, i.e. in the roughness layer, the surface layer and the subsurface

layer. Since viscosity and wakes are suspected of playing a critical role in the vertical mixing length distribution, the concept of damping effect presented in Chapter 2 should be considered. An empirical correction of the mixing length has been introduced by van Driest to take into account the *damping effect* (van Driest, 1956). In small relative submergence conditions, the buffer layer plays a key role and more importantly on the change in level of the velocity curve. As recalled by (Nezu, 2005), the buffer layer “*can no longer be neglected in turbulence research*”.

Another crucial aspect for the turbulent open channel flow is the *velocity-defect law* introduced in Chapter 2 and measured in the experimental result. While this effect is noteworthy in order to describe the velocity profiles and the mixing length distribution in the outer layer, this aspect has been identified as 2<sup>nd</sup> order correction. Moreover, it brings complexities into the model. For these two reasons, it has been decided to neglect this effect in the model for the moment.

### 2.4.3 Mixing length distribution and damping effect: from idealized smooth surfaces to rough permeable beds

For an idealized smooth surface, to account for the damping effect of the viscous sub layer on the turbulent mixing processes, the empirical van Driest mixing length distribution is commonly suggested (van Driest, 1956; Pope, 2001):

$$l_{m,vD} = \kappa(z - z_b) \left( 1 - \exp \left( -\frac{1}{Re_{vD}} \frac{(z - z_b)u_*}{\nu} \right) \right), \quad (3.17)$$

This correction is purely empirical and reproduces well the experimental results for open channel flows over smooth walls. It is built on a comparison between the local Reynolds number in the viscous sub layer (where the velocity profile is linear, i.e.  $U_x(z) = (z - z_b)u_*/\nu$  and a calibrated non dimensional number  $Re_{vD}$  (the van Driest Reynolds number). This local Reynolds number is estimated by  $Re_l = \frac{U_x(z)z}{\nu} = \frac{u_*^2(z - z_b)^2}{\nu^2}$  and Equation 3.17 becomes:

$$l_{m,vD} = \kappa(z - z_b) \left( 1 - \exp \left( -\frac{\sqrt{Re_l}}{Re_{vD}} \right) \right) \quad (3.18)$$

The value of the van Driest Reynolds number  $Re_{vD}$  has been empirically estimated at  $Re_{vD} \sim 26$  by van Driest himself.

For a *rough surface*, it is generally suggested that the roughness increases the turbulence at the interface leading to a lower role of the viscous damping effect, and a modification of the closure is needed. This reflection has been eluded in the original paper of van Driest (1956), and the paper of Krogstad (1991) propounds different modifications and developments.

At this point, two observations can be formulated:

- In natural conditions, a viscous regime may be observed in the roughness layer and just below the roughness crest. This is a situation that can convey the importance of the damping effect. For open channel flows with water, these conditions are clearly met for regular centimetric sediments and low submergence.
- Secondly, if the turbulent regime is observed in the roughness layer, the role of the roughness

geometries on the transfer of momentum in the vertical direction  $z$  is unclear. The interaction between the flow and the 3D complex shapes of the protuberances generates wakes that diffuse the momentum in the transverse directions, i.e. along the vertical but also horizontally in the  $y$  direction.

A general expression to account for the damping effect due to the viscous effect and eventually the wake structures is an intricate problem to study, since turbulence penetration in the roughness layer and in the subsurface domain is controlled by numerous factors. It is not the objective here to provide a general formulation from highly permeable walls to non permeable walls. In the course of this study, only flows where the transfer of momentum under the roughness layer ( $z < z_t$ ) by turbulence is negligible are considered. This approach contrasts with Durán *et al.* (2012), who obtained a differential equation on the mixing length that gives a non zero value of the mixing length below  $z_t$ . Although this approach has the advantage of estimating the penetration of the turbulent mixing effect in the bed, it is more complex to apply and not justified for most natural bed cases. Arguments are developed below for considering a negligible role of the turbulence stress in the subsurface layer.

#### 2.4.4 How negligible is the turbulent mixing in the subsurface layer ( $z < z_t$ ) ?

In contrast to the van Driest approach on a smooth wall, the velocity will not follow the linear trend  $u(z) = (z - z_b) u_*^2 / \nu$  expected for a smooth wall, since the subsurface layer velocity  $U_{x,SSL}$  under the roughness layer imposes a boundary velocity to the system for  $z < z_t$ . Nevertheless, the above mentioned framework assumes that the turbulence is damped when the local Reynolds number  $Re_l$  is low compared to  $Re_{vD}$ . With this in mind, the local Reynolds number is given by providing an estimate of  $U_x(z < z_t) \sim U_{SSL}$ , verified when the turbulence does not penetrate the subsurface layer. For a tilted bed,  $U_{x,SSL}$  is given by the equilibrium between drag forces and the gravity force. Using the Ergün Equation 3.4 to express the drag components, a 2<sup>nd</sup> order equation on  $U_{x,SSL}$  is obtained:

$$0 = gi - A_E \frac{(1 - \epsilon)^2 \nu}{\epsilon d_p^2} U_{x,SSL} - B_E \frac{(1 - \epsilon)}{d_p} U_{x,SSL}^2 \quad (3.19)$$

The pore Reynolds number is thus considered as the local Reynolds number  $Re_l = Re_p = \frac{U_{x,SSL} d_p \epsilon}{6(1 - \epsilon) \nu}$ , with  $U_{x,SSL}$  deduced from Equation 3.19. The square root of this number, as it is defined in Equation 3.18, can be compared to  $Re_{vD}$ .

**Numerical application:** Consider the typical orders of magnitude in a gravel bed river<sup>3</sup> : The slope is  $i \sim 1\%$ ,  $d_p \sim D_{50} \sim 0.05$  m,  $\nu_{water} \sim 1 \times 10^{-6} \text{ m}^2 \cdot \text{s}^{-1}$ . By solving Equation 3.19 for an idealized subsurface context (a packed bed with a narrow granulometry gives a porosity  $\epsilon \sim 0.4$ ), we obtain  $U_{x,SSL} = 0.04 \text{ m} \cdot \text{s}^{-1}$ . The pore Reynolds number is estimated at  $Re_l = 24$ . According to the ratio in the van Driest correction 3.18, we obtain  $\frac{\sqrt{Re_l}}{Re_{vD}} \sim 0.18$ . Introducing this ratio in Equation 3.18, the penetration of a turbulent mixing layer may be negligible in the subsurface layer. This supposition is reinforced if the subsurface particle-size distribution are

---

<sup>3</sup>The orders of magnitude are taken from the upper Roubion catchment (Drôme, France) (Liébault & Piégay, 2001).

finer than in the roughness layer. As it is generally the case.

Solving  $\frac{\sqrt{Re_l(i, d_p)}}{Re_{vD}} = 1$  for a dense porous media ( $\epsilon \sim 0.4$ ), the slope and the sediment size  $d_p$  delimiting two domains may be obtained. These domains are depicted in Figure 3.5. In the left domain, for fine sediments, ( $\sqrt{Re_l} < Re_{vD}$ ), the mixing length is expected to be negligible in the subsurface layer (i.e.  $z < z_t$ ). In the right domain, for larger sediments, a non negligible role of the turbulence in the subsurface layer can be predicted.

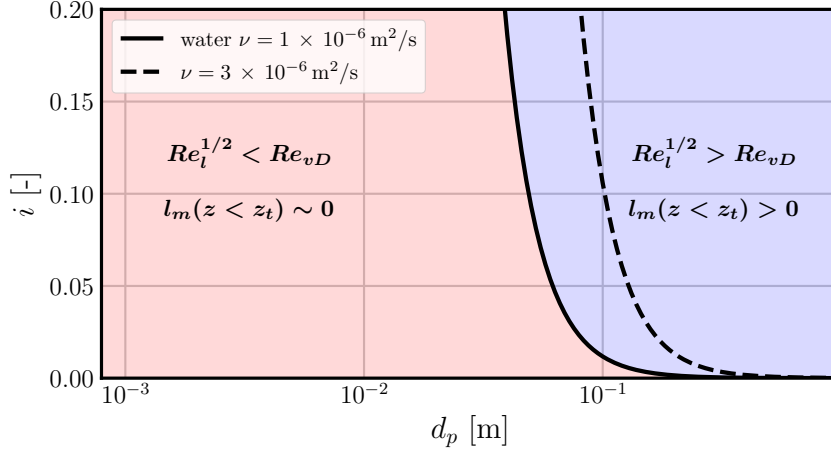


Figure 3.5 – Slope/diameter diagram characterizing the turbulent penetration under the *roughness layer* ( $z < z_t$ ) based on the van Driest approach for a dense porous bed ( $\epsilon \sim 0.4$ ). The boundary is estimated by solving the equation  $Re_l(i, d_p) = Re_{vD}^2$ . The continuous line represents the water boundary (at 293° K) and the dotted line the boundary for a slightly more viscous fluid (the viscosity of the benzyl-alcohol/ethanol mixture used further in the experimental work).

Looking at previous diagram, some comments may be made. For low sizes of sediments, typically under 5 cm in diameter, the penetration of turbulence is not possible. The boundary decreases sharply from high slopes to lower slopes. This is a trend that is anti-correlated by the growth of the sediment size when the river bed slope increases. For sizes of sediments bigger than 0.1 cm, it is expected that turbulence will occur inside the porous bed. Several studies assume a negligible role of turbulence penetration inside the bed. This diagram is a first step to clarify the domain of application of this assumption. Also, it must be noted that, for a real subsurface layer, fine sediments generally occupy the large pores created by the larger stones that constitute the river bed. Thus, the turbulent penetration role in the subsurface layer must take into account these smaller sizes. In a similar manner, the permeability of natural porous media composed of sand and gravel is estimated from effective diameter calculated from the smallest fraction of the grain-size distribution ( $d_{10}$  for instance in Chapuis (2004)).

In Figure 3.6, the critical role of the porosity value may also be observed. For highly porous media the limit curve is significantly shifted to the left, whereas lower porosity eventually caused by the presence of finer particles, shifts the limit to the right. The porosity at the roughness crest being  $\epsilon \sim 0.9$  to 1, this diagram gives an indication in which domain the flow at the roughness crest can be dominated by viscosity. Typically, turbulence penetration is not expected for sediment lower than 1 cm when  $i < 1\%$ .



This prediction will be discussed with regard to the experimental work performed in the next chapters with a slightly more viscous fluid  $\nu_f \sim 3 \times 10^{-6} \text{ m}^2 \cdot \text{s}^{-1}$  on centimetric beads, i.e. typically where the regimes in the roughness layer and at the roughness crest are not clear.

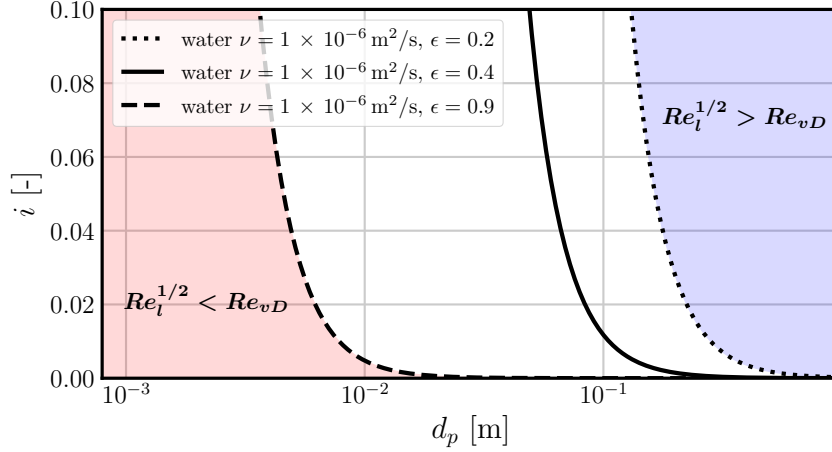


Figure 3.6 – Slope/diameter diagram characterizing the turbulent penetration under the roughness crest ( $z < z_t$ ) based on the van Driest approach for the water and various porosities. The boundary is estimated by solving the equation  $Re_t(i, d_p, \epsilon) = Re_{vD}^2$ .

#### 2.4.5 Closure choice and adaptation to a continuous interface

With the different aspects discussed above, the Van Driest correction is kept in its original form with a no-penetration condition of the turbulence in the subsurface layer, i.e.  $l_m(z < z_t) \sim 0$ . In natural flows and for non mobile beds, it is an arguable hypothesis for the subsurface layer with grain sizes lower than 10 cm. Within this framework, the grain size in the roughness layer can be different from the one in the subsurface layer and eventually much larger. Thus, mountain river beds with large grains ( $d_{50} > 5 \text{ cm}$ ) lying on a relatively lower permeable medium, i.e with a lower grain size distribution ( $d_{50} < 5 \text{ cm}$ ) or a lower porosity, fall within the scope of this hypothesis.

An important point must be clarified. How do we define the  $Re_t$  for a given elevation  $z$ ?

If E.R. van Driest utilized the theoretical velocity profile over a smooth surface to define  $Re_t$ , this possibility does not exist here.

Firstly, the rough surface has an undefined surface position and  $z - z_b$  must be defined differently. Based on reasoning developed during the dispersive stress parametrization, Equation 3.9 establishes a link between  $\ell(z)$  and  $\epsilon(z)$ , the following equality may be written:

$$z_{rc} - z_t = \int_{z_t}^{z_{rc}} \sqrt{1 - \ell^2(z)} dz = \int_{z_t}^{z_{rc}} \sqrt{\frac{\epsilon(z) - \epsilon_b}{1 - \epsilon_b}} dz \quad (3.20)$$

Equivalently the altitude  $z$  is estimated from the integral:

$$Z_{vD} = z - z_t = \int_{-\infty}^z \sqrt{\frac{\epsilon(z) - \epsilon_b}{1 - \epsilon_b}} dz \quad (3.21)$$

With this definition, there is no need to define an origin. Equation 3.21 gives  $Z_{vD}(z < z_t) = 0$  and  $Z_{vD}(z > z_{rc}) = z - z_t$ , the usual linear trend of the mixing length for  $z \rightarrow +\infty$  in the Equation 3.18.

Secondly, without analytical prediction of the velocity,  $Re_l$  is estimated from the local velocity. Equation 3.18 becomes :

$$l_m^* = \kappa Z_{vD} \left( 1 - \exp \left( -\frac{\sqrt{Z_{vD} U_x(z)/\nu}}{Re_{vD}} \right) \right) + C_{vD} l_p \quad (3.22)$$

$C_{vD}$  is an empirical constant that is introduced with regard to the experimental work performed in Chapter 5, to take into account dispersive effects by the presence of grains.  $l_p$  is the pore length scale introduced in Chapter 2. This choice will be explained in Chapter 5.

This mixing length distribution provides a clear advantage through the integration of the porosity profile. However, it results in difficulties in developing an analytical solution and in computing the profile for various cases, since the *damping effect* depends on the velocity.

The discussion on the turbulent mixing term closes here. This closure, like the original closure of Van Driest, is purely empirical and will be tested with the experimental results in Chapter 5. Further improvements of the model are possible with the integration of the *velocity-defect law* or by employing the *double-averaging* framework to explain the different values of  $\kappa$  measured in low submergence flows in the literature.

## 2.5 Summary

The *momentum equation* for a unidirectional steady flow within the *double-averaging* framework is given by:

$$\epsilon \rho_f g i = \frac{d\tau_d}{dz} + \frac{d\tau_t}{dz} + \frac{d\tau_v}{dz} + f_{p,x} + f_{v,x} \quad (3.23)$$

The following closures are employed to model the vertical structure of a flow over a permeable rough bed:

Type	-	Double-averaged form	Closure choice	Parameters
Drag forces	$f_{v,x} + f_{p,x}$	$\frac{1}{V} \overline{\int_{S_{int}} \nu \rho_f \frac{d\tilde{u}_x}{dz} - \tilde{p} e_x \cdot n dS}$	$A_E \frac{(1-\epsilon)^2 \nu \rho_f}{\epsilon d_p^2} U_x + B_E \frac{(1-\epsilon) \rho_f}{d_p} U_x^2$	$A_E, B_E, d_p$
Dispersive stress	$\tau_d$	$-\rho_f \epsilon \langle \tilde{u}_x \tilde{u}_z \rangle$	$\rho_f \epsilon \sqrt{\frac{1-\epsilon}{1-\epsilon_b}} \lambda_+ \left( 1 - \sqrt{1 - \frac{1-\epsilon}{1-\epsilon_b}} \right) U_x^2$	$\lambda_+, \epsilon_b$
Viscous stress	$\frac{d\tau_v}{dz}$	$\rho_f \nu \langle \overline{\frac{d^2 u_x}{dz^2}} \rangle_s - f_{v,x}$	$\rho_f \nu \epsilon \frac{d^2 U_x}{dz^2} + \rho_f \nu \frac{d\epsilon}{dz} \frac{dU_x}{dz} + \rho_f \nu U_x \frac{d^2 \epsilon}{dz^2}$	$\nu$
Turbulent stress	$\tau_t$	$-\rho_f \epsilon \langle \overline{u'_x u'_z} \rangle$	$\rho_f \epsilon l_{m,t}^{*2} \left( \frac{dU_x}{dz} \right)^2$ with $l_{m,t}^* = \kappa Z_{vD} \left( 1 - \exp \left( -\frac{\sqrt{Z_{vD} U_x(z)/\nu}}{Re_{vD}} \right) \right) + C_{vD} l_p$	$C_{vD}, Z_{vD} = \int_{-\infty}^z \sqrt{\frac{\epsilon - \epsilon_b}{1 - \epsilon_b}} dz$

Table 3.1 – Summary of the closure choices for the governing Equation 3.23.

### 3 Numerical simulations

This section delivers an overview of the capabilities of the model for predicting profiles in various hydraulic conditions. For this purpose, Equation 3.23 has been solved numerically. The computation is based on finite difference technique. Following the numerical scheme presented in Appendix B, an Euler semi-implicit scheme has been implemented to guarantee stability and to ensure convergence.

#### 3.1 Porosity profile

The porosity profile is an essential component for low submergence flows, since it controls the roughness layer depth and the interactions with the permeable bed. Quantitatively,  $U_x$  is highly dependent on  $\epsilon$  in Equation 3.4. The porosity profile is required as an input in the model and can be reconstructed from experimental measurements (the strategy employed in Chapter 5) or given by a function reproducing a realistic profile. As explained above, the porosity profile varies from the bulk porosity at  $z_t$  to reach 1 at  $z_{rc}$  defining the Roughness Layer (RL) and the roughness thickness  $h_{RL}$ . Experimentally,  $h_{RL}$  scales with the grain diameter for narrow grain size distribution.

A *cosinus* function with the following parametrization was chosen to guarantee smoothness of  $\epsilon$  at  $z_t$  and  $z_{rc}$ :

$$\epsilon(z) = 1 - 0.5(1 - \epsilon_b) \left( 1 + \cos \frac{(z - z_{rc})\pi}{C_p d_p} \right) \quad \text{for } z_{rc} < z < z_{rc} - C_p d_p \quad (3.24)$$

with,

$$\begin{aligned} \epsilon(z) &= 1 & \text{for } z > z_{rc} \\ \epsilon(z) &= \epsilon_0 & \text{for } z < z_{rc} - C_p d_p \end{aligned}$$

$C_p$  is a factor such as  $h_{RL} = C_p d_p$  and represents the relative expansion of the roughness layer thickness. The cosinus porosity profile reproduces well experimental profiles of bi-disperse stacks of beads having a narrow grain-size distribution as observed in the result part (Chapter 4 and Chapter 5).

#### 3.2 Real case scenarios

##### 3.2.1 Hydraulic conditions

Three real case scenarios with water ( $\nu_{water} = 1 \times 10^{-6} \text{ m}^2 \text{ s}^{-1}$  and  $\rho_{f,water} = 10^3 \text{ kg m}^{-3}$ ) have been simulated to illustrate the model. Focusing on small relative submergence flows, the relative submergence  $S_m$  is fixed at one. The porosity profiles are synthesized by Equation 3.24. The hydraulic conditions for each scenario are as follows:

1. In the first scenario  $\mathcal{P}$ , water runs on coarse sand of 2 mm diameter with a low gravity

gradient  $i=0.5\%$ . The vertical profiles are plotted in the Figure 3.7.

2. In the second scenario  $\mathcal{Q}$ , water runs on stones of 10 cm diameter with a slope of 5% and is depicted in Figure 3.8. These orders of magnitude are typical of a gravel bed river.
3. The third case is the reference case indicated by the letter  $\mathcal{R}$ . It is a water flow on 1 cm diameter sediment with a  $i = 1\%$  slope. The profiles are drawn in Figure 3.9. This reference is produced from the typical order of magnitude of the experiment presented later and corresponds to an averaged case. It serves to obtain a visualization of the responsiveness of the model to the hydraulic conditions in the next section.

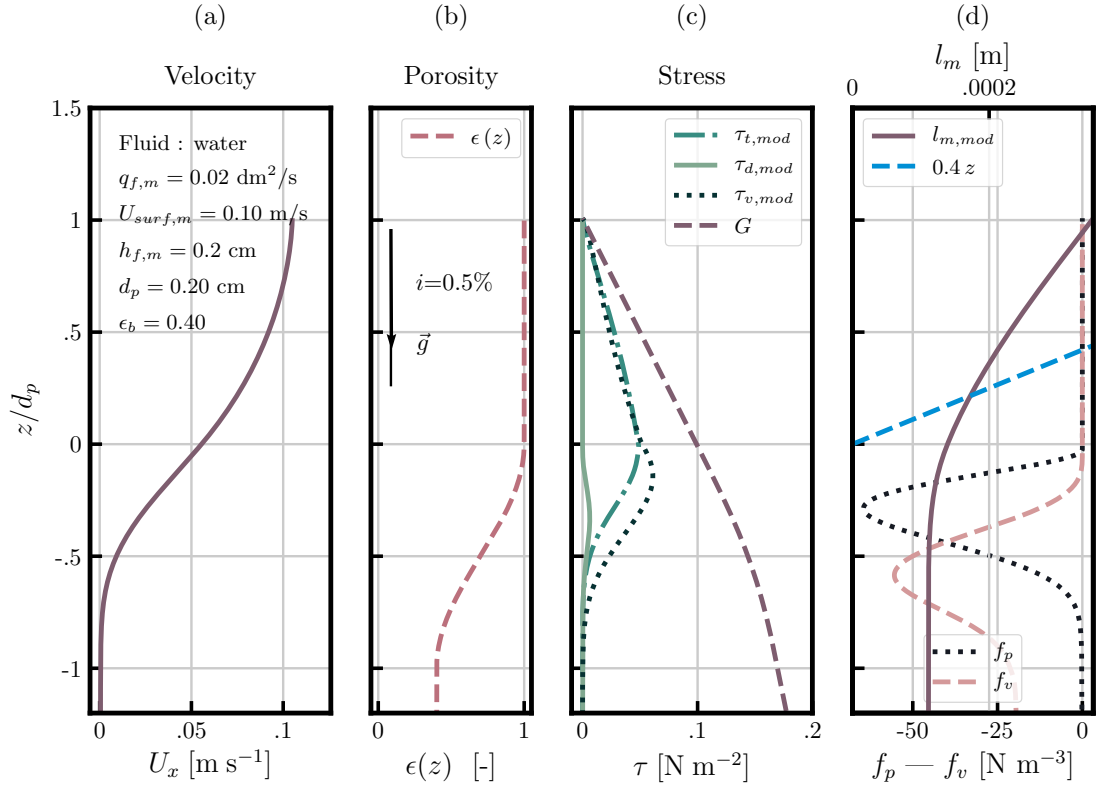


Figure 3.7 – Case  $\mathcal{P}$  low relative submergence flow on coarse sand. Flow characteristics are summarized in Table 3.3.

For all these cases, the parameters of the model have been fixed (see details in Table 3.2). The sediment depth  $h_s$  is equal sediment size. The Ergün parameters are fixed to  $A_E = 180$  and  $B_E = 7.5$  (the usual values), while the other parameters are fixed according to the experimental results (see Chapter 5 for details on the calibration).

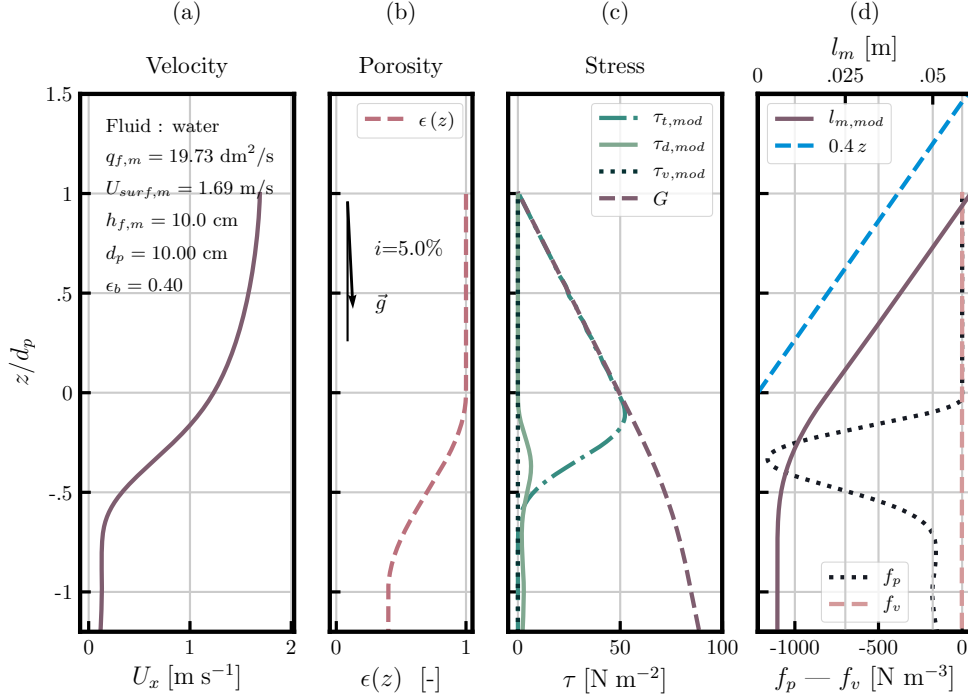


Figure 3.8 – Scenario  $Q$ , typical of a gravel-bedded river. Flow characteristics are summarized in Table 3.3. .

$A_E$	$B_E$	$\lambda_+$	$C_p$	$Re_{vD}$	$C_{vD}$	$\epsilon_b$
180	1.75	0.3	1	70	0.03	0.4

Table 3.2 – Reference parameters of the model

### 3.2.2 Figures details

Each graphical representation of the scenarios (Figures 3.7, 3.8, 3.9) have been compartmentalized into 4 subplots (a) (b) (c) and (d) where 10 profiles in total have been plotted:

- (a) The mean velocity profile  $U_x$  with an indication of the modelled flow discharge per unit width  $q_{f,m}$ , the flow depth  $h_{f,m}$ , the surface velocity  $U_{surf,m}$ , the particle-size  $d_p$  and the bulk porosity  $\epsilon_b$ .
- (b) The porosity profile  $\epsilon$  with an indication of the slope.
- (c) The viscous  $\tau_v$ , the turbulent  $\tau_t$  and the dispersive  $\tau_d$  stresses. In this axis, the integration of the gravity  $G = \int_z^{h_f} \epsilon(z) g i dz$  is also plotted.
- (d) The viscous and pressure drag ( $f_v$  and  $f_p$ ) with the reference axis at the bottom and the mixing length distribution with the reference axis at the top. The reference mixing length function  $l_r = \kappa(z - z_{rc})$  is plotted as it represents the slope limit of  $l_m$  for  $z \rightarrow +\infty$ .

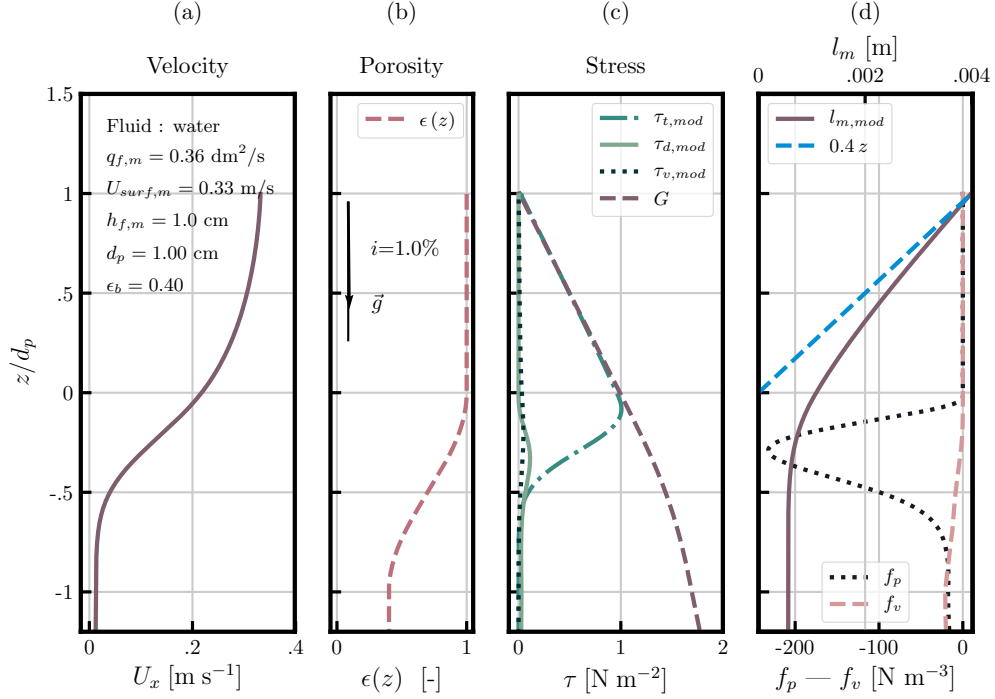


Figure 3.9 – The reference case  $\mathcal{R}$ , the hydraulics condition used in our laboratory. Flow characteristics are summarized in Table 3.3.

### 3.2.3 Comments on the three scenarios

Regarding the three scenarios, the following comments may be drawn:

1. Scenario  $\mathcal{P}$  - Figure 3.7. From the viscous shear and the viscous drag profiles, a significant role of the viscosity is noticeable. Turbulence stress becomes negligible compared to the viscous stress at the interface where the *damping effect* highly influence the mixing length distribution. The gradient of the mixing length distribution is much smaller than the von Kàrmàn constant. This scenario shows the importance of the viscosity for shallow water flows over sand.
2. Scenario  $\mathcal{Q}$  - Figure 3.8. In this scenario, typical characteristics of a gravel bed river are tested. The flow is thus fully turbulent with high Froude and Reynolds numbers. In this case the role of the viscosity is negligible. The dispersive stress plays a minor role but is still observable. The slope of the mixing length reaches  $\kappa \sim 0.4$  sharply. Simulated velocities are about 2 m/s which correspond to the order of magnitudes observed in gravel bedded rivers (Chapter 6 depicts stream surface velocities from a real case scenario with  $V_{surf}$  ranging from 0.5 m/s to 2 m/s).
3. Scenario  $\mathcal{R}$  - Figure 3.9. This scenario is close to the real case scenario of the experiment. In this case, the viscosity role is lower than for case  $\mathcal{P}$  but it is still significant, since the damping is observable in the surface layer: the slope of mixing length is also lower than  $\kappa$ .

Case	$d_p$ [m]	$h_f$ [m]	$q_f$ [dm <sup>2</sup> /s]	$i$ [%]	$S_m$	$Re_b$	$h_+$	$Fr$	$Re_p$
$\mathcal{P}$	0.002	0.002	0.02	0.5	1	410	20	0.85	1.21
$\mathcal{Q}$	0.1	0.1	17.6	5	1	$3 \times 10^5$	22142	1.63	13171
$\mathcal{R}$	0.01	0.01	0.33	1	1	$6.3 \times 10^3$	313	1.11	137

Table 3.3 – Characteristics of the scenarios.  $q_f$  is the fluid discharge per unit width. While the non dimensional numbers are defined in Chapter 2, the definitions are slightly modified here with the specificities of flows over a rough permeable bed.  $Re_b = \frac{\langle U_x \rangle_{h_f} h_f}{\nu}$  is the bulk Reynolds number where  $\langle U_x \rangle_{h_f} = \frac{1}{h_f} \int_{z_*}^{z_*+h_f} U_x(z) dz$  is the mean surface layer velocity,  $h_+ = \frac{u_* h_f}{\nu}$  is the friction Reynolds number,  $Fr = \frac{U_{x,z=h_f}}{\sqrt{gh_f}}$  the Froude number and  $Re_p = \frac{U_{x,z_*=-d_p} d_p}{\nu}$  is the particle Reynolds number where  $z_* = z - z_{rc}$  is the vertical distance from the roughness crest.

### 3.3 Velocity structure and flow characteristics

In this section, the variations of the velocity profiles in regard to common variables used in laboratories or in the field are depicted, i.e. *the flow depth, the slope, the grain diameter*. Lastly, the effects of the *porosity profile* variations are discussed. Note that, for each variable, only one characteristic is compared to the referential case  $\mathcal{R}$  (the dashdotted line in all figures of this section).

#### 3.3.1 Flow depth

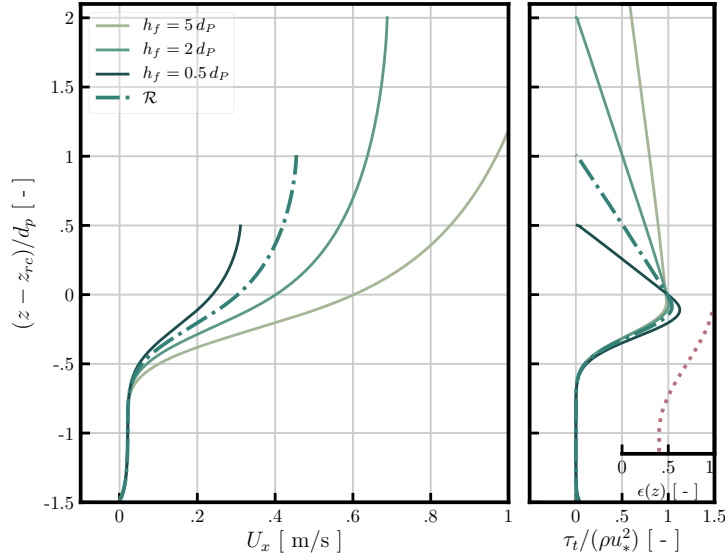


Figure 3.10 – Velocity profiles for four fluid depths ( $h_f = 5 d_p, h_f = 2 d_p, h_f = d_p$  and  $h_f = 0.5 d_p$ ). The surface elevation for the highest fluid depth  $h_f = 5 d_p$  is not visible. The porosity profile is plotted at the left of the figure (dotted line).

By increasing the flow depth, the surface velocities increase as observed in Figure 3.10. The



subsurface velocities stay constant and the surface influence is damped for  $\frac{z-z_{rc}}{d_p} \sim -0.5$ . In the reference regime, the increase of the flow discharge has thus a minor influence in the penetration of the velocities inside the bed. The trend of the non dimensional turbulent stress supposes that the scaling with  $u_*$  is appropriate. The scaling with the flow depth is suggested in regard to the growth of the free surface elevation. However, the scaling on the diameter permits the mechanisms at the interface to be observed. The duality between two scales, *diameter* and *flow depth*, is a recurrent problem for graphical representation of flows over permeable beds.

### 3.3.2 Slope

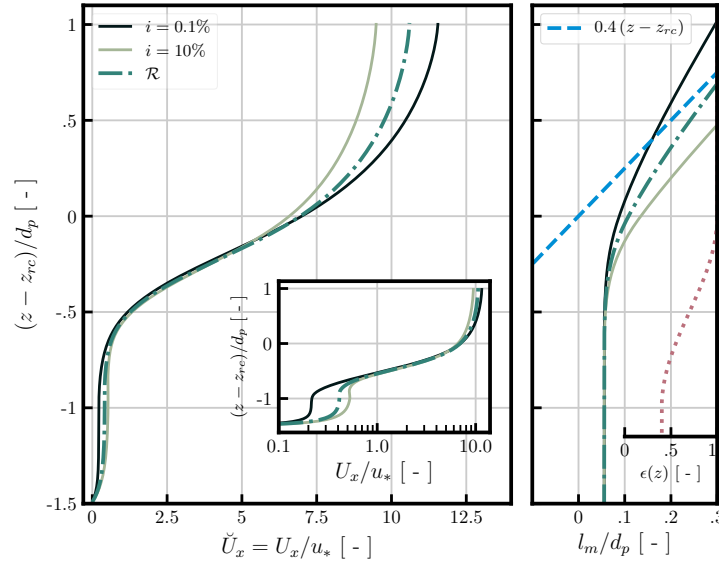


Figure 3.11 – Slope influence on the non dimensional velocity profiles. The dimensional velocities increase across the entire depth. However, the non dimensional velocities, depicted on this figure, increases in the subsurface layer whilst it decreases in the surface layer. The velocities are plotted in a log scale to emphasize the velocity differences in the subsurface layer. The mixing length trend is also influenced by the slope increase.

In contrast to the flow depth, the slope influences the velocities across the entire depth, i.e in the *roughness layer*, the *surface layer* and the *subsurface layer*. This can be observed in Figure 3.11 where the velocity profiles have been scaled with the shear velocity  $u_* = u_p = (g d_p i)^{1/2}$ . In that case,  $h_f$  is equal to  $d_p$  in all profiles, a situation that is simplified since scaling on  $d_p$  or  $h_f$  is equivalent. It avoids the duality of the two vertical scalings. The three profiles are computed for  $i = 0.1\%$ ,  $i = 10\%$  and the reference case  $\mathcal{R}$  where  $i = 1\%$  (the dashdotted line).

In all layers, the growth of gravity projection increases velocities. It might be expected that, with the scaling, the curve may collapse, but this is not the case. The non dimensional velocity  $\check{U}_x$ , such that  $\check{U}_x = U_x/u_*$ , increases in the *subsurface layer* while it decrease in the *surface layer*. This result is remarkable and necessitates some discussion.

These differences in behavior may be explained by the hydrodynamic changes in the roughness

layer, which have two different origins. The velocity magnitudes in the roughness layer are the result of the competition between the drag forces of the porous bed and the shear stresses from the surface. As the subsurface velocity increases, it also influences the damping function that plays an active role in describing the entire velocity profile in the surface. When the slope increases, the *damping effect* decreases and the velocities are smaller relatively to  $u_*$  (see the mixing length distribution in Figure 3.11).

In the subsurface layer,  $\check{U}_x$  increases with the slope. This can be explained by resolving the Ergün Equation 3.19. If Equation 3.19 is rearranged in terms of the non dimensional velocity:

$$1 = A_E \frac{(1-\epsilon)^2 \nu}{\epsilon^2 d_p u_p} \check{U}_{x,ss} + B_E \frac{1-\epsilon}{\epsilon} \check{U}_{x,ss}^2 \quad (3.25)$$

Its solution is:

$$\check{U}_{x,ss} = \frac{\sqrt{(a_E/u_p)^2 + 4b_E} - a_E/u_p}{2b_E} \quad (3.26)$$

With  $a_E = A_E(1-\epsilon)^2 \nu / (\epsilon^2 d_p)$  and  $b_E = B_E \frac{1-\epsilon}{\epsilon}$ . Since  $(1-4b_E) < 0$ , it is a function that increases with  $u_p$  to reach the limit  $\check{U}_{x,ss} = 1/\sqrt{b_E} = \sqrt{\frac{\epsilon}{B_E(1-\epsilon)}}$  for  $u_p \rightarrow +\infty$ .  $\check{U}_{x,ss} = 1/\sqrt{b_E} \sim 0.4$  for a densely packed bed (i.e.  $\epsilon \sim 0.4$ ). This trend is the consequence of the quadratic term in the Ergün equation. Thus, it can be observed in Figure 3.11 that the velocity gap between  $i = 0.1\%$  and  $i = 1\%$  is much higher than between  $i = 1\%$  and  $i = 10\%$ . The order of magnitude of the non dimension subsurface velocity is indeed about the order of magnitude of the limit velocity  $\check{U}_{x,ss} \sim 0.4$  in this example.

### 3.3.3 Grain size

With the grain size, an influence is expected in the subsurface layer due the dependence in  $d_p$  of the Ergün law. However, according to Figure 3.12, the effects are observed in all layers with a relative submergence fixed at one.

Case	$d_p$ [m]	$h_f$	$i$ [%]	$Re_b$	$h^+$	$Re_p$
D1	0.001	0.001	1	147	10	0.31
D2	0.003	0.003	1	1210	51	7.6
D3	0.05	0.05	1	53105	3503	2035
D4	0.5	0.5	1	$1.4 \times 10^6$	$1.1 \times 10^5$	137

Table 3.4 – Characteristics of the different grain size scenarios

In the four scenarios compared to the reference case, particle-size ranges from 1 mm to 50 cm. In these situations, it must be borne in mind that the regimes will vary significantly. In the  $d_p = h_f = 1$  mm-case, it is expected that viscous regime is dominant in the permeable bed and the viscous sublayer thickness may be large in proportion to the flow depth. However, for the 50 cm-case, the viscous shear has no effect. The penetration inside the roughness layer is highly dependent on the *damping effect* that is also dependent on the pore size  $l_p$  as given by the mixing

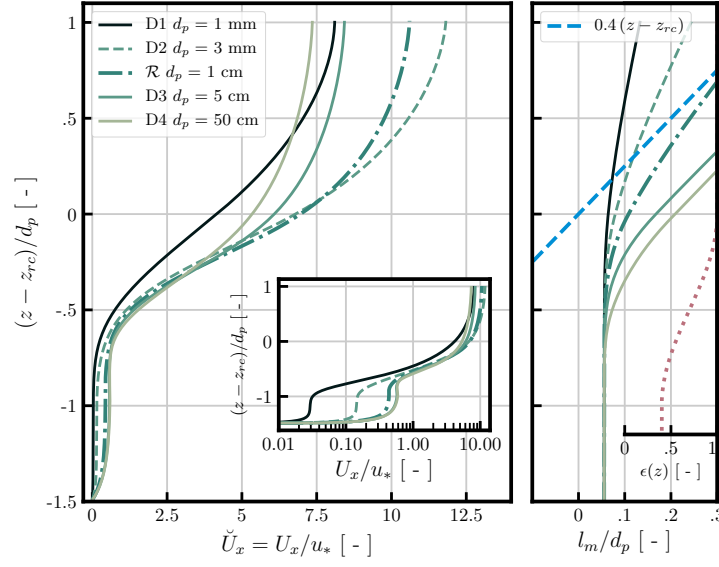


Figure 3.12 – Grain size influence on the non dimensional velocity profiles.

length distribution Equation 3.22. Between the profile  $d_p = 5$  cm and  $d_p = 50$  cm, we observe a significant difference in the penetration of about  $0.1 d_p$ . This interconnection between grain size and *damping effects* is crucial to understand the behaviour of the velocity in the roughness layer and the surface layer.

### 3.3.4 Continuous porosity profile

With all the parameters fixed, the continuous porosity profile defined by Equation 3.24 also plays an important role for the behavior of  $U_x$ . If in natural packed beds composed of stones the porosity normally reaches a bulk porosity  $\epsilon_b$  close to 0.4, there is a variety of structures where the porosity can be different. Vegetated channel where porosity is slightly lower than 1 is an example. Also, in rivers, the roughness layer thickness  $h_{RL}$  and the bulk porosity  $\epsilon_b$  can be reduced by the presence of finer alluvium. It has for consequence to reduce the permeability of the subsurface layer. With a porosity imposed at 0 in the subsurface layer, it is also possible to simulate an impermeable bed (case P4 here). The profiles are presented in Figure 4.2.

For  $C_p = 1$  the roughness height  $h_{RL}$  is equal to the mean grain-size. Modifying this parameter is important to characterize the roughness type. In this first presentation of the model, only the cosinus function Equation 3.24 is used but the possibilities of defining another profile are infinite. For a real scenario, it is advisable to use a estimated porosity profile from measurements.

The two first scenarios (P1 and P2), show an influence inside the bed: the lower the bulk porosity is, the lower the bed is permeable. The shift in the surface velocity is then attributed to a higher level where the local Reynolds number is higher than the van Driest Reynolds number.

For the scenario (P3),  $C_p$  is changed to 0.5. The trend shows the crucial role of this parameter, since it shifts the vertical position where the boundary layer starts. In this case, higher velocities

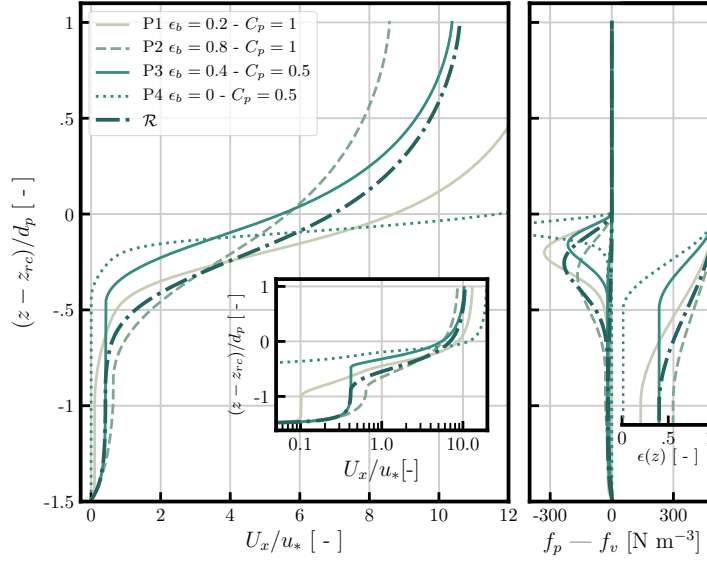


Figure 3.13 – Porosity structure and bulk porosity influence on the non dimensional velocity profiles.

are observed at the surface while the velocities in the roughness layer are smaller than the reference case ( $\mathcal{R}$ ). This effect might be surprising. In fact, it is again the *damping effect* that plays a role in this trend. With  $C_p = 0.5$  the velocities are higher in the roughness layer and the *damping effect* is less important. Its effect is to reduce the apparent turbulent viscosity in this region.

### 3.4 Gibilaro-DiFelice and Ergün equations

As discussed in Section 2.1, the parametrization for predicting pressure and viscous drags is subject to controversy since a large range of porosity is observed. Here, the effects of two laws that deal with solid/fluid interactions are directly tested in the 1D model from the reference case  $\mathcal{R}$  introduced in Section 3.2. The Ergün Equation 3.4 that has been recalled in this chapter and the Gibilaro-DiFelice Equation 2.36 presented in Chapter 2.

The two profiles are plotted in Figure 3.14. The small difference in the *subsurface layer* reveals the similarity of the two approaches for predicting velocities in the permeable medium. In the Gibilaro profile, a slight increase of the velocity due to the diminution of the quadratic term of the drag is observed. This difference for higher porosity is to be expected and might modify significantly the vertical profiles where the pressure drag forces are the dominant effect.

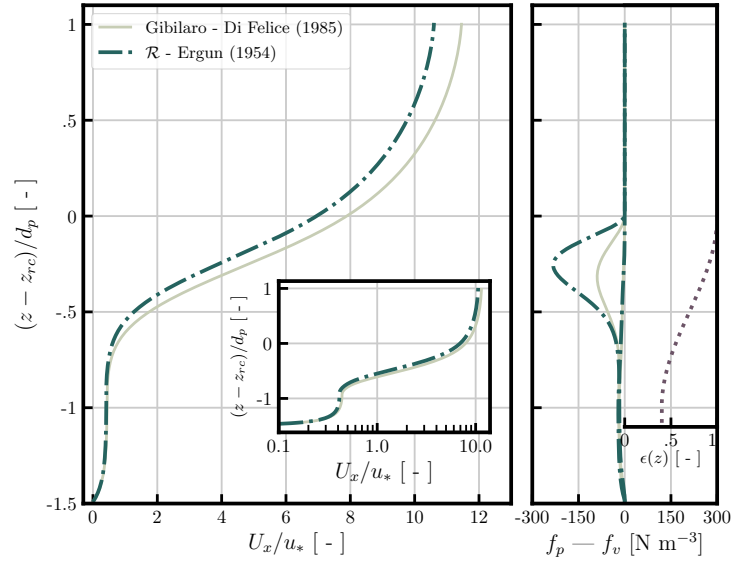


Figure 3.14 – Porous medium law influence

### 4 Summary of the theoretical development

In this chapter, a 1D model describing the vertical structure of a turbulent flow over a rough permeable beds has been devised solving the *double-averaged momentum equation*. By comparison with previous attempts to model flow over porous bed, the principle difference consists of sharp but continuous porosity profile at the sediment/fluid interface. Indeed, most of the models usually consider a jump condition, i.e., a porous region and a surface region split by a local boundary (a Brinkman condition for instance). The porosity profile defines three layers: the *subsurface layer*, the *surface layer* and the *roughness layer*.

This framework seems more appropriate for predicting velocity profiles for small relative submergence. However, the closure must be constructed in an adequate manner. The Ergün equation has been employed to model the viscous and pressure drag in the permeable bed. Moreover, no closure being available for the dispersive stress in the literature, a mechanistic approach has been suggested to parameterize this term. The viscous shear stress has been discussed to choose an appropriate closure among the different choices available in the literature. Finally, the turbulent mixing length theory has been revisited to obtain a phenomenological closure. This closure definition is based on the van Driest approach and has been adapted to the continuous porosity profile. This is the second most important feature of this model: the absence of vertical reference to solve the model.

Finally, the suitability of this model is illustrated by plotting different numerical outputs from various natural environments. The influence of different parameters on the vertical velocity structure is exposed. The *roughness layer* plays a key role in the vertical structure of the flow, since it imposes how the turbulence develops, conditioned by the van Driest damping effect.

This model aims to be valid for various applications, ranging from low gradient rivers to high gradient gravel bedded rivers. Different closure choices are vulnerable to criticism :

- The validity of a porous media equation such as the Ergün equation is questionable for porosity close to one near the roughness crest.
- The turbulent mixing length is based only on the empirical *damping effect* phenomenology derived by van Driest, and observed in the experimental results. Another important feature has been observed in the experimental results, it is the *velocity-defect law* essential to predict velocities in the outer layer. Not yet introduced in the model, this effect is also present in small relative submergence conditions.
- The dispersive stress expression is built on physical arguments arguable for spherical packed beds, and correspond to the measure for this type of bed configuration. Real bed scenarios involve more complex deviation of the velocity, and further experimental investigations are required to test the expression developed in this chapter.

This model has been developed by synergies with an experimental set-up that is able to measure locally the fluid velocities at the interface and inside the porous media. Within the *double-averaging* framework, the different terms of the *double-averaged momentum equation* can be computed and compared to the outputs of the model. The next chapter is devoted to presenting the materials and the method permitting these measures. Chapter 5 presents the results and the comparison with this model.

## Experimental work **Part II**





# 4

## Experimental procedure

---

Owing to the difficulty in measuring fluid velocities inside porous media, there is a significant lack of experimental work describing flows over rough permeable beds with small relative submergence conditions. Herein, a combination of refractive index matched scanning (RIMS) and particle image velocimetry (PIV) is employed to measure velocities from the *surface layer* to the *subsurface layer*. This methodology is referred to as PIV-RIMS in the rest of this manuscript. This method provides local information on the mean velocities, turbulence statistics, and solid element positions in three dimensions.

The data are collected continuously, with a laser sheet moving in the transverse direction. This is a configuration that contrasts with most previous PIV measurements, where the laser sheet is fixed. According to the *double-averaging* concept, the mean *turbulent stress* and *dispersive stress* are deduced from the local information. While this concept is essential for averaging quantities collected in the region of interest and comparing experimental outputs with the *double-averaged momentum equation*, it requires metrological precautions: temporally due to the turbulence, and spatially because of the local disturbance of the mean velocities.

This chapter is structured as follows:

1. Section 1 is devoted to present the set-up and materials
2. Section 2 describes the potential of the PIV-RIMS methodology
3. Section 3 verifies the repeatability and uniformity in the flume, to allow derivation of profiles describing the vertical structure of the flow in nearly uniform conditions with high confidence.

## 1 Experimental setup

### 1.1 Flume and materials

The experiments were performed in a narrow flume (6-cm wide and 2.5-m long) with an adjustable slope  $i$ , as shown in Figure 4.1. A constant head tank provided a steady fluid discharge to the system with the flow being driven by gravity. The flume was randomly filled with

## Chapter 4. Experimental procedure

borosilicate beads of two diameters (7 and 9 mm in equal proportions,  $d_{50} = 8$  mm) to constitute the porous bed<sup>1</sup>. However, before each run, the porous bed was flattened to form a uniform sediment height of  $h_s = 5$  cm. Flow disturbance from the inlet was reduced by straighteners and the region of interest was placed at a distance far enough from the permeable grid (this grid maintained the beads and let the flow seep inside the bed) to obtain a quasi-uniform flow. The outlet condition is of considerable importance in gravity driven flows over highly permeable beds. For example, if the outlet wall is impermeable, a dead flow zone appears upstream for a large distance. Therefore, we chose to keep the outlet wall permeable to guarantee a flow within the entire porous bed. This decision introduced a high pressure discontinuity at the outlet, which raised a question over the uniformity of the flow. This problem is discussed in Section 3.2.

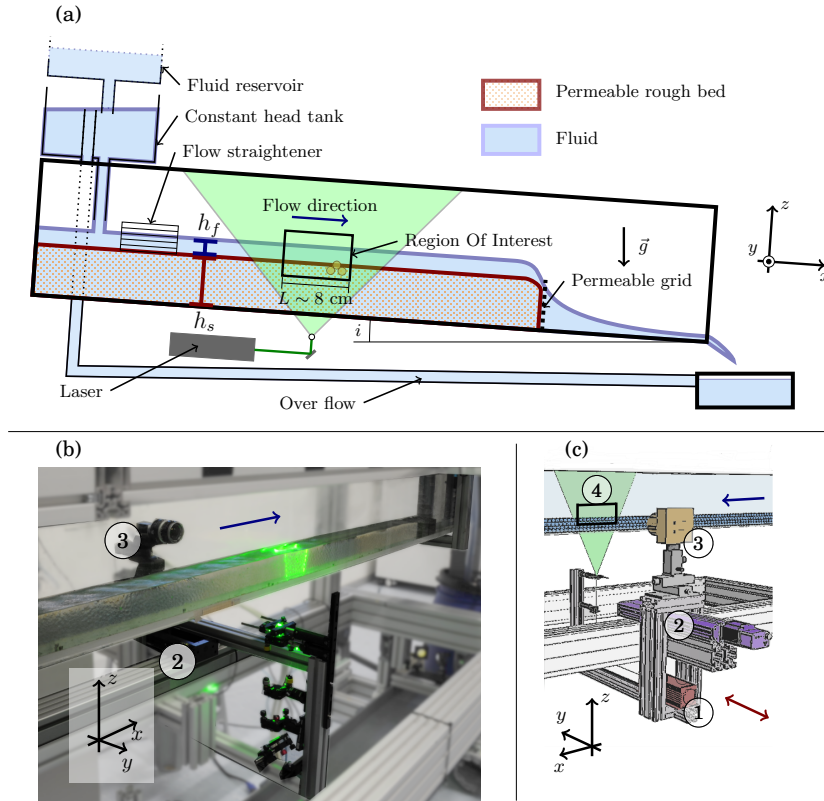


Figure 4.1 – (a) Scheme of the experimental set-up. (b) Photograph during flow (c) 3D vizualization. ① : laser; ② : linear unit for displacement along the  $y$ -axis; ③ : high frequency camera; ④ : laser sheet

The isoindex fluid was prepared with 40% ethanol and 60% benzyl alcohol by volume. With these proportions, the isoindex fluid matches the borosilicate refractive index  $n_f \approx n_{boro-silicate-glass} \approx 1.472 \pm 0.002$  at  $20^\circ\text{C}$  (see the refractive index measurements in Figure D.1 in Appendix D). This mixture has physico-chemical characteristics close to those of water. The cinematic viscosity was measured at  $20^\circ\text{C}$  with a Cannon-Ubbelohde viscosimeter:  $\nu_f = 3.0 \pm 0.1 \text{ mP} \cdot \text{s}$ , and the fluid density was measured at  $\rho_f = 0.95 \pm 0.01 \text{ kg} \cdot \text{m}^{-3}$  (see the

<sup>1</sup>If the bed is composed of beads with the same diameter, a self-structured arrangement is generated provoking undesirable bias in the averaged porosity and velocity profiles

density measurements in Figure D.2 in Appendix D). These quantities are in agreement with the independent measures made by Chen *et al.* (2012). According to Chen *et al.* (2012), the surface tension is about  $\sigma_f = 31 \pm 1 \text{ mN} \cdot \text{m}^{-1}$ , i.e., it is half that of water. The surface tension effects are assumed to be negligible for this problem.

The reservoir containing the fluid (approx. 10 L) delivers the flow to a second reservoir where an overflow pipe maintains the fluid head, ensuring a steady flow discharge into the flume. Two valves control the desired flow discharge: the first valve is manual and regulates the base flow, while the second is an electro-valve, and adjusts the flow to the desired flow discharge  $q_f$ . As observed in Figure 4.1-(a), the reservoir is fixed at the upstream end of the flume to obtain fixed head between runs when the flume is inclined. According to the small angle conditions, the effect of the inclination on the pressure head between the reservoir and the flume appeared to be negligible. The relative accuracy of the total flow discharge was estimated as  $\delta q_f / q_f \sim 5\%$  (See Figure D.3 in Appendix D for details on the determination of the accuracy of the flow discharge).

The fluid mixture is chemically stable, but the free surface in contact with air favors evaporation of the ethanol, thereby reducing its proportion over time, and by consequence the refractive index. Thus, a regular addition of ethanol is necessary. The refractive index matching value  $n_f$  was therefore controlled using a Digital Refractometer (ATAGO RX-5000  $\alpha$ ) between each run. In addition, a small amount of Rhodamine B was added to the fluid to increase the contrast between the beads and the fluid. This configuration {BAE/glass beads/Rhodamine B} was previously tested in our laboratory to determine the position of beads in three dimensions to investigate granular segregation (e.g., van der Vaart *et al.* (2015)). However, this is the first time that this configuration is employed to measure interstitial fluid velocities.

## 1.2 Optics

Frame sequences were recorded with a Basler acA2040-180kc high-frequency camera operating at a speed of 420 frames per second and a resolution of  $1496 \times 700$  pixel (“pixel” is abbreviated by “px” hereafter). The focal length of the objective was 35 mm, with an aperture of  $f/2.8$ . The camera was placed at roughly 30 cm from the side wall (this distance varies when scanning) to obtain a field of vision of  $73.8 \times 34.5 \text{ mm}^2$ . Thus, the mesoscopic scale  $L$  on which spatial averagings are performed is about 8 cm, i.e. ten bead diameters. The micro-metric seeding particles for the PIV were hollow glass spheres of 8–12  $\mu\text{m}$  in diameter. Mounted on a linear unit, the laser sheet travelled through the medium illuminating the micrometric tracers (laser diode-pumped solid state, 4 W, 532 nm). The linear movement of the laser sheet perpendicular to the flow aimed to scan the Region Of Interest (ROI) of a specific width while images were being recorded.

## 1.3 Coupling between PIV and RIM for measuring interstitial flow in previous contributions

The combination of a PIV technique and *refractive index matching* to study liquid-granular flows in rectilinear flumes was previously employed in two recent pioneering contributions:

- Ni & Capart (2015) developed a method that permitted internal measurements of liquid-granular flows with transverse and longitudinal scans.
- Voermans *et al.* (2017) provided the first detailed experimental investigation using *refractive index matching* to study flows over permeable rough beds.

The motivations behind these experimental contributions were close to the present experimental work, and helped to develop this scanning methodology. However, the experimental conditions diverge over one principle point that is crucial to the purpose of this thesis: to obtain steep slopes with small relative submergence conditions, solid/liquid density ratio must be close to the stones/water ratio of natural rivers. It is therefore essential to ensure that the sediment stays at rest while it is still free to move. Indeed, as recalled by Maurin *et al.* (2018), buoyancy plays a crucial role in determining the effect of the slope on the sediment transport rate and motion threshold. Here, the density of the borosilicate glass was  $\rho_s = 2.2 \times 10^3 \text{ kg m}^{-3}$  giving a density ratio for the present study of  $(\rho_s/\rho_f)_{\text{this study}} = 2.3$ . The two cited contributions had density ratios of  $(\rho_s/\rho_f)_{\text{Ni and Capart}} = 1.39$  and respectively  $(\rho_s/\rho_f)_{\text{Voermans et al.}} = 1.24$ , while for underwater sediment  $(\rho_s/\rho_f)_{\text{under-water sediment}} \sim 2.5$ .

### 1.4 Transverse scanning and mean porosity profiles

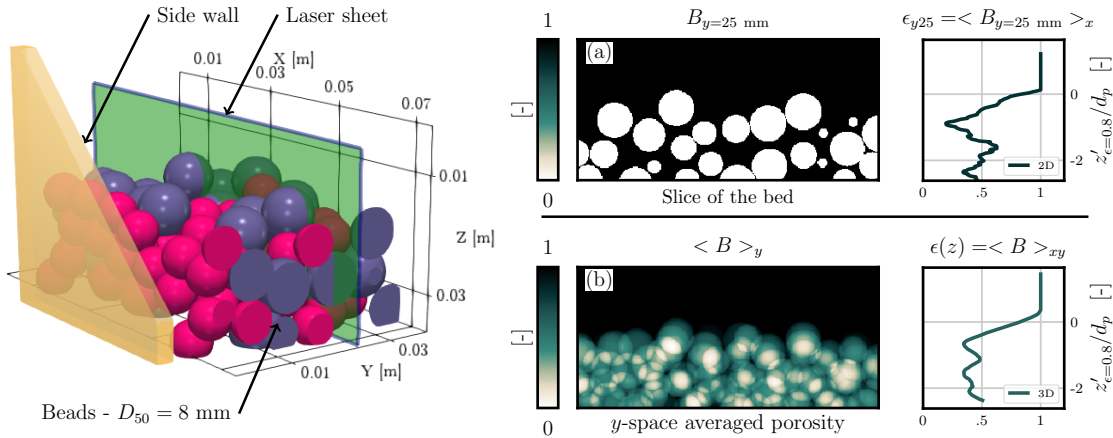


Figure 4.2 – Porosity measurement with RIMS, the beads are localized to build the porosity matrix  $B(x, y, z)$ . (a) The  $B$  field averaged along  $x$  on a slice positionned at  $y_m = 25 \text{ mm}$  from the wall (the laser sheet position in the 3D vizualisation); (b) averaging performed along  $x$  and  $y$  of  $B$  allows a smooth porosity profile to be retrieved. The altitude is noted  $z'_{\epsilon=0.8}$  which is defined by  $z'_{\epsilon=0.8} = z - z_{\epsilon=0.8}$  where  $z_{\epsilon=0.8}$  is the altitude where the porosity is equal to 0.8.

The image acquisitions during the linear movement of the laser along the  $y$  axis yield the bead positions  $(x_b, y_b, z_b)_n$ , as well as an estimate of their diameters  $D_n$ . From the known positions, a spatial 3D matrix of the porosity  $B(x, y, z)$  is built for the 3-dimensional region of interest with a resolution of approximately a tenth of a bead diameter (this porosity matrix is equivalent to the *roughness geometry function* in Nikora *et al.* (2001)). Each cell of the 3D matrix takes a value of 0 if the cell contains a bead, and 1 if not. When a bead surface crosses a cell, the porosity is calculated according to the proportion of the void occupying the cell. The averaged

porosity for a slice at a position  $y$  of the laser sheet is obtained by averaging<sup>2</sup> the matrix along the  $x$  axis  $\epsilon_{y=25 \text{ mm}}(z) = \langle B(x, y = 25 \text{ mm}, z) \rangle_x$ . The global vertical porosity profile is derived by averaging the 3D porosity matrix in the two directions of  $x$  and  $y$ :  $\epsilon(z) = \langle B \rangle_{xy}$  (see Figure 4.2).

The time and space averaged depth<sup>3</sup> is defined by  $h_f = \langle \overline{(z_{surf}(x, t) - z_b)} \rangle$  where  $z_{surf}$  is the free surface position and  $z_b$  the bed position. The bed elevation was fixed at the altitude where  $\epsilon = 0.8$  noted  $z_{\epsilon=0.8}$ , i.e. slightly below the roughness crest  $z_{rc}$ . Although, there is no consensus on the vertical reference definition for a rough bed, this choice seems appropriate for comparing profiles from various bed structure, as will be explained in Section 3.1.2.

## 2 Velocimetry and transverse scans

### 2.1 Image velocimetry processing

The roughness layer contains significant velocity magnitude differences that require a sizeable dynamic range in the image velocimetry tools. Furthermore, the interstitial flow zones between beads are small. These two aspects led me to evaluate different methodologies, from classical PIV to more elaborate PTV (particle tracking velocimetry) methods. The open source library *openCV* written in the *Python* language provided the best performance with respect to our metrological needs. This library and its algorithms originate from the computer vision community, and are rarely used by the fluid mechanics community.

The algorithm is based on the measurement of the local *Optical Flow* by mean of a pyramidal implementation of the Lukas-Kanade method (Bouguet, 2001). Optical flow method obtains the displacement field by minimizing the square of the *Displaced Frame Difference* (DFD). The methodology is similar to PIV algorithms but is optimized to extract the displacement of any feature. Indeed, in classical PIV, algorithms are optimized for the displacement of particle only. To understand better what are the equations involved in the algorithm used and the difference with classical PIV see for instance Liu & Shen (2008); Heitz *et al.* (2010); Boutier (2012). In turbulent fluid mechanic, this methodology has been implemented in pioneering work of Miozzi *et al.* (2008) and latter by Zhang & Chanson (2018). The details on the Image velocimetry method applied to this experimental set-up are available in Appendix C.

### 2.2 Quantities of interest within the double-averaging framework

Turbulent flows over rough permeable beds exhibit strong spatial and temporal heterogeneities. As explained in the Introduction and Chapter 3, the *double-averaging* concept (e.g. Nikora *et al.* (2007)) is adequate to address this problem. Here, the turbulent stress  $\tau_t = -\rho_f \langle u'_x u'_z \rangle$  and the dispersive stress  $\tau_d = -\rho_f \langle \tilde{u}_x \tilde{u}_z \rangle$  may be conveniently deduced and compared to the modelling of the *double-averaged momentum equation*. Thus, an experimental evaluation of the spatial disturbances  $(\tilde{u}_x, \tilde{u}_z)$  and the fluctuations  $(u'_x, u'_z)$  on a specific region of interest, where the two-dimensional assumption is respected, is required to calculate the turbulent stress and the

---

<sup>2</sup>The discrete spatial averaging is defined by  $\langle \eta \rangle_x = \frac{1}{M} \sum_{x_0}^x \eta(x_j)$  where  $M$  is the number of cells in the  $x$  direction and the averaging in the two direction of the space parallel to the mean bed by  $\langle \eta \rangle_{xy} = \frac{1}{MN} \sum_{x_0}^x \sum_{y_0}^y \eta(x_j, y_k)$  where  $N$  is the number cell in the  $y$  direction.

<sup>3</sup>The discrete time averaging  $\bar{\eta} = \frac{1}{n_T} \sum_{t_0}^{t_N} \eta(t_j)$  where  $n_T$  is the number of time step

dispersive stress. This is the objective of the PIV-RIMS methodology.

It is recalled that the disturbance for any position can be estimated by  $\tilde{u}_i = \overline{u}_i(x, y, z) - \langle \overline{u}_i \rangle$ . Where  $u_i(x, y, z, t)$  is the instantaneous local velocity in the direction  $i$ ,  $\overline{u}_i(x, y, z)$  the local time averaged velocity and  $\langle \overline{u}_i \rangle$  is double-averaged velocity in a thin ‘slab’ parallel to the mean bed at the mesoscopic scale. In the  $x$  direction  $U_x = \langle \overline{u}_x \rangle$  and if the flow is unidirectional at the mesoscopic scale  $\langle \overline{u}_y \rangle = \langle \overline{u}_z \rangle = 0$ , one of the assumption required to get the two-dimensional flow assumption that can be verified here experimentally. The other fundamental assumption behind the two dimensionality is the uniformity along  $x$  and  $z$ . They are carefully verified in the course of this chapter. Postulate the two-dimensionality of the flow is relevant when quantities are averaged at the mesoscopic scale (e.g. the discussion of Nikora *et al.* (2007) [p881]). Details on the theoretical background of the *double-averaging* procedure are available in Appendix A.

In the surface layer only (i.e., the altitudes  $z > z_{rc}$  where  $\epsilon(z) = 1$ ), the *double-averaged momentum equation* gives:

$$0 = \rho_f g(h - z) \sin \zeta + \tau_t + \tau_d + \tau_v. \quad (4.1)$$

In the permeable bed below the roughness crest (i.e., the altitudes where  $\epsilon(z) < 1$ ), these assumptions are no longer valid because of drag interactions.

### 2.3 Constraints on the laser sheet displacement when measuring by scanning

In Section 1.4, the scanning methodology used to detect bead positions and acquire porosity profiles was revealed. The fluid velocities can also be collected during this laser sheet displacement. This experimental choice aims to reduce the data storage and the duration of the experimental work. However, this presents several constraints with regard to the spatial and temporal heterogeneities of the flow. An analogy may be formulated to help this problem to be understood. As an example, a flatbed photo scanner requires an adjustment of the chariot velocity for a given digital resolution. Similarly, the laser sheet is moving in the transverse direction with a constant velocity  $V_{MLS}$  (MLS: Moving Laser Sheet). Here, the local fluid velocities collected during this translation depend on the length scale of the spatial disturbance of the flow  $L_u$ , which depends on the topography.  $L_u$  may have the same order of magnitude as the mean radius of the particle, i.e.  $d_{50}/2$ . To pursue the analogy, when digitalizing a picture,  $L_u$  would be the length scale of the spatial variations of the colors.

To obtain a measured point with a given  $V_{MLS}$  the following condition applies

$$V_{MLS} < f L_u, \quad (4.2)$$

Where  $f$  is the frame acquisition rate.

However, contrary to a classical photo scan, the local information fluctuates with time. A wait of a specific instant  $T_u$  is required to access the global statistics of the local flow (average and standard deviation). This affects the measurement strategy significantly, and a second constraint

appears:

$$V_{MLS} < L_u/T_{u'}, \quad (4.3)$$

per laser sheet position  $y_l$  during the translation. However, the laser sheet having a certain thickness (about 1 mm), information yielded at an instant  $t$  is already averaged over the thickness of the laser sheet. With the transverse scan procedure, time and space are mixed and it is therefore crucial to carefully evaluate this procedure by comparing measurements with a fixed laser sheet at  $y_m$  over a long period and the averaged quantities yielded for the PIV-RIMS procedure at the position  $y_m$ .

## 2.5 Evaluation of the scanning methodology

### 2.5.1 Flow characteristics and evaluation procedure

To assess the scanning performance, two runs were conducted using the hydraulic characteristics detailed in Table 4.1 with the same bed arrangement. In the first run, velocities were obtained by PIV for a fixed laser sheet positioned at  $y_l = 25$  mm from the side wall. The second run was performed by scanning the medium with a laser sheet moving from  $y_l = 2$  mm to  $y_l = 40$  mm with the PIV-RIMS methodology. The delay  $T_u'$ , required to obtain confident time-averaged quantities, is first derived from the fixed laser sheet measurements. A duration of 20 s on a specific slice of the flow gives a robust evaluation of the turbulence statistics for measurement points around protuberances to provide an estimate of  $T_u'$ . The velocity of the moving laser sheet  $V_{MLS}$  may then be deduced from the constraints of Equation 4.2 and Equation 4.3. The final evaluation of the methodology is made by comparing the mean velocities and the turbulent stress deduced from the scanning methodology with the measurements obtained with the fixed laser sheet at the position  $y_l = 25$  mm. Table 4.2 summarized the characteristics of the Moving Laser Sheet run and the Fixed Laser Sheet run.

$i$	$W$ [cm]	$Q$ [mL/s]	$q_f$ [ $\times 10^3$ m <sup>2</sup> /s]	$h_f$ [mm]	$U_{surf}$ [m/s]
0.5%	6.0	182	3.0	11	0.34

$U_b$	$Re_b$	$Fr$	$U_{SSL}$ [m/s]	$d_{50}$ [mm]	$Re_{SSL}$	$S_m$ [-]
0.28	1026	1.04	0.015	8	41	1.35

Table 4.1 – Experimental conditions for the test of the PIV-RIMS methodology,  $U_{surf}$  is the surface velocity,  $Re_b = U_b h / \nu$  is the surface Reynolds number,  $Fr = U_{surf} / \sqrt{g h}$  is the Froude number,  $U_{SSL}$  is the mean subsurface layer velocity,  $Re_{SSL} = d_{50} U_i / \nu$  is the interstitial Reynolds number,  $S_m = h_f / d_{50}$  is the relative submergence.

	Type	$y_m$ [mm]	$T_{tot}$ [s]	$f$	$V_{MLS}$ [m·s <sup>-1</sup> ]
Case 1	Fixed Laser Sheet (FLS)	25	20	210	0
Case 2	Moving Laser Sheet (MLS)	2 – 40	20	210	0.002

Table 4.2 – Experimental conditions for the Fixed Laser Sheet and the Moving Laser Sheet.

### 2.5.2 Temporal and spatial averaging measurements with the fixed laser sheet

Figure 4.4 depicts the steps from the temporal averaging to the spatial averaging of flow quantities with the laser sheet fixed at  $y_m = 25$  m. As an example, the time averaging procedure for the horizontal velocity  $u_x$  is shown in Figure 4.4 – (a2) while the spatial averaging along  $x$  is



shown in Figure 4.4 – (a3) (the light-green curves give an idea of the spatial variability of the time averaged velocities along  $x$ ). The time-averaged field of the vertical velocity  $\overline{u_z}$  shown in Figure 4.4 – (b2) is an ideal illustration of why spatial averaging is unavoidable. Indeed, this quantity exhibits large spatial heterogeneity and the approximation of a spatially uniform and unidirectional flow becomes meaningful only at an appropriate mesoscopic scale over which the average is performed. Regarding Figure 4.4 – (b3), the spatially averaged vertical velocity profile  $\langle \overline{u_z} \rangle$  can be reasonably assumed to be zero and the quasi-uniform and unidirectional flow assumption is therefore empirically verified at this scale (about 10 bead diameter). Anticipating the following developments, by scanning along  $y$  PIV-RIMS procedure enlarges the averaging domain, and these assumptions are more strongly verified.

The time averaged turbulence intensities along  $x$  and  $z$  in Figure 4.4 – (c2) and Figure 4.4- (d2) respectively show large spatial heterogeneities. Hot spots are visible for  $|\overline{u'_x}|$  just after the top of the protuberances due to the generation of a turbulent wake behind the body.  $|\overline{u'_z}|$  remains more homogeneous but presents some high magnitude zones inside the turbulent wakes but also in front of the beads lying on the top of the bed. Inside the permeable bed the turbulence activity is negligible and is more likely due to an artefact of the measure. It can be considered as an indicator of the errors performed on the small velocities by the PIV proceeding giving  $\Delta|\overline{u'_i}|_{small} \pm 2$  mm/s. The largest velocities at the free surface are subject to higher inaccuracy owing to the difficulties in measuring displacements at the surface<sup>4</sup>. It can be similarly observed by the artificial increase of turbulence intensities at the surface in Figures 4.4 – (c3,d3). If the vertical turbulence intensities are assumed to be zero at the free surface then the observed fluctuation might be due to the inaccuracy at this altitude giving  $\Delta|\overline{u'_i}|_{high} \pm 5$  mm/s.

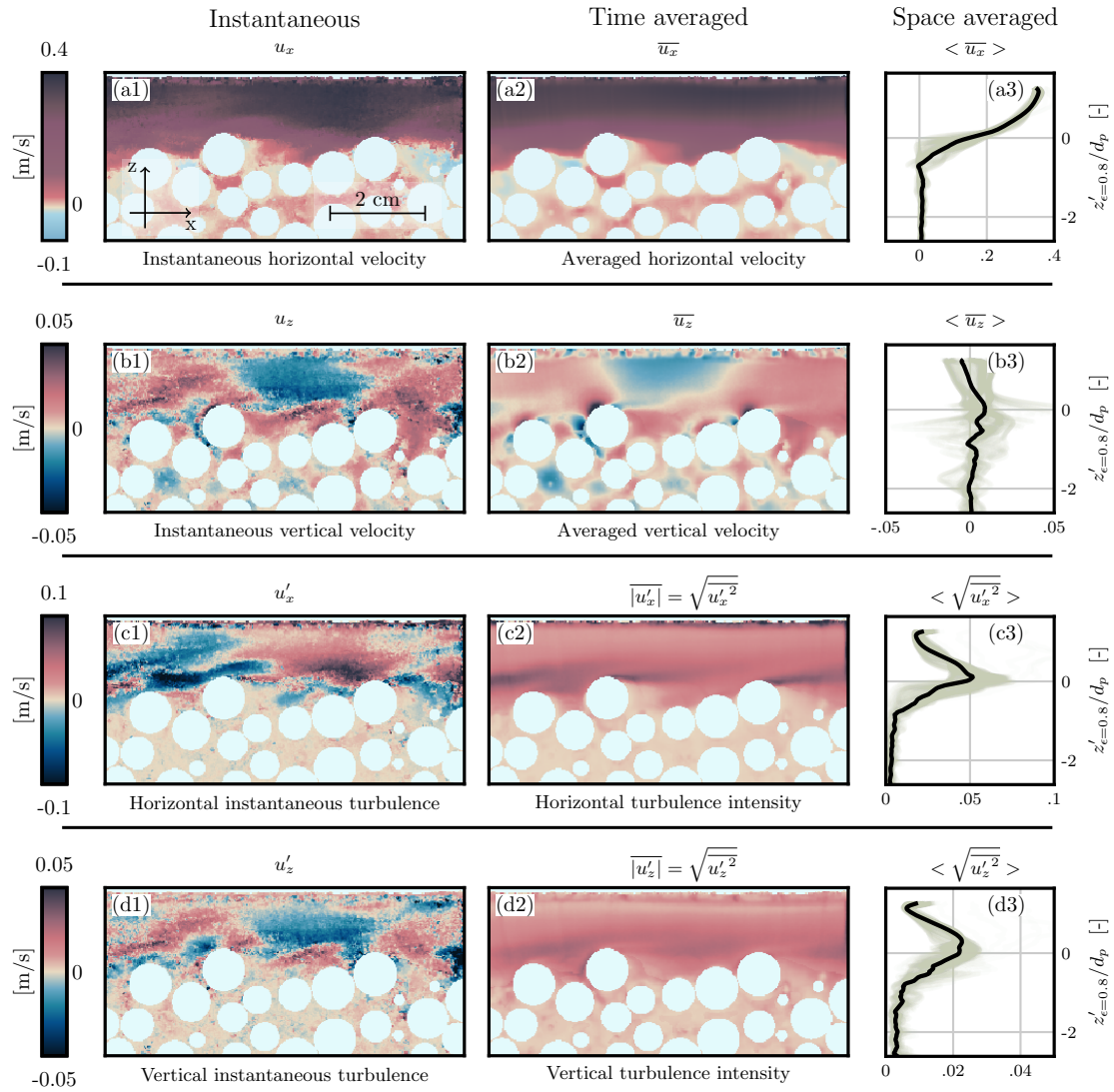
For the turbulent stress  $\tau_t$ , the trend globally compensates the integrated gravity momentum flux (as expected with the momentum balance Equation 4.1 when the dispersive and viscous stresses are negligible inside the surface layer).

The spatial disturbance fields  $\tilde{u}_z$  and  $\tilde{u}_x$  shown in Figures 4.4 – (f2,g2) also exhibit large heterogeneities but contrary to the turbulence intensities these are more likely localised around the beads than in the wakes (note that the spatial disturbance can be positive or negative which is not the case for the turbulence intensities). The observation of these disturbance mappings corroborate the theoretical assumptions made in Chapter 3 on the dispersive shear stress. As observed in Figure 4.4 – (f2), there are small zones in front and behind the bead where horizontal velocity is slower. In these zones the vertical velocity is more likely oriented upward. As a result, the dispersive stress which is calculated by  $\tau_d = < -\rho_f \tilde{u}_x \tilde{u}_z >$ , is more likely to be positive than negative at the interface (see Figure 4.4-(h3)). Note that, for this fixed laser sheet case, measurement is constrained in a single slice of the flow and dispersive stress is negative at the top of roughness elements. This feature is not observed when averaging is performed on a larger domain with the PIV-RIMS procedure as observed in Section 2.6.2. Regarding the dispersive stress mapping in Figure 4.4 – (h2), the positive effect on the dispersive stress is both observed in front and behind the protuberances where the *velocity deficit* is important.

Regarding the Figure 4.4 – (h1), the instantaneous dispersive stress does not have an equivalent instantaneous mapping. Indeed, form induced shear stress is the result of the multiplication  $\tilde{u}_x$  and  $\tilde{u}_z$  that are already time-averaged quantities.

---

<sup>4</sup>The lighting of the surface produce a continuous line with low contrasts as observed in Figure C.1. The 'Good Feature To Track' algorithm normally suppresses these low contrast features but noise persists in this zone. Also, the large displacements due to large velocities close to the surface increase the inaccuracy



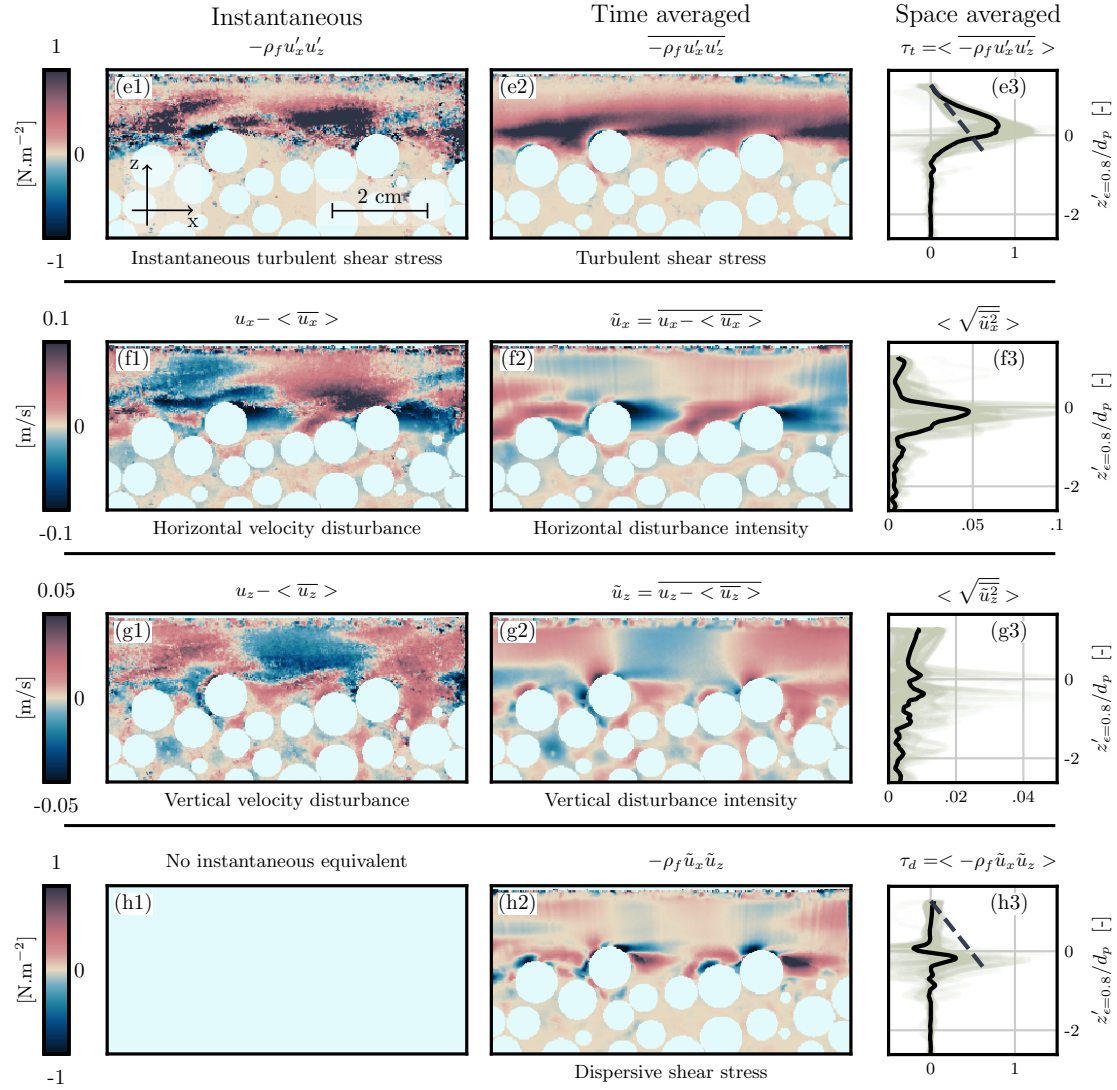


Figure 4.4 – From instantaneous to *double-averaged* quantities. In this configuration, the laser sheet is fixed at the position  $y_m = 25$  mm from the side wall and recorded the flow during 20 s. The units for each quantities are given on the left side. The instantaneous measurements are randomly selected, but each of them is shown for the same instant. For the turbulent stress and dispersive stress, the dotted line shows the integrated gravity from the surface elevation  $\rho g (z_{surf} - z) i$ .

## 2.5.3 Turbulence statistics

Height measurement points have been positioned to study the turbulence statistics on the PIV datum with a fixed laser sheet. They are located around a protuberance formed by a glass bead at the top of the permeable bed as shown in the Figure 4.5-(a). Note that the 3D structure can be visualized in Figure 4.2 since it is the highest bead of the bed crossed by the laser sheet. Examination of Figure 4.6 reveals that the turbulence properties show a strong dependence on the spatial location of the measurement point. This heterogeneity can also be observed in the 2D time averaged statistics in Figures 4.4 – (a2, b2, c2, d2, e2, f2, g2, h2).

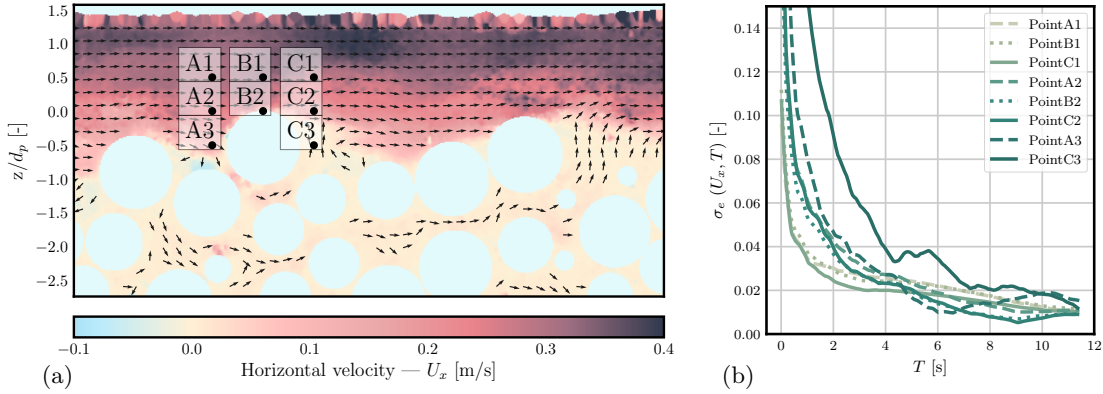


Figure 4.5 – (a) Points of interest surrounding a bead at the top of the permeable bed for statistical analysis of the turbulence; (b) evolution of the standard deviation of the empirical error  $\sigma_e(U_x, t) = \frac{1}{n} \sum_{i=0}^n \sqrt{\left( (\overline{U_x})_T^i - (\overline{U_x})_{T_{tot}} \right)^2 / (\overline{U_x})_{T_{tot}}}$ , where  $(\overline{U_x})_T^i$  is the averaged velocity estimated on  $n = 700$  samples of duration  $T$  against the empirical average calculated over  $T_{tot} = 20$  s. The uncertainty is under 10% after 2 s.

If the measurement point is situated above the roughness crest (A1, B1, C1), the turbulence is spatially homogeneous with a weak intensity. For the points at the roughness crest altitude (A2, B2, C2), the intensity increases and differences between them are observable. Finally, for the lowest level in the rough layer (A3, C3), the statistics will be spatially drastically different. For C3, the averaged velocity is close to 0 and the signal-to-noise ratio is therefore very low, whereas for A3 in front of a bead, the velocities are higher with a high turbulence intensity relative to the mean velocity. Differentiation of the velocity profile along the stream according to the presence of protuberances has been extensively detailed by Mignot *et al.* (2009b,c), and this dissertation does not go further into this classification. Here, this brief turbulence statistic analysis is essentially performed to identify the region where  $T_u'$  is the largest. On Figure 4.5 – (b), an empirical error on the averaged velocity in the function for the duration of the measure  $T$  has been plotted. The flow zones corresponding to the point C3 establish the strongest constraint on the desired continuous scan methodology and we may observe that  $T_u'$  for C3 is in the order of 2 s to obtain a relative error lower than 10%.

In this configuration and with  $T_u' \sim 2$  s, the more restrictive condition is the inequality (4.3), because the constraint on the topography Equation 4.2 is largely respected  $f \gg 1/T_u' = 0.5$  Hz. Hence, the maximum velocity of the moving laser sheet required to obtain satisfactory continuous scan measurements may be estimated by Equation 4.3 at  $V_{MLS,max} \sim \frac{L_u}{T_u'} \sim 2$  mm/s if  $L_u$  is

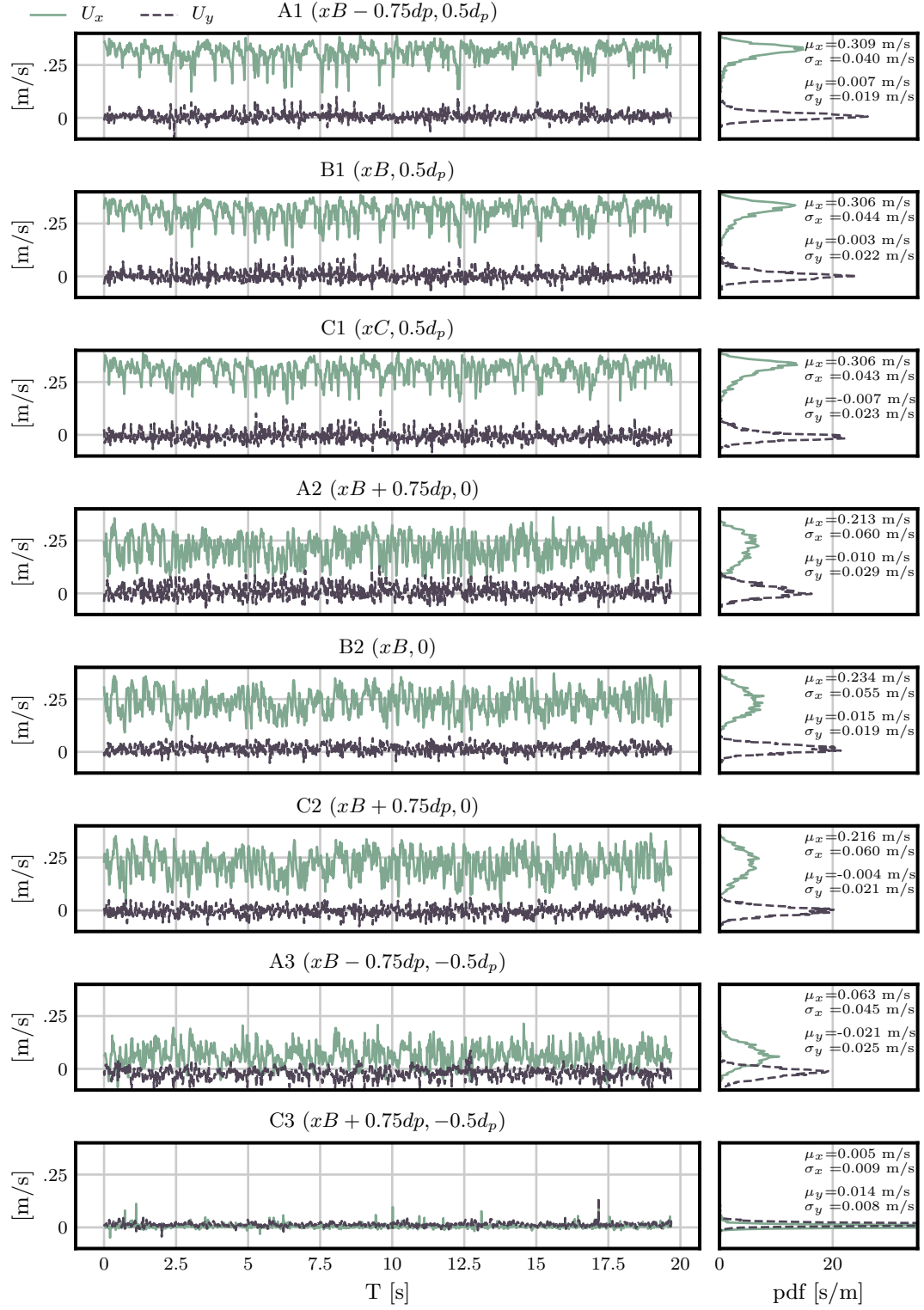


Figure 4.6 – Temporal fluctuations for 8 measurement points as shown in Figure 4.5–(a).

approximated by  $d_{50}/2 \sim 4$  mm.

### 2.5.4 Results of the evaluation

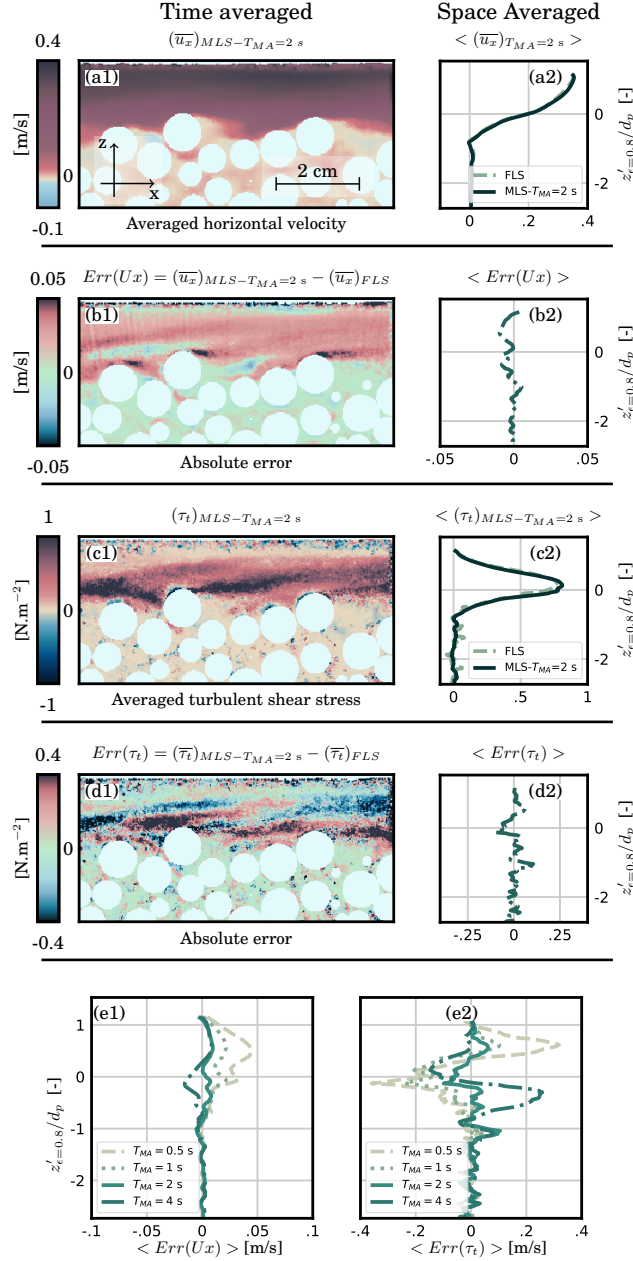


Figure 4.7 – Comparison of estimated profiles at the position  $y_m = 25$  mm with the fixed and the moving laser sheet methods. The error is thus defined by  $Err(\theta) = \langle (\theta)_{MLS-T_{MA}} \rangle_x - \langle (\theta)_{FLS} \rangle_x$ , where  $\theta$  is the velocity profile  $U_x$  or the turbulent stress  $\tau_t$ .  $T_{MA}$  is the averaged time or equivalently the distance  $D_{MA}$  framing the position  $y_m$ . These results show that error is satisfactory for both velocity measurement and turbulent statistics when  $T_{MA} \sim 2s$ .

Now that an appropriate estimate of scanning velocity has been provided with respect

to Equation 4.3, the Moving Laser Sheet (MLS) run is performed by fixing  $V_{MLS} = 2$  mm/s. Figures 4.7 – (a1,c1) provide the time averaged velocity and turbulent stress fields at the position  $y_m = 25$  mm from the moving laser sheet run. Figures 4.7 – (a2,c2) compare the resulting profiles (averaged along  $x$ ) from the moving laser sheet and fixed laser sheet procedures. A good collapse is shown between the averaged velocity and the turbulent stress at the position  $y_m$  of the laser sheet with both FLS and MLS procedures. The Figures 4.7 – (b1,d1) represent the absolute differences observed between the 2D field at  $y_m$ .

An estimate of error profiles is obtained by subtracting the velocity and *turbulent stress* profiles of the FLS experiment from those of the MLS experiment at  $y = 25$  mm (Figures 4.7 – (b2,d2)). Various  $T_{MA}$  have been tried and as observed in Figures 4.7 – (e1,e2) The smallest error profiles are obtained for  $T_{MA} = 2$  s, which corresponds to the prediction made in Section 2.5.3. If  $T_{MA}$  is smaller or bigger than 2 s (or respectively  $D_{MA} = 1$  mm), the error increases.

## 2.6 Preliminary results from the PIV-RIMS method

### 2.6.1 3D vizualisation and the side-wall effect on the flow

Having assessed the relative accuracy of the technique by comparing it with fixed laser sheet methods, different measurements are possible. As a first example, the effect of the side-wall on the flow may be evaluated. Figure 4.8 represents a 3D visualization of the flow, i.e., the horizontal component of the velocity represented on the wall of a cuboid that demarcates the 3D region of interest. The velocity  $\bar{u}_x$  increases with  $y$  for positions further away from the side-wall. This increase can also be observed in Figure 4.9 where  $\bar{u}_x$  has been averaged along the streamwise direction  $x$  and plotted for different altitudes  $z'_{\epsilon=0.8}$ . This allows estimation of the region of the flow where the side-wall effects are negligible (a recurrent problem in the hydraulic experiments) from a distance of  $Y = 10$  mm (where  $Y = y - y_w$  is the transverse distance from the wall position  $y_w$ ). This also demonstrates that measurements at less than 5 mm will be strongly affected by the wall, an observation that raises questions over studies where the measurements are performed close to the side-wall. These observations provide an a posteriori justification for the use of the index matching method to explore the flow at a reasonable distance from the side-wall, and provide insights for obtaining profiles that can be used to evaluate the terms of the simple 2D case of the *double-averaged momentum equation* in the following developments.

Interestingly, in Figure 4.9, the velocities close to the free surface ( $z'_{\epsilon=0.8} = 9$  mm) and the wall ( $Y < 7$  mm) are lower than deeper velocities ( $z'_{\epsilon=0.8} = 2$  mm and  $z'_{\epsilon=0.8} = 4$  mm) at the same distances. This phenomenon may be interpreted in terms of turbulent and dispersive activities that are stronger close to the bed. These mixing processes actively convect laterally (in the  $y$  direction) momentum from the middle of the flume to the side wall at these lower altitudes, while at the vicinity of the free surface this transfer is less active. While I'm know furnishing here more development focussing on the averaged profile in the middle of the flume, this unexpected preliminary result constitutes by itself a piece of work for future investigation on the wall effect in flumes.



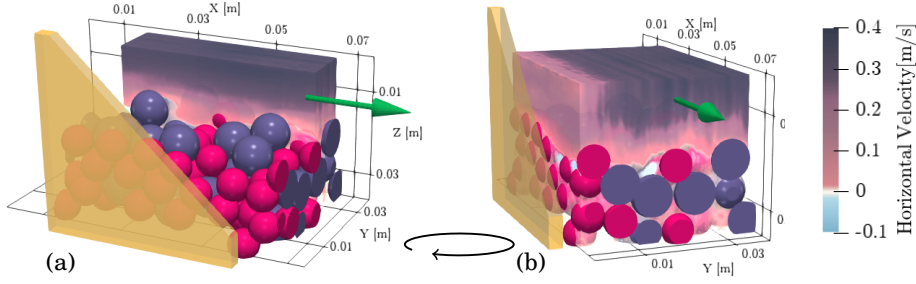


Figure 4.8 – 3D visualization of the horizontal velocity (a) Side view of a slab of the velocity field at the fixed laser sheet position  $y_m = 25$  mm (the same position as the fixed laser sheet results above - see Fig 4.4); (b) Frontal view of the flow, sliced along  $y$ . This view allows appreciation of the side-wall effect.  $Y$  is the distance from the side wall.  $Z$  and  $X$  are arbitrary referenced.

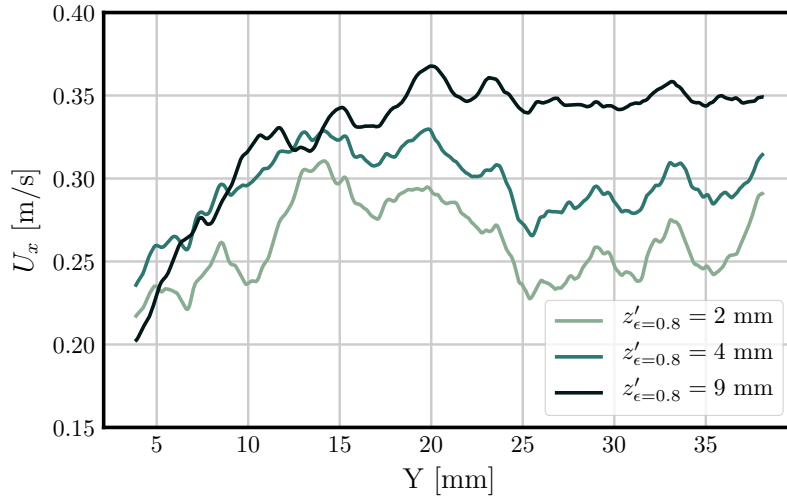


Figure 4.9 – Side wall effect. The horizontal velocity profile has been averaged along the streamwise direction  $x$  and plotted for different altitude  $z'_{\epsilon=0.8} = z - z_{\epsilon=0.8}$  as function of the distance from the sidewall  $Y$ .

### 2.6.2 PIV-RIMS procedure and double-averaged profiles

The main advantage of the PIV-RIMS methodology consists of averaging of flow quantities on an area along the  $x$  and  $y$  direction as expected in the *double-averaging* framework. The ‘smooth’ profiles of the flow quantities are obtained at the mesoscopic scale in the same way that the spatially averaged porosity profiles were computed in Figure 4.2.

The side wall effect was found to be negligible at 10 mm from the walls in Sections 2.6.1. Thus, all the following vertical profiles in this dissertation are the result of the *double-averaging*



method performed in the  $x$  and  $y$  directions with the laser sheet moving from  $Y = 10$  mm to  $Y = 40$  mm.

A significant difference is observed between the two experimental procedures for the dispersive stress while the turbulent stress has a close behaviour. With the fixed laser sheet, the averaging procedure along  $x$  does not include the variability in the direction  $y$ . However, with PIV-RIMS the laser sheet moves along  $y$  and the profiles are averaged along  $x$  and  $y$  containing the variability of the physical interactions in the transverse direction. Thus, the PIV-RIMS procedure is expected to provide a better representation of what dispersive stress is at the mesoscopic scale. It allows the model and the closure developed for the *double averaged momentum equation* in Chapter 3 to be compared with the experimental profiles. Generally, as observed in previous studies (Voermans *et al.*, 2017; Fang *et al.*, 2018), and further in this dissertation, the dispersive stress at the mesoscopic scale exhibits a positive trend at the interface with a maximum localized just below the roughness crest (here at the altitude  $z_{\epsilon=0.8}$ ).

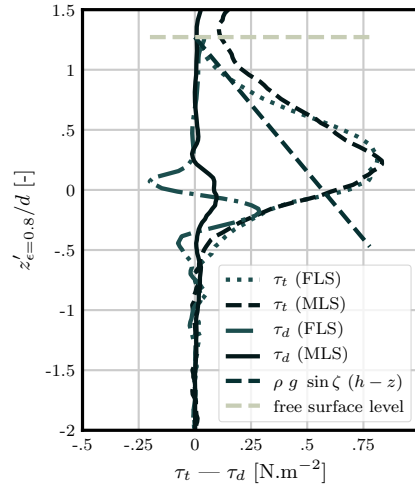


Figure 4.10 – Comparaision of the dispersive and turbulent stresses obtained with the fixed laser sheet (FLS) and PIV-RIMS methodology which relies on the moving laser sheet (MLS) procedure. In contrast to the fixed laser sheet procedure, PIV-RIMS captures the variability of the interactions in the transverse direction  $y$ . The resulting averaged profiles are a better representation of the profiles at the mesoscopic scale.

### 3 Repeatability and uniformity

#### 3.1 Repeatability: the crucial role of bed arrangement

##### 3.1.1 Repeatability at the mesoscopic scale

Two consecutive *double-averaged* velocity profiles employing the PIV-RIMS methodology with equal flow characteristics (slope and flow discharge) indicate good repeatability of the experimental procedure when the bed is not rearranged (see Figure 4.11). Regarding the results of Secs. 2.6.1 and 2.6.2, the profiles are averaged between  $Y = 10$  mm and  $Y = 40$  mm to avoid the sidewall influence. This good repeatability is a consequence of the steadiness of the flow discharge and the accuracy of the PIV-RIMS procedure.

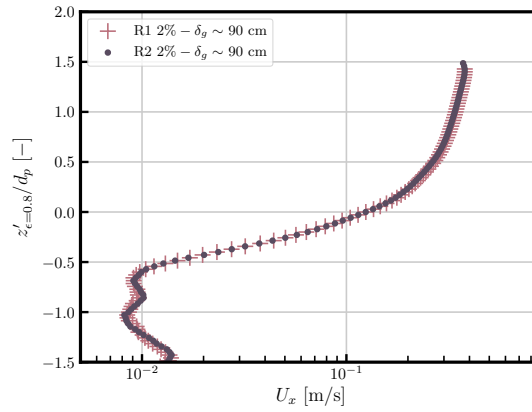


Figure 4.11 – Comparison between two replicates using the PIV-RIMS procedure with both having equal bed structure and flow characteristics. The logarithmic scale facilitates appreciation of the slight scattering in the subsurface layer.

However, with the mesoscopic averaging lengths ( $\sim 8$  cm in the  $x$  direction and  $\sim 3$  cm in the  $y$  direction) and the bead sizes ( $d_p \sim 1$  cm) having similar orders of magnitude, there is no guarantee that the porosity and velocity profiles will be reasonably close from one run to another when the bed structure is reset, i.e. rearranged and flattened for a new run. The reproducibility of experimental results for a rough bed mostly depends on this rearrangement and must be carefully analyzed.

To this end, ten porosity and velocity profiles are compared in Figure 4.12. These were measured with a constant flow discharge ( $q_f = 0.30 \text{ dm}^2/\text{s}$ ) and varying slopes (1%, 2% and 4%). Initially, the bed was randomly mixed and flattened with a rule fixing  $h_s = 5$  cm. The region of interest was placed at a distance  $\delta_g = 90$  cm from the outlet (see Figure 4.13, the effect of this distance on the uniformity of the flow is investigated in the next section). In addition, it was revealed that slight variations in the slope may have important effects on the profiles. To include this source of inaccuracy, the inclination is reset before each run. The accuracy on the slope is about  $\delta\zeta \sim 0.1\%$ , with the relative error being more important for low slopes. Using this procedure, it was expected that the different sources of inaccuracy could be covered in a few

runs<sup>5</sup> allowing this experimental work to be reproducible.

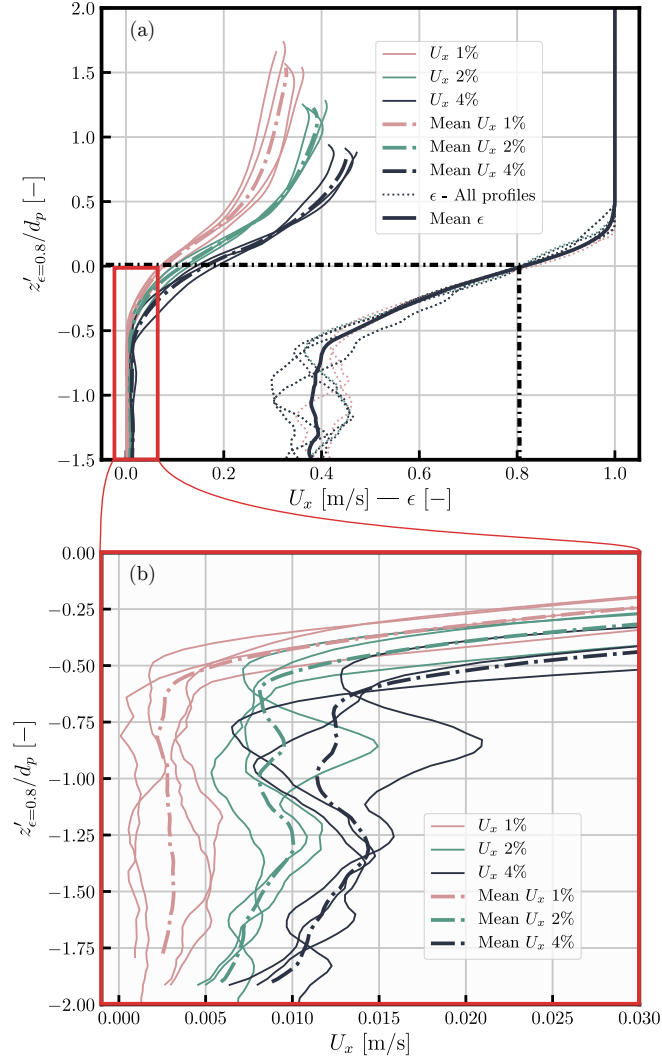


Figure 4.12 – Reproducibility evaluation with different bed structures. (a) Velocity profiles (continuous and dashed lines) and porosity profiles (dotted lines) for different slopes with a constant flow discharge  $q_f = 0.30 \pm 0.015 \text{ m}^2/\text{s}$ . The vertical reference is fixed for the altitude  $z_{\epsilon=0.8}$  where  $\epsilon = 0.8$ . The modified coordinate is given by  $z'_{\epsilon=0.8} = z - z_{\epsilon=0.8}$ . (b) Zooming into the roughness and subsurface surface velocities.

### 3.1.2 Inter-comparisons: the vertical origin definition

Inter-comparisons between vertical profiles are only possible if a vertical origin is defined. There is no generalized approach to fix this origin for rough beds, and scientists generally select a measurable vertical position by default. This choice is also highly dependent on the scientific

<sup>5</sup>the number of runs was limited because of the computational cost

field. For instance,  $z_{rc}$  is a good candidate to obtain reliable values of the von Kármán constant  $\kappa$  ( $z_{rc}$  is generally determined for the altitude where  $\epsilon(z_{rc}) = 0.99$  defined as  $z_{\epsilon=0.99}$  (Pokrajac *et al.*, 2006)).

Other vertical origins are also considered in the literature. According to Nezu & Nakagawa (1993) (pp. 25-27) the range of this reference should be about  $0.15d_p$ – $0.3d_p$  below the top of the roughness element, while in Mignot *et al.* (2009b) the average bed elevation is selected. Voermans *et al.* (2017) also used the RIM technique to determine the porosity profiles. For mono-dispersed bed cases (beads with equal diameters only), they identified an inflection point in the porosity profiles where they fixed the origin. In the present bi-dispersion scenario, no manifest inflection point is detectable on individual porosity profiles.

Thus, different origin levels are arguable in our case. The roughness crest is not a good candidate as it introduces large scatter between profiles<sup>6</sup>. The vertical reference was positioned in an altitude where less scatter between the porosity profiles is observed, and was fixed at  $z_{\epsilon=0.8}$  (See Figure 4.12). The reference point obtained with this ‘scatter minimization’ is located at about  $0.3d_p$  from the roughness crest, which is the shift that Voermans *et al.* (2017) obtained with the porosity inflection option and is in the order of magnitude of what Nezu & Nakagawa (1993) prescribed. This similarity has the advantage of allowing a direct comparison of the results with the study of Voermans *et al.* (2017). The Reynolds numbers calculated with this technique are also slightly different to those estimated with the roughness crest height, as the flow depth  $h_f$  is calculated from a lower altitude.

### 3.1.3 Scatters in the porosity and the velocity profiles

In the *roughness* and *surface layers*, the porosity profiles plotted in Figure 4.12 have similar trends from one experiment to another, with slight differences observed at the roughness crest due to the presence of individual particles on the top. In the subsurface zone (localized at  $z'_{\epsilon=0.8} < -0.5d_p$  in all runs) the profiles show more scatter. This is a consequence of the spatial limitation of the *region of interest*. Nevertheless, the porosity profile trends agree with the packed bed porosities  $\epsilon_b \sim 0.4$  in regard to the calculated mean porosity from all runs.

## 3.2 Uniformity: the permeable grid influence

At the upstream end, straighteners (honeycomb) stabilize the flow provided by a constant head tank, before it runs over the bi-dispersed glass beads (as observed in Figure 4.1 – (a)). Downstream, a permeable grid lets the flow seep inside the bed to guarantee an upstream subsurface flow in the entire bed height (see the zoom on this part of the flume Figure 4.13). The effect of the outlet condition, which contains the granular bed, is generally neglected or omitted in laboratory flumes, whilst it is of primary importance when bed permeability is high.

In this situation, the fluid seeps inside the bed a few centimeters before the permeable grid, causing a diminution of the flow depth. Thus, the pressure drop on the permeable grid located at  $x_g$  influences the whole system: the subsurface flow increases, and by conservation of the flow, reduces the surface flow. Consequently, the flow is expected to be non-uniform until it reaches a

---

<sup>6</sup> At the mesoscopic scale,  $z_{\epsilon=0.99}$  is highly influenced by individual grains slightly higher than the average bed. It has for effect to shift the origin at an inappropriate altitude making inter-comparison between profiles difficult.

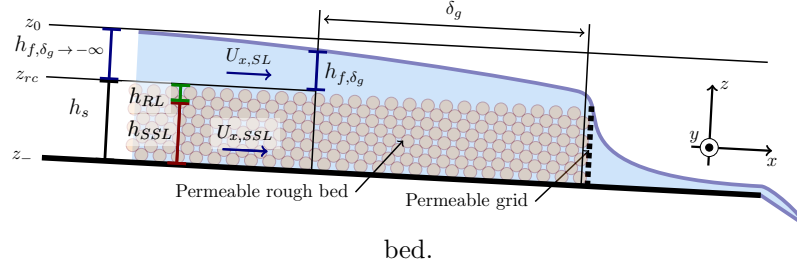


Figure 4.13 – Permeable outlet condition to ensure a subsurface flow. Measurements must be performed at a distance  $\delta_g$  sufficient to ensure that the boundary effect of this condition is negligible.

certain distance from the outlet  $\delta_g$ .

### 3.2.1 Influence of the permeable grid on the subsurface flow

A quantitative estimation of  $\delta_g^\alpha$ , i.e., the distance from the grid where the ratio between the surface flow and the theoretical surface flow in a uniform situation is  $\alpha$  is estimated and given in Appendix 3,

With the simple Darcy framework, the following relationship has been derived:

$$\delta_g^\alpha = \left[ \frac{q_f - \alpha(q_f - \frac{Kg}{\nu} h_s i)}{\frac{Kg}{\nu} h_s} - i \right]^{-1} (h_s + d_p) / 2 \quad (4.6)$$

**Numerical application:** With  $\nu_{BAE} = 3 \times 10^{-6} \text{ m}^2/\text{s}$ ,  $d_p = 8\text{mm}$ , the permeability is estimated with the Karman-Cozeny relation  $K = \frac{\epsilon^3 d_p^2}{180(1-\epsilon)^2} \sim 6.32 \times 10^{-8} \text{ m}^2$ . The sediment depth is manually fixed at  $h_s = 0.05 \text{ m}$ . With  $i = 2\%$  (the average slope in our experiment) and  $\alpha = 0.8$ , we obtain a distance  $\delta_g^{0.8} = 0.68 \text{ m}$ .

This approach predicts that the gate has a role at a relatively long distance in comparison with the flume length ( $\sim 2 \text{ m}$ ). To reduce the outlet discontinuity, a buffer medium (BM) with a permeability higher than the subsurface layer ( $K_{BM} > K_{SSL}$ ) was added at the outlet, to ensure that the outlet conditions do not reduce the subsurface layer velocities. However, the diminution of this effect does not imply that the effect remained negligible. In the following, the effect is estimated empirically to conclude on a negligible role of the permeable gate when  $\delta_g$  is sufficiently large.

### 3.2.2 Verification of the nearly uniform conditions

To verify the nearly uniform conditions at  $\delta_g = 90 \text{ cm}$ , we executed a set of experiments at shorter and longer distances from the outlet  $\delta_g$ , whereas the previous repeatability tests were all performed at  $\delta_g \sim 90 \text{ cm}$  (Figure 4.12). The longest distance is  $\delta_g = 110 \text{ cm}$ , and is possibly influenced by the inlet conditions. The shortest distance is  $\delta_g = 60 \text{ cm}$ .

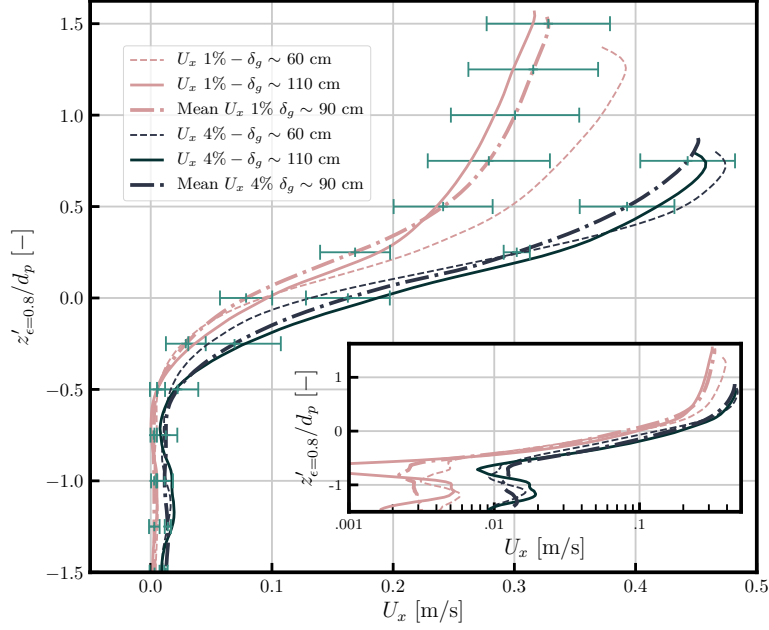


Figure 4.14 – Velocity profiles for various  $\delta_g$  to evaluate the flow uniformity in the channel. The dashed-dotted lines represent the averaged velocity profiles at  $\delta_g = 90$  cm. The error bars show the deviations from the averaged profiles due to the modification of bed structure. This amplitude is to obtain an estimate of the 95% interval where  $\sigma_{U_x}(z)$  is the standard deviation at the altitude  $z$  calculated from the profiles presented in Figure 4.12. The continuous lines are the profiles measured at  $\delta_g = 60$  cm and the dashed lines were measured at  $\delta_g = 90$  cm. At bottom right, the same profiles are plotted with a logarithmic scale to emphasize the differences for low velocities.

In Figure 4.14, an important effect of the outlet for  $\delta_g = 60$  cm and for  $i = 1\%$  may be observed. In this situation, higher velocities are measured in the surface and subsurface, whilst the depth is lower than in the mean profile at  $\delta_g = 90$  cm. This is in agreement with what is expected from Equation D.3, where the subsurface flow increase contributes to a decrease in the flow depth. For  $i = 4\%$ , differences between profiles cannot be statistically attributed to an outlet effect. Indeed, the noise due to the between-run rearrangement of the bed at a constant position is more important than the difference between the profiles at various distances. This analysis suggests that a nearly uniform flow is obtained at  $\delta_g = 90$  cm, as the differences between the profiles at  $\delta_g = 110$  cm and  $\delta_g = 90$  cm are not statistically significant. The results are presented in the following analysis, with all the profiles shown being measured at  $\delta_g = 90$  cm.

## 4 Summary of the experimental procedure

As a first step, this chapter presented the PIV-RIMS technique that captures the averaged quantities of turbulent flows within the *double-averaging* approach. This technique has been employed for a turbulent unidirectional flow over a permeable rough bed. The measurement of this flow type necessitates access to the interstitial flow. Scanning with the isoindex technique (RIMS) has demonstrated its capacity to obtain reliable porosity profiles  $\epsilon(z)$ . Coupled with the PIV processing, the surface and interstitial velocities have been deduced from the image sequences of the RIMS. The PIV-RIMS methodology minimizes the data storage requirements and duration of the experiment, but requires the parameters to conform to certain criteria. The velocity of the moving laser sheet  $V_{MLS}$  must be slow enough to extract the spatial and temporal variability of the flow. In order to neglect the wall effect on the mean flow the profiles are obtained by averaging between  $Y = 10$  mm and  $Y = 40$  mm.

It follows therefrom that the repeatability as well as the uniformity have been carefully checked. Due to the limited dimensions of the region of interest, it has been shown that the first order effect on repeatability is bed rearrangement that highly influences mean vertical porosity structure and, by consequence, velocity profiles. Nevertheless, this effect has been quantified to be small enough to differentiate profiles at mesoscopic scale with varying slopes. Due to the permeable grid influence at the outlet, uniformity assumption is also subject to question. Distance between region of interest and outlet positions has been set at  $\delta_g = 90$  cm to obtain satisfactory uniform flows.

In next chapter, this technique is employed to provide various vertical profiles used to explore shallow water flows over rough permeable walls.





# 5

## Experimental results

---

In this chapter, experimental results on gravity driven flows over rough permeable beds are reported. The PIV-RIMS methodology presented in Chapter 4 yielded the *double-averaged* vertical structure for flow quantities such as mean velocity and porosity, as well as the turbulent, dispersive, and viscous stresses. Here, nine runs following this procedure are depicted with different flow characteristics, including two grain sizes, various slopes (0.5% to 8%) and flow depths. The profiles are compared with the experimental work of Voermans *et al.* (2017), in which the *double-averaging* approach was also employed.

The empirical mixing length distributions are shown to be in agreement with the main discoveries in turbulent open channel flows, these being the *damping effect* and *velocity defect law*. To the best of my knowledge, these well-known open-channel flow features are here reported for the first time for steep slopes with roughness sizes larger than 0.1 mm.

In addition, the closures presented for the model developed in Chapter 3, which reproduces the *double-averaged* vertical profiles, are tested. Using the model, vertical profiles are computed from the various flow characteristics of the 9 runs and are compared with the measured profiles. The agreement between the model and experiment is good. The crucial role of the damping effect on the mixing length distribution is then revealed.

### 1 Characteristics of the vertical profiles

The parameters defining each experimental run have been listed in Table 5.1. In these runs, the flow discharge remains constant while the slope varies from 0.5% to 8% and flow depth  $h_f$  from 5 to 16 mm. To constitute the permeable bed, two bi-dispersed mixes  $[d_1/d_2]$  of borosilicate glass beads were tested. Each mix consisted of two types of bead sizes in equal proportions by mass. Thus the median diameter  $d_p$  was the average of the two bead diameters giving:

- Runs A:  $[d_1 = 7 \text{ mm and } d_2 = 9 \text{ mm}] \ d_p = 8 \text{ mm}$
- Runs B:  $[d_1 = 13 \text{ mm and } d_2 = 15 \text{ mm}] \ d_p = 14 \text{ mm}$

Run	A1	A2	A3	A4	B1	B2	B3	B4	B5
Beads mix 50/50 [mm]	7-9	7-9	7-9	7-9	13-15	13-15	13-15	13-15	13-15
$d_p = d_{50}$ [mm]	8	8	8	8	14	14	14	14	14
$i$ [%]	0.5	1	2	4	0.5	1	2	4	8
$q_f \times 10^3$ [m <sup>2</sup> /s]	3.03	3.03	3.03	3.03	3.03	3.03	3.03	3.03	3.03
$\epsilon_b \pm 0.04$	0.38	0.38	0.38	0.38	0.4	0.4	0.4	0.4	0.4
$h_f \pm 1$ [mm]	13	12	10	7	16	14	10	7	5
$u_*$ [mm/s]	26	35	45	53	28	37	45	54	61
$u_{*,V}$ [mm/s]	27	31	37	45	28	30	45	39	45
$u_p$ [mm/s]	20	28	40	56	26	37	52	75	105
$U_b$ [m/s]	0.26	0.28	0.32	0.37	0.24	0.26	0.28	0.33	0.36
$U_{surf}$ [m/s]	0.34	0.36	0.41	0.47	0.31	0.34	0.36	0.41	0.43
$U_{SSL}$ [mm/s]	1.72	3.43	6.33	9.94	6.52	7.42	12.93	21.65	37.93
$Re_b$	1147	1150	1095	873	1272	1230	952	814	582
$Re_{surf}$	1507	1494	1409	1116	1649	1583	1230	1009	682
$h^+$	116	143	154	125	149	172	154	131	98
$Re_p$	4.6	9.1	16.9	26.5	30.4	34.6	60.4	101	177
$Re_{RL}$	48	66	97	161	199	224	299	381	562
$K_{CK}$ [mm <sup>2</sup> ]	0.06	0.06	0.06	0.06	0.19	0.19	0.19	0.19	0.19
$Re_K$	2.2	3.0	3.8	4.4	4.1	5.4	6.6	7.9	9.0
$Fr$	0.92	1.04	1.29	1.79	0.78	0.92	1.13	1.54	1.96

Table 5.1 – Hydraulic parameters for the nine runs.  $q_f$  is the flow discharge per unit width,  $U_b$  is the surface layer mean velocity,  $U_{surf}$  is the free surface velocity,  $u_* = \sqrt{gh_f i}$  the shear velocity,  $u_p = \sqrt{gd_p i}$  the particle velocity,  $U_{SSL}$  the subsurface layer mean velocity,  $Re_p = \frac{U_{SSL} d_p}{\nu}$  is the particle Reynolds number,  $Re_{RL} = \frac{U_{RL} d_p}{\nu}$  the roughness layer Reynolds number where  $U_{RL}$  is the mean velocity in the roughness layer,  $K_{CK} = \frac{\epsilon_b^3}{180(1-\epsilon_b)^2} d_p^2$  is the Carman-Kozeny equivalent permeability,  $Re_K = \frac{\sqrt{K_{CK}} u_*}{\nu}$  is the permeability Reynolds number,  $Fr = \frac{U_{surf}}{\sqrt{gh_f}}$  is the Froude number, and  $u_{*,V}$  is the shear velocity deduced from the total shear stress, as explained in Section 2

In all runs, the experimental procedure remained identical to the experimental procedure presented in Chapter 4. The profiles were spatially averaged in a volume located in the middle of the flume, i.e., between  $Y = 10$  mm and  $Y = 40$  mm, thereby avoiding undesirable wall effects and allowing supposition of two-dimensionality for the flow. Indeed, the wall effect was found to be negligible for distances of  $Y > 10$  mm from the sidewall in Chapter 4 – Section 2.6.1.

Vertical profiles for the runs A1 and A3 ( $d_p = 8$  mm) are shown in Figure 5.1 to introduce the vertical flow structure, i.e., the double averaged velocity, in relation to porosity structure and stresses.

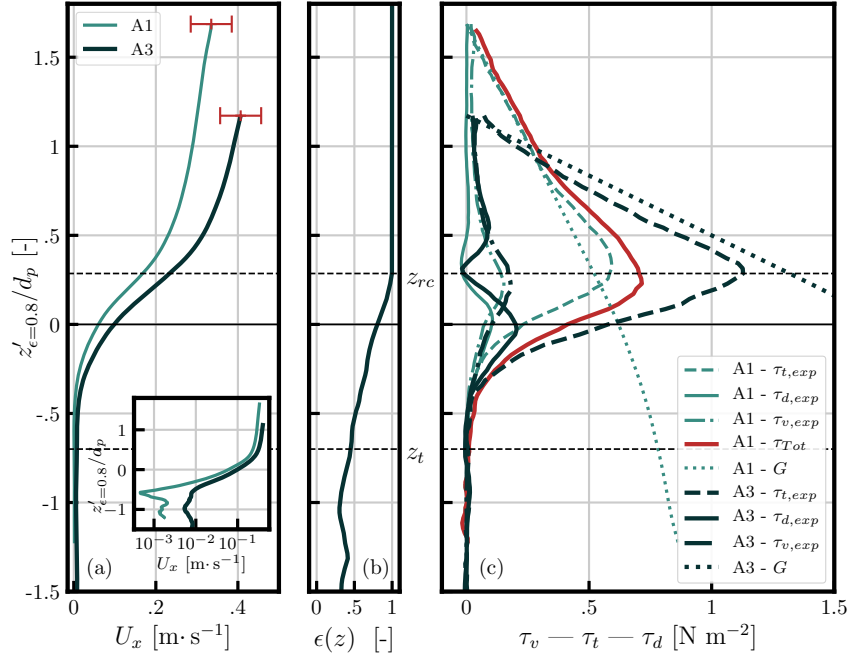


Figure 5.1 – Vertical profiles for the runs A1 ( $i = 0.5\%$ ) and A3 ( $i = 2\%$ ) with a constant flow discharge. (a) Velocity profiles: the subsurface velocities are shown with a logarithmic scale on the abscissa. The thin horizontal error bars represent the uncertainties at the free surface level. (b) The porosity profile. (c) The turbulent stress compared with  $G$  defined by Equation 5.1; the turbulent  $\tau_t$ , dispersive  $\tau_d$  and viscous  $\tau_v$  stresses, as well as the total stress  $\tau_{Tot}$  (for run A1 only;  $\tau_t = \tau_v + \tau_t + \tau_d$ ). The dashed horizontal lines represent the roughness crest elevation  $z_{rc}$ , (i.e for  $z'_{\epsilon=0.99} = 0$ ) and the troughs of the roughness element  $z_t$ . The vertical distance is normalized by the mass-median-diameter  $d_p$  and defined by  $z'_{\epsilon=0.8} = z - z_{\epsilon=0.8}$  where  $z_{\epsilon=0.8}$  is the altitude where  $\epsilon = 0.8$ .

## 1.1 Porosity profiles

The porosity profiles are shown in Figure 5.1-(b). They are identical for all A runs, as the bed was not rearranged between runs. As explained previously, the porosity profile allows definition of the different layers of the flow: the roughness layer being located between the roughness crest  $z_{rc}$  and the troughs of the roughness element  $z_t$  (where  $\epsilon \sim \epsilon_b$ ); the surface layer and the subsurface layer are respectively situated above and below these altitudes. The definition of the layers can

be visualized in Chapter 3 - Figure 3.1.

The origin was fixed at the altitude where  $z'_{\epsilon=0.8} = 0$  to make it convenient to compare profiles between runs, in agreement with the discussion in Section 3.1.2 of Chapter 4. While  $z_{rc}$  can be correctly positioned at  $z'_{\epsilon=0.99} = 0$ , it is difficult to identify the position of  $z_t$ , as the porosity fluctuates strongly between the roughness layer and the subsurface layer. Indeed, this position should be at  $\epsilon \sim \epsilon_b$ . Thus, the following arbitrary definition was adopted:  $z_t$  is located at  $z'_{\epsilon=0.8} \sim -0.7 d_p$ . With these values chosen for  $z_t$  and  $z_{rc}$ , the roughness layer thickness is then approximately  $d_p$ , since the origin  $z_{\epsilon=0.8}$  was found to be  $0.3 d_p$  lower than  $z_{rc}$ .

### 1.2 Velocity

Between A1 and A3, the slope increases from 0.5% to 2%. The projection of the gravity force on the streamwise direction when slope increases affects the velocities in the different layers of the flow, i.e, in the surface, subsurface, and roughness layers. However, the  $U_x$  increment depends on the layer observed.

As observed in Figure 5.1-(a), subsurface velocities are multiplied by 3.8, while the free surface velocity is multiplied by 1.23. This difference is a consequence of the different natures of the interactions in each layer. The flow in the porous media is influenced by drag forces, while the surface flow is mostly influenced by the vertical transfer of momentum by turbulence.

### 1.3 Turbulent, dispersive and viscous stresses

The turbulent stress  $\tau_t = -\langle u'_x u'_z \rangle$  is plotted in Figure 5.1-(c) and is compared with the total gravity force between the free surface  $z_{surf}$  and the altitude  $z$ . For a unidirectional flow with turbulence dominating, the following relationship can be obtained:

$$G = \int_z^{h_{surf}} \epsilon(z) \rho_f g i dz \sim \tau_t = -\rho_f \langle u'_x u'_z \rangle \quad (5.1)$$

In other words, the measured turbulent stress at an altitude  $z$  compensates for the integrated gravity forces of the overlying layers of the flow. As the turbulent stress depends on the determination of the local turbulence, inaccuracies are expected in this measure. Nevertheless, the measure shows that the turbulent stress follows the  $G$  trend until an altitude roughly located at  $z'_{\epsilon=0.8} \sim 0.3 d_p$ , i.e. more or less the roughness crest  $z_{rc}$ . The roughness layer is reached at lower altitudes and the turbulence stress decreases. The role of the turbulence seems to become negligible at  $z'_{\epsilon=0.8} \sim -0.2 d_p$  for A1 and  $z'_{\epsilon=0.8} \sim -0.3 d_p$  for A3. Note that the altitude where turbulence is negligible<sup>TM</sup> is lower when the maximum shear stress is higher.

The measured dispersive stress  $\tau_d = -\rho_f \langle \tilde{u}_x \tilde{u}_z \rangle$ , as well as the calculated viscous stress  $\tau_v = \rho_f \nu \frac{dU_x}{dz}$ , are plotted in Figure 5.1-(c). These 2 stresses are one order of magnitude lower than the turbulent stress. The effects seem negligible, but as explained in Chapter 3, viscosity may play an important role in the *damping effect*. This effect is detailed in Section 3.7 when the mixing length distributions are studied.

---

## 1. Characteristics of the vertical profiles

The peak altitudes for turbulent and viscous stresses are situated around the roughness crest and correspond to the location of the inflection point of the velocity profile. The dispersive stress peaks are positioned at a lower altitude and correspond to the origin defined by  $z'_{\epsilon=0.8} = 0$ .

## 2 Voermans *et al.*'s (2017) measurements and findings

Voermans *et al.*'s (2017) study is a major contribution that employed an experimental procedure similar to the PIV-RIMS procedure, i.e., it combined RIM and an image velocimetry technique to measure the vertical flow structure across the interface. Thus, Voermans *et al.*'s (2017) approach influenced significantly this result part for the analysis of the vertical structure presented in Section 3 and provides insights into the interface mechanisms. This study is therefore regularly cited in this chapter, and this section aims to present the similarities and the difference between this study and my contribution, to clarify further comparisons. Voermans *et al.* (2017) suggest a strong link between the permeability Reynolds number defined by  $Re_K = \sqrt{K}u_*/\nu$ , and the flow behavior at the interface. Indeed, by comparing the effect of the bed shear stress with the permeable properties of the bed, this number is good indicator of the hydrodynamics at the interface.

Note that the term *Sediment-Water Interface* (SWI) employed in Voermans *et al.* (2017) is here fixed at an altitude located at  $z'_{\epsilon=0.8} = 0$ <sup>1</sup>. However, the interface between the surface flow and the subsurface is more likely to be a transition region materialized by the roughness layer. Then,  $z'_{\epsilon=0.8} = 0$  is considered to be equivalent to the SWI, to be consistent with the notation employed in this dissertation.

In Voermans *et al.* (2017), experiments were performed for deep and low gradient flows while the PIV-RIMS set-up has been built to facilitate adjustment of the bed angle to allow steep stream conditions to be reached. These experimental conditions produced low submergence conditions with the presence of a free surface. Consequently, higher surface and subsurface velocities and stresses were measured, providing  $Re_K$ <sup>2</sup> values ranging from 2 to 9, while those in Voermans *et al.* (2017) ranged from 0.3 to 6. These differences in the hydraulic conditions are shown in Figure 5.2, while the flow characteristics of the runs of Voermans *et al.* (2017) are provided in Table 5.2. Voermans *et al.*'s (2017) profiles were provided to me by J.J. Voermans himself. The subsurface flows were more important in my experiments because of the increase in the gravity contribution with steeper slopes.

Case	$d_p$	$K_{KC}$	$u_{*,V}$	$U_b$	$Re_K$	$h^+$
L11	25	0.69	2.78	28	1.71	119
L14	25	0.69	8.09	80	4.97	347

Table 5.2 – Hydrodynamic properties of Voermans *et al.* (2017) for two experimental cases describing the vertical structure of flows adjacent to a packed bed of glass beads.

In the presence of a free surface, the flow depth estimation is able to provide the shear velocity  $u_* = \sqrt{gh_f i}$  based on a control volume force balance, while Voermans *et al.* (2017) employed an alternative definition of the shear velocity from the total stress maximum, such as  $u_{*,V} = \sqrt{\tau_{Tot,max}}/\rho_f$  (where  $\tau_{Tot,max}$  is the maximum of  $\tau_{Tot}$  profile as shown in Figure 5.1). These variations in the definition of the shear stress are common in the literature and are a source

<sup>1</sup>various vertical origin choices exist in the literature. The origin choice employed in this PhD have been detailed in Chapter 4 Section 3.1.2. The definition of the origin is indeed essential for small relative submergence flow conditions.

<sup>2</sup> $Re_K = \sqrt{K}u_*/\nu$  is calculated with  $K$  given by the Carman-Kozeny formula  $K_{CK} = \frac{\epsilon_b^3}{180(1-\epsilon_b)^2}d_p^2$

of confusion, as recalled by Pokrajac *et al.* (2006) for instance. Since Voermans *et al.*'s (2017) paper is a major contribution relating the vertical structure across the interface, their alternative definition of shear velocity was also computed for my data, and is shown in Table 5.1, to allow comparison between the contributions. This shows that a significant difference between  $u_{*,V}$  and  $u_*$  may appear for low submergence conditions rising the complications for comparing results with this study.

Despite the difference in the hydraulic conditions, most of the observations made by Voermans *et al.* (2017) are also applicable to my results. For instance, Voermans *et al.* (2017) suggested that the physical behavior of the flow at  $z'_{\epsilon=0.8} = 0$  may be explained by the value of the permeability Reynolds number  $Re_K$ . In particular, they found that a value of  $Re_K \approx 1 - 2$  is seen to be an important threshold when turbulence starts to dominate  $z'_{\epsilon=0.8} = 0$  as opposed to viscous stress. It is indeed what it is observed in the run A1 having a smaller  $Re_K \sim 2.2$  number where  $\tau_t > \tau_v$ .

Moreover, as emphasized by Voermans *et al.* (2017), all flows presenting a sediment-fluid interface seem to possess an inflectional velocity profile. This suggestion is also confirmed in my work, as shown in Figure 5.1, and is consistent with Breugem *et al.* (2006).

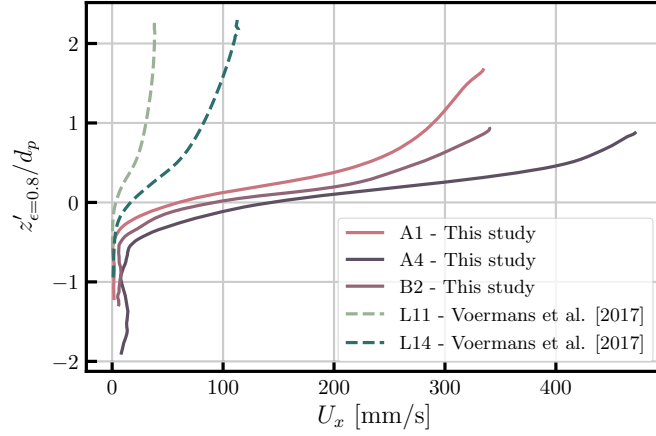


Figure 5.2 – Comparison of vertical velocity structures between Voermans *et al.* (2017) and the PIV-RIMS profiles (this study).

### 3 Vertical structures

#### 3.1 Mean velocity structure

Vertical velocity profiles for B runs ( $d_p = 14$  mm) are plotted in Figure 5.3 and are compared with the mean porosity profiles. Note that the porosity profiles have a different behavior to those of the A runs shown in Figure 5.1. For the B runs, bulk porosity is reached for  $z'_{\epsilon=0.8} \sim -0.5d_p$ , while for the A runs it is around  $z'_{\epsilon=0.8} \sim -0.7d_p$ . This behavior was repeatable, and cannot be attributed to just a measurement inaccuracy. It reflects the complex self-structuring of the porous bed, which depends on various factors (channel width, sediment depth, and relative difference between the bead diameters of the bi-dispersed medium). For the B runs, the evolution of the velocity with the slope is similar to that described previously for the A1 and A3 runs, i.e., an

increase in the velocities within the different layers of the flow. The increase at the surface relies on the dynamics of the turbulent exchanges at the surface, while the increase in the subsurface depends on interactions with the porous bed.

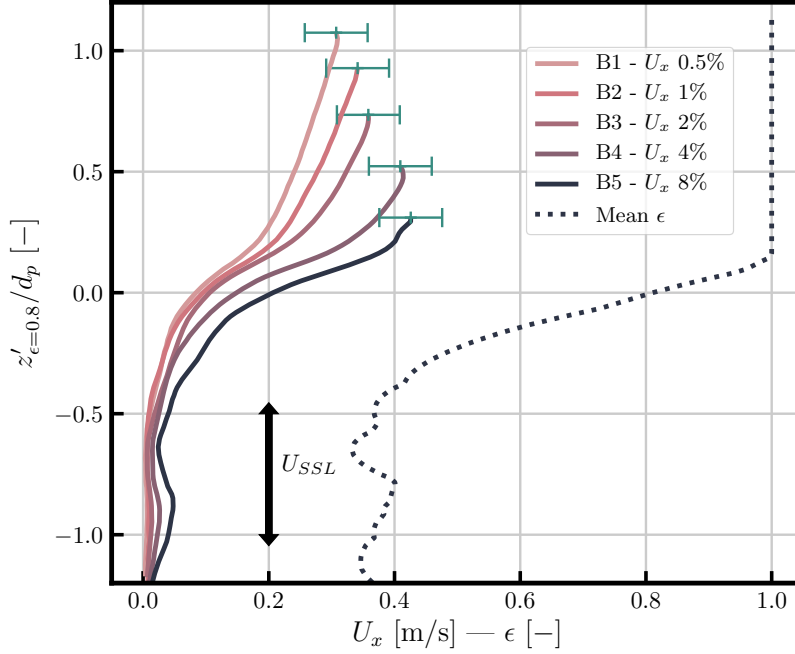


Figure 5.3 – Velocity profiles (continuous) and porosity profiles (dotted lines) for the B runs ( $d_p = 14$  mm,  $q_f = 0.30 \text{ m}^2/\text{s}$ ). The mean subsurface velocities  $U_{x,SSL}$  are the depth averaged velocities between the altitudes  $z'_{\epsilon=0.8} = -0.5 d_p$  and  $z'_{\epsilon=0.8} = -1 d_p$ . The order of magnitude of the inaccuracy of the surface velocities (green error bars) is estimated at  $2\sigma_{U_{x,surf}} \sim 0.005$  m/s. It is the maximum surface velocity inaccuracy evaluated in Section 3.1. The characteristics of these profiles are detailed in Table 5.1.

Non-dimensional mean velocity structures are depicted in the semi-logarithmic plots Figures 5.4 – (a,b). Observation of the subsurface layer velocities reveals that the order of magnitude of the non-dimensional velocities  $\check{U}_x = U_x/u_p$  was between 0.05 and 0.5, the maximum being observed for run B5, which had a steeper slope and larger bead diameter. These trends are in agreement with the Ergün equation, which stipulates an increase in permeability when the bead diameter increases. In Chapter 3 – Section 3.3.2, the Ergün equation was resolved given that  $\check{U}_x$  tends to be towards the asymptotic limit 0.4 when  $i$  increases. It is indeed the order of magnitude observed in the subsurface layer. The evolution of the mean subsurface velocities  $U_{x,SSL}$  as a function of the slope  $i$  and a comparison with the Ergün predictions are studied in detail in Section 3.2.

In the free surface layer,  $\check{U}_x$  follows an opposite trend, i.e. it decreases while the slope increases. This trend can be explained by the scaling choice with  $u_p$ , since the surface velocities are more likely to scale with  $u_*$ . The scaling choice for velocities and length differs between the surface and subsurface variables owing to the different nature of the interactions involved in each region. A unique and appropriate scaling has not been identified. Table 5.3 summarizes this



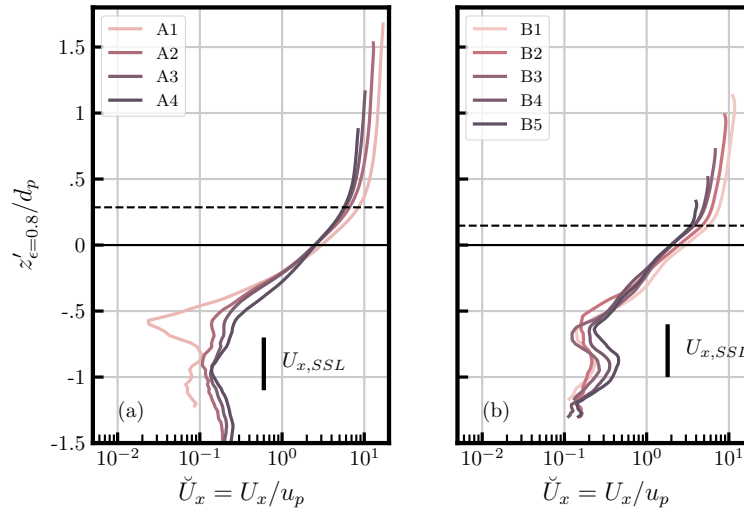


Figure 5.4 – Mean velocity structures for the nine experimental cases, plotted with a logarithmic scale to emphasize the differences at low velocities (a) [A1, A2, A3, A4] (b) [B1, B2, B3, B4, B5]. The vertical bold line frames the altitudes where the mean subsurface velocity  $U_{x,SSL}$  was calculated. The horizontal dotted line denotes the roughness crest in the two sets of experiments.

	Surface layer	Subsurface layer
Length	Flow depth $h_f$	Median grain size $d_p$
Velocities	$u_* = \sqrt{gh_f i}$	$u_p = \sqrt{gd_p i}$
Non-dimensional velocities	$U'_x = U_x/u_*$	$\check{U}_x = U_x/u_p$
Main phenomenon	vertical momentum transfer by turbulence	drag forces on the solid walls

Table 5.3 – Summary of the different length scales associated with the subsurface layer and the surface layer. At the interface, the roughness layer does not have a specific scale, but is a combination of these two scales.

duality problem.

For the scaling profiles, an arbitrary choice between the bead diameter and the flow depth must be made, depending on the layer of interest. At the interface between the surface and subsurface layer, i.e., in the roughness layer, the involved interactions are a complex combination of the phenomena observed in the adjacent subsurface and surface layers. The scaling choice for the roughness layer cannot therefore be clearly stated.

### 3.2 Measured subsurface velocities and Ergün equation

The subsurface velocities were directly extracted from the vertical profiles by defining the subsurface region roughly between the elevation  $z'_{\epsilon=0.8} \approx -1.7d_p$  and  $z'_{\epsilon=0.8} \approx -0.7d_p$  for  $d_p = 9$  mm and  $z'_{\epsilon=0.8} = -0.4d_p$  and  $z'_{\epsilon=0.8} = -d_p$  for  $d_p = 14$  mm (the rough vertical positions where the velocities were extracted are shown in Figure 5.4). Points were extracted from the A and B runs, but other runs were also considered, to take into account the variability in the measurement due to the different bed structures (the runs presented in Section 3.1 of Chapter 4 for example).

The Ergün equation and the linear term called the Carman-Kozeny equation are defined by:

$$\frac{f_{part \rightarrow fluid}}{\rho_f g \epsilon} = i = \underbrace{A_E \frac{(1-\epsilon)^2 \nu}{g \epsilon^2 d^2} U_{x,SSL}}_{\text{Carman-Kozeny}} + \underbrace{B_E \frac{(1-\epsilon)}{d \epsilon} U_{x,SSL}^2}_{\text{Ergün}} \quad (5.2)$$

The measured velocities in relation to the most common porous media laws are shown in Figure 5.5 for the A runs and Figure 5.6 for the B runs. Although large variation is observed in the low subsurface velocities owing to variabilities in the bed configuration, the linear Carman-Kozeny equation is adapted for low  $Re_p$ . For higher velocities, i.e.  $Re_p > 20$ , the linear relationship is no longer valid. This result justifies the use of a non-linear porous media equation to describe the subsurface velocities of steep streams. However, although the Ergün law is appropriate for predicting the quadratic trend, it is not clear which grain size scale would represent this trend. According to these measures, the Ergün equation calculated with the lower grain-sizes is a better candidate for a high Reynolds number. This result is to be expected, because in porous media, the smallest particles characterize the pore sizes (fine particles occupy the large pores and reduce the permeability).

As expected, in a large grain size situation, the velocities in the subsurface layer are higher. The particle Reynolds number reached 175 for the higher slope 8% and the Carman-Kozeny estimation was no longer valid for the 2% slope case.

### 3.3 Turbulence structure

The normalized turbulence intensities in the vertical and streamwise directions, as well as the normalized turbulent stresses, are shown in Figures 5.7 – (a,b,c) for A runs.

In Figures 5.7 – (a,b), turbulence intensities in the streamwise and vertical direction increase from the free surface to the interface, with a maximum being localized to between the roughness crest and  $z'_{\epsilon=0.8} = 0$ .

Various universal expressions for turbulence intensities have been provided in the past. For smooth walls, Nezu & Nakagawa (1993) popularized the semi-empirical relation for  $\langle \|u'_x\| \rangle / u_*$  and  $\langle \|u'_y\| \rangle / u_*$  giving:

$$\left( \langle \|u'_x\| \rangle / u_* \right)_{theo} = 2.3 \exp(-(z - z_b)/h_f) \quad (5.3)$$

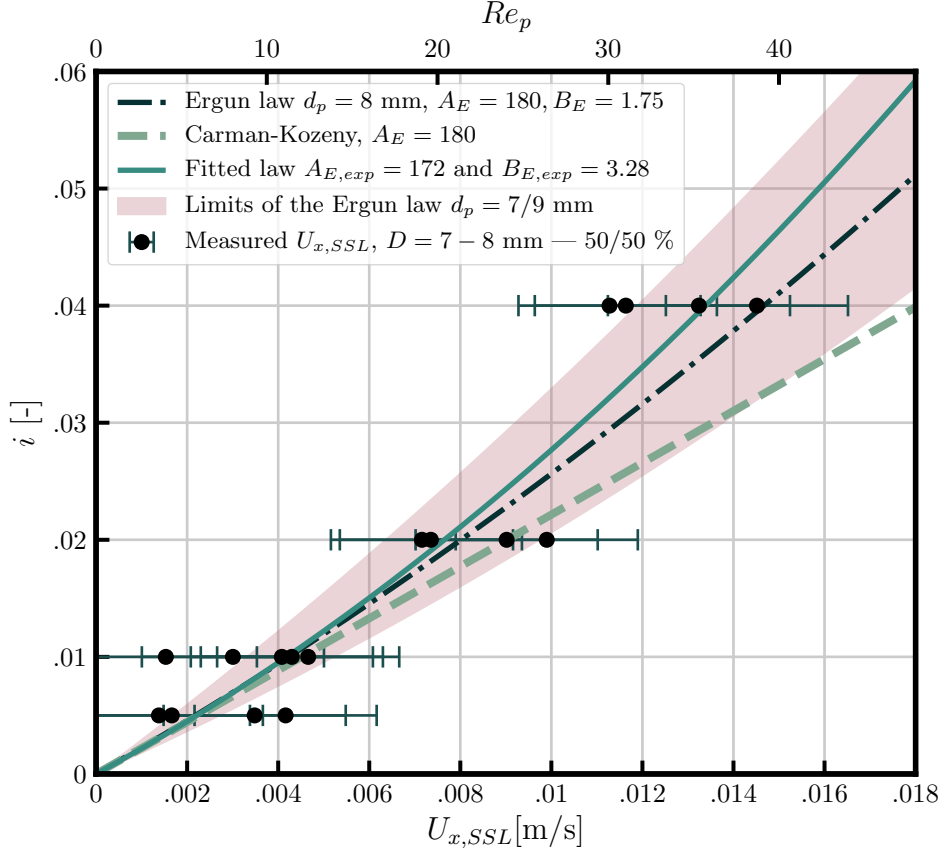


Figure 5.5 – Measured subsurface velocities in a bi-disperse media  $D = 7 - 9$  mm for 17 runs. Various bed structures and slopes ( $i = 0.5 - 4\%$ ) were tested. The data are compared with the linear Carman-Kozeny law (dashed line) and the Ergun law (dashdotted line) calculated with the median grain diameter ( $d_p = 8$  mm) and the measured averaged bulk porosity ( $\epsilon_b = 0.39$ ). The top axis is scaled with the particle Reynolds number  $Re_p = \frac{U_{x,SSL} d_p}{\nu}$ . The light-red ‘fill-between’ curve represents the upper and lower limits of the Ergun law with  $d_p = 7$  mm and  $d_p = 9$  mm respectively. The continuous line is a fitted Ergun law giving  $A_{E,exp} = 172$  and  $B_{E,exp} = 3.28$ .

$$\left( \overline{|u'_z|} / u_* \right)_{theo} = 1.27 \exp(-(z - z_b)/h_f) \quad (5.4)$$

with  $z_b$  being the distance from the smooth bed. These curves are plotted in Figures 5.7-(a,b) with  $z - z_b$  arbitrarily given by  $z'_{\epsilon=0.8}$ , although this vertical origin choice cannot be considered as universal for rough beds. The trends of this semi-empirical relationship correspond to the observed trends, with good orders of magnitude for all the experimental distributions. However, the measured turbulence intensities are systematically lower than the predicted ones. This behavior for steep streams was previously observed by Nezu (1977), and later for steep-slope open-channel flows by Tominaga & Nezu (1992), where a more complex expression for the turbulence intensity distribution was suggested. These alternative expressions take into consideration the fundamental role of the van Driest *damping effect*. The similarities with the measured turbulence

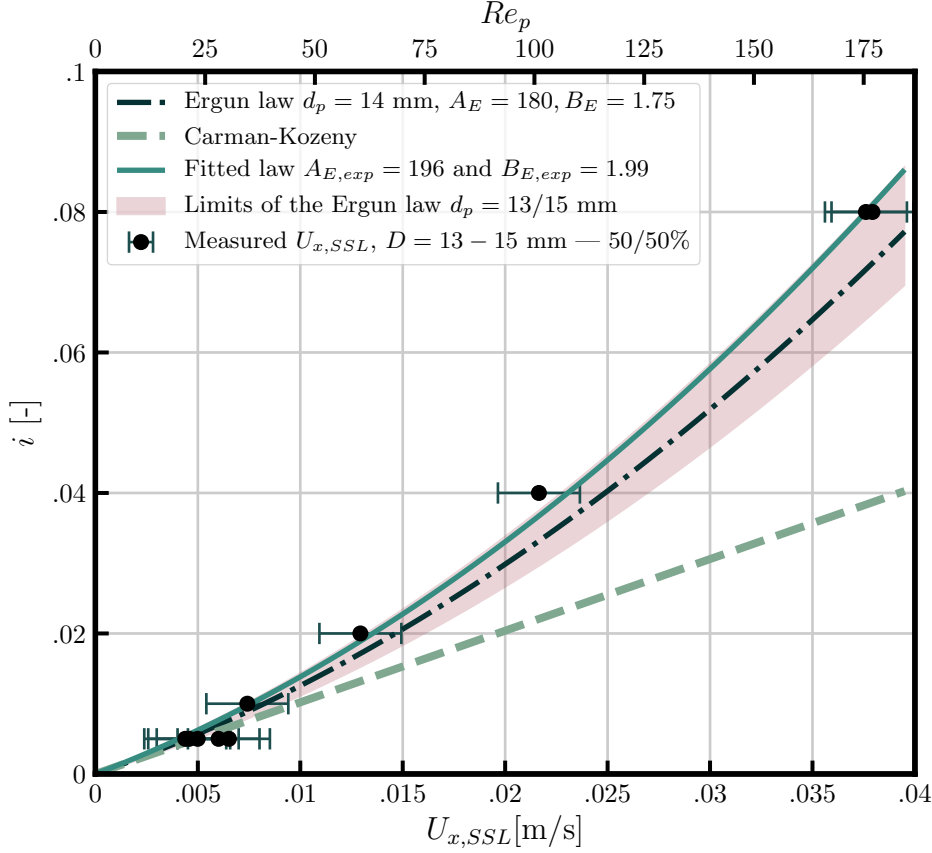


Figure 5.6 – Measured subsurface velocities in a bi-disperse media ( $D = 13/15$ ) mm for 11 runs. Various bed structures and slopes ( $i = 0.5 - 8\%$ ) were tested. The data are compared with the linear Carman-Kozeny law (dashed line) and the Ergun law (dashed and dotted line) calculated with a median grain diameter of ( $d_p = 14$  mm) and the measured averaged bulk porosity ( $\epsilon_b = 0.35$ ).

intensity profile suggests that the van Driest *damping effect* also plays an important role in reducing turbulence near a rough bed. Hereafter, the influence of the damping effect will be detailed when studying the mixing length distribution.

At the roughness crest, similarities for obstructed shear flows were popularized by Ghisalberti & Nepf (2009), giving  $(\langle |u'_x| \rangle)_{z_{rc}}/u_* \sim 1.8$  and  $(\langle |u'_z| \rangle)_{z_{rc}}/u_* \sim 1.1$ . Here, the measured streamwise turbulence intensities  $(\langle |u'_x| \rangle)_{z_{rc}}/u_*$  were slightly lower than 1.8, exhibiting values between 1.5 and 1.7. The values of the vertical intensities  $(\langle |u'_z| \rangle)_{z_{rc}}/u_*$  were about 0.7, while the expected similarity value was about 1.1. The normalization with  $u_*$  to obtain these similarities again raises the problem of the choice of  $u_*$ , with multiple variants for its definition existing in the literature for rough open channel flow. To obtain the expected similarities provided by Ghisalberti & Nepf (2009), Voermans *et al.* (2017) was forced to modify the shear velocity definition (initially defined by  $u_{*,V}$ ). However, the authors also found values of 0.5-0.7 for  $(\langle |u'_z| \rangle)_{z_{\epsilon=0.8}}/u_*$ , which are consistent with my observations at  $z_{\epsilon=0.8}$ . While the modification of  $u_*$  may provide the similarity expected by Ghisalberti & Nepf (2009), I argue that the damping

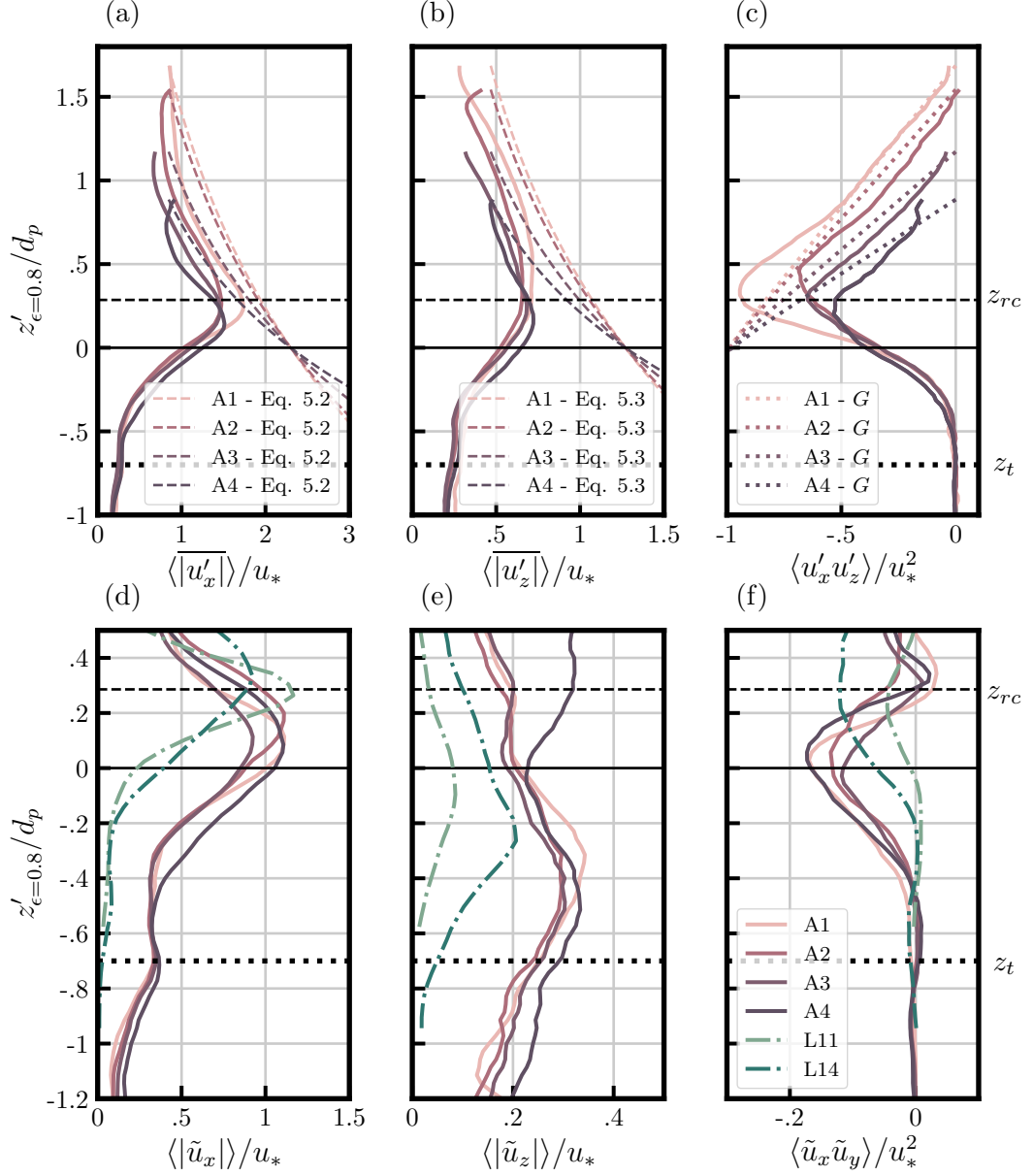


Figure 5.7 – Bulk temporal and spatial statistics for A runs (A1, A2, A3, A4) normalized with the shear velocity  $u_*$  with varying slopes: (a) streamwise and (b) vertical turbulence intensity. The dashed lines are semi-theoretical curves for the turbulence intensities given by Nezu & Nakagawa (1993) (Equation 5.3 and Equation 5.4) (c) Turbulent stress with dotted lines representing  $G$  normalized by  $\rho u_*^2$ ; (d) streamwise and (e) vertical disturbance intensities; (f) dispersive stress. The green dashed and dotted lines are the profiles L11 and L14 measured by Voermans *et al.* (2017)

effect is an essential component for explaining the lower turbulence intensities, and must be taken into consideration for both my hydraulic conditions and those of Voermans *et al.* (2017). Indeed, in both experimental works the velocities at the interface were low, and the local Reynolds

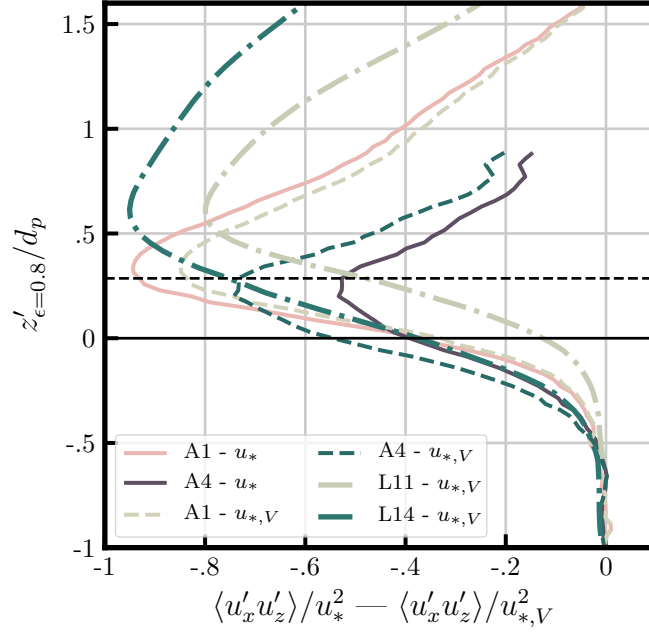


Figure 5.8 – The turbulent stress structures for two different shear stress definitions and a comparison with Voermans *et al.* (2017) data

number took values in the order of magnitude of  $R_l = O(100)$ , which is the order of magnitude of the van Driest Reynolds number, as explained in Chapter 3 Section 2.4. In other words, the similarities provided by Ghisalberti & Nepf (2009) may not be valid for flows where the damping effect still plays an important role at the roughness crest.

The maximum of the normalized turbulent stress was found to range between 0.5 and 1, in agreement with most antecedent studies (Nikora *et al.*, 2001; Mignot *et al.*, 2009a; Voermans *et al.*, 2017). A systematic decrease of the  $\langle u'_x u'_z \rangle / u_*^2$  peak with the slope  $i$  and with  $Re_K$  can be noticed. This behavior conflicts with the results of Voermans *et al.* (2017), where an increase in the non-dimensional turbulent stress with  $Re_K$  was observed. Again, the normalized shear stress was crucially linked with the definition of  $u_*$ , and this decrease may be the consequence of the shear velocity being defined by  $u_{*,V}$ . As can be observed in Figure 5.8, while the normalization by  $u_{*,V}$  modifies the amplitudes of the turbulent stress, the maximums continue to decrease while  $Re_K$  increases.

Another feature of low submergence conditions is also brought to light: in the A3 and A4 runs, the altitudes of the turbulent shear stress peaks are localized below  $z_{rc}$ . In general, it is observed that the measured maximums tend to penetrate the permeable bed when  $Re_K$  increases. At these lower levels, the drag forces are likely to increase and play a growing part in the total shear stress; this might explain the relative diminution of the turbulent stress.

### 3.4 Disturbance and dispersive stress

The normalized horizontal and vertical disturbance intensities ( $\langle |\tilde{u}_x| \rangle / u_*$ ,  $\langle |\tilde{u}_z| \rangle / u_*$ ), as well as the dispersive stress profiles  $\langle \tilde{u}_x \tilde{u}_y \rangle / u_*^2$ , are shown in Figures 5.7 – (d,e,f) for the A runs and are compared with the runs L11 and L14 of Voermans *et al.* (2017). The normalized profile shows similarities with the measurements of Nikora *et al.*'s (2001), where a maximum is found for each profile at altitudes below the roughness crest. As for L11 and L14, the vertical positions of the maxima for  $\langle |\tilde{u}_x| \rangle$  and  $\langle |\tilde{u}_z| \rangle$  are distinctly different, with the distance between the maxima being about  $0.5d_p$ . However, when compared with L11 and L14, the absolute elevations of the peaks in the A runs are shifted downwards. For L11 and L14, the peak for  $\langle |\tilde{u}_x| \rangle$  and the dispersive stress  $\langle \tilde{u}_x \tilde{u}_y \rangle /$  coincide with  $z_{rc}$ , while for the A runs the dispersive stress exhibits a local minimum at  $z_{rc}$ . For the A runs, the maxima of  $\langle \tilde{u}_x \tilde{u}_y \rangle /$  are positioned at  $z'_{\epsilon=0.8} = 0$ . These disturbance intensities and dispersive stress features for the A runs seem to coincide with the numerical simulation performed by Fang *et al.* (2018), where the peaks for  $\langle |\tilde{u}_x| \rangle$  and  $\langle |\tilde{u}_z| \rangle$  are also positioned below the roughness crest.

### 3.5 Dispersive stress: parametrization and experimental profiles

#### 3.5.1 Comparison between the closure and experimental dispersive stress profiles

In the course of Chapter 3, a closure for the dispersive stress  $\tau_d = -\rho_f \epsilon \langle \tilde{u}_x \tilde{u}_z \rangle$  was achieved from mechanistic arguments in Section 2.2. The expression is given by:

$$\tau_d = \rho_f \epsilon \sqrt{\frac{1 - \epsilon(z)}{1 - \epsilon_b}} \lambda_+ \left( 1 - \sqrt{1 - \frac{1 - \epsilon(z)}{1 - \epsilon_b}} \right) U_x^2 \quad (5.5)$$

Here, this closure is tested on the empirical dispersive stress profiles. Equation 5.5 requires the experimental velocity  $U_x$  and the porosity  $\epsilon$  profiles as inputs. Additionally, the parameter  $\lambda_+$ , which represents the fraction of the fluid volume where the cross product  $\tilde{u}_x \tilde{u}_z$  is positive, must be fixed. With  $\lambda_+ = 0.3$ , the behavior of the profiles can be determined.

Thus, the assumptions made in Chapter 3 to obtain this closure, which is built on an interdependence between the local disturbances and the averaged porosity, allow these profiles to be reproduced, and will therefore be introduced as a closure in the 1D model.

### 3.6 Complete and approximated formulae

An approximation of the dispersive stress was suggested in Chapter 3, and this approximation is valid for a porosity close to 1, i.e. just below the roughness crest, giving:

$$\tau_d \sim 1/2 \rho_f \epsilon \lambda_+ \left( \frac{1 - \epsilon(z)}{1 - \epsilon_b} \right)^{3/2} U_x^2(z) \quad (5.6)$$

In Figure 5.10, it can be observed that the 2 closures give very similar profiles. Thus, the two formulations seem appropriate for modeling the dispersive stress at the interface of the rough

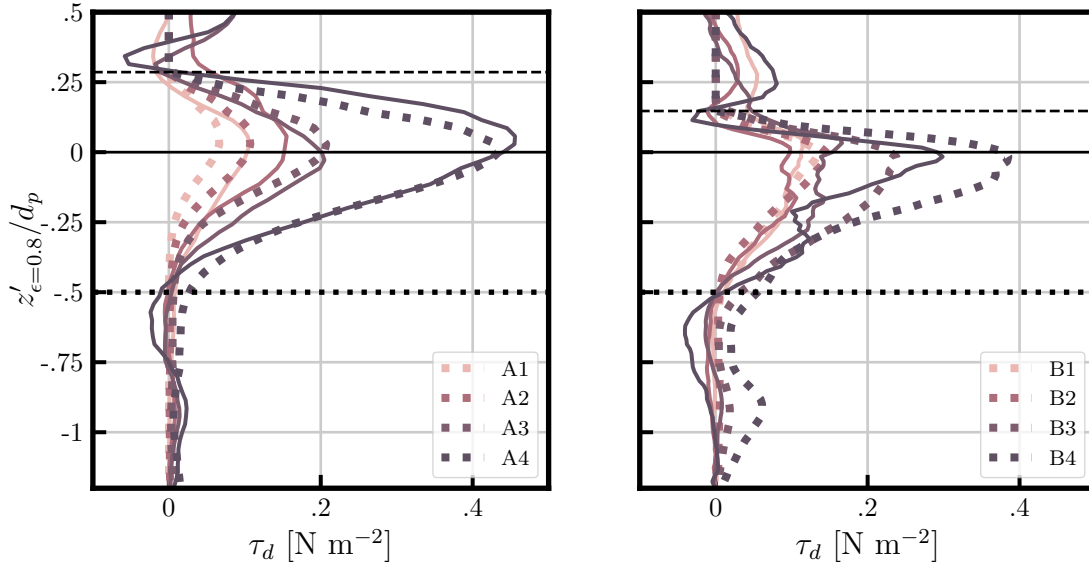


Figure 5.9 – Experimental dispersive stress distributions in comparison with the closure Equation 5.5 .

permeable bed.

### 3.7 Mixing length distribution

Measured mixing length distributions across the interface have not been previously described in the literature. This section is therefore devoted to presenting the structure of these profiles and the similarities with previous investigations and discoveries on deep flows.

#### 3.7.1 Methodology to compute the mixing length distribution

Two methods are regularly employed to determine the mixing-length distribution:

1. The first evaluates the local turbulent stress  $u'_x u'_z$  from the local velocity fluctuation to obtain a mixing length expression by:

$$l_m^* = \frac{\sqrt{-\langle u'_x u'_z \rangle}}{\frac{dU_x}{dz}} \quad (5.7)$$

2. The second method considers that the turbulent stress dominates in the surface layer and approximates the turbulent stress term by  $-\langle u'_x u'_z \rangle \sim G = g(h - z)i$ .

The second method presents the clear advantage that it is independent of the turbulent measurements that usually show large variability; it has been employed several times in the past (e.g. Nezu & Rodi (1986); Revil-Baudard *et al.* (2015)). However, the mixing length values thereby deduced are not valid when the flow is influenced by the bed, i.e., where other forces



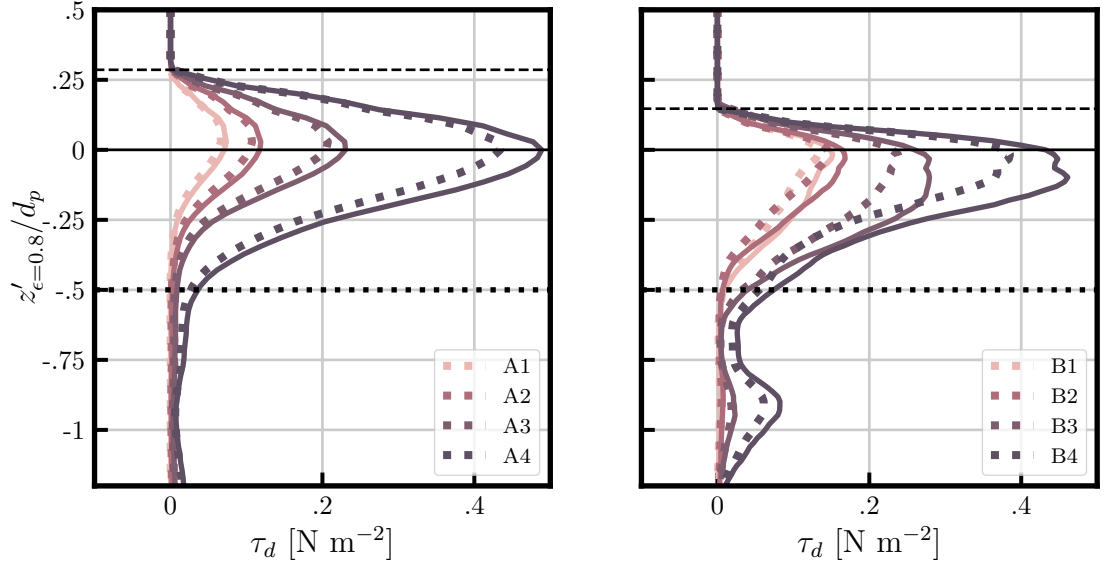


Figure 5.10 – Measured vertical dispersive stress profiles from the closure Equation 5.5 in comparison with the simplified closure Equation 5.6

compensate the gravitational contribution, such as drag forces, form induced stress, or viscous stress. For instance, in the measured turbulent stress profiles shown in Figure 5.1, the turbulence stress does not compensate the gravity action below the roughness crest. Thus, the mixing length determination with this second method is not valid inside the roughness layer while the turbulence continues to play a critical role.

Here, the turbulent stress measurements are accurate and coincide with  $G$ . Thus, by directly solving Equation 5.7 using the turbulence measurements, the first method can be used to obtain an estimation of the mixing length distribution in the roughness layer. This method was employed to deduce the mixing length distributions for flows over vegetated canopies in Ghisalberti & Nepf (2004). The mixing length distributions are traditionally normalized by the flow depth  $h_f$  (or equivalently the *shear layer thickness* in Ghisalberti & Nepf (2004)), as was performed for the profiles shown in Figure 5.11.

### 3.7.2 Surface layer and mixing length

For the surface layer (i.e. for  $z > z_{rc}$ ), the collapse between the measured  $l_m/h_f$  profiles is good. This is encouraging with regard to the use of the mixing length approach to model the vertical mixing length distribution.

This distribution is similar to that previously depicted by Nezu & Rodi (1986). In particular, the measure shows that the mixing length does not follow the traditional Von Kármán linear trend  $l_m = \kappa z \sim 0.4z$  and must be differently parameterized. Above  $z'_{\epsilon=0.8} = 0.7h_f$  the mixing length decreases as the surface is approached. For (A1, A2, A3, B1, and B2) the decrease seems to show a trend towards zero at the free surface. This decreasing trend is known, and was previously linked to the *velocity defect law* effect described in the literature (Coles, 1956; Nezu & Rodi, 1986).

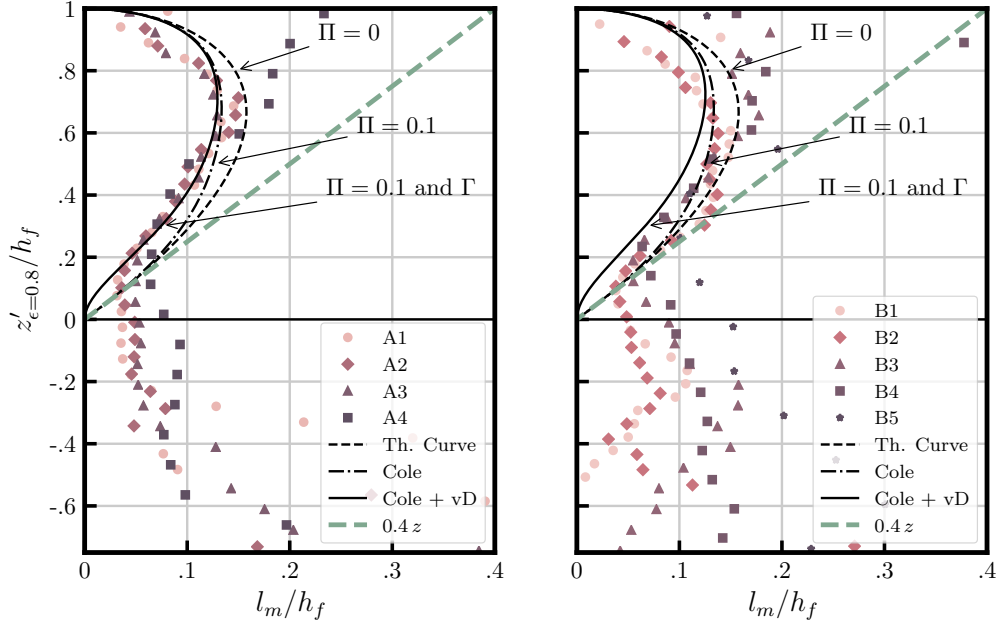


Figure 5.11 – Depth-normalized distribution of the mixing-length evaluated from Equation 5.7. [Left] A runs ( $d_p = 8$  mm); [Right] B runs ( $d_p = 14$  mm).

Furthermore, near the roughness crest  $z_{rc}$ , the increase in the mixing length is not linear, but increases progressively. This second behavior is also known and is associated with the *damping effect*. All the profiles exhibit a local maximum within the roughness layer between the roughness crest and  $z'_{\epsilon=0.8} = 0$ . This local maximum, as well as the global behavior of the mixing length profiles, coincides with the observations of Ghisalberti & Nepf (2004).

In Figure 5.11, two theoretical curves that are commonly employed to model the mixing length phenomena in open-channel flows are plotted. These mixing length distributions are the results of (Coles, 1956) and (van Driest, 1956) contributions. It introduces a velocity defect law (called the Coles wake function) and a turbulence damping effect. Thus, according to Nezu & Rodi (1986), the mixing length distribution  $l_m$  is given by:

$$l_m = h_f \kappa \sqrt{1 - z'_{\epsilon=0.8}/h_f} \left[ \frac{h_f}{z'_{\epsilon=0.8}} + \pi \Pi \sin\left(\pi \frac{z'_{\epsilon=0.8}}{h_f}\right) \right] \Gamma \quad (5.8)$$

where

$$\Gamma = 1 - \exp\left(\frac{-u_* z'_{\epsilon=0.8}}{\nu 26}\right)$$

is the van Driest damping function (presented in Chapters 2 and 3) and  $\Pi$  is the Coles parameter expressing the strength of the wake function (more details are available in Nezu & Rodi (1986) or in Pope (2001) [pp- 305-308]). Note that the distance from the wall is here given by  $z'_{\epsilon=0.8}$ , while the reference is not clearly established for rough permeable walls. Nevertheless, a comparison between the mixing length profiles and theoretical curves is possible. The introduction of the damping effect and the wake function coincides with the measured data for the A runs. For

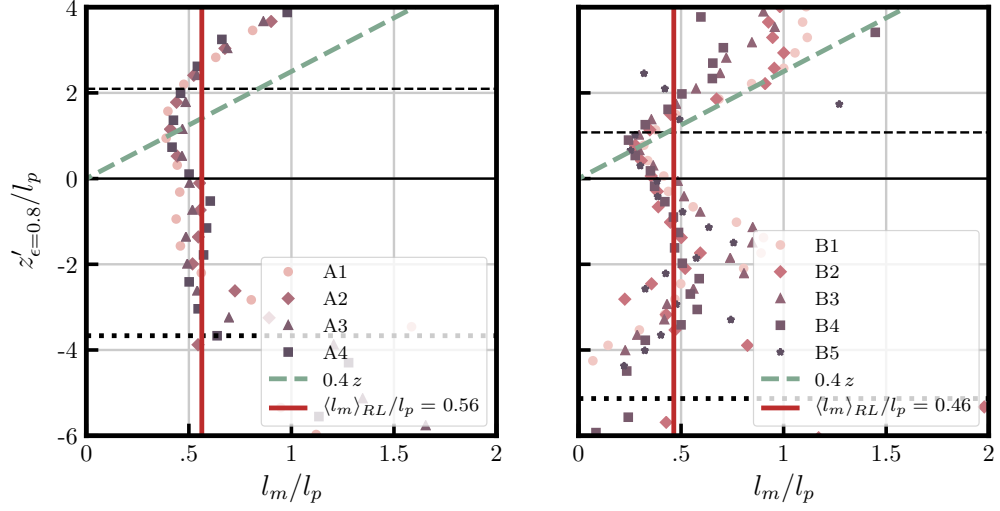


Figure 5.12 – Mixing-length distribution evaluated from Equation 5.7 in the roughness layer. [Left] The A runs ( $d_p = 8$  mm); [Right] the B runs ( $d_p = 14$  mm). The continuous line represents the best fit in the roughness layer, i.e. between the roughness crest and a level slightly below  $z'_{\epsilon=0.8} = 0.001$  mm

modeling purposes, this example shows the importance of developing closures where the mixing length distribution depends on the *damping effect* and the *velocity defect law*.

While the observations were similar in the B runs, the similarity with the theoretical curves is less clear, and larger variability is observed around the theoretical curves. It is also observable that the curve is shifted upwards, thereby suggesting that  $z_{\epsilon=0.8}$  is not an appropriate origin for the B runs. The difficulty in fixing an origin for the two different diameters suggests that this reference cannot be universal for a rough permeable bed, and will depend on the *turbulence penetration length* in the rough permeable bed. This turbulence penetration length depends mainly on the roughness size characterizing the wakes around protuberances. It also depends on the subsurface velocities, since the damping effect depends on the local velocity in the roughness layer, as discussed in Chapter 3 – Section 2.4. In this section, the following closure was developed:

$$l_m^* = \kappa Z_{vD} \left( 1 - \exp \left( - \frac{\sqrt{Z_{vD} U_x(z)/\nu}}{Re_{vD}} \right) \right) + C_{vD} l_p \quad (5.9)$$

where the distance  $Z_{vD}$  is equivalent to the traditional distance from the bed  $z$  and is defined by:

$$Z_{vD} = z - z_t = \int_{-\infty}^z \sqrt{\frac{\epsilon(z) - \epsilon_b}{1 - \epsilon_b}} dz \quad (5.10)$$

It seems important to recall that the  $Z_{vD}$  definition does not require an arbitrary origin via the integration procedure. Inspired by Li & Sawamoto (1995), this strategy has already been

employed in Maurin *et al.* (2016) for bed load transport modeling, and it also seems appropriate here, in the context of a non-mobile bed.

Equation 5.9 was constructed with a dependence on the porous length scale  $l_p$  from the right term  $C_{vD} l_p$ . This dependence is depicted in the following section.

### 3.7.3 Roughness layer and mixing length

In the roughness layer, considerable variability is observable in Figure 5.11. This is the consequence of an inadequate normalization with the flow depth, since the turbulence scale is more likely to be controlled by the geometries of the protuberances in this region (as summarized in Table 5.3). According to Figure 5.12, the normalization with the porous length scale  $l_p(d_p, \epsilon) = \frac{V_v}{A_v} = \frac{\epsilon_b d_p}{6(1-\epsilon)}$  as defined in Chapter 2 – Section 2.1.3 appears to be an appropriate scaling choice for the roughness layer. Indeed, the eddies are more likely to scale with the pore sizes than with the diameter of the beads.

In Equation 5.9,  $l_m^*$  is equal to  $C_{vD} l_p$  when porosity reaches the bulk porosity  $\epsilon_b$ . Thus, the proportionality constant  $C_{vD}$  was evaluated by averaging  $l_m^*$  values from the vertical position  $z'_{\epsilon=0.8} = 0$  to  $z'_{\epsilon=0.8} = -0.7d_p$ .

For the A and B runs, these averaged  $C_{vD}$  values are 0.56 and 0.46 respectively. The value 0.5 is then used in following development when the model is compared with the measurements in Section 4.

It is clear that Equation 5.9 is not intended to model all of the complexity of the mixing length distributions. Two main experimental observations are not considered in this model:

- The maximum in the empirical mixing length cannot be retrieved with Equation 5.9, since the mixing length is monotonically increasing in this model.
- The velocity defect law is not taken into account.

This simplified model for the mixing, together with the different closures developed in Chapter 3, are tested on the experimental runs in the next section.

## 4 Numerical 1D model and experimental results

In Chapter 3, different closures were suggested to parameterize the terms of the *double-averaged momentum equations*. The Ergün equation was employed to close the *viscous* and *pressure* drag forces and the usual parameterizations of  $A_E = 180$  and  $B_E = 1.75$  were evaluated as good candidates for the measured subsurface velocities in Section 3.2. A closure for the dispersive stress was also obtained based on mechanistic arguments, and the experimental dispersive stress was tested with  $\lambda_+ = 0.3$  in Section 3.5. For the mixing length, it has been established that the ‘wake’ factor  $C_{vD}$  should be equal to 0.5 in Section 3.7.3, while the van Driest Reynolds number  $Re_{vD}$  has not yet been parameterized.

Having identified the different parameterizations, the following section aims to compare

---

## 4. Numerical 1D model and experimental results

---

the numerical 1D model with the measured vertical profiles. Details of the model and various simulations have already been provided in Chapter 3.

The following parameters were employed in the model for all runs:

$h_s$ [cm]	$A_E$	$B_E$	$\lambda_+$	$Re_{vD}$	$C_{vD}$
5.0	180	1.75	0.3	70	0.5

Here, contrary to the simulations performed in Chapter 3 with synthetic porosity profiles, actual measured mean porosity profiles are entered into the model. Moreover, the 1D vertical model requires a value for the altitude  $h_f$  as an input. The strategy employed was to obtain  $h_f$  such that the simulated flow discharge  $q_{f,mod}$  was equal to the experimental flow  $q_{f,exp}$  discharge. In this situation, the model requires a loop to simulate several scenarios with specific hydraulic conditions until  $q_{f,mod} = q_{f,exp}$ . Importantly, the vertical reference has been imposed at  $z_{\epsilon=1}$  since the reference  $z_{\epsilon=1}$  is only useful to compare profile with different bed structures.

### 4.1 Reference parametrisation

In Figure 5.13, the different vertical profiles of the A3 run are shown, i.e., the velocity  $U_x$ , the porosity  $\epsilon$ , the dispersive  $\tau_d$ , turbulent  $\tau_t$ , and viscous  $\tau_v$  stresses, the mixing length  $l_m$ , and the drag forces  $f_v$  and  $f_P$ . Details on the organization of this figure were given in Chapter 3 – Section 3.2.2, where synthetic profiles were simulated and analyzed.

The agreements between the observed velocity, stresses, and mixing length and those predicted by the model are satisfactory. The viscous and pressure drag forces ( $f_P$  and  $f_v$ ) were only modeled, as they were not actually measured.

Similarly, the A and B runs were described in Appendix E. They also all show good agreement with the profiles, thereby confirming that the model is able to reproduce velocity profiles for different flow characteristics. However, the velocity is generally under estimated, an effect that is more visible for low slopes and could be related to the inaccuracy of the measured slope. Indeed, this underestimation is most important in the 0.5% profiles, where the slope is possibly higher than expected with consideration of the maximum shear stresses.

In this model,  $Re_{vD}$  was fixed at 70 for all runs to obtain the best collapse with the measured mixing length profiles in the different runs. Interestingly, it is also the van Driest Reynolds number suggested by Krogstad (1991) for rough surface conditions. Note that this value is also highly dependent on the definition of  $Z_{vD}$ , as well as whether the velocity defect law in the surface layer is considered.

Nevertheless, the mixing length parameterization Equation 5.9 seems appropriate for predicting both the behavior in the roughness layer via  $C_{vD}$ , and that in the surface layer.

### 4.2 Damping effect influence

This section aims to visualize the importance of the damping effect in the simulation.

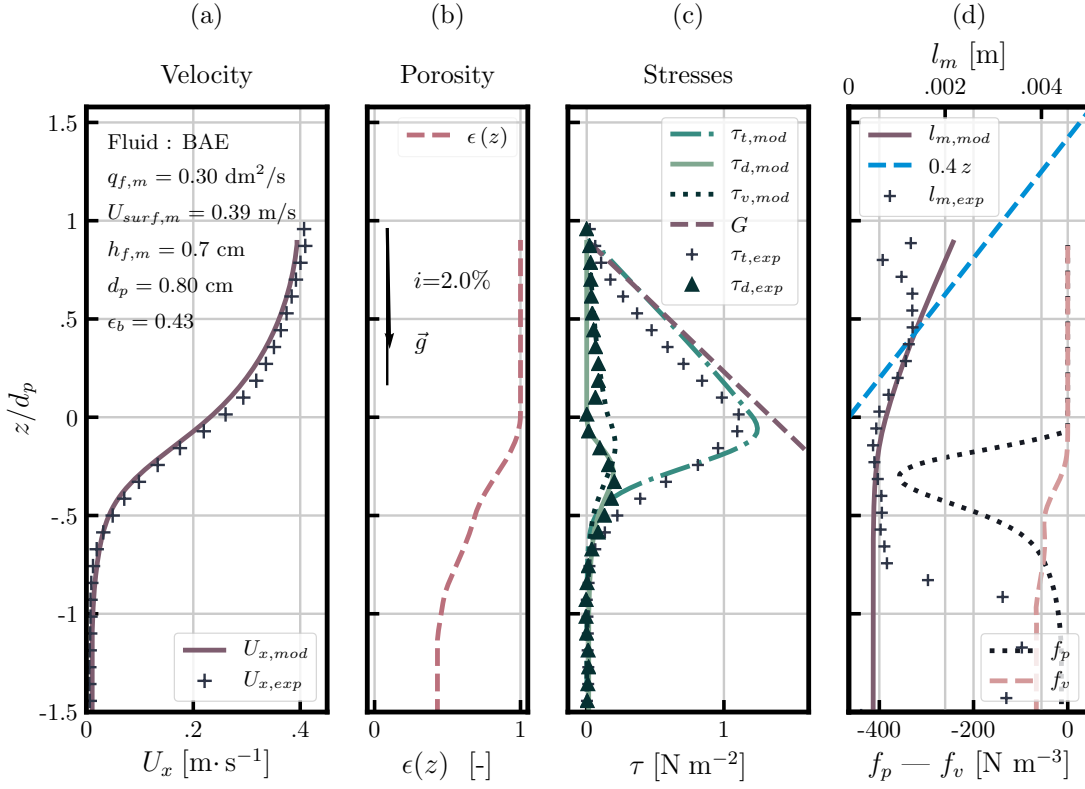


Figure 5.13 – Simulations with damping effect and experimental profiles for the run A3 ( $i = 2\%$ ,  $d_p = 8$  mm). Vertical profiles of (a) velocity, (b) porosity, (c) turbulent  $\tau_t$ , dispersive  $\tau_d$  and viscous  $\tau_v$  stresses and (d) pressure and viscous drag forces. The mixing length  $l_m$  is also plotted with reference axis at the top. The vertical origin is set at  $z_{\epsilon=1}$ . The origin could be set at  $z_{\epsilon=0.8}$  like the previous graphs which compared profiles with different bed structures. However, there is no need to compare profile since only one run is tested to compare with the simulation.

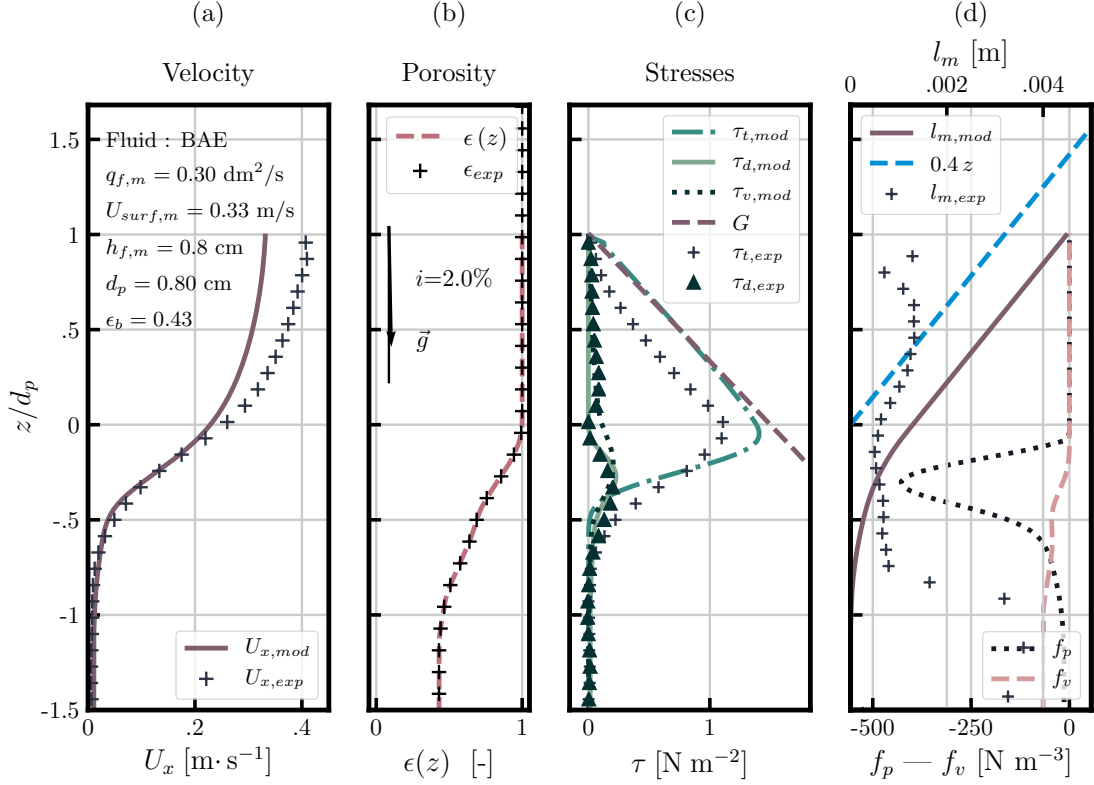


Figure 5.14 – Profile simulation for the run A3 ( $i = 2\%$ ,  $d_p = 8$  mm) without the damping effect. Vertical profiles of (a) velocity, (b) porosity, (c) turbulent  $\tau_t$ , dispersive  $\tau_d$  and viscous  $\tau_v$  stresses and (d) pressure and viscous drag forces.

In Figure 5.14, the damping effect was neglected so that the mixing length Equation 5.9 was simplified to obtain:

$$l_m^* = \kappa Z_{vD} \quad (5.11)$$

With this assumption, it can be observed in Figure 5.14 that the mixing length is overestimated at the roughness. This over estimation increases the modeled vertical momentum exchange because of turbulence at the roughness crest, and results in an underestimation of the velocities in the surface layer.

While consideration of the damping effect was shown to correctly reproduce the mixing length distribution in Section 3.7, its critical role has also been demonstrated here. Indeed, the damping effect is responsible for reducing the turbulent viscosity when the local Reynolds number is low enough. As a result, the velocities in the surface remain high with this effect.

## 5 Summary of the experimental results

In this Chapter, the measured profiles produced by the PIV-RIMS procedure have been depicted. When the slope is increased, the velocity magnitude responds in a manner coherent with what is expected, i.e., an increase in velocities in the subsurface, roughness, and surface layers. The turbulent stress measurements are also coherent with the linear trend expected when turbulence dominates in the surface layer.

Two mixtures of bi-dispersed beads were tested, with these showing that higher median bead sizes result in higher subsurface velocities. The measured subsurface velocities for increasing slopes followed the trend expected by the Ergün equation, and demonstrate the fundamental role of the quadratic term. As a result, the Ergün equation was found to be a good candidate for modeling drag and viscous forces.

The vertical profiles for velocities, turbulence intensities, and turbulent stress showed close similarities with the observations of Voermans *et al.*'s (2017), despite differences in the hydraulic conditions due to the steeper slopes. These similarities are: the presence of an inflectional point for the velocity; the dominant role of the turbulence stress at the roughness crest for  $Re_K > 2$ ; and similarities between the turbulent intensities.

However, comparison with the semi-theoretical curve for the turbulence intensities shows that the prediction systematically over predicted the turbulence. This suggests that the damping effect could play a non-negligible role in reducing the turbulence intensities and the mixing length in and above the roughness layer.

Similarities with Voermans *et al.* (2017) were also observed for disturbance and dispersive stress. Among the various similarities, the dispersive stress also exhibits a maximum localized at  $z'_{\epsilon=0.8} = 0$  just below the roughness crest. The trend in the dispersive stress is well reproduced by the assumptions made in Chapter 3 to produce the dispersive stress closure with  $\lambda_+ = 0.3$ .

The mixing length distributions were also computed from the turbulent stress measures and showed good agreement with the semi-empirical model popularized by Nezu & Rodi (1986). This shows the importance of the *van Driest damping effect*, as well as the *velocity defect law*, in modeling of the mixing length profile.

Having described and justified the relevance of the different closure choices made in Chapter 3, the model was tested on the hydraulic conditions of runs A and B. Good agreement between theoretical profiles and mean profiles was observed with the model parameters staying equal, although the simplified model suggested for the mixing length showed a different trend in the roughness layer. Indeed, mixing length exhibits a local minimum close to the roughness crest and decreases at the vicinity of the free surface. This observation was systematic in this experimental work and has also been observed in a previous contribution studying obstructed shear flows with higher permeable medium (Ghisalberti & Nepf, 2004). Regarding this similitude, the semi-empirical mixing length function could be improved in order to reproduce more faithfully this trend.



# 6

## Real case scenario and mountain river monitoring

---

In the Introduction chapter, a picture of the Navizence river was presented in Figure 2.1, and this is depicted at different scales in Figure 6.1. This mountain river is regularly monitored by a UAV (Unmanned Aerial Vehicle, commonly known as a drone) that takes aerial images. The drone pictures or videos allow confident evaluation of the hydraulic conditions from real case scenarios. For example, an array of pictures of the river can be used to reproduce a highly resolved *Digital Terrain Model* (DTM) with a vertical accuracy of  $\pm 10$  cm. This DTM can then be employed to deduce the local river slope. In addition, pictures of the river may provide insights on the bed materials and their size distribution. With aerial videos, stream surface velocities can be deduced using the same image velocimetry algorithm employed for the PIV-RIMS procedure presented in Appendix B. These different procedures providing slopes, grain sizes, and free surface velocities of the stream from drone aerial images are presented in Appendix F.

This last chapter presents measurements from a real case scenario and explains some of the mechanisms with the help of the model developed and tested in this manuscript. The hydraulic conditions are collected from aerial drone image sequences of a Region Of Interest (ROI) of the Navizence. The objective is to describe the order of magnitude of the flow characteristics in a real-case scenario, and evaluate the applicability of the 1D model developed in Chapter 3 to predict flows. These predictions are then discussed, and raise the problem of how to define flow depth, and by consequence also bed shear stress, in these shallow waters. These quantities are fundamental, since the manner in which they are defined may explain the trends of fundamental hydraulic equations such as the flow resistance or the critical Shields number.

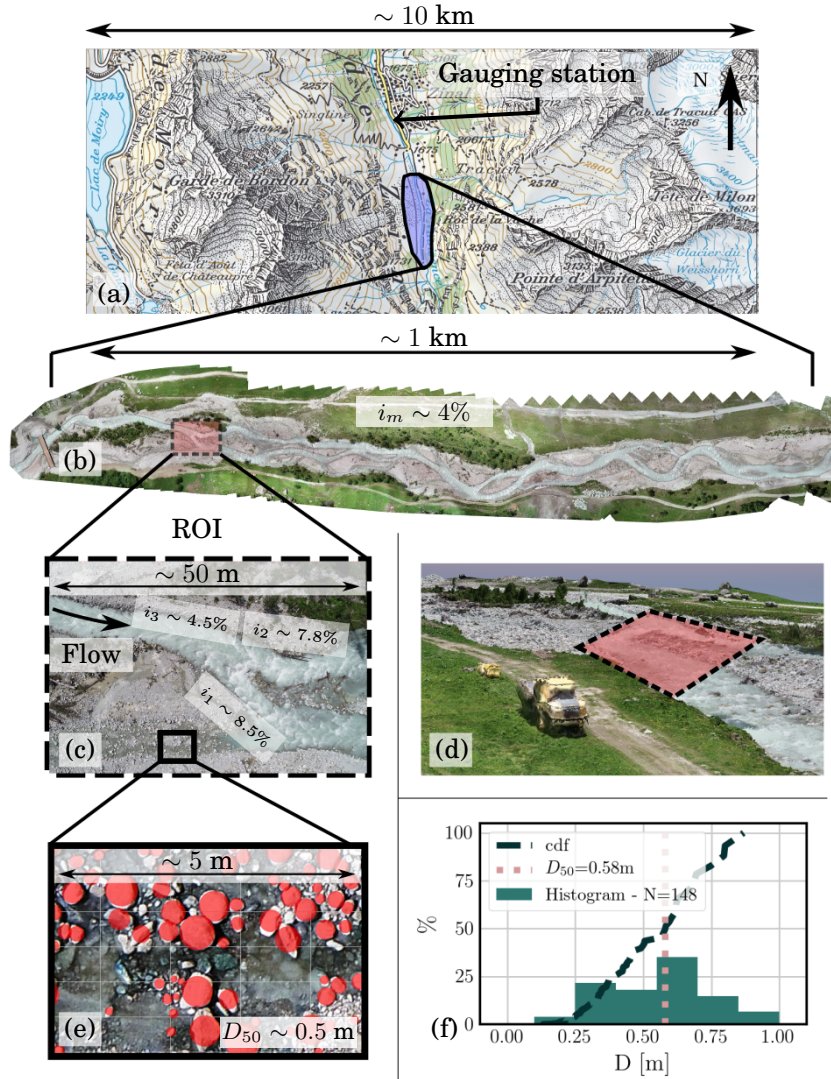


Figure 6.1 – Location of the region of interest (ROI) (a) At the valley scale, the river drains a glaciated alpine catchment. The monitored zone of the river is situated up stream of the Zinal gauging station. (b) Aerial ortho-photography at the kilometer scale. (c) ROI for the free surface velocimetry measurement. The principal channel is separated into two smaller channels, and from upstream to downstream, the slope varies sharply from  $\sim 4.5\%$  to  $\sim 8.2\%$ . (d) Side view of the ROI in the digital terrain model, the presence of a truck provides an appreciation of the elevation accuracy of the DTM for slope estimations. (e) At the grain scale, the grain size distribution is measured in the bed in a dead arm of the river. The red disks represent the equivalent surface area of the stones. (f) The grain size distribution on 148 stones provides an estimation of the median grain size diameter  $D_{50,b} = 0.58$  m. Details on the procedure to obtain the river slope from the DTM and grain size distribution are given in Appendix F.2 and F.3

# 1 From surface velocity to flow depth

## 1.1 Site, slope and grain size distribution

As shown in Figs. 6.1 – (a,b,c), the region of interest is located 2-km upstream of a gauging station that continuously measures the flow depth and discharge. This ROI is also represented by the red rectangle on the digital terrain model in Figure 6.1 – (c). At this site, the slope varies sharply. The technical procedure to obtain the slope and grain-size distribution of the bed are detailed in Appendix F.2 and F.3 and summarized below.

- Slopes were directly measured on the digital terrain model. At the intermediate scale, spatial heterogeneities in the flow are observable. The main channel has a slope of  $i \sim 4.5\%$ . In the middle of the ROI, the main channel is split into two smaller channels, both having higher slopes of  $i \sim 7.8\%$  to  $i \sim 8.5\%$ .
- Grain size measurements were obtained on a dead arm proximal to the running water (see Figure 6.1- b. The grain-size distribution in this region is larger than the grain-size distribution on the bank, and is more likely representative of the grain-size distribution under the flows. The mass-median diameter is given by  $D_{50} = 0.58$  m.

## 1.2 Velocities

Using the same image velocimetry algorithm employed for the PIV-RIMS methodology in Chapter 4, the velocities at the surface of the river can be obtained from aerial videos. The image velocimetry procedure is described in Appendix 1, and the velocity field is shown in Figure 6.2 – (a). In Appendix 1, the coherence between the measured surface velocities and the discharge measured at a gauging station was verified. The total width of the downstream transect is given by the addition of the two small channels  $W_{12} = W_1 + W_2 \sim 8 \pm 1$  m, and for the upstream main channel the width is  $W_3 = 7 \sim 7 \pm 1$  m. In Figure 6.2 – (b), the upstream velocities are much higher than the downstream velocities, despite an increase in the slope. The widening of the channel decreases the water depth and the velocities.

## 1.3 Depth and relative submergence estimation

The flow depth  $h$  is usually deduced from knowledge of the bulk depth averaged velocity  $U_b$ , the bank width  $W$ , and the discharge  $Q_{tot}$ , by employing the following equation:

$$h_b^* = \frac{Q_{tot}}{U_b W} \quad (6.1)$$

The star subscript on  $h_b^*$  identifies the flow depth deduced from this equation using the discharge. In Equation 6.1, computation of  $h_b^*$  requires an estimate of the depth averaged velocity  $U_b$  deduced from the free surface velocity measurement  $U_{surf}$ . The ratio of these two velocities defines what is usually called the velocity coefficient  $\alpha = U_b/U_{surf}$ . This value is commonly set at 0.85, but no consensus on this coefficient is available for steep streams (Dramais *et al.*, 2011). This value is highly dependent on the relative submergence, as shown by Welber *et al.* (2016).

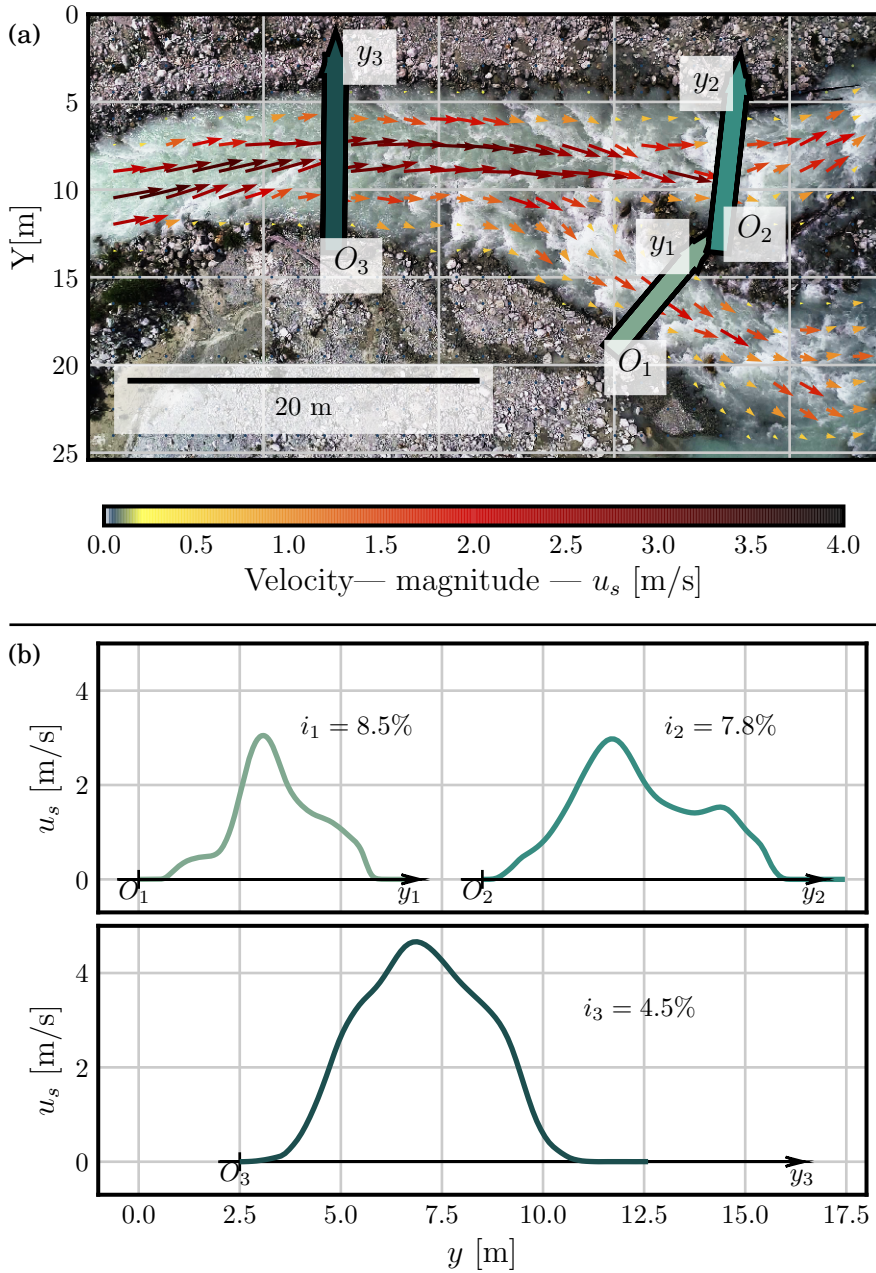


Figure 6.2 – (a) Free surface velocity field obtained from image processing of the aerial videos. Three transects were positioned on the ROI to obtain an estimation of the variation of the velocities along the stream. (b) Surface velocity profiles are given for three transects  $O_{y,1}$ ,  $O_{y,2}$ , and  $O_{y,3}$ .

The river discharge is continuously measured at the Zinal gauging station. Surface velocity measurements from aerial drone videos were performed at 12:00 h, giving  $Q_{tot} = 7 \pm 0.5 \text{ m}^3/\text{s}$ . The time precision is important, owing to the diurnal melting cycles shown on the 24 hour hydrograph

in Appendix F. With the ROI being located 2-km upstream of the gauging station, the total discharge is expected to be lower. However, the tributaries that feed the river between the ROI location and the gauging station are much smaller than the main river, and these contributions can be considered as negligible in the first order.

The bulk flow depth  $h_b^*$  is then calculated by Equation 6.1 with  $\alpha = 0.85$ . This bulk value is employed to deduce a bulk submergence  $S_b^* = h_b^*/d_p$ . The equivalent flow depth for the downstream separated channels ( $O_{y,1}$  and  $O_{y,2}$ ) is provided by the following equation:

$$h_{b,12}^* = \frac{Q_{tot}}{(U_{b,1}W_1 + U_{b,2}W_2)} \quad (6.2)$$

Hydraulic conditions and results of the computation for bulk quantities are summarized in Table 6.1.

Transect	$i$ [%]	$d_p$ [cm]	$W$ [m]	$U_{surf}$ [m/s]	$U_b$ [m/s]	$h_b^*$ [m]	$Re_b$	$S_m^*$
$O_{y,1}$	8.5 %	58	3.7	1.62	1.37	0.51	$6.2 \times 10^5$	0.89
$O_{y,2}$	7.8 %	58	5.8	1.66	1.41			
$O_{y,3}$	4.5 %	58	6.0	3.03	2.57	0.45	$11.6 \times 10^5$	0.76

Table 6.1 – Hydraulic properties in the 3 transects  $O_{y,1}$ ,  $O_{y,2}$  and  $O_{y,3}$ . The bulk quantities  $H_b^*$ ,  $Re_b$ , and  $S_m^*$  are combined quantities for the downstream transects  $O_{y,1}$  and  $O_{y,2}$ .

Surprisingly, the bulk flow depth estimation for transect  $O_{y,3}$  denoted  $h_{b,3}^*$ , is lower for the upstream region than for  $h_{b,12}^*$ , despite the slope increase. This results in the bulk relative submergence being higher for the downstream transects, while observations suggest the opposite trend. These computed values could be attributed to errors in measurement of the bank width or the surface velocities. However, it must be emphasized that evaluation of the bulk flow depths using Equation 6.1 and Equation 6.2 is different from  $h_f$ .  $h_f$  represents the surface layer thickness above the top of the roughness element, while  $h_b^*$  integrates flows from the surface with those in the permeable bed layers.

This real case scenario example illustrate the problem of defining a flow depth for such systems, where a significant part of the flow is flowing through the permeable bed, i.e., the roughness layer and the subsurface layer. The 1D model developed in Chapter 3 is therefore useful to clarify the proportions of flux in the different layers.

## 1.4 Simulation of velocity profiles

In this section, 1D profiles solving the double-averaged momentum equation are computed from the model developed in Chapter 3 with the parametrizations given in Section 3.2 of Chapter 3. In these simulations, the sediment depth is equal to the median grain size and the porosity profile is simulated by employing the procedure in Section 3.1 of Chapter 3 with a cosine function, giving  $\epsilon(z = -d_p) = \epsilon_b = 0.4$

Two simulations are generated and are shown in Figure 6.3 and Figure 6.4, representing the profiles for upstream  $i \sim 4.5\%$  and downstream  $i \sim 8.2\%$  conditions respectively (the slope for

the downstream conditions is the averaged slope of transects 1 and 2). The grain size diameter employed for the simulation is  $d_p = D_{50} = 58$  cm. The strategy for simulating these profiles is the same as that employed in Chapter 5 to simulate the vertical profile corresponding to the PIV-RIMS experimental profile, i.e., by iteration to reach the discharge per unit width  $q_f$ . Here, the discharge for the downstream and upstream conditions are computed by  $q_{f,12} = Q_{tot}/(W_1 + W_2) = 1.17 \text{ m}^2/\text{s}$  and  $q_{f,3} = Q_{tot}/W_3 = 0.73 \text{ m}^2/\text{s}$  respectively.

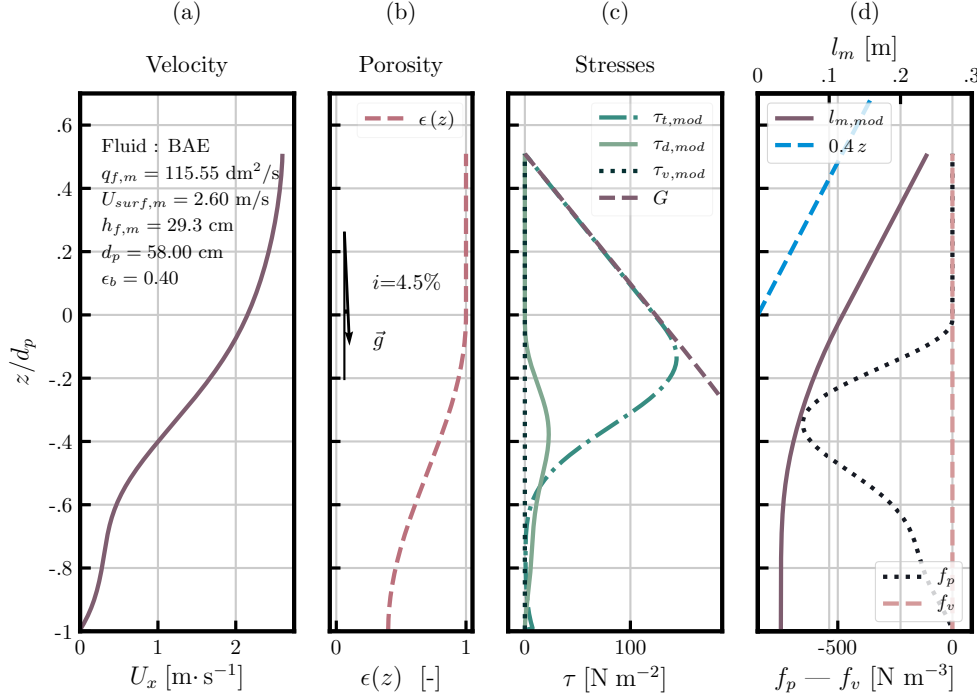


Figure 6.3 – Profile simulation for the upstream condition  $i = 4.5\%$ . Vertical profiles of (a) velocity, (b) porosity, (c) turbulent  $\tau_t$ , dispersive  $\tau_d$ , and viscous  $\tau_v$  stresses, and (d) pressure and viscous drag forces with mixing length on the top abscissa.

Examination of the simulated drag force profiles in Figure 6.3 - (d) and Figure 6.4 - (d) and the stresses reveals that the viscous effects are completely negligible for these hydraulic conditions. However, according to the closure developed in Chapter 3, the simulated dispersive stress seems to play a non-negligible role.

These modeled profiles are coherent with the measurements. The simulated surface velocity for the upstream condition corresponding to the transect  $O_{y,3}$  is 2.6 m/s, while the measurement gave an averaged velocity of 3.0 m/s. Similarly, for the downstream conditions, the simulated surface velocity gives 2.39 m/s, while the measured mean surface velocity was about 1.6 m/s in transects 1 and 2, with the maximum observed being about 2.2 m/s in Figure 6.2 - (b). Thus, the simulated surface velocities are within the same order of magnitude, which is a first step in evaluating the coherence of the model for simulation of flows in real-case scenarios.

With reference to the differences observed between the downstream and upstream regions, the

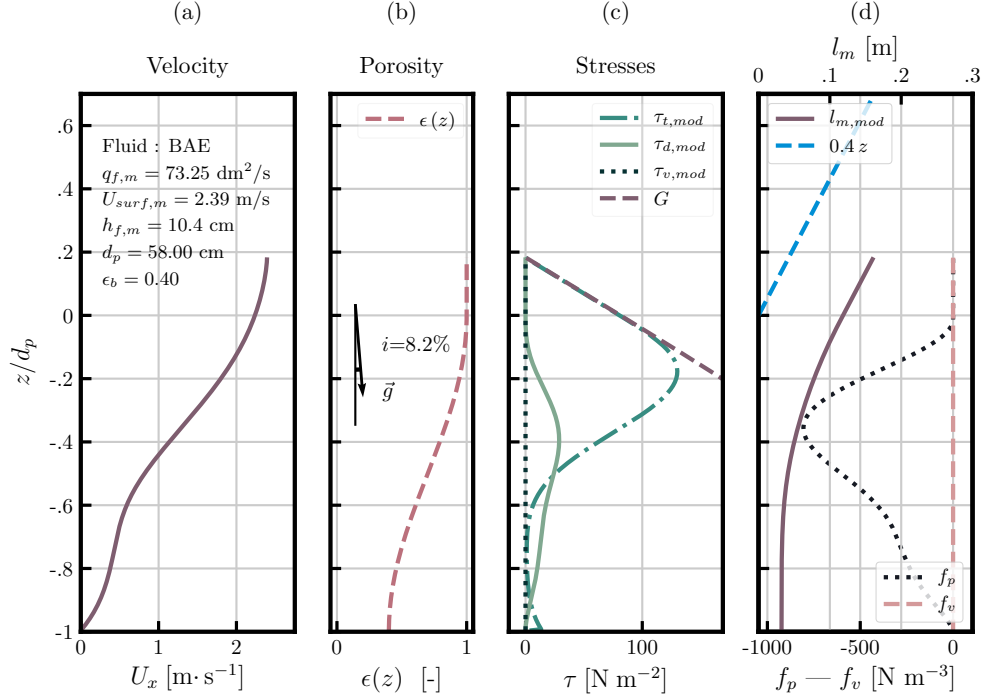


Figure 6.4 – Profile simulation for the downstream conditions  $i = 8.2\%$ . Vertical profiles of (a) velocity, (b) porosity, (c) turbulent  $\tau_t$ , dispersive  $\tau_d$ , and viscous  $\tau_v$  stresses, and (d) pressure and viscous drag forces with mixing length on the top abscissa.

surface velocity is lower for the upstream conditions than for the downstream region, where the slope is larger. This difference is also in agreement with the field observations. The simulated flow depths  $h_{f,m,3} = 29.3$  cm and  $h_{f,m,12} = 10.4$  cm are lower than the bulk flow depths deduced from the discharge  $h_{b,3}^* = 51$  cm and  $h_{b,3}^* = 45$  cm, and follow an opposite trend. Indeed, the resulting relative submergence values  $S_{m,3} = h_{f,3}/d_p = 0.50$  and  $S_{m,12} = h_{f,12}/d_p = 0.18$  coincide with a reduction in the relative submergence when the slope increases from upstream to downstream. This confirms that the bulk submergence  $S_m^*$  is inadequate to evaluate the real submergence in mountain rivers.

Encouraged by the coherence of the model, the next section of this Chapter will be devoted to presenting flow resistance predictions from the model in relation to traditional flow resistance equations.

## 2 Depth and flow resistance formulas

The 1D model was employed to simulate vertical profiles with various hydraulic conditions: 6 flow depths, 4 grain sizes, and 3 slopes were tested to perform  $N = 6 \times 4 \times 3 = 72$  simulations. Each simulation is a combination of these different hydraulic characteristics, i.e.,  $dp = [0.002, 0.01, 0.1, 1]$ ,  $h_f = [0.001, 0.01, 0.1, 1, 3, 8]$ ,  $i = [0.001, 0.005, 0.05]$ . Then, profiles

were simulated using grain sizes and flow depths varying over 3 orders of magnitude from the millimeter to meter scales, thus providing various relative submergence conditions. The slope was varied from 0.1% to 5%, to cover flows from lowland to mountain river environments.

From these simulations, the bulk velocity  $U_b$  is given by the depth averaged velocity between the surface and  $z = -d_p/2$  (here  $z = 0$  corresponds to the roughness crest altitude).

Classical friction laws were compared with the simulated profiles. In Figure 6.5, the non-dimensional Chézy coefficient given by  $C = U_b/\sqrt{gh}$  is plotted against the relative submergence.  $h$  is the flow depth, which is computed differently in the literature. Since the beginning of this manuscript,  $h$  has been given by  $h_f$ , which is the thickness of the surface layer above the roughness crest, although other flow depth definitions are generally employed in the field. Indeed, because of the complications in evaluating the flow depth in mountain streams, determination of this length may be the source of the variation between the measurements and the estimates deduced from the empirical laws.

For this example, two other definitions were selected:  $h'_f = h_f + d_p/2$  and  $h_f^* = q_f/U_b$ .  $h'_f$  provides an idea of the upper limit of the flow depth that can be measured by applying classical rules to mountain streams, while  $h_f^* = q_f/U_b$  is the flow depth estimated from the discharge. This last definition is the most common definition employed in mountain streams (Rickenmann & Recking, 2011) or laboratory flumes with small submergence conditions (Prancevic & Lamb, 2015). To be consistent, the relative submergence definitions also change with the flow depth definition, giving  $S_m = h_f/d_p$ ,  $S'_m = h'_f/d_p$  and  $S_m^* = h_f^*/d_p$ .

The classical laws selected for the comparisons are the Chézy-Eytelwein law

$$C = 16,$$

the Strickler law

$$C = 24(h/d_p)^{1/6}/g^{1/2},$$

the Keulegan law

$$C = 1/0.4 \ln(12 * h/d),$$

and the Rickenmann & Recking (2011) law

$$C = 4.41 (h/d_p)^{1.9} (1 + (h/d_p/1.3)^{1.6})^{-1.08} \quad (6.3)$$

The backgrounds behind the Chézy, Strickler, and Keulegan laws were given in detail in Chapter 2. The law of Rickenmann & Recking (2011) is a logarithmic matching equation calibrated on 2890 field measurements.

Note that  $h/d_p$  in each equations may be one of the three definitions of the submergence given above:  $S_m = h_f/d_p$ ,  $S'_m = h'_f/d_p$  and  $S_m^* = h_f^*/d_p$ .

Each of the 72 simulations have been represented by symbols on Figure 6.5: 'triangles' are plotted using  $h_f$  definition, 'stars'  $h'_f$  and 'plus'  $h_f^*$ . Experimental points from the procedure detailed in Chapter 5 have also been plotted and represented by 'circles'.

Figure 6.5 shows that the simulation and classical laws give similar orders of magnitude



and that their trends coincide. It confirms that under various hydraulic conditions, the model is coherent with most empirical laws, such as those of Chézy, Strickler, or Keulegan.

For high relative submergence flows ( $S_m > 10$ ), the simulated points do not show substantial variability between the flow depth definitions. This is a consequence that  $d_p$  is negligible with respect to  $h_f$  and  $h'_f = h_f + d_p/2 \sim h_f$ . For low relative submergence conditions ( $S_m < 10$ ), variability is more important, reflecting the importance of the flow depth definition. It is not surprising to see that the curve given by Rickenmann & Recking (2011) is between the  $h'_f$  (plus symbols) and  $q_f/U_b$  (stars) points. Indeed, this equation was calibrated on field measurements where the flow depth is determined from these procedure and is generally higher than the distance between the surface and the roughness crest.

Experimental points symbols and 'triangle'  $h_f^*$  are more likely following the Keulegan law. This trend appears to be coherent since Keulegan law was calibrated with the flow depth corresponding to the surface layer thickness.

With a submergence higher than  $10^2$ , the trend of the points does not seem to follow the trend of the Keulegan or Strickler laws. Interestingly, this observation was also found by Rickenmann & Recking (2011). While these authors suggest that this behavior might be a consequence of dunes or antidunes (comment on Figure 1 of the mentioned article), the model suggests that this trend is the result of the underlying physical processes of an open channel flow with high relative submergence.

It also suggests that the friction law tends to show a limit more or less corresponding with the Chézy-Eytelwein coefficient  $C \sim 16$ , and questions the use of the Keulegan or Manning Strickler law for flows with relative submergence higher than  $10^2$ .

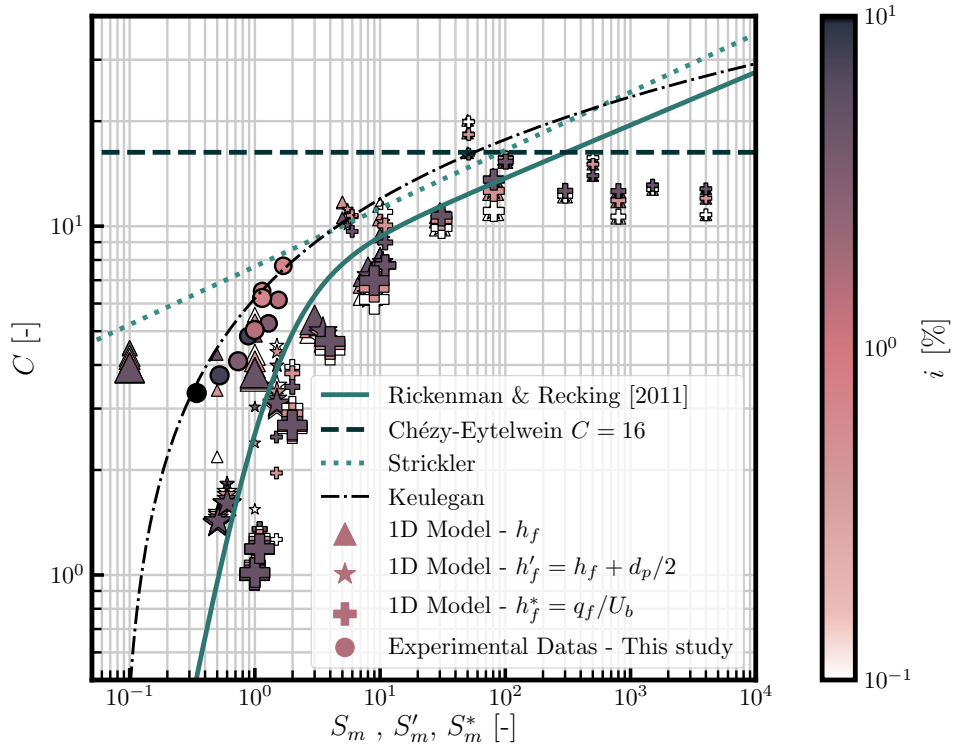


Figure 6.5 – Simulations from the 1D model in terms of the non-dimensional Chézy coefficient  $C$  versus relative submergences  $S_m = h_f/d_p$ ,  $S'_m = h_f/d_p$  or  $S_m^* = h_f^*/d_p$ . Three different flow depth definitions are tested, represented by three different symbols, as detailed in the legend. The size of the symbols are a function of the grain-size, and their color is an indicator of the slope. Experimental points from Chapter 5 are represented by circles and calculated with  $h_f$ .

### 3 Consequences for the critical Shields stress

#### 3.1 Preamble

To close this last chapter, the critical bed shear stresses were investigated with the 1D model. As mentioned in the introduction, the bed is traditionally assumed to become mobile when hydrodynamic forces on grains, evaluated through the bed shear stress, cross a defined threshold. Indeed, observations revealed that the low sediment transport rates exhibit a transition to rapid growth rates when the bed shear stress increases.

This transition allows the definition of a non-dimensional bed shear stress threshold, also called the critical Shields stress, which is given by:

$$\Theta_{th} = \frac{\tau_{b,th}}{(\rho_s - \rho_f) g d} = \frac{\rho_f h_f i}{(\rho_s - \rho_f) d} \quad (6.4)$$

$\tau_{b,th}$  is the critical bed shear stress that is generally given by  $\rho_f g h i$ . By varying the discharge, the flow depth  $h$  where the critical bed shear stress is reached is calculated. As mentioned above, the flow depth  $h$  can be estimated by various methods, i.e., from direct measurement or by deduction from discharge and velocities.

Investigations of compiled field and open-channel flume data sets show that  $\Theta_{th}$  increases with bed slope, while rationally, gravitational contributions should reduce it (Lamb *et al.*, 2008; Recking *et al.*, 2008). Interestingly, these two investigations on large data-sets were published the same year as a very similar power function calibrated on field data:

$$\Theta_{th,Lamb} = 0.15 i^{0.25} \sim \Theta_{th,Recking} = 0.13 i^{0.24} \quad (6.5)$$

More recently, different authors have investigated the role of subsurface flow interactions with the surface flow (Maurin *et al.*, 2018; Lamb *et al.*, 2017). While both articles neglected the lift effect, the authors suspected that this effect could play a crucial role in the process of sediment transport. This hypothesis is plausible, as both the porosity and velocity gradients are high at the interface between the surface and subsurface flows. However, these studies illustrate the fundamental role of the turbulence in explaining incipient motion on steep slopes.

This section will therefore estimate the role of the lift force, as well as the turbulence, in explaining the trend in the critical Shields number according to the slope.

#### 3.2 Mechanistic model and methodology

To obtain critical Shields stress, the approach is similar to Recking (2009) or Lamb *et al.* (2008). It is realized in terms of the force balance on individual grains. However, contrary to these two previous contributions, the grain subject to the forces is not positioned above the roughness crest, but is one of the particles constituting the rough permeable bed, as shown in Figure 6.6. Thus, the particle is positioned at the vertical coordinate  $z_p$ , i.e. at a distance  $d_p/2$  below the roughness crest. The determination of the velocity structure at the mesoscopic scale

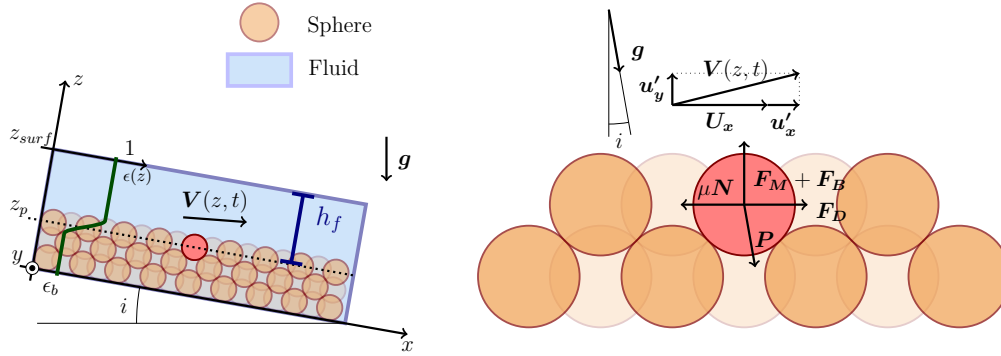


Figure 6.6 – Force balance on a grain situated at the top of the permeable bed.  $F_D$ ,  $F_M$ ,  $P$ ,  $F_B$  and  $\mu N$  are the forces due to drag, lift, weight, buoyancy and friction, respectively.  $\mathbf{V}$  is the instantaneous velocity vector, and  $u_x = U_x + u'_x$  the instantaneous magnitude along  $x$

by the 1D model allows an approximation of the averaged velocity around this particle to be obtained, to allow an estimation of the hydrodynamic forces to be deduced.

The drag force was computed by the expression of Dallavalle:

$$F_d = \frac{\pi}{8} \rho_f d^2 \left( 0.63 + 4.8 \left( \sqrt{\nu / (u_x d)} \right)^2 u_x^2 \right) \quad (6.6)$$

It must be emphasized that the velocity fields around grains at the roughness top exhibit high spatial heterogeneities, and it is therefore difficult to simplify the mechanism to a drag force given for an individual sphere. Moreover, this force should be estimated by taking into consideration the hindrance effect, as was presented in Chapter 3 with the use of a voidage function (see Di Felice (1994) for details).

However, as a first attempt to estimate the critical Shields stress, the simplest approach adopted, i.e., by neglecting the hindrance effects and by estimating the bulk force at the middle of the grain.

Because velocity varies sharply from the top of the grain to the bottom, the circulation of the velocity and by consequence the lift force is expected to play an important role. Indeed, lift effect is due to the circulation of the velocity around the grain: this is in fact a manifestation of the Magnus force<sup>1</sup>.

According to Petit *et al.* (2012), the lift force  $\mathbf{F}_M$  in a unidirectional flow can be expressed

<sup>1</sup>The term ‘Magnus force’ is traditionally employed when the circulation of the fluid is the consequence of the rotation of the object. Since the calculation the force from the fluid circulation with or without the rotation of the object is identical, some authors (Petit *et al.*, 2012) also refer to the term ‘Magnus force’ to deal with the lift force due to the fluid circulation in any situation.

by:

$$F_M = \rho_f \mathbf{V} \times \mathbf{\Gamma} \cdot \mathbf{e}_x = -\rho_f u_x(z_P) \int_C \mathbf{v} \cdot d\mathbf{l} \approx -C_M \rho_f \frac{\pi}{8} u_x(z_P) (v_+(t) - v_-(t)) d^2 \quad (6.7)$$

where  $\mathbf{\Gamma} = \int_C \mathbf{v} \cdot d\mathbf{l}$  is the circulation along the contour ( $C$ ). In a simplified approach  $\mathbf{\Gamma}$  reduces to the difference between a top and a bottom velocity that are  $v_+$  and  $v_-$ .  $C_M$  is generally given as 0.5.

The weight in the  $x$  direction is given by:

$$P_x = \rho_s \frac{4}{3} \pi R^3 g i = \rho_s V_p g i \quad (6.8)$$

with  $V_p$  the volume of the sphere. The buoyancy force is given by  $F_B = V_p \rho_f g$  and the normal force is thus  $N = P_y - F_B - F_M$ , with  $P_y = \rho_s V_p g \cos(\text{atan}(i)) \sim \rho_s V_p g$  the projected weight on  $y$ . Knowing the friction coefficient  $\mu$ , the friction force is then computed by:

$$F_f = \mu N = \mu(P_y - F_B - F_M) \quad (6.9)$$

For a given hydraulic condition, the estimation of the critical Shields number is obtained when the total forces in the stream wise direction  $P_x + F_D$  exceed the friction force  $F_f$  that permits the onset of motion. In the algorithm, this procedure is made by iteration until  $F_f - P_x - F_D \sim 0$ . With this condition reached, the flow depth  $h$  required to estimate the critical Shields number in Equation 6.4 is computed in 3 different manners: with the surface layer thickness  $h_f$ , with  $h'_f = h_f + d_p/2$  and with a method based on the conservation of mass by computing

$$h_f^s = (q_{tot} - q_{SSL})/U_{surf} \quad (6.10)$$

where  $q_{SSL}$  is the subsurface discharge. This method diverges slightly from  $h_f^* = q_{tot}/U_{surf}$  employed in the above section investigating flow resistance equation.  $h_f^s$  definition has been employed in the experimental work Prancevic & Lamb (2015) who verified the increase of the critical Shields stress with slope and compared experimental results with Equation 6.5. This study found a good agreement and published details on the procedure. Thus, the following section consists to simulate the runs of this study.

### 3.3 Simulations and critical shear stress estimations

The following Table 6.2 summarizes the hydraulic conditions that were tested with the 1D model to yield  $h$  with the three different definitions described above, i.e.,  $h_f$ ,  $h'_f$  and  $h_f^s$ . These simulated runs utilized the hydraulic parameter involved in one of the sets of Prancevic & Lamb (2015).

Run	$i$ [%]	$d_p$ [mm]	$h_{f,exp}^s$ [mm]	$S_m^s$	$\Theta_{th}^s$
1	3.3	15	26.8	1.75	0.04
2	5.8	15	21.1	1.41	0.05
3	9.8	15	16.0	1.06	0.063
4	11.9	15	15.6	1.04	0.075
5	14.0	15	14.2	0.94	0.08
6	17.1	15	12.9	0.86	0.09
7	21.6	15	11.3	0.75	0.01
8	23.6	15	11.4	0.76	0.11

Table 6.2 – Hydraulic conditions of the Prancevic & Lamb (2015) runs. Flow depth was estimated by Equation 6.10. The relative submergence  $S_m^s$  and critical Shields stress  $\Theta_{th}^s$  are calculated with  $h = h_{f,exp}^s$ .

Three types of processing have been performed:

1. The first set neglected the lift force introduced by Equation 6.7 and did not consider turbulence.
2. In the second set, the lift force was introduced but the turbulence remained neglected.
3. In the third set, the turbulence is introduced while the lift force is neglected.
4. In the fourth set of runs, the lift force and turbulence were introduced. The manner in which the turbulence was parametrized is detailed in the corresponding section.

### 3.3.1 Without lift force and without turbulence

As a first test, lift and turbulence are neglected, i.e.,  $F_M = 0$  and  $u_x = U_x$ .

In these conditions, it is observed in Figure 6.7 that the predicted Shields stress is much higher than is usually measured in the field, i.e., the trend provided by the calibration curve on the field data of (Recking *et al.*, 2008) and the experimental points of Prancevic & Lamb (2015). The critical Shields stress is relatively stable and fluctuates between 2 and 3. It is clear that these values are too high, and that the origin of this shift may be due to other interactions such as the lift force or turbulence.

### 3.3.2 With lift force and without turbulence

With the introduction of the lift force, an additional vertical force must be considered. This has the effect of diminishing the vertical component and reducing the friction force, and by consequence the critical Shields stress. In Figure 6.8,  $\Theta_{th}$  it is about 0.4, and decreases down to 0.1 for larger slopes. The different definitions of flow depth do not significantly influence the trends. However, the values commonly measured are not yet reached, except for high slopes. The introduction of the turbulence to explain the onset of motion may improve the coherence with the measured values.

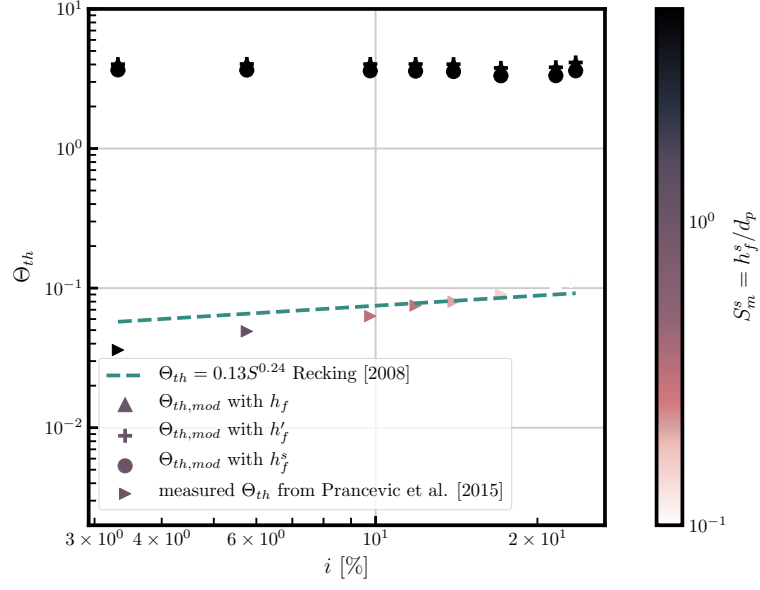


Figure 6.7 – Critical Shields number versus slope simulated from the hydraulic conditions of Prancevic & Lamb (2015) (see Table 6.2). Without turbulence and without lift forces ( $F_M = 0$  and  $u_x = U_x$ ).

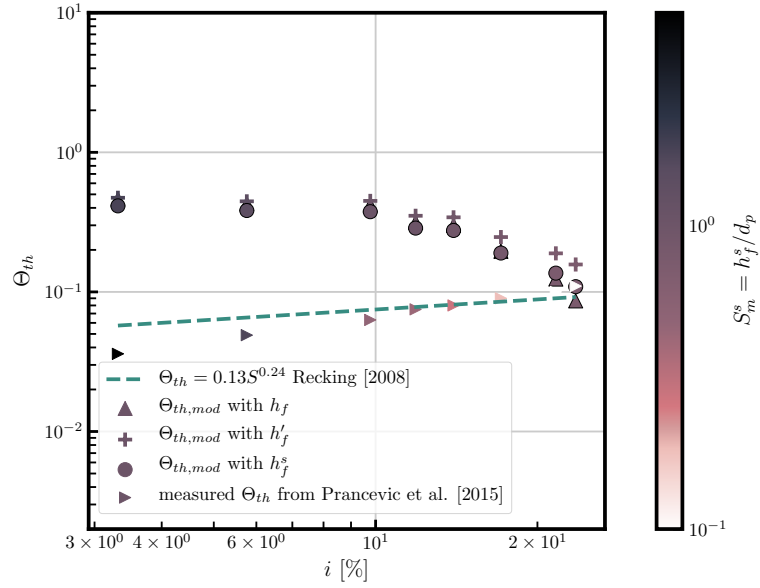


Figure 6.8 – Critical Shields number versus slope simulated from the hydraulic conditions of Prancevic & Lamb (2015) (see Table 6.2). Without turbulence and with lift force ( $F_M$  given by 6.7 and  $u_x = U_x$ )

## 3.3.3 With turbulence and Without lift force

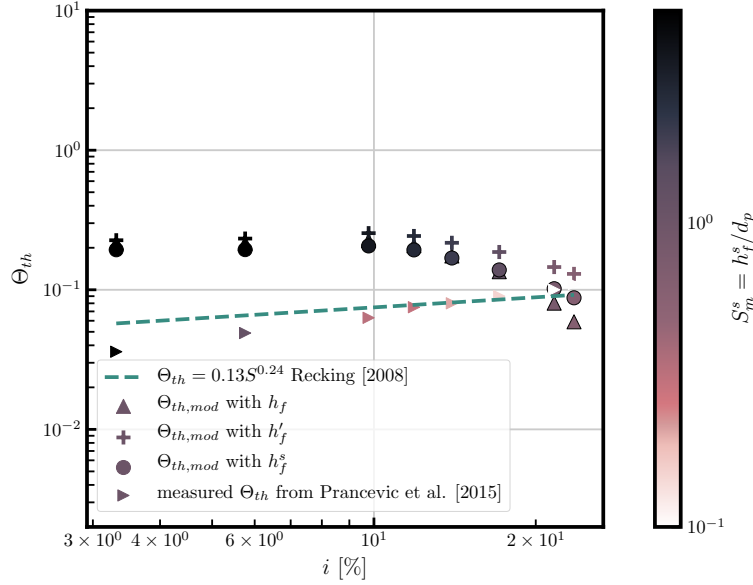


Figure 6.9 – Critical Shields number versus slope simulated from the hydraulic conditions of Prancevic & Lamb (2015) (see Table 6.2). With turbulence and without lift force ( $F_M$  given by 6.7 and  $u_x = U_x$ )

Many papers have investigated the statistics of turbulence in relation to the sediment entrainment threshold, and have suggested a significant role in the particle momentum balance (See Paintal (1971); Schmeeckle *et al.* (2007); Lamb *et al.* (2008); Prancevic & Lamb (2015), for instance). The idea behind these studies is that the instantaneous velocity fluctuates and can be temporarily much higher than the mean velocity around particles. As measured in Chapter 4 and 5, turbulence penetrates into the permeable bed, i.e. around particles. Measurements show that at the roughness crest, turbulence intensity profiles scale with the shear velocity, to reach a maximum of  $\langle |u'_x| \rangle \sim 1.5 u_*$  near the roughness crest for streamwise intensity (See Figure 1.7 of Chapter 3). However, it has also been shown that the damping effect is crucial with the hydraulic conditions of the set-up ( $Re_b = O(1000)$ ). When the damping effect is negligible, Nezu & Nakagawa (1993) suggested that for a smooth bed,  $\langle |u'_x| \rangle \sim 2. u_*$  near the wall. However, it must be emphasized that the turbulence intensity is obtained by calculating the standard deviation, and higher instantaneous velocities may be observed. To obtain higher velocities, the probability density functions of the turbulence fluctuations in Figure 4.6 of Chapter 4 are instructive. While no theoretical probability density function was fitted, one can observe that the maximum of the velocity is limited, and that extreme sweep events rarely exceed the standard deviation.

Thus, as a first attempt to include the turbulence in the model, the following arbitrary choice will be used to represent the velocity magnitude that might temporarily dislodge a grain. The velocity  $u_x$  is given by  $U_x + 2 u_*$  on the bead position  $z_p$ . The factor 2 is not fundamental to explain the following results, similar trends were observed with factors varying from 1 to 3.



By introducing the turbulence, the trend of the critical Shields stress shown in Figure 6.9 is similar to the trend of the previous set (turbulence and no lift). However, it does not explain the increase of the Shields number when slope increase. To have a complete overview, we must combine the two effects: turbulence and lift force.

### 3.3.4 With turbulence and lift force

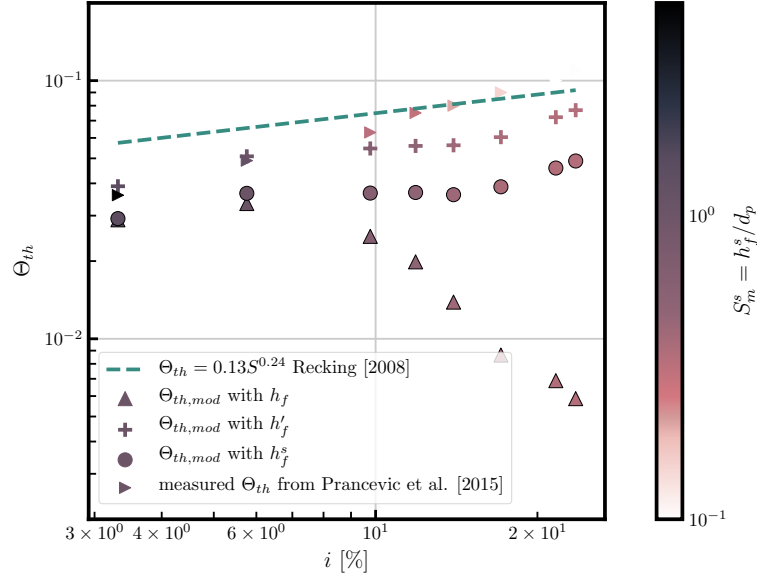


Figure 6.10 – Critical Shields number versus slope simulated from the hydraulic conditions of Prancevic & Lamb (2015) (see Table 6.2). With turbulence  $u_x = U_x + 3u_*$  and lift force ( $F_M$  given by 6.7 and  $u_x = U_x$ ). Note that compared to the above Figure 6.8, the limits for the  $\Theta_{th}$  axis have been changed

Here, contrary to the previous simulations, Figure 6.10 shows an increase in the critical Shields stress calculated with slopes and by defining the fluid depth by  $h'_f$  and  $h_f^s$ . This result corresponds with the well documented experimental results of Lamb *et al.* (2008) and Recking (2009). Moreover, the flow depth definition also seems to be of primary importance, since the Shields stress calculated with  $h_f$  systemically provides a decrease. The observed values range from around 0.03 to 0.06 for slopes of about 20 %.

A comparison of Figure 6.8 and Figure 6.10 suggests that both the lift force and the turbulence effect might play a critical role in explaining the onset of motion mechanisms. The lift force alone allows a substantial reduction in the critical Shields number, of about one order of magnitude. Additionally, the increasing trend seems to be closely related to the turbulence influence, since the more the relative submergence is important, the more the turbulent intensity at the roughness crest is important.

## 4 Conclusions on mountain river monitoring

In this chapter, the surface velocities from a mountain stream were collected by an image velocimetry technique yielding flow depth and relative submergence. Inconsistencies have been raised between the calculated relative submergence and field observations. To explain these values, vertical profiles were generated from the 1D model developed in Chapter 3 and tested in Chapter 5.

These simulations showed that the modeled vertical profiles are consistent with the field observations, giving stream surface velocities of the same order of magnitude. These modeled profiles suggest that the flow depth  $h_f$ , defined by the thickness of the surface layer, is much smaller than the flow depth  $h_f^*$  estimated from the flow discharge, by a factor of approximately 2 in these conditions, i.e., a small relative submergence and  $i$  between  $4\% < i < 8\%$ .

Owing to the difficulty in measuring flow depth,  $h_f^*$  is generally employed to calibrate flow resistance and critical Shields stress estimations for field and laboratory flumes. It must be emphasized that with small relative submergence conditions, the flow depth estimated by this technique complicates the interpretation of these empirical equations. This effect becomes more important for low relative submergence conditions. Furthermore, it has been shown that for a high relative submergence, the non-dimensional Chézy number tends to a maximum that is coherent with the Chézy-Eytelwein calibration and experimental points provided by Rickenmann & Recking (2011), while it diverges from the Keulegan prediction. More investigations are required to evaluate the underlying processes behind these trends.

Lastly, the evolution of the critical Shields stress with the slope has also been investigated. A simple force balance model on a grain allows the threshold of entertainment to be predicted. It is suggested that both turbulence activity and the lift force due to the fluid circulation around the grain (sometimes also called Magnus force) have an important effect on the value of this threshold. Moreover, the increasing trend seems to be related to a decrease in turbulence intensities when the slope increases in agreement with Lamb *et al.* (2008) suggestions. Again, the flow depth determination is also critical, and may explain the large variability found in the literature for sediment transport predictions when flow exhibit small relative submergence.

# 7

## Conclusion and outlook

---

The object of this thesis was to develop and test a model for predicting the vertical structure of turbulent flows in mountain rivers. To this end, the double-averaging concept applied to open channel flows formed a fundamental tool and served for the construction of a 1D model, as well as for the interpretation of experimental results.

With this procedure, closures for the *double-averaged momentum equation* applied to an open-channel flow over a permeable rough bed were devised in Chapter 3. This 1D model relies fundamentally on the spatial averaging procedure at the mesoscopic scale producing a *continuous porosity profile*. In a simplified approach, three layers can be identified by the porosity profile, with these being the *subsurface*, *roughness* and *surface* layers. While the subsurface and roughness layers constitute the underlying permeable bed, the surface layer begins at the top of the roughness element and ends at the stream surface. The roughness layer is a critical transition region where porosity varies sharply. Across the interface, hydrodynamic processes rely both on drag forces from protuberances and turbulent boundary layer mechanisms. *Double-averaged momentum equation* produced terms that required closure, including drag forces, and three stresses: the turbulent, dispersive, and viscous stresses.

To test this model, an experimental procedure capturing flows over a rough permeable medium was devised and presented in Chapter 4. Owing to the complications of measuring interstitial flows in the roughness and subsurface layers, a methodology coupling refractive index matching with particle image velocimetry was developed. This methodology was called PIV-RIMS in this study. The isoindex fluid used was a mixture of Benzyl-Alcohol and Ethanol, and flowed over centimetric glass spheres in a narrow flume with small relative submergence conditions and steep slopes ( $0.5 \% < i < 8 \%$ ). Contrary to previous studies employing the isoindex technique to measure fluid velocities (Voermans *et al.*, 2017), the density ratio between the glass and fluid was higher. This characteristic was essential for reaching steep slopes with the glass spheres staying at rest while still being free to move. With the PIV-RIMS procedure, the medium was scanned yielding instantaneous velocities in three dimensions. Averaging over time and space

within the double averaging procedure allowed the mean velocity and stresses to be computed.

In Chapter 5, nine runs employing the PIV-RIMS procedure and yielding vertical flow structures in various hydraulic conditions were depicted. The slopes varied from 0.5% to 8%, the grain sizes from 8 to 14 mm, and the relative submergence from 0.3 to 1.6. The measurements obtained show the coherence of the velocity profiles and turbulence statistics with previous investigations on open channel flows (Nezu, 2005). Fully turbulent flows were observed when experiments were performed at intermediate Reynolds numbers, i.e.,  $Re = O(1000)$ . In these conditions, the viscous effect is expected to play a critical role. This effect relies not simply on the viscous stress, but more importantly on the van Driest *damping effect*, which states a reduction of turbulence near the wall when the local Reynolds number is small. Furthermore, *velocity defect law* effect is observed near the free surface. As far as I know, these two open-channel flow features are here exhibited for steep slopes in small relative submergence conditions for the first time.

The closures of the 1D model developed in Chapter 3 were devised with insights obtained from experimental results.

*Drag forces* in the permeable bed were predicted by the Darcy-Ergün equation. This equation is commonly employed for flow predictions in a homogeneous permeable medium. Devised for a high Reynolds porous flow, predictions made with the Darcy-Ergün equation coincide with subsurface velocity measurements. The Darcy-Ergün equation is also coherent with drag force predictions in the roughness layer, where velocity and porosity are higher near the roughness crest.

Classical *turbulent stress*, based on the Prandtl mixing length theory, was also adapted to the double-averaging approach. Although the mixing length classically requires a fixed reference in open channel flows, this reference is not clearly materialized with smooth porosity profiles. The alternative mixing length function, including the *van Driest* damping effect, is then computed from the porosity profile without the need for a vertical reference.

While *dispersive stress* has received experimental and numerical attention this last decade (Mignot *et al.*, 2009a; Dey & Das, 2012; Voermans *et al.*, 2017; Fang *et al.*, 2018), it has never achieved a closure. Then, I developed an expression for the *dispersive stress* based on mechanistic arguments. The trend of this modeled stress is coherent with previous dispersive stress measurements and those of this study presented in Chapter 5.

In Chapter 6, I analyzed field-data from a real-case scenario on the Navizence mountain river. Stream surface velocities, grain size distributions, and slopes were deduced from drone aerial photography. This information served to understand the complications underlying the flow depth and bed shear stress predictions with small relative submergence conditions. The consistency between field stream surface velocities and 1D model predictions was established. The model shows that an important part of the flow passes through the roughness layer in mountain rivers, and suggests that the flow depth deduced from the discharge does not represent the thickness of the surface layer. Finally, the trend of the classical flow resistance and critical Shields stress equations were investigated. The variability observed for low submergence conditions suggest that definitions of flow depth must be clarified when a specific formulae is employed. The increase observed for the critical Shields stress versus slope is coherent with our simulation if the turbulence activity as well as the lift force due to the fluid circulation around the grain

---

(sometimes also called Magnus force) are considered in the force balance on a single grain.

Additional experimental or theoretical investigations for attaining a better understanding of flows over permeable rough beds were identified for future research:

- Experimentally, the PIV-RIMS procedure measured stream-wise and vertical components of velocity. The procedure can be improved to allow the third component to be obtained, by coupling it with a tomographic PIV technique, or by simply rotating the laser sheet. With knowledge of all the components, a better resolution of the wakes around protuberances might be obtained, and this could explain the mechanisms responsible for mixing length distributions.
- From experiments, the role of the velocity defect law was also revealed. This effect has not yet been incorporated in the model, and it might improve the prediction of vertical profiles.
- In Chapter 3, the non-universality of the von Karman constant has been identified to be a consequence of the inadequate log-law framework when relative submergence is small. By comparing thoroughly existing experimental data sets with the 1D model a clearer explanation of this *non-universality* may be revealed.
- The double-averaged momentum equation could also be studied more closely to pair terms of the equation with the permeability Reynolds number ( $Re_K = \frac{\sqrt{K}u_*}{\nu}$ ). To go further, by simplifying this equation and employing methodologies such as the perturbation method, it would be possible to produce a function respecting the behavior of the velocity profile across the interface. This function could eventually replace the logarithmic approach that produces confusion in low relative submergence conditions. A low relative submergence is indeed a ubiquitous feature of mountain rivers.

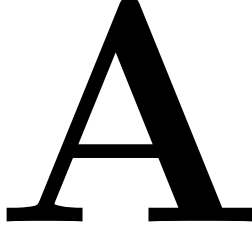
The 1D model solving the Navier-Stokes equation at the mesoscopic scale has only been tested for unidirectional flows over static granular beds, but insights on the vertical structure may also improve sediment transport models in turbulent conditions. For instance, it may be implemented in classical Eulerian-Eulerian models where both solid and fluid phases are resolved continuously (Revil-Baudard & Chauchat, 2013) or for simulations that combine the Discrete Element Method (DEM) with a continuous description of the fluid (Maurin *et al.*, 2015). It can also be adapted to recent approaches employing Material Point Method (MPM) (Gao *et al.*, 2018). These diverse approaches gain attention from computer graphics researcher as well as from practitioners due to their ability to model complex scenarios with the fluid equations being averaged at the mesoscopic scale to reduce computational cost.



## Appendix **Part III**







### 1 Definitions

#### 1.1 Time averaging

Considering any quantity  $\theta$  describing the flow (the pressure  $p$ , or the velocities, for instance), the time-averaging procedure is defined as:

$$\bar{\theta}(x, y, z) = \frac{1}{T} \int_T \theta \, dt \quad (\text{A.1})$$

In flow measurement issues, attention must be paid to this procedure. The duration must be large enough to obtain the time averaged velocity as well as the turbulence statistics. Due to the spatial heterogeneity of some flows, the fluctuations due to turbulence vary at different time scales depending on the location of the measure. For instance, to obtain an accurate time average velocity in the roughness layer, the duration is about 1 second for my experiment (see Chapter 4).

#### 1.2 Space averaging

The superficial spatial averaging on a volume  $V_0$  with time averaged quantity is defined as:

$$\langle \bar{\theta} \rangle_s = \frac{1}{V_0} \iiint_{V_0} \bar{\theta} \, dV \quad (\text{A.2})$$

The intrinsic spatial averaging procedure on the volume occupied by the fluid  $V_f$  is defined as:

$$\langle \bar{\theta} \rangle = \frac{1}{V_f} \iiint_{V_0} \bar{\theta} \, dV \quad (\text{A.3})$$

## Appendix A. Double-averaging methodology

---

The porosity is defined by  $\frac{V_f}{V_t} = \epsilon$  and we obtain the logical relation  $\langle \bar{\theta} \rangle_s = \epsilon \langle \bar{\theta} \rangle$ .

Because of the strong gradients in flow properties in the vertical direction in open-channels, it is convenient to define the area averaging over a plane parallel to the mean bed as:

$$\langle \theta \rangle_{A0} = \frac{1}{A_0} \iint_{A_0} \langle \bar{\theta} \rangle_{\delta_z} dx dy \quad (\text{A.4})$$

Volume averaging and plane averaging procedure are similar if the volume averaging domain  $V_0$  is designed to form a thin slab of height  $\delta_z$  parallel to the averaged bed. In the following, I will always consider this configuration, and we may write  $\langle \theta \rangle_{A0} = \langle \theta \rangle(z)$ . This is a quantity that is only dependent on  $t$  and  $z$ .

With these considerations, any instantaneous flow variable may be composed in a manner similar to a *Reynolds decomposition*:

$$\theta(x, y, z, t) = \langle \bar{\theta} \rangle(z) + \tilde{\theta}(x, y, z) + \theta'(x, z, t), \quad (\text{A.5})$$

where  $\tilde{\theta}(x, z)$  is the local deviation against the averaged variable  $\langle \bar{\theta} \rangle$ , a quantity that can be estimated by  $\tilde{\theta}(x, z) = \bar{\theta} - \langle \bar{\theta}(x, z, t) \rangle$ .

### 1.3 Spatial averaging theorem

The spatial averaging theorem is one of the most employed theorems for multiphase flows Jackson (2000). His mathematical background is available in (Howes & Whitaker, 1985) and results in the following formulation :

$$\left\langle \frac{d\theta}{dx_i} \right\rangle_s = \frac{d\langle \theta \rangle_s}{dx_i} + \frac{1}{V_{tot}} \int_{S_{int}} \theta \mathbf{e}_i \cdot \mathbf{n} dS \quad (\text{A.6})$$

Where  $x_i$  ( $i=1,2$ , and  $3$ ) demotes to the directions  $x$ ,  $y$  and  $z$  and  $u_i$  corresponds to the velocity components  $u_x$ ,  $u_y$  and  $u_z$ .  $\mathbf{n}$  is the inwardly directed unit vector normal to the solid element surface,  $S_{int}$  is the extent of the water-bed surface bounded by the averaging domain.

Or equivalently, when we work with the intrinsic quantities:

$$\left\langle \frac{d\theta}{dx_i} \right\rangle = \frac{1}{\epsilon} \frac{d\langle \theta \rangle}{dx_i} + \frac{1}{\epsilon} \frac{1}{V_{tot}} \int_{S_{int}} \theta \mathbf{e}_i \cdot \mathbf{n} dS \quad (\text{A.7})$$

If the solid element are immobile, the spatial averaging theorem applied to time averaged quantity results in the time-space averaging of hydrodynamic quantities:

$$\left\langle \frac{\partial \bar{\theta}}{\partial x_i} \right\rangle = \left\langle \frac{\partial \bar{\theta}}{\partial x_i} \right\rangle = \frac{1}{\epsilon} \frac{\partial \langle \bar{\theta} \rangle}{\partial x_i} + \frac{1}{\epsilon} \frac{1}{V_{tot}} \int_{S_{int}} \bar{\theta} \mathbf{e}_i \cdot \mathbf{n} dS \quad (\text{A.8})$$

## 2 Double-averaged Navier-Stoke equations

### 2.1 Continuity equation

The *double-averaging* concept applied on the continuity equation of an incompressible flow gives:

$$\overline{\left\langle \frac{\partial u_i}{\partial x_i} \right\rangle}_s = 0 \quad (\text{A.9})$$

Using the theorem Equation A.8, the following development can be obtained:

$$\overline{\left\langle \frac{\partial u_i}{\partial x_i} \right\rangle}_s = \frac{\partial \epsilon \langle \overline{u_i} \rangle}{\partial x_i} + \frac{1}{V} \int_{S_{int}} \overline{u_i} \mathbf{e}_x \cdot \mathbf{n} \, dS = 0 \quad (\text{A.10})$$

The no-slip condition on the solid walls impose  $u_i(\mathbf{r}_s) = 0$  where  $\mathbf{r}_s$  is the position of the solid surface on which the integration is performed. It results in the simpler form:

$$\frac{\partial \epsilon \langle \overline{u_i} \rangle}{\partial x_i} = \frac{\partial \langle \overline{u_i} \rangle_s}{\partial x_i} = 0 \quad (\text{A.11})$$

It is the superficial velocity that is conserved

### 2.2 Double-averaged momentum equation

The *double-averaged momentum equation* is obtained by averaging in time and space the *Navier-Stokes* equations:

$$\overline{\left\langle \frac{\partial u_i}{\partial t} + u_j \frac{\partial u_i}{\partial x_j} \right\rangle}_s = g_i - \overline{\left\langle \frac{\epsilon p}{\partial x_j} \right\rangle}_s + \frac{\partial}{\partial x_j} \epsilon \overline{\left\langle \nu \frac{\partial u_i}{\partial x_j} \right\rangle}_s \quad (\text{A.12})$$

The Einstein convention, which prescribes a summation over each repeated index, is adopted. Applying the theorem Equation A.8 and the no slip condition on the solid surfaces, the following relation called the *double-averaged momentum equation* is deduced:

$$\begin{aligned} \frac{\langle \overline{u_i} \rangle}{\partial t} + \langle \overline{u_j} \rangle \frac{\langle \overline{u_i} \rangle}{\partial x_j} = & g_i - \frac{1}{\rho_f \epsilon} \frac{\partial \epsilon \langle \overline{p} \rangle}{\partial x_j} - \frac{1}{\epsilon} \frac{\partial \epsilon \langle \widetilde{u_i} \widetilde{u_j} \rangle}{\partial x_j} - \frac{1}{\epsilon} \frac{\partial \epsilon \langle \overline{u_i' u_j'} \rangle}{\partial x_j} + \frac{1}{\epsilon} \frac{\partial}{\partial x_j} \epsilon \langle \nu \frac{\partial \overline{u_i}}{\partial x_j} \rangle \\ & + \frac{1}{\epsilon} \frac{1}{\rho_f V_f} \iint_{S_{int}} \overline{p} \mathbf{n} \cdot \mathbf{e}_i \, dS + \frac{1}{\epsilon} \frac{1}{V_f} \iint_{S_{int}} \nu \frac{\partial \overline{u_i}}{\partial x_j} \mathbf{n} \cdot \mathbf{e}_i \, dS \end{aligned} \quad (\text{A.13})$$

Where  $g_i$  is the projected gravity in the direction  $i$ .

### 2.3 Simplifications for gravity driven open channel flows with uniform conditions

In some circumstance, a spatially averaged flow may be considered as uniform, steady and unidirectional in the  $x$  direction. It is the targeted experimental conditions in rectilinear laboratory flume (at a sufficient distance from the side wall). Then, the spatial averaging is made on distances such that all spatially averaged hydrodynamic quantities  $\langle \bar{\theta} \rangle$  depend only on the vertical coordinate  $z$  (in other words the derivatives along  $x$  and  $y$  are equal to zero). Moreover, the flow being unidirectional,  $\langle \bar{u}_y \rangle = \langle \bar{u}_z \rangle = 0$ . In addition, for gravity driven flow only, the pressure gradient along  $x$  is also equal to zero.

Thus, the *double-averaged momentum equation* Equation A.13 becomes:

$$0 = g_x - \frac{1}{\epsilon} \frac{d\epsilon \langle \tilde{u}_x \tilde{u}_z \rangle}{dz} - \frac{1}{\epsilon} \frac{d\epsilon \langle \bar{u}'_x \bar{u}'_z \rangle}{dz} + \frac{d\tau_v}{dz} + f_{Px} + f_{Vx} \quad (\text{A.14})$$

Here, all the terms depends only on the variable  $z$  and the equation must therefore be written with the *total differential* notation. This equation is employed as the governing equation for the theoretical development of this thesis.

### 2.4 Lemma on porosity and the gradient of the intrinsic velocity

From Equation A.8, by letting  $\epsilon$  be a constant locally, the porosity lemma takes the form:

$$\frac{\partial \epsilon}{\partial x_i} \mathbf{e}_{\mathbf{x}_i} = -\frac{1}{V} \int_{S_{int}} \mathbf{n} dS \quad (\text{A.15})$$

$$\frac{\partial \epsilon}{\partial x_i} \frac{\partial U_i}{\partial x_i} = -\frac{1}{V} \frac{\partial u_i}{\partial x_i} \int_{S_{int}} \mathbf{e}_{\mathbf{x}_i} \mathbf{n} dS \quad (\text{A.16})$$

## 3 Spatial averaging and homogeneous porous media laws

In this section, the Equation A.13 is developed for a porous media in order to provide the Darcy law. Consider a steady flow ( $\frac{\partial \bullet}{\partial t} = 0$ ) in an homogeneous porous medium subject to gravity forces only. In this porous medium, all the averaged quantities, over a volume bigger than variation at the pore scale, are uniform in space, i.e.  $\frac{\partial \langle \bullet \rangle}{\partial x_i} = 0$ .

In this conditions the above equation become:

$$0 = g_i - \frac{1}{\epsilon} \frac{1}{V_f} \iint_S \bar{\mathbf{p}} \mathbf{n} \cdot \mathbf{e}_i dS + \frac{1}{\epsilon} \frac{1}{V_f} \iint_S \nu \frac{\partial \bar{u}_i}{\partial x_j} \mathbf{n} \cdot \mathbf{e}_i dS \quad (\text{A.17})$$

The gravity force is compensated by local pressure forces and local viscous forces.

At this stage, it is tempting to identify the local viscous force terms of the classical Darcy law, and the pressure forces in terms of a drag force as it is proposed in Nikora *et al.* (2007). However, regarding Whitaker (1986) work, another development might be achieved for the viscous forces.

It is possible to decompose the integration of the viscous term by :

$$\begin{aligned} \frac{1}{\epsilon} \frac{1}{V_f} \iint_S \nu \frac{\partial \bar{u}_i}{\partial x_j} \mathbf{n} \cdot \mathbf{e}_i dS &= \frac{1}{\epsilon} \frac{1}{V_f} \iint_S \nu \frac{\partial U_i}{\partial x_j} \mathbf{n} \cdot \mathbf{e}_i dS + \frac{1}{\epsilon} \frac{1}{V_f} \iint_S \nu \frac{\partial \tilde{u}_i}{\partial x_j} \mathbf{n} \cdot \mathbf{e}_i dS \\ &= \frac{1}{\epsilon} \frac{1}{V_f} \iint_S \nu \frac{\partial \tilde{u}_i}{\partial x_j} \mathbf{n} \cdot \mathbf{e}_i dS \end{aligned} \quad (\text{A.18})$$

Because  $\bar{u}_i = U_i + \tilde{u}_i$  and  $\frac{\partial \langle u_i \rangle}{\partial x_i} = \frac{\partial U_i}{\partial x_i} = 0$

As developped in Whitaker (1986) the permeability in the Darcy-Forchheimer law is more likely identified as:

$$\frac{1}{\epsilon} \frac{1}{V_f} \iint_S \nu \left( \frac{\partial \tilde{u}_i}{\partial x_j} - \tilde{p} \right) \mathbf{n} \cdot \mathbf{e}_i dS = -\frac{\epsilon}{K_i} - \frac{\epsilon F}{K} \quad (\text{A.19})$$

where  $K$  is the traditional permeability and  $F$  is the Forchheimer correction that depends on  $U_x$ .

When a gradient of the velocity appears at macroscopic scale  $\frac{\partial U_x}{\partial x_j} \neq 0$  an additional term appears in the integration witch can be easily identified with the lemma Equation (A.16):

$$\frac{1}{\epsilon} \frac{1}{V_f} \iint_S \nu \frac{\partial \langle u_i \rangle}{\partial x_j} \mathbf{n} \cdot \mathbf{e}_i dS = -\frac{\nu}{\epsilon} \frac{\partial \epsilon}{\partial x_i} \frac{\partial u_i}{\partial x_j} \quad (\text{A.20})$$

This additional term is important for a system where porosity and velocity vary sharply as observed in our experimental work. It is discussed in the following section.

## 4 Viscous shear stress and spatial averaging

This section focuses on the theoretical development found in the literature to close the viscous shear stress. This discussion is not essential for the understanding of this thesis but participates for the closure choice of the viscous shear stress in of the *double-averaged momentum equation*. As far as I know, there is a substantial lack of discussion in the literature on the viscous shear stress in conditions of large porosity and velocity gradients. The spatial averaged viscous term of the local Navier-Stokes equation is developed within the spatial averaging approach. It is shown, that the spatial averaging results in various strategy for the closure of the viscous shear stress. While the Einstein correction of the viscosity is commonly used for fluidized beds and sheet flows, a different expression of the viscous stress appears when the spatial averaging is performed on a periodic porous bed. This last approach has been developed by the scientific

## Appendix A. Double-averaging methodology

---

community studying homogeneous porous media, whereas the former has been developed for flows with dilute suspension.

### 4.1 Spatial averaging of the viscous shear stress

We first require that the local variations of the viscosity are negligible. The viscous term of the Navier-Stokes equation is thus given by:

$$\overline{\left\langle \mu \frac{d^2 u_x}{dz^2} \right\rangle} = \mu \overline{\left\langle \frac{d^2 u_x}{dz^2} \right\rangle} \quad (\text{A.21})$$

In Equation (A.21), it is the average of a gradient, whilst it is the gradient of an average that is desired. We can obtain the gradient by employing the spatial averaging theorem Equation A.8 (Anderson & Jackson, 1967; Nikora *et al.*, 2007).

$$\overline{\left\langle \frac{du_x}{dz} \right\rangle} = \frac{1}{\epsilon} \frac{d\epsilon \langle \bar{u}_x \rangle}{dz} + \frac{1}{V} \overline{\int_{S_{int}} u_x \mathbf{e}_x \cdot \mathbf{n} dS}$$

where the right term represents the integral of the velocity on the surface wall and  $\mathbf{n}$  is the normal vector. Because of the no slip condition on solid wall, the integral is equal to zero. The theorem Equation A.8 for this expression and the total viscous forces are given by:

$$f_{v,tot} = \rho_f \nu \epsilon \overline{\left\langle \frac{d^2 \bar{u}_x}{dz^2} \right\rangle} = \rho_f \nu \frac{d^2 \epsilon U_x}{dz^2} + \frac{\rho_f \nu}{V} \overline{\int_{S_{int}} \frac{du_x}{dz} \mathbf{e}_x \cdot \mathbf{n} dS} = \frac{d\tau_v}{dz} + f_{v,x} \quad (\text{A.22})$$

It is tempting to identify  $f_{v,x}$  to the integration of the viscous forces on the solid walls, but more developments are required to identify the drag forces  $f_{v,x}$  from the integral. Depending on the domain of application, it is indeed the development of the integral that is unclear for porous bed conditions with the presence of a significant porosity gradient.

### 4.2 Spatial averaging for dilute spherical particles in a pure straining flow: Einstein correction

It is important to frame the domain of validity of the present development. A pure straining flow is considered with highly dilute spherical neutral buoyant suspensions such that the flow perturbations due to the particles will not influence the flow on other particles. In these conditions  $U_x = 0$  and the total force acting on the particle is zero. This configuration is only conceptual, to provide a relation between stresses at the surface and space averaged strain rate resulting in space averaged rheology of the fluid/particle mixture.

Because of the dilution, the integral of the viscous stresses over all particles is the same and it is possible to demonstrate that the left term of the Equation (A.22) is related to the strain rate  $\frac{d^2 U_x}{dz^2}$  (see the monograph of Leal (2007), pp 470-476 for general developments in 3 dimensions), giving the equality :

$$\frac{\rho_f \nu}{V} \int_{Sphere} \frac{du_x}{dz} \mathbf{e}_x \cdot \mathbf{n} dS = \rho_f \nu \frac{4\pi}{3} \frac{5}{2} R^3 \frac{d^2 U_x}{dz^2}$$

The averaging is performed on the volume fraction of sphere such that  $V = \frac{4\pi}{3} \frac{5}{2} R^3 / (1 - \epsilon)$  and gives the final expression of the viscosity force par unit volume (the calculation is usually done as a function of the solid fraction  $\phi = 1 - \epsilon$ ):

$$f_{v,tot} = \rho_f \nu \frac{d^2 \epsilon U_x}{dz^2} + \rho_f \nu \frac{5}{2} (1 - \epsilon) \frac{d^2 U_x}{dz^2}$$

If  $\epsilon \sim 1$  (which is expected for the validity of this relation), the result of A. Einstein developed in the course of his Ph.D. dissertation (1906) is retrieved:

$$f_{v,tot} = \rho_f \nu (1 + \frac{5}{2} (1 - \epsilon)) \frac{d^2 U_x}{dz^2} = \rho_f \nu^* \frac{d^2 U_x}{dz^2} \quad (\text{A.23})$$

With  $\nu^* = \nu (1 + \frac{5}{2} (1 - \epsilon))$

It might be surprising to apply a closure developed for dilute particles for bed load transport over a densely packed bed as it has been suggested by Ouriemi *et al.* (2009); Revil-Baudard & Chauchat (2013) for instance. However, it is the only known development that theoretically establishes a relation between the strain rate and the porosity. This situation might explain why the scientists working on sheet flows are tempted to apply this correction even if the domain of validity seems not adapted. In the next subsection, this approach is compared with the porous media approach where a correction on the viscosity has never been considered in the equations.

### 4.3 Spatial averaging for a unidirectional flow in a porous medium with a porosity gradient

Following Whitaker (1996) the development of the volume averaged viscous term on the  $x$  component of a unidirectional flow gives :

$$\begin{aligned} \overline{\epsilon \langle \rho_f \nu \frac{d^2 u_x}{dz^2} \rangle} &= \rho_f \nu \frac{d^2 \epsilon U_x}{dz^2} + \frac{1}{V} \overline{\int_{S_{int}} \rho_f \nu \frac{du_x}{dz} \mathbf{e}_x \cdot \mathbf{n} dS} \\ &= \rho_f \nu \frac{d^2 \epsilon U_x}{dz^2} - \rho_f \nu \frac{d\epsilon}{dz} \frac{dU_x}{dz} + \frac{1}{V} \overline{\int_{S_{int}} \rho_f \nu \frac{d\tilde{u}_x}{dz} \mathbf{e}_x \cdot \mathbf{n} dS} \end{aligned} \quad (\text{A.24})$$

Here, the pressure drag forces are omitted to concentrate the attention on the viscous effects. Assuming that  $\tilde{u}_x = M(x, y, z) U_x$  and  $\tilde{p} = m(x, y, z) U_x$  where  $m$  and  $M$  are functions depending on the bed geometry, the right term represents the viscous forces acting on the particles  $f_{v,x}$ .

## Appendix A. Double-averaging methodology

---

The rest may be considered as the *viscous shear stress*, giving:

$$\frac{d\tau_v}{dz} = \rho_f \nu \frac{d^2 \epsilon U_x}{dz^2} - \rho_f \nu \frac{d\epsilon}{dz} \frac{dU_x}{dz} = \rho_f \nu \left( \epsilon \frac{d^2 U_x}{dz^2} + \frac{d\epsilon}{dz} \frac{dU_x}{dz} + U_x \frac{d^2 \epsilon}{dz^2} \right) \quad (\text{A.25})$$

In an homogeneous porous medium, it is generally assumed that the two left terms are negligible because the porosity gradient at the scale of the averaged volumes are small. With these assumptions, the famous Brinkman term is given by:

$$f_{v,tot} = \frac{d\tau_v}{dz} = \rho_f \nu \epsilon \frac{d^2 U_x}{dz^2}$$

For specific rough-bed arrangements, it is not evident that the other terms that involve the gradient of the porosity in the  $z$  direction in the Equation A.25 are negligible. The variation of the porosity is sharp and is eventually of the same order of magnitude as the variation of the velocity. The paper of Ochoa-Tapia & Whitaker (1995) attempts to overcome this problem by considering two separate domains, and by introducing a momentum jump transfer condition. In the present case, where the porosity is continuous, there is no need to impose a jump condition. As has been previously mentioned, here is the main difference with previous works on flow over porous media where authors admit a lack of clarification at the transition (e.g. Tilton & Cortelezzi (2008); Rosti *et al.* (2015)).

While the dilute conditions are not respected in packed beds permitting the adoption of the Einstein correction, this rises the problem of the relation between the viscosity and the porosity. Then the question arises: how should the viscosity be modified for porous beds with bed load transport where a porosity gradient is observed? Any corrections have been previously investigated for rigid beds and further theoretical and experimental works are needed to suggest a general effective viscosity that relies on strong arguments.

Furthermore, in addition to the traditional Brinkman correction, other terms emerge within the spatial averaging framework that are usually neglected or simply omitted. The variation of velocities in the porous medium generally follows a high variation of porosity, and in some case, the additional terms might be non-negligible.

Thus, the closure of the *viscous shear stress* is given by the following form:

$$\frac{d\tau_v}{dz} = \underbrace{\rho_f \nu \epsilon \frac{d^2 U_x}{dz^2}}_{\text{Brinkman term}} + \underbrace{\rho_f \nu \frac{d\epsilon}{dz} \frac{dU_x}{dz} + \rho_f \nu U_x \frac{d^2 \epsilon}{dz^2}}_{\text{Additional terms}} + \underbrace{\rho_f \nu^* \frac{d^2 U_x}{dz^2}}_{\text{Einstein correction (neglected)}} \quad (\text{A.26})$$

For the experimental work presented in this thesis the vertical transfer of momentum is more likely influenced by the *dispersive stress* or *turbulent stress* than the viscous diffusion. A different experimental set-up is required to explore the influence of the porosity (or solid fraction) on the effective viscosity with or without bed load transport from viscous to turbulent regimes.



# B

## Numerical resolution of the 1D model

---

In this Appendix, the details concerning the discretization of the governing equation for the 1D numerical model are provided. A transient solver to reach the steady state has been employed (  $\frac{\partial U_x}{\partial t}$  expected to tend toward zero to reach the desired steady state) . It is a stable method and might be useful for dynamical systems for future utility.

For numerical suitability, the Eq 3.23 of Chapter 3 can be reformulated in an equivalent form :

$$\frac{\partial U_x}{\partial t} = \mathcal{G} + \mathcal{L}U_x + \mathcal{P}\frac{\partial U_x}{\partial z} + \mathcal{S}\frac{\partial^2 U_x}{\partial z^2} \quad (\text{B.1})$$

with

$$\mathcal{G} = \epsilon g \sin \zeta, \quad (\text{B.2})$$

$$\mathcal{L} = A_E \frac{(1-\epsilon)^2 \nu}{\epsilon d^2} + B_E \frac{(1-\epsilon)}{d} U_x + \frac{\partial \mathcal{D}}{\partial z} U_x + \nu \frac{\partial^2 \epsilon}{\partial z^2}, \quad (\text{B.3})$$

$$\mathcal{P} = (2U_x \mathcal{D}) + \nu \frac{\partial \epsilon}{\partial z} + \frac{\partial \epsilon l_M^2}{\partial z} \frac{\partial U_x}{\partial z}, \quad (\text{B.4})$$

$$\mathcal{S} = \nu \epsilon + 2\epsilon l_M^2 \frac{\partial U_x}{\partial z}, \quad (\text{B.5})$$

and

$$\mathcal{D} = \epsilon \lambda_+ \sqrt{\frac{1-\epsilon}{1-\epsilon_b}} \left( 1 - \sqrt{1 - \frac{1-\epsilon}{1-\epsilon_b}} \right). \quad (\text{B.6})$$

## Appendix B. Numerical resolution of the 1D model

---

After defining the porosity profile  $\epsilon(z)$  describing the roughness layer thickness, this non linear equation can be solved numerically using a semi-implicit scheme. The values are calculated at the node of the scheme and the velocity in the cells. The equations is solved with a spatial step  $\Delta z$  and a time step  $\Delta t$ . On the bottom of the permeable bed, the non-slip condition  $U_x(z_b) = 0$  and at the free surface  $\frac{\partial U_x}{\partial z}(z_{surf}) = 0$  are imposed. The number of nodes is  $N = 300$  and the grid size is deduced by  $\Delta z = \frac{z_{surf} - z_b}{N}$ . The time step is fixed at  $\Delta t = 10^{-4} s$ . The convergence of the scheme has been observed for various scenarios depicted in Chapter 3 - Sec.3.2. The scheme becomes unstable when the roughness layer thickness is not resolved, i.e when  $\Delta z > h_{RL}$  ( $h_{RL}$  usually scale with the grain size  $d_p$ ).

The semi-implicit scheme is given by:

$$\begin{aligned}
 \frac{U_x(t + \Delta t, z) - U_x(t, z)}{\Delta t} = & \mathcal{G} + \mathcal{L}_z U_x(t + \Delta t, z) \\
 & + \frac{1}{2} \mathcal{P}_{z+\Delta z/2} \frac{U_x(t + \Delta t, z + \Delta z) - U_x(t + \Delta t, z)}{\Delta z} \\
 & + \frac{1}{2} \mathcal{P}_{z-\Delta z/2} \frac{U_x(t + \Delta t, z) - U_x(t + \Delta t, z - \Delta z)}{\Delta z} \\
 & + \left[ \mathcal{S}_{z+\Delta z/2} \frac{U_x(t + \Delta t, z + \Delta z) - U_x(t + \Delta t, z)}{\Delta z} \right. \\
 & \left. - \mathcal{S}_{z-\Delta z/2} \frac{U_x(t + \Delta t, z) - U_x(t + \Delta t, z - \Delta z)}{\Delta z} \right] / \Delta z
 \end{aligned} \tag{B.7}$$

The scheme is *semi-implicit* because, at each time step,  $\mathcal{L}_z$ ,  $\mathcal{P}_z$  and  $\mathcal{S}_z$  are calculated with  $U_x(t, z)$  calculated at time step  $t$ . The linear system can after be resolved to obtain  $U_x(t + \Delta t)$ .

# C

## Image velocimetry processing

This Appendix details the 3 principle steps of the image velocimetry algorithm employed to yield the velocity field from a consecutive images. The test on the PIV challenge as well as the internet adress to access to the detail of the algorithm are provided at the end of this Appendix.

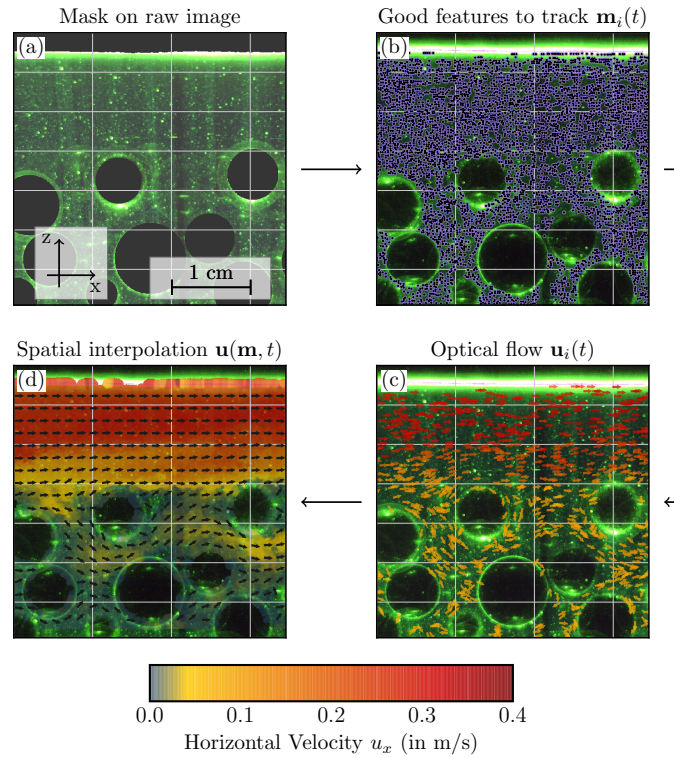


Figure C.1 – Graphical overview of the workflow: from the raw image to the velocity field.

## 1 Pre-processing

For a given laser sheet position  $y_m$ , a mask is generated from the bead positions to restrict the measurement to the interstitial flow zones and the surface flow. Similarly, the fluctuating fluid/air interface is detected to mask the upper part of the frame [see Figure C.1(a)].

To improve image contrast, the Contrast-Limited Adaptive Histogram Equalization (CLAHE) algorithm (grid size =  $32 \times 16$  px, clip limit = 8) is employed. Hot pixels (with constant high-intensity values) may be present during the recording, as well as local and temporary (long duration in comparison with the particle displacement) hot spots due to reflection. To solve this problem, a background removal procedure is performed by subtracting the average frame.

Before any velocity measurements, the algorithm *Good Feature To Track* (GFT) selects features that hold a good contrast, i.e., that are able to provide accurate velocity estimates (Shi, 1994) [see Figure C.1(b)]. This pre-selection presents two advantages: first, by discarding low-quality points it diminishes errors, and secondly, it decreases the number of potential interrogation windows, thereby making the algorithm more efficient. With classical PIV methods, the entire domain is usually computed on regularly spaced interrogation windows. With this strategy, low-quality measurements are generally discarded using post-processing methods, whereas the method employed here avoids processing those zones with a low signal-to-noise ratio. At the end of this step, the points  $\mathbf{m}_i = (x, z)_i^T$  are selected and the velocimetry processing is launched.

## 2 Velocimetry processing

The velocimetry algorithm measures the local (region-based) *optical flow* by means of a pyramidal implementation of the Lukas-Kanade method (Bouguet, 2001) [see Figure C.1(c)]. With this method, the square of the *Displaced Frame Difference* is minimized. To better understand the equations involved in this algorithm and its link with classical PIV, details of the procedure are provided in the following, with these being based on the papers of Heitz *et al.* (2010) and Liu & Shen (2008).

Given a position  $\mathbf{m} = (x, z)^T$  in the image and the intensity function  $I(\mathbf{m}, t)$  of the image field, the velocity field is denoted as

$$\mathbf{u}(\mathbf{m}) = (u_x(\mathbf{m}), u_z(\mathbf{m}))^T \quad (\text{C.1})$$

The Optical Flow Constraint (OFC) equation representing the brightness constancy may be written as

$$\frac{\partial I}{\partial t} = \mathbf{u} \cdot \nabla I \quad (\text{C.2})$$

Equation C.2 is the linear formulation of the matching formula between 2 consecutive images,

and is also known as the *Displaced Frame Difference*:

$$I(\mathbf{m} + \mathbf{d}(\mathbf{m}), t + \delta t) - I(\mathbf{m}, t) = 0 \quad (\text{C.3})$$

Where  $\mathbf{d}(\mathbf{m})$  denotes the displacement field between 2 images. With the Lukas-Kanade method, the displacement field between two consecutive images is determined by minimizing the square of the *Displaced Frame Difference* model

$$\mathbf{d}(\mathbf{m}) = \arg \min_{\mathbf{d}} \sum_{\mathbf{r} \in W(\mathbf{m})} (I(\mathbf{r} + \mathbf{d}, t + \delta t) - I(\mathbf{r}, t))^2 \quad (\text{C.4})$$

Where  $W(\mathbf{m})$  is the interrogation window around the point of interest. Since  $I(\mathbf{m}, t)$  is independent to  $\mathbf{d}$ , Equation C.4 is equivalent to:

$$\mathbf{d}(\mathbf{m}) = \arg \min_{\mathbf{d}} \sum_{\mathbf{r} \in W(\mathbf{m})} I(\mathbf{r} + \mathbf{d}, t + \delta t)^2 - 2I(\mathbf{r} + \mathbf{d}, t + \delta t)I(\mathbf{r}, t) \quad (\text{C.5})$$

Equation C.5 shows that the minimization of the square of the *Displaced Frame Difference* includes the correlation between two consecutive images. The displacement field estimated with this method is thus equivalent to the displacement field obtain by classical PIV if the quantity  $\sum_{\mathbf{r} \in W(\mathbf{m})} I(\mathbf{m} + \mathbf{d}(\mathbf{m}), t + \delta t)^2$  does not depend on  $\mathbf{d}$ . This assumption is implicitly performed in classical cross correlation techniques, but is locally strengthened when the small interrogation windows or large velocity gradients are considered. This is probably why this method works better for the current study problem, where small pore sizes limit the windowing.

The ‘pyramidal’ implementation aims to increase the dynamic range, i.e., to deal with large pixel motion. The pyramid refers to the successive low pass filtering and sub-sampling of the image sequence. The levels of the pyramid (1,2,3,...) represent the number of passes and the resolution of the image for the first pass on which the Lukas-Kanade velocimetry method is executed. For example, if the image has a resolution of 400×400 px and the level of the pyramid is 2, the first image has a resolution of 100×100 px. In this image, the pixel motions are smaller, and the Lukas-Kanade method (with the same window size) measures the global movement to introduce a shift for the second pass. This methodology is the equivalent of the iterative multi-grid method commonly performed in fluid mechanics (Scarano & Riethmuller, 1999). For this experiment, the pyramidal Lukas-Kanade method is parametrized with a 16 × 16 px window and three pyramidal levels.

At the end of this step, the velocity is obtained for each of the selected points  $\mathbf{u}_i = (u_x, u_z)_i^T$  [see Figure C.1 (c)].

### 3 Post processing and interpolation scheme

The final step consists of an interpolation process to obtain a velocity field from the isolated points where velocity is known, filling the gaps where the image quality was poor or where the number of seeding particles was too small. This step is commonly performed in particle

## Appendix C. Image velocimetry processing

tracking velocimetry (PTV) algorithms, but is computationally expensive. Recent improvements in the Visualization ToolKit (VTK) library allow implementation of a tree-like data structure to partition the 2D space and create buckets (methods that are commonly used in 3D graphics or 3D game engines). The search for the points or closer neighbors is then more efficient.

Before the interpolation process, the velocity vectors are subjected to two filters to detect potential outliers. The first filter detects and suppresses isolated points, while the second filter detects outliers by making comparisons with the local averaged velocity.

A Gaussian interpolation scheme with a kernel of 15 px radius and a standard deviation of 5.6 px is used. Finally, using this process the velocity field between two images can be reproduced [see Figure C.1 (d)].

### 4 Test on the 4th PIV challenge - Case A

An overview of the literature on the application of Lukas-Kanade techniques to fluid mechanics reveals only a few contributions (Miozzi *et al.*, 2008; Zhang & Chanson, 2018). The algorithm developed for the purpose of this PhD, was tested on the image sequences of the 4th PIV Challenge Case A (Kähler *et al.*, 2016) to assess on its performance. The resulting velocity measurements (Figure C.2, Figure C.3 and Figure C.4) show a good agreement with the main measures performed by the twenty leading participant of the 4th PIV Challenge. The main code, termed *opyflow* and the algorithms to provide the figures below showing the results of the test have been uploaded to GitHub (<https://github.com/groussea/opyflow>). To my opinion, and regarding different comments from manuscripts in the domain (e.g. Boutier (2012); Heitz *et al.* (2010)), this methodology seems more accurate and efficient than traditional PIV methodologies.

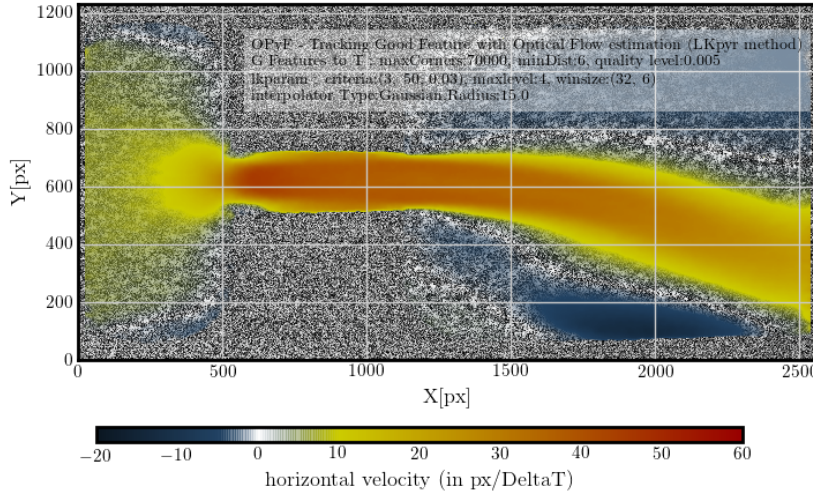


Figure C.2 – Displacement measured on the 4th PIV Challenge . Case A (e.g. Kähler *et al.* (2016))

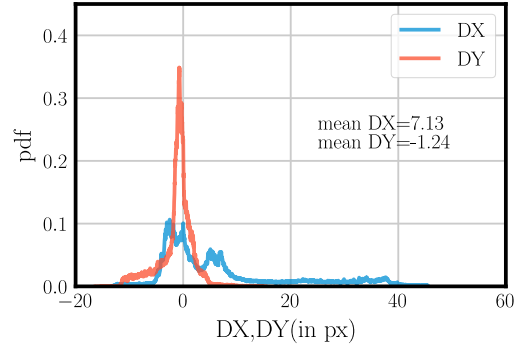


Figure C.3 – Histogram of the vertical and horizontal displacement measured on the 4th PIV Challenge . Case A (e.g. Kähler *et al.* (2016))

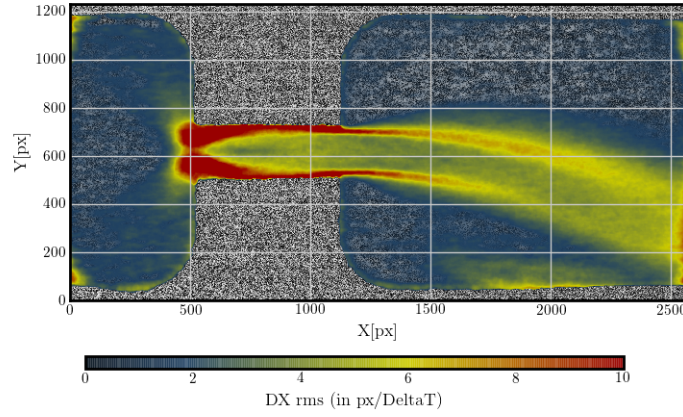


Figure C.4 – Root mean square of the displacements measured on the 4th PIV Challenge . Case A (e.g. Kähler *et al.* (2016))





# D

## Complements for the experimental procedure

---

This Appendix complements the experimental procedure in three sections:

- Section 1 - Figure D.1 shows the refractive index evolution of the Benzyl-Alcohol/Ethanol mixture with the proportion of Ethanol in the mixture  $\phi_{Eth}$ . These measurements provided a proportion of 40 % of Ethanol in volume (40/60 mixture) to obtain the matched refractive index. The accuracy on the isindex measure is given by the constructor  $\delta n = \pm 0.00004$  (e.g. the instruction manual of the Digital Refractometer ATAGO RX-5000  $\alpha$ ). Figure D.2 presents the viscosity and density measurements performed on the 40/60 mixture.
- Section 2 - Figure D.3 shows the calibration curve of the constant head tank system. The accuracy on the flow discharge has been estimated with the sum of the square of the residuals (SSR):  $\delta q_f \sim 2\sqrt{SSR}$  and the value of 5% is calculated with the lowest value of  $q_f$ .
- Section 3 - The calculations to obtain the distance from the permeable grid where the flow may be considered as uniform is developed. The scheme of this problem is given in Figure 4.12 of Chapter 4.

# 1 Benzyl Alcohol/Ethanol mixture

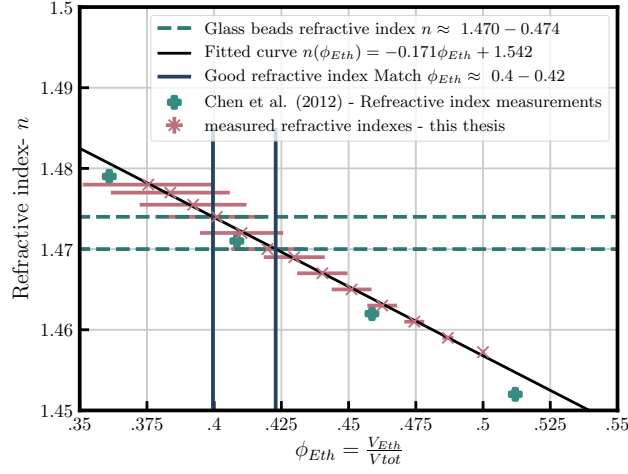


Figure D.1 – Measure of the refractive index of the Benzyl-Alcohol/Ethanol mixture (BAE) for various volume fractions of ethanol ( $\phi_{Eth}$ ) and comparison with the datas of Chen *et al.* (2012). The accuracy on the volume fraction increases while volume fraction decreases. It is the consequence of diluting an initial solution of BAE from the volume fraction  $\phi_{Eth} = 0.5$  by progressively adding Benzyl Alcohol. All the measurements have been done at  $273^\circ K$ .

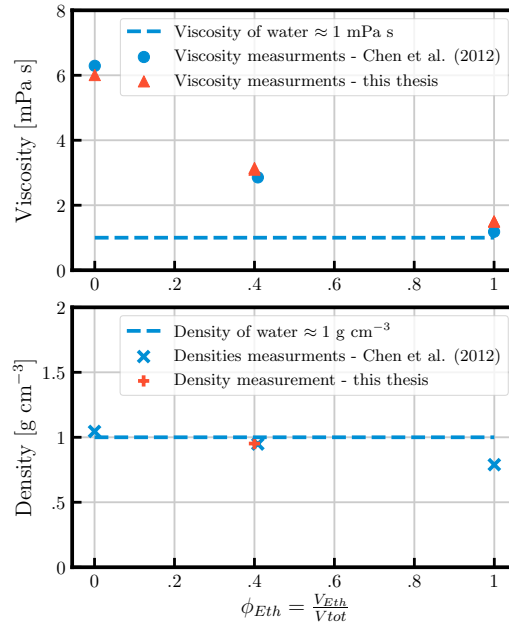


Figure D.2 – Measure of viscosity and density of the 40/60 Benzyl-Alcohol/Ethanol mixture for various volume fractions of Ethanol and comparison with the datas of Chen *et al.* (2012). The horizontal dashed lines represent the values for the water. The measurements have been done at  $273^\circ K$ .

## 2 Calibration curve of the constant head tank system

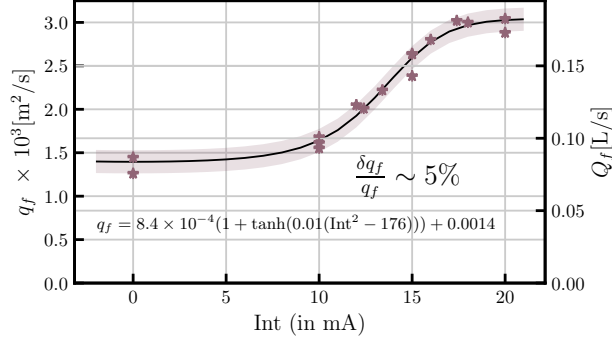


Figure D.3 – Calibration curve of the flow discharge  $q_f$  at the inlet of the flume as a function of the intensity (Int) of the electro-valve. The base flow  $q_{f,0} = 0.0014 \text{ m}^2/\text{s}$  is regulated with a manual valve. The maximum flow is  $0.003 \text{ m}^2/\text{s}$  and is reached when the electro-valve is fully open. A  $\tanh$  curve calibration scaled with the square of the Intensity permit the estimation of the flow discharge for a given Intensity. Calibration is done by filling a recipient with a measured volume.

## 3 Influence the permeable grid distance from the measure estimated with Darcy law

This Appendix is the development to obtain a quantitative estimation of  $\delta^\alpha$ , i.e. the distance from the grid where the surface flow is  $\alpha\%$  of the theoretical surface flow in a uniform situation (see Figure 4.13). The problem is posed within Darcy framework.

Let  $z_{fs}(\delta_g)$  be the free surface level at the distance  $\delta_g$ . The pressure drop between the constant air pressure on the grid and the fluid pressure at an altitude  $z$  is given by  $\Delta P(z) = P_{air} - P(z)$ , where  $P(z)$  is the static pressure  $P(z) = P_{air} + \rho_f g(z_f - z)$ .

Thus, the subsurface velocity  $U_{SSL}(z)$  at an altitude  $z$  will be both influenced by the gravity gradient and the pressure drop and can be predicted, at first approximation, by :

$$\epsilon U_{x,SSL}(z) = -\frac{K}{\rho_f \nu} \left( \frac{\Delta P(z)}{D_g} + \rho_f g i \right) \quad (\text{D.1})$$

The linear behaviour within the Darcy framework for the subsurface layer flow is not expected at the outlet where velocities increase. However, the quadratic term of the Ergün equation usually decreases the permeability and the linear approximation has for effect to overestimate the flow inside the porous bed at the outlet.

## Appendix D. Complements for the experimental procedure

---

Thus, the increase of the total subsurface flow discharge  $q_{f,h_{SSL}}$  is given as a function of  $\delta_g$ :

$$q_{f,h_{SSL}}(\delta_g) = \int_0^{h_{SSL}} \frac{Kg}{\nu} \left( \frac{z_f(\delta_g) - z}{\delta_g} + i \right) dz = \frac{Kg}{\nu} h_{SSL} \left[ \frac{h_f(\delta_g) + h_{RL} + \frac{h_{SSL}}{2}}{\delta_g} + i \right] \quad (D.2)$$

At this point, it is observed that for  $\delta_g \rightarrow +\infty$ , flow discharge in the bed tends to its expected steady value  $q_{f,h_s}^1 = \frac{Kg}{\nu} h_s i$  and the steady surface flow is given by  $q_{f,SL+RL}^1 = q_f - q_{f,SSL}^1$ .

Equation D.2 involves  $h_f(\delta)$  which is non uniform along  $x$ . To resolve this equation, a relation between surface elevation and subsurface flow discharge which is quite complex due to the non uniformity of both surface velocity and depth. Instead,  $h_{SL}$  is supposed to be negligible with respect to  $h_{SSL} + h_{RL}$ . This assumption seems reasonable since  $h_f$  is about 0 at the outlet condition. Also we must scale  $h_{RL}$  and  $h_{SSL}$ . As experimentally observed  $h_{RL} \sim d_p$  and the subsurface layer thickness is given by  $h_{SSL} \sim h_s - d_p$ , where  $h_s$  is the initial total sediment depth fixed manually.

As a next step, the distance  $\delta_g$  where the surface flow decrease is negligible is obtained. Providing the condition  $q_{f,SL} > \alpha q_{f,SL}^1$ , where  $\alpha$  is the quality coefficient (that should be close to one to obtain a nearly uniform flow), the following equation is obtained:

$$q_{f,SL}^\alpha(\delta_g^\alpha) = q_f - q_{f,h_s}(\delta_g^\alpha) = q_f - \frac{Kg}{\nu} h_s \left[ \frac{h_{RL} + \frac{h_{SSL}}{2}}{\delta_g^\alpha} + i \right] = \alpha q_{f,SL}^1 \quad (D.3)$$

The distance  $\delta^\alpha$  above which this condition is verified is then provided by:

$$\delta_g^\alpha = \left[ \frac{q_f - \alpha(q_f - \frac{Kg}{\nu} h_s i)}{\frac{Kg}{\nu} h_s} - i \right]^{-1} (d_p + (h_s - d_p)/2) \quad (D.4)$$

# E

## Vertical structure: experimental measurements and modeling

---

This Appendix compares the experimental vertical profiles with numerical simulations from 1D model. The tested runs were depicted in Chapter 5 and flow characteristics of the runs are summarized in Table 5.1. The strategy employed for the comparison was to obtain  $h_f$  such that the simulated flow discharge  $q_{f,mod}$  was equal to the experimental flow  $q_{f,exp}$  discharge. The model requires a loop to simulate several scenarios with specific hydraulic conditions until  $q_{f,mod} = q_{f,exp}$ .

Each graphical representation have been compartmentalized into 4 subplots (a) (b) (c) and (d) where 10 profiles in total have been plotted:

- (a) The mean velocity profile  $U_x$  with an indication of the modelled flow discharge per unit width  $q_{f,m}$ , the flow depth  $h_f, m$ , the surface velocity  $U_{surf,m}$ , the particle- size  $d_p$  and the bulk porosity  $\epsilon_b$ .
- (b) The porosity profile  $\epsilon$  with an indication of the slope.
- (c) The viscous  $\tau_v$ , the turbulent  $\tau_t$  and the dispersive  $\tau_d$  stresses. In this axis, the integration of the gravity  $G = \int_z^{h_f} \epsilon(z) g i dz$  is also plotted.
- (d) The viscous and pressure drag ( $f_v$  and  $f_p$ ) with the reference axis at the bottom and the mixing length distribution with the reference axis at the top. The reference mixing length function  $l_r = \kappa (z - z_{rc})$  is plotted as it represents the slope limit for  $z \rightarrow +\infty$ .

## Appendix E. Vertical structure: experimental measurements and modeling

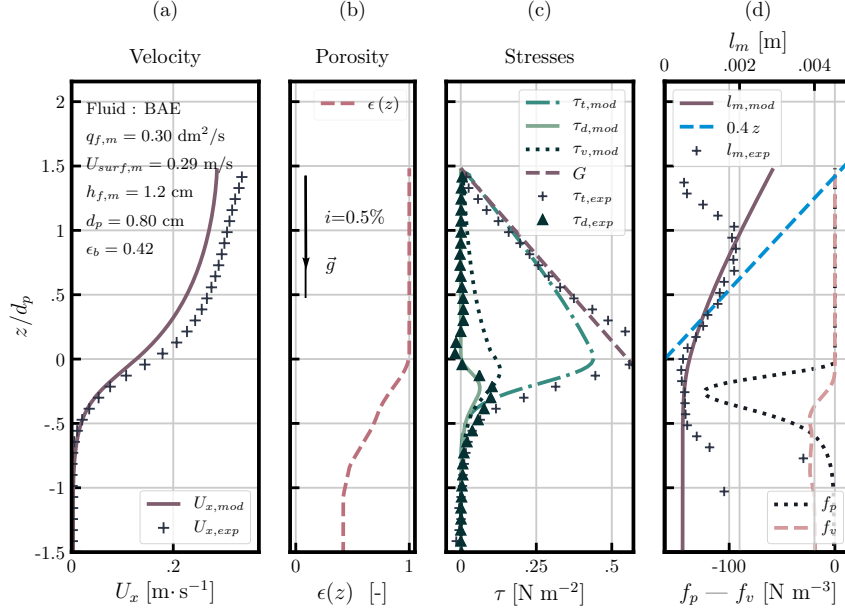


Figure E.1 – Run A1 - Simulated and measured profiles

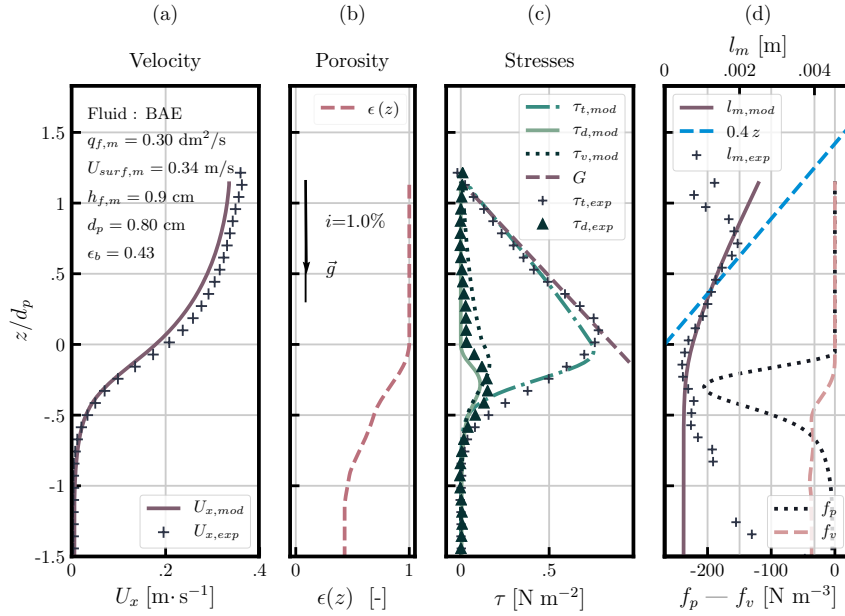


Figure E.2 – Run A2 - simulated and measured profiles

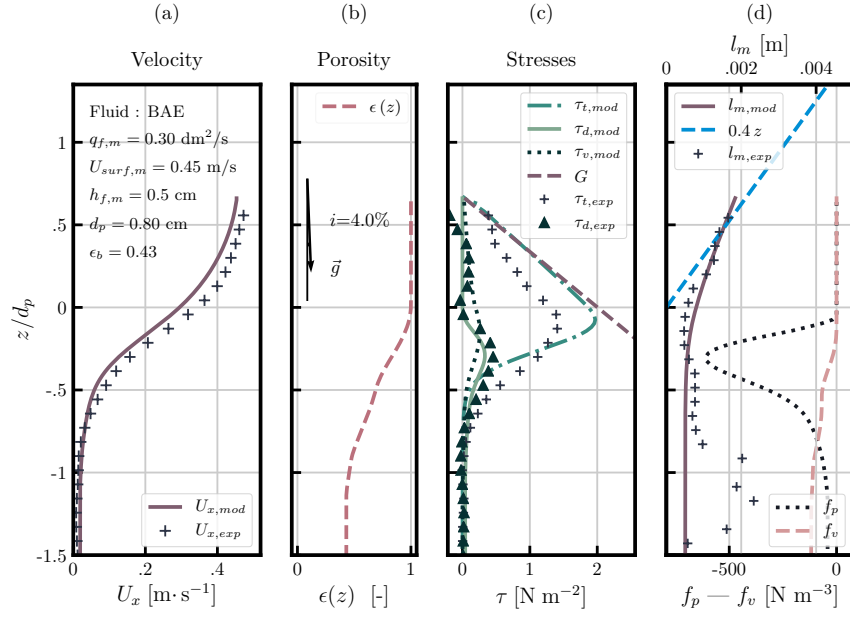


Figure E.3 – Run A4 - Simulated and measured profiles

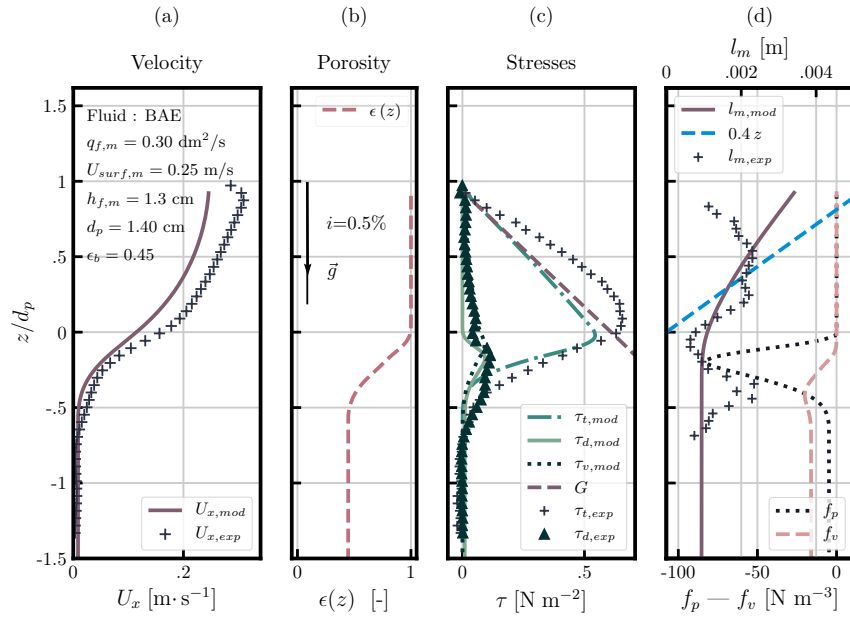


Figure E.4 – Run B1 - Simulated and measured profiles

## Appendix E. Vertical structure: experimental measurements and modeling

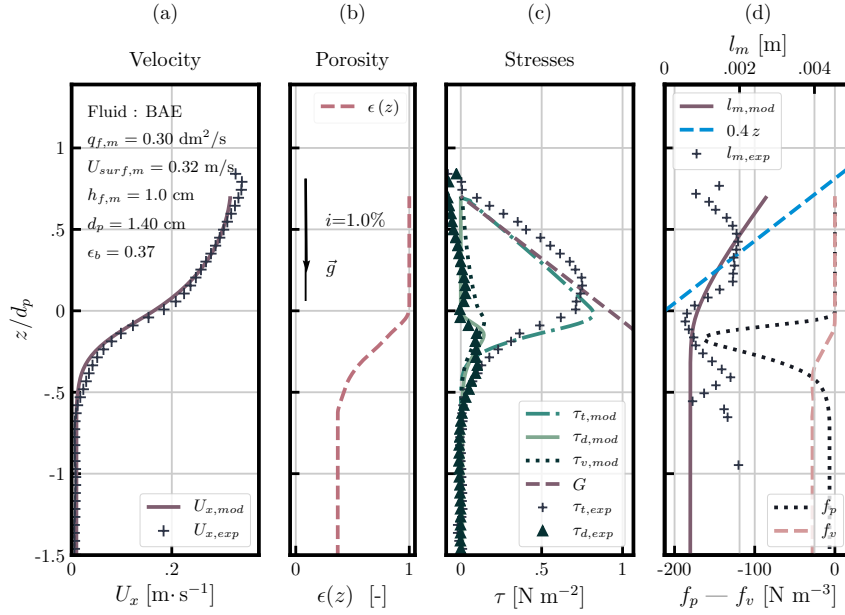


Figure E.5 – Run B2 - Simulated and measured profiles

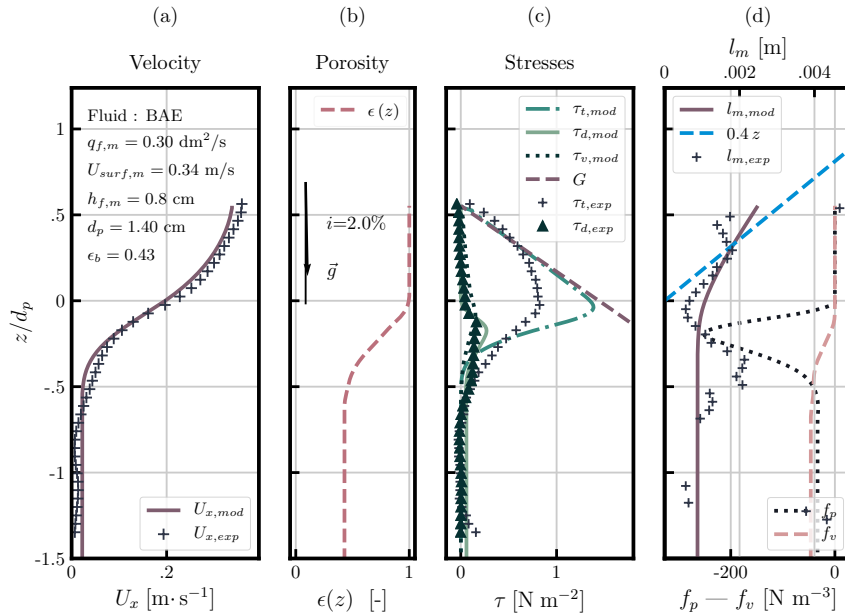


Figure E.6 – Run B3 - Simulated and measured profiles



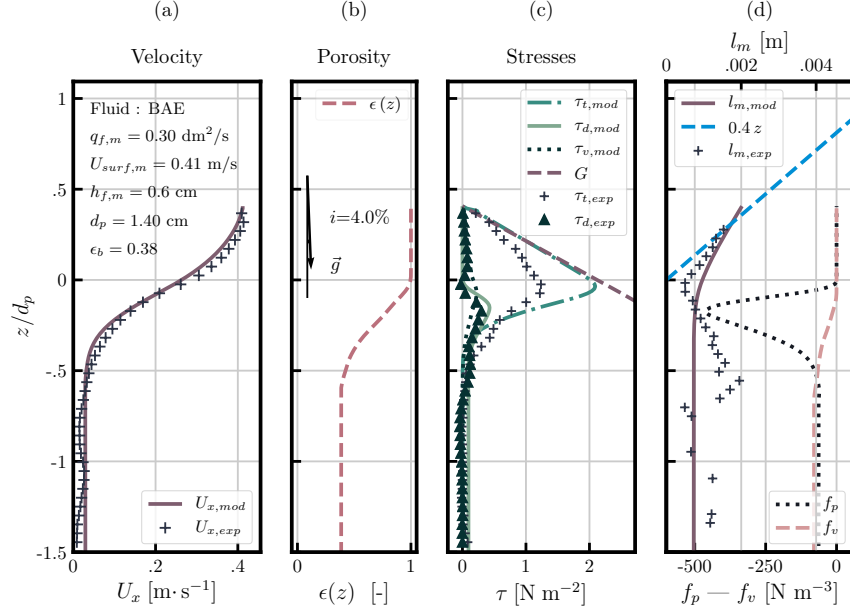


Figure E.7 – Run B4 - Simulated and measured profiles

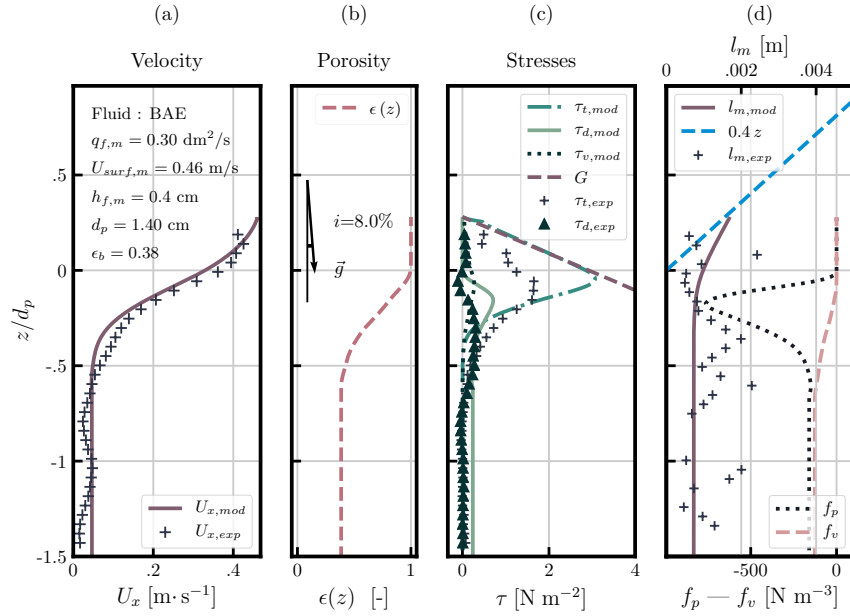


Figure E.8 – Run B5 - Simulated and measured profiles



# F

## Free surface velocity, slope, and grain size measurements in a gravel-bed river

---

### 1 Image-based velocimetry measurement of free surface flow in a gravel bed river: methodology and testing

The image velocimetry algorithm presented in Appendix C is also able to capture the convection of surface features in streams from videos. Using this method, stream surface velocities were extracted from aerial videos taken by a camera installed on a UAV (Unmanned Aerial Vehicle; commonly known as a ‘drone’). This technique was employed in Chapter 6 to estimate free surface velocities in the Navizence river. The purpose of this Appendix is to assess the reliability of this technique for providing accurate free surface velocity measurements by comparing estimates of discharge deduced from surface velocity with discharge measured at a gauging station. This technique has recently been popularized for flood monitoring, and is commonly termed Large Scale Particle Image Velocimetry (LSPIV) (Le Coz *et al.*, 2010; Dramais *et al.*, 2011).

#### 1.1 Site and region of interest

Videos of free surface flows were captured during a field campaign on the Navizence river upstream of Zinal (Wallis - Switzerland) on 20th of June 2018 at 12:00 h (just before the flood events of 2nd of July 2018, which destroyed the gauging station). The region of interest from which the free surface velocimetry was measured was placed a few meters upstream of a gauging station (see Figure F.2). This close proximity between the gauging station and site of the water surface velocimetry measurement is required to allow comparison of estimates. However, the stream gauge was under a bridge, and it was not therefore possible to directly measure the surface velocity at this location. Therefore, images were taken just upstream of the bridge. The average slope of the river was estimated at  $S \sim 4\% \pm 0.5\%$  (measurements performed on a digital terrain model; the slope measurement procedure is detailed in Section 2) and the flow was torrential  $Fr \sim 1 - 2$ . Owing to snow and glacier melt in June, the depth and discharge were higher than the annual average. The water was charged with fine sediments making the water opaque, which may have improved the quality of the measurements. Indeed, if water is clear, stones located

## Appendix F. Free surface velocity, slope, and grain size measurements in a gravel-bed river

---



Figure F.1 – Location of the gauging station

under the flow constitute motionless features that may significantly disturb the signal. The images were taken vertically from a drone flying at an altitude of 30 m (see Figure F.3).

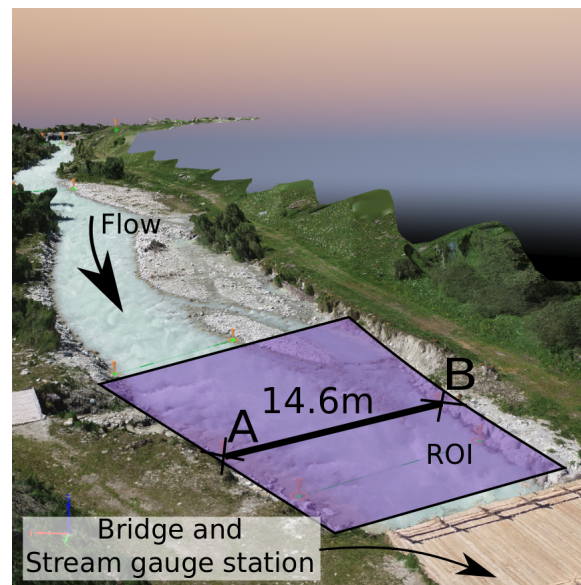


Figure F.2 – The region of interest (ROI) upstream of the stream gauge station, which was situated under a bridge. The image was extracted from a digital terrain model computed with Pix4D software.

## 1. Image-based velocimetry measurement of free surface flow in a gravel bed river: methodology and testing

---

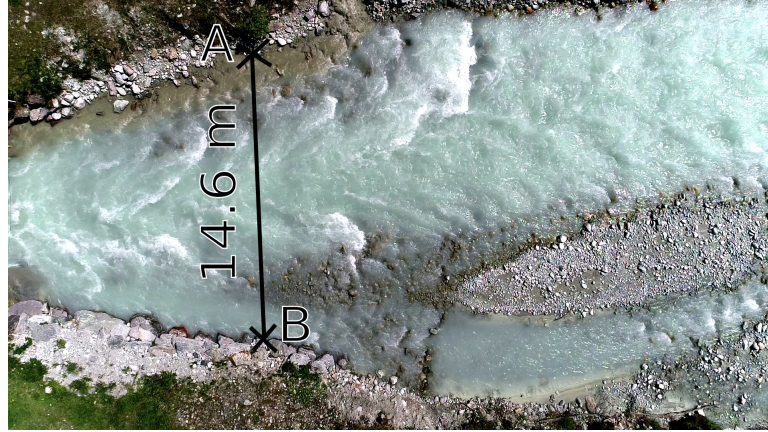


Figure F.3 – Raw image of the region of interest showing the scale  $14.6\text{m} \approx 700\text{ px}$ .

Raw image properties :

- Drone model: Phantom Pro
- View angle: vertical
- Frame per seconds (fps):  $f_{raw} = 120$
- Resolution:  $1920 \times 1080\text{ px}$
- Altitude:  $30\text{ m}$
- Focal length:  $8.8\text{ mm}$
- Scale:  $S \sim 0.020\text{ m/px}$

### 1.2 Discharge definition

The discharge at any point of the river may be defined by

$$Q = U_b W H_b^* \quad (\text{F.1})$$

where  $U_b$  is the bulk depth averaged velocity,  $W$  the bank width, and  $H_b^*$  the bulk flow depth. Here, the term bulk is employed for spatially averaged values. At the gauging station, the discharge  $Q_G$  and the flow depth  $H_{b,G}^*$  are continuously recorded. In the following developments, an estimate is provided of the discharge  $Q_D$  deduced from the drone image sequences of the stream at the gauging station. This value is then compared with  $Q_G$  to assess the reliability of the method.

### 1.3 Methodology

#### 1.3.1 Image velocimetry algorithm

The algorithm details are available in Appendix C.

#### 1.3.2 Displacement constraint

Image velocimetry processing includes constraints to optimize the process. The time interval between two consecutive images must be adjusted to provide acceptable deformations. As with classical PIV, a displacement  $D_{px}$  of 1 to 20 px between 2 frames is ideal. To respect this condition, an estimate of the minimum velocity must be provided to allow the minimum displacement between 2 frames to be deduced. In this situation, the lowest velocities  $U_{surf,min}$  occur near to the banks, and were estimated to be 0.4 m/s. To respect a minimum displacement of 1 px for these regions, the maximum processing frame rate was set to

$$f_{p,max} = \frac{U_{surf,min}}{D_{px} S} \approx 20\text{Hz}.$$

The processing frame rate is defined by  $f_p = \frac{1}{\delta t}$  the inverse of the time interval between 2 consecutive processed images. Thus,  $f_p$  was set to 12 Hz to allow the measurement of low velocities.

Note that the maximum velocity is also critical to fix the upper limit of the required rate. Here, for  $f_p = 12$ , we could measure speeds of 4.8 m/s without difficulty. However, the algorithm employed here is also suitable for larger deformations on the image (see Appendix C for details).

### 1.4 Results

#### 1.4.1 Instantaneous measurement

In Figure F.4, the results from image velocimetry processing of two consecutive images of the stream temporally spaced at  $\Delta T = \frac{1}{f_p} = 83$  ms can be visualized.

With only two consecutive images, the measure provides the correct direction of the flow and the order of magnitude expected for this type of torrential flow ( $U_{surf} \sim 2 - 3$  m/s).

#### 1.4.2 Fluctuations and estimation of the accuracy

Turbulence at the surface induces fluctuations in the velocity. Moreover, noise is also expected in this method, with sources including the relative displacement of the drone and variation in the time interval between two images. Here, the order of magnitude of the noise is estimated to provide an idea of the accuracy of the method.

The first step was to observe the standard deviation over the entire surface to identify important hot spots (A1 and B1) of fluctuation upstream of the bridge. This was accomplished

## 1. Image-based velocimetry measurement of free surface flow in a gravel bed river: methodology and testing

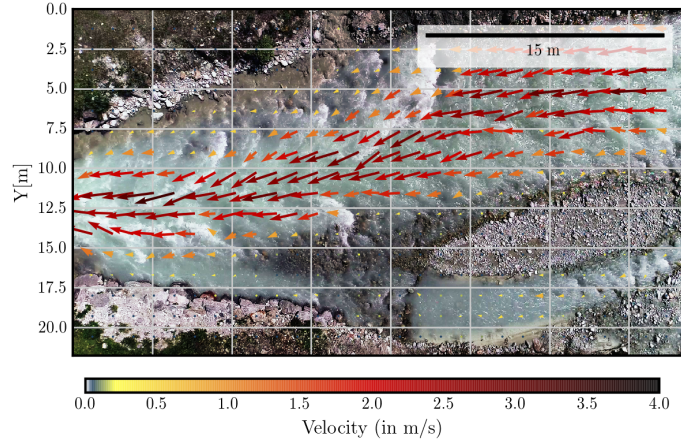


Figure F.4 – Instantaneous free surface velocity measurement performed using the image velocimetry algorithm. The instantaneous velocity is measured from two consecutive frames spaced of  $\Delta T = \frac{1}{f_p} = 83$  ms.

by looking at the spatial repartition of the standard deviations of the velocity magnitude  $\sigma_{||\mathbf{u}||}$  (see Figure F.5). The point A1 is one of the hottest spots of fluctuation in this area.

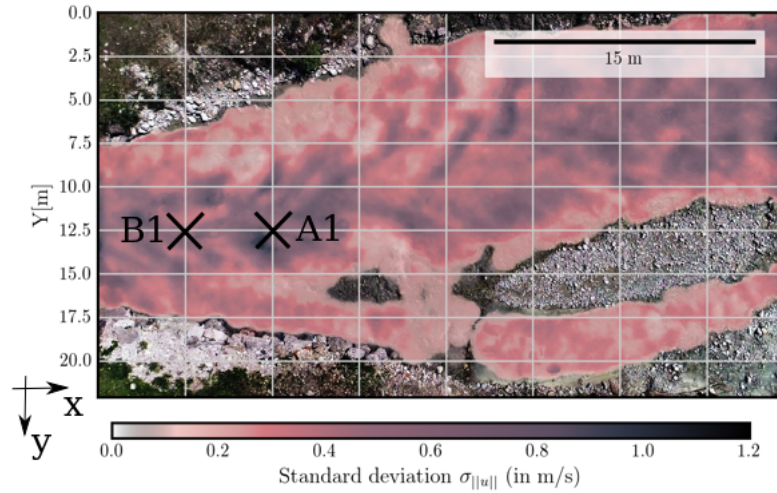


Figure F.5 – Standard deviation of the velocity magnitude calculated from the surface over a video of 9 seconds (111 pairs of images).

The second step was to observe the time evolution of the measured velocity at these hot spots to allow estimation of the probability density function (see Figure F.6). The empirical standard deviation was around  $\sigma_U \sim 0.2$  m/s for both directions. The relative accuracy was then estimated at  $\frac{\sigma_U}{U} \sim 5\%$ .

As a final step, an estimate of the minimum time needed to obtain a tolerable accuracy for the measure is given. Figure F.7 shows that the accuracy of the measure is low, even for short

## Appendix F. Free surface velocity, slope, and grain size measurements in a gravel-bed river

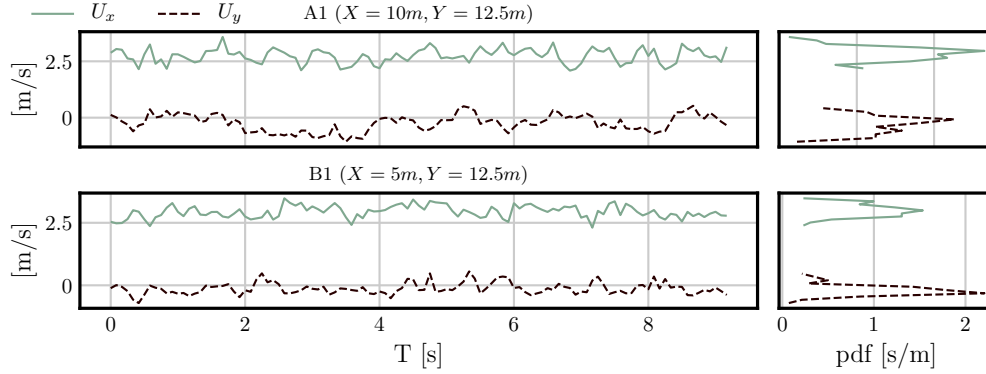


Figure F.6 – [Left] - Temporal evolution of the velocities, [right] - Probability Density Function (PDF) of the measured velocities.

recordings. Indeed, at the measurement point A1, which represents the highest fluctuation zone, the relative accuracy is about  $\sigma_e \sim 10\%$  for 0.2 s and rapidly diminishes to reach an asymptotic value of  $\sigma_e \sim 2\%$  for 2 s of measurement.

The estimated standard deviation of the empirical error as a function of the sampling time interval is plotted in Figure F.7. The empirical error is estimated by taking random samples in 9 s of record and given by  $\sigma_e(U_x, T) = \frac{1}{n} \sum_{i=0}^n \sqrt{\left( (\overline{U_x})_T^i - (\overline{U_x})_{T_{tot}} \right)^2 / (\overline{U_x})_{T_{tot}}}$ , where  $(\overline{U_x})_T^i$  is the averaged velocity estimated on  $n = 30$  samples on duration T against the empirical average calculated on  $T_{tot} = 9$  s. The uncertainty is under 2% after 2 s.

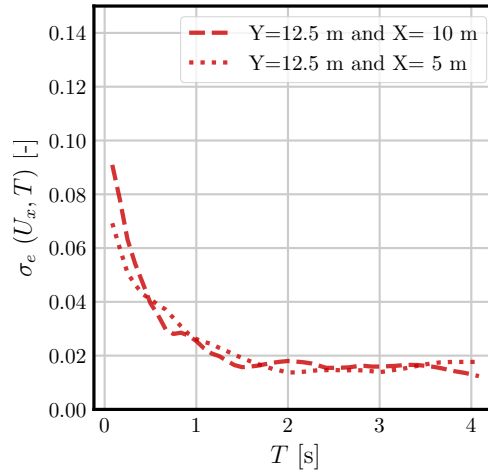


Figure F.7 – Estimated standard deviation of the empirical error as a function of the sampling time interval.



## 1. Image-based velocimetry measurement of free surface flow in a gravel bed river: methodology and testing

### 1.4.3 Measurements from the gauging station

Measurements of the water depth and estimated discharge from the gauging station are given in Figure 8. The video was recorded at 12:00 h. At a time-scale of the order of a day, this corresponds to the minimum discharge of the diurnal cycle, giving  $Q_G \approx 7.5 \text{ m}^3/\text{s}$ . In June, the discharge is highly influenced by diurnal fluctuations in temperature, because waters from snow and glacier melt are the main contributors to the total discharge.

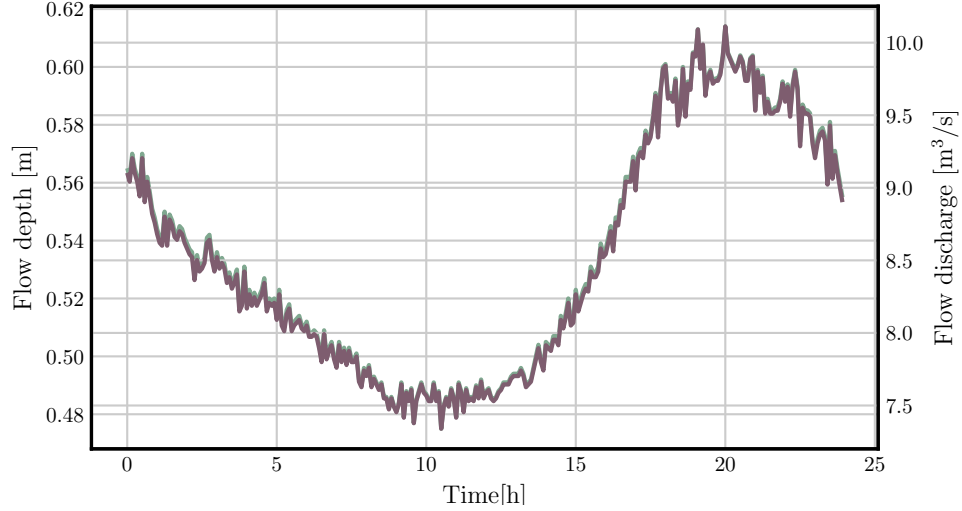


Figure F.8 – Discharge and water depth evolution on 20th of June 2018.

To estimate the discharge at the gauging station at 12:00 h from the surface velocities captured by the drone, a method must be provided to predict the velocity under the bridge.

### 1.4.4 Measurements on transverse sections upstream of the gauging station

The width of the river decreases significantly in the immediate vicinity of the bridge structure, with a funnel effect increasing the river depth and velocity. To observe this effect, five transverse sections were positioned upstream of the bridge (see Figure F.9). The velocity magnitudes were then traced for different Y positions on these transverse sections (see Figure F.10). Lower velocities are shown at the borders, while the maximum velocities corresponded with Y positions in alignment with the center of the bridge. This effect was expected, and it was also expected that the velocity under the bridge would have an equivalent profile, owing to the boundary conditions along the wall of the bridge.

An extrapolation to the surface velocities at the position of the bridge is then performed. This procedure consists of selecting the time-averaged velocities higher than 1 m/s on each transect and averaging them (See Figure F.11).

Thus, a first approximation to the free surface velocity at the gauging station can be estimated by  $\bar{U}_{surf,1} \approx 2.23 \text{ m/s}$ . A maximum value can also be given from the peak observed upstream  $\bar{U}_{surf,max} \approx 3 \text{ m/s}$ . Finally, the surface velocity is estimated from an average of these two limits

## Appendix F. Free surface velocity, slope, and grain size measurements in a gravel-bed river

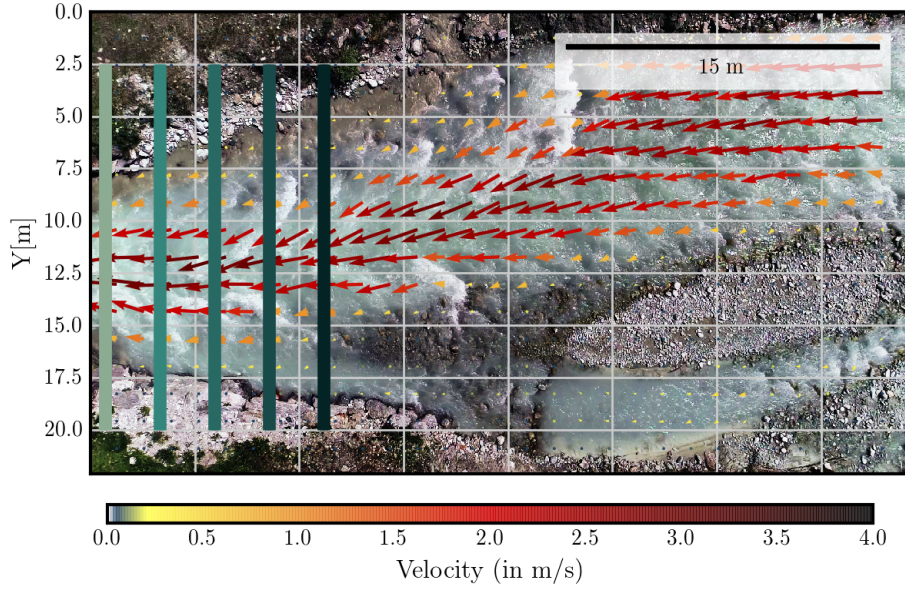


Figure F.9 – Time averaged velocity field and position of the transverse section upstream of the gauging station.

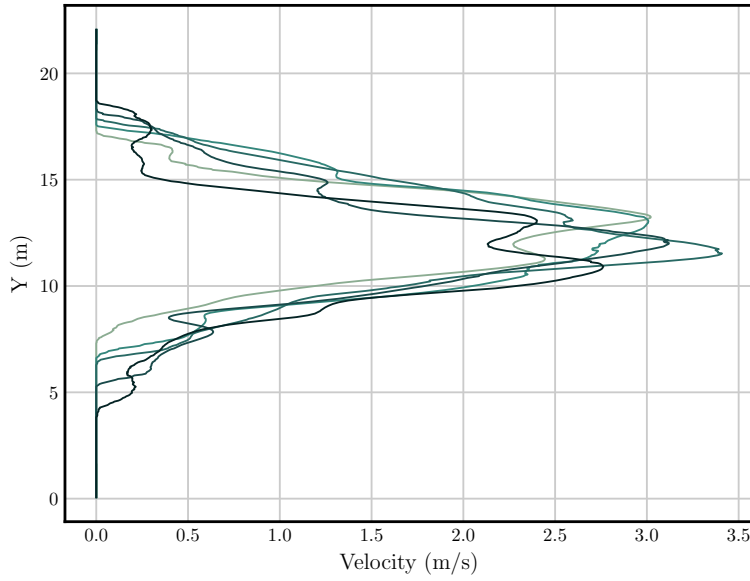


Figure F.10 – Time averaged velocities at the transverse section upstream of the gauging station.

bounded by the extreme values:  $\overline{U}_{surf} \approx 2.6 \pm 0.4$  m/s.

The bank width at the gauging station was estimated at  $W \approx 6. \pm 0.1$  m. If we consider the flow depth estimated by the gauging station at noon  $H_{12h} \approx 0.5 \pm 0.1$  m, it is possible to

## 1. Image-based velocimetry measurement of free surface flow in a gravel bed river: methodology and testing

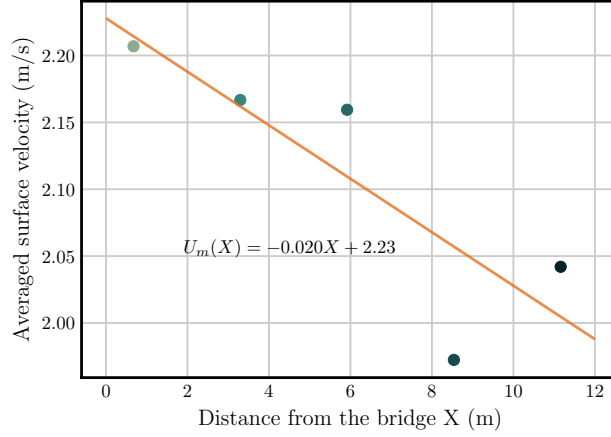


Figure F.11 – Averaged surface velocities on the transects shown in Figure F.9.

calculate the discharge by evaluating the depth-averaged velocity from Equation F.1.

### 1.4.5 From the surface velocity to the depth-averaged velocity

In Equation F.1, computation of the discharge from the videos requires an estimate of the depth averaged velocity  $U_b$  deduced from the free surface velocity measurement  $U_{surf}$ . The ratio of these two velocities defines what is usually called the *velocity coefficient*  $\alpha = U_b/U_{surf}$ . This value is usually set at 0.85, but no consensus on this coefficient is available for steep streams (Dramais *et al.*, 2011). This value is highly dependent on the relative submergence as shown by Welber *et al.* (2016).

As a first approximation,  $\alpha$  was deduced from the logarithmic profile using the Keulegan calibration (details on the log-law of the wall are provided in Chapter 2):

$$\alpha_{Keul} = \frac{\langle \bar{U} \rangle_z}{\bar{U}_{surf}} \approx \left( 1 - \frac{1}{\ln(12.2 H_b/D_{50})} \right) \quad (F.2)$$

While the gauging station monitors a gravel bed river, hydraulic conditions at the gauging station emplacement are not those of the flow in the natural stream. At the gauging station, the water flows over a concrete weir, and the roughness is therefore locally very low and the submergence high. Thus, with  $H_b \sim H_{12h} \approx 0.5 \pm 0.1$  m and  $D_{50} \approx 10$  cm,  $\alpha_{Keul1} = 0.76$  and  $D_{50} \approx 1$  cm  $\alpha_{Keul2} = 0.85$ .

Note that with this approach, the submergence also has a critical influence on  $\alpha$ . However, this methodology, which is based on a fully vertical logarithmic profile, underestimates the depth-averaged velocity. Indeed, the assumption behind the logarithmic profile states that the mixing length, which regulates the intensity of the vertical exchanges, is proportional to the distance from the bed. However, various effects tend to reduce this mixing length value, such as the damping effect and the velocity defect law *damping effect* or the *velocity defect law* (Nezu &

## Appendix F. Free surface velocity, slope, and grain size measurements in a gravel-bed river

---

Rodi, 1986; Pope, 2001). With these effects, the apparent turbulent viscosity near the wall and near the free surface are in reality lower than the values predicted by the log-law assumptions. Consequently, the difference between  $U_b$  and  $U_{surf}$  is lower than predicted by the log-law.

In these conditions, a numerical simulation that directly solves the double-averaged momentum equation was employed (see Chapter 3 for the details of the model), with  $D_{50}$  set at 0.05 cm, which is an intermediate diameter between the averaged median grain size of the river bed (measured in Section 3) and the lower roughness size of the concrete weir. In such conditions, it was shown in Chapter 6 that  $\alpha_{model} = \langle \overline{U}_{model} \rangle_z \approx 0.85 \overline{U}_{surf,model}$ .

$\alpha = 0.85$  is indeed the ratio between the surface and depth-averaged velocity for a regular intermediate submergence  $S_m \sim 1 - 30$ . It must be emphasized that this value for a high relative submergence at the gauging station is not expected upstream, e.g., in the riffle region. In these zones,  $\alpha$  may show important deviations from 0.9, as highlighted by Welber *et al.* (2016) and discussed in Chapter 6.

The predictions for the log law and the model give:

$$\begin{aligned} Q_{D,12h,Keul1} &= 0.76 \overline{U}_{surf} W H_{12h} \approx 5.7 \pm 0.8 \text{ m}^3/\text{s} \\ Q_{D,12h,model} &= Q_{D,12h,Keul2} = 0.85 \overline{U}_{surf} W H_{12h} \approx 6.63 \pm 0.8 \text{ m}^3/\text{s} \end{aligned}$$

The inaccuracy of  $\pm 0.8 \text{ m}^3/\text{s}$  is due to inaccuracies in the extrapolated surface velocity under the bridge. These two estimates must be compared with the estimation at the station, which gives  $Q_G \approx 7.7 \text{ m}^3/\text{s}$ .

### 1.5 Conclusions on the evaluation

While the inaccuracy on  $Q_D$  is high, a similar order of magnitude is observed between discharges estimated from the gauging station and discharges estimated by the relation  $\langle \overline{U} \rangle_z \approx 0.85 \overline{U}_{surf}$ , confirming the ability of the image-based methodology to provide surface velocities within the correct order of magnitude. This also verifies the coherence with the model predictions and the 0.85 factor prescribed for intermediate submergence flows by fluvial engineers. However, the discharge given by the gauging station is also subject to inaccuracy, and no information on this is detailed here. To conclude with this comparison, it is recalled that this estimate is highly dependent on the velocity extrapolations under the bridge, and further explorations are needed to more precisely determine accuracy.

## 2 Estimation of local slopes

In this section, another region of the river upstream from the gauging station is considered, at the site where the velocity measurements in Chapter 6 were made. For a region of interest in the river, the slope was manually estimated using the *Pix4D-mapper* software (Vallet *et al.*, 2011). This software allows the extraction of 3D coordinates  $M(x_m, y_m, z_m)$  from the Digital

Terrain Model (DTM)<sup>1</sup>.

It was not possible to create 3D reconstructions under the surface of the water from the raw images taken by the drone. In general, 3D under water reconstruction is a recurrent problem, even for transparent and still water, where diffraction considerably affects the measurement. Consequently, it was not possible to obtain the slope from bottom bed measurements. Nevertheless, the elevations of the banks at the vicinity of the running water are given with a relatively good accuracy. Under the assumption that the averaged gradient of the bank and the bed follow the same trend, the bed slope can be estimated.

With regard to accuracy, estimates of the dimensions of objects on preliminary measurements on the DTM using conventional rules revealed an error of  $\delta x = \delta y = \pm 0.02$  m for the  $x$  and  $y$  coordinates. For the elevation  $z$ , two sources of error have been identified. The first is caused by imprecision in the 3D reconstruction method, and the second is human-related, as we must decide which point represents the local elevation of the bank. Combining these two sources of error, an inaccuracy of  $\delta z = \pm 0.1$  m is considered along the  $z$  coordinate.

To obtain a qualitative estimate of the slope at one transect, we manually consider two pairs of points in the proximity of the transect on the left and right banks. For each bank, we estimate the slope by comparing the coordinates of the two points, one downstream, and a second one upstream of the transect.

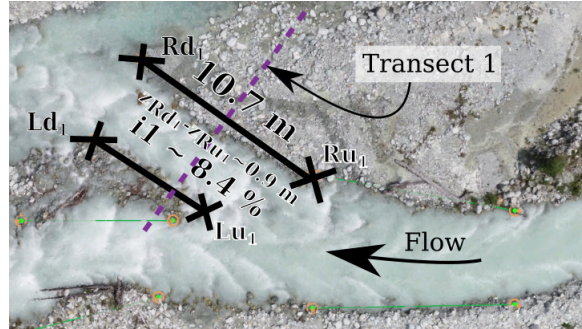


Figure F.12 – Measurement of the local slope using the Pix4D mapping software

Figure F.12 is a screen shot of the *Pix4D software* during the measurement procedure showing the different lines over which the slope was measured. We here focus on measurement of the slope of Transect 1, the arm of the river situated in the upper left of the image. On the right bank of the river arm we measured two points, one downstream,  $Rd1(x_{Rd1}, y_{Rd1}, z_{Rd1})$ , and one upstream,  $Ru1(x_{Ru1}, y_{Ru1}, z_{Ru1})$ .

The distance between the two points is given by  $D_{R1,u-d} = \sqrt{(x_{Rd1} - x_{Ru1})^2 + (y_{Rd1} - y_{Ru1})^2}$

<sup>1</sup>The DTM has been computed with *Pix4D-mapper* from drone (UAV) aerial photographs. The drone used was the same model used recorded the videos for the free surface velocity estimates. It is made from photography taken at regular intervals from the sky. 3D mapping is deduced using 3D reconstruction from multiple image method (aero-triangulation) and computer vision algorithm such as feature matching by machine learning methods to identify points with the same absolute location from different images (Vallet *et al.*, 2011)

## Appendix F. Free surface velocity, slope, and grain size measurements in a gravel-bed river

The slope on the right bank is estimated by the formula:

$$i_{1R} = \frac{D_{R1,u-d}}{(z_{Ru1} - z_{Rd1})} \quad (\text{F.3})$$

The same procedure is performed on the left bank to obtain  $i_{1L}$ .

The average slope is given by the average of the two slopes, i.e.,  $i_1 = \frac{i_{1R} + i_{1L}}{2}$ .

The inaccuracy in the estimation of the slope is large, being dominated by the inaccuracy on the vertical axis, and is given by  $\frac{\delta(i)}{i} \sim \frac{\delta z}{(z_{Ru1} - z_{Rd1})} \sim \frac{1}{10} \sim 10\%$ .

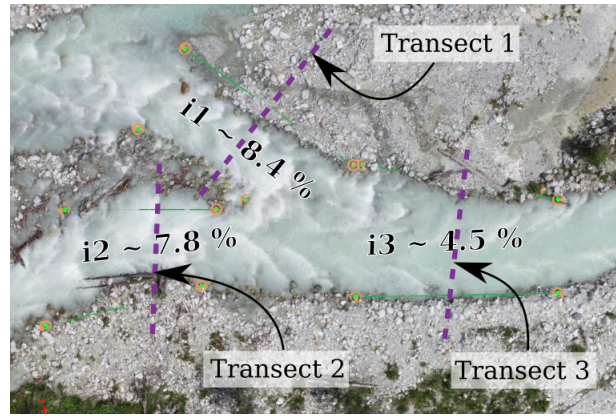


Figure F.13 – Estimates of 3 local slopes by employing the Pix4D mapping software

### 3 Grain-size distribution and median grain diameter

The average grain diameter in the river bed was estimated from the raw images acquired by the drone and used to build the digital terrain model. These images have a resolution of 1.3 cm/px, which is sufficient to measure the size of the stones. A dead arm proximal to the running water and close to the region of interest was selected. The average diameter in this region was bigger than the estimated average diameter on the banks, and was a better representation of the size of the obstacles in interaction with the running water. A total of 148 grain diameters were measured with a tool developed on Python that allows the minor and major axis of each particle to be measured. Figure 14 shows circular regions with equivalent areas to the measured particles. Particles under 5 cm in diameter were too small to be measured, and the grain-size distribution is therefore likely to be overestimated. As  $D_{84}$ <sup>2</sup> is commonly employed to determine the roughness length of gravel bed rivers, we suppose that the overestimation of  $D_{50}$  provides a satisfying estimation of the bed roughness length. In this region, the  $D_{50}$  is estimated at 0.58 m.

<sup>2</sup>The grain diameter for which 84% of the grains in mass are below this value.



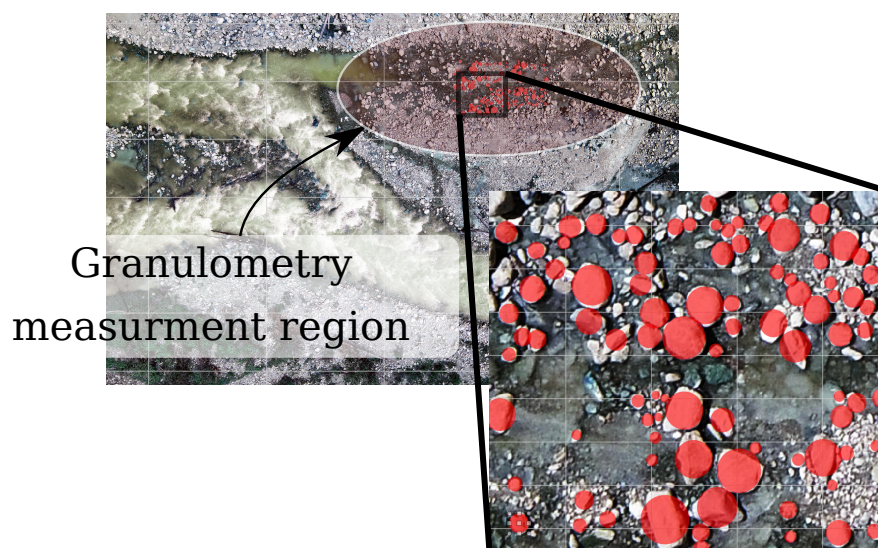


Figure F.14 – The region of interest in which the river bed grain sizes were measured was located in the dead arm. The red disks represent the area covered by the selected individual measured stones.

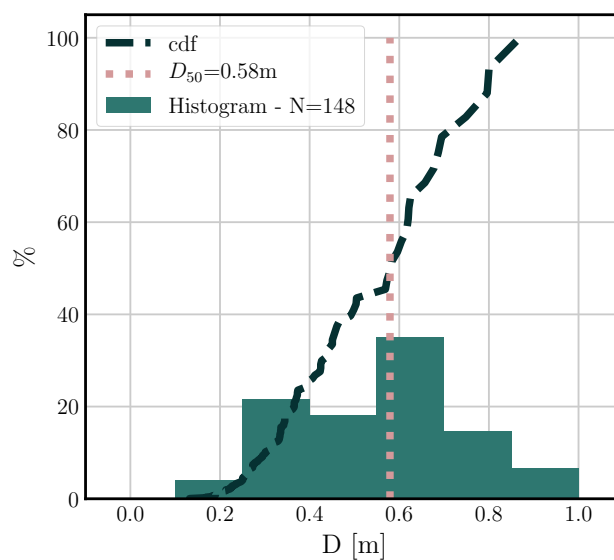


Figure F.15 – Particle size distribution in the dead arm and mass median grain diameter estimated at  $D_{50} = 0.58$  m.





## Bibliography

---

- AGUIRRE-PE, J. & FUENTES, R. 1990 Resistance to flow in steep rough streams. *Journal of Hydraulic Engineering* **116** (11), 1374–1387.
- ANDERSON, T. B. & JACKSON, R. 1967 Fluid mechanical description of fluidized beds. equations of motion. *Industrial & Engineering Chemistry Fundamentals* **6** (4), 527–539.
- BATHURST, J. C. 1985 Flow resistance estimation in mountain rivers. *Journal of Hydraulic Engineering* **111** (4), 625–643.
- BAYAZIT, M. 1976 Free surface flow in a channel of large relative roughness. *Journal of Hydraulic Research* **14** (2), 115–126.
- BEAVERS, G. S. & JOSEPH, D. D. 1967 Boundary conditions at a naturally permeable wall. *Journal of fluid mechanics* **30** (1), 197–207.
- BENCALA, K. E. & WALTERS, R. A. 1983 Simulation of solute transport in a mountain pool-and-riffle stream: A transient storage model. *Water Resources Research* **19** (3), 718–724.
- BLOIS, G., BEST, J. L., SAMBROOK SMITH, G. H. & HARDY, R. J. 2014 Effect of bed permeability and hyporheic flow on turbulent flow over bed forms. *Geophysical Research Letters* **41** (18), 6435–6442.
- BOANO, F., HARVEY, J. W., MARION, A., PACKMAN, A. I., REVELLI, R., RIDOLFI, L. & WÖRMAN, A. 2014 Hyporheic flow and transport processes: Mechanisms, models, and biogeochemical implications. *Reviews of Geophysics* **52** (4), 603–679, arXiv: <https://agupubs.onlinelibrary.wiley.com/doi/pdf/10.1002/2012RG000417>.
- BOUGUET, J.Y. 2001 Pyramidal implementation of the affine lucas kanade feature tracker description of the algorithm. *Intel Corporation* **5** (1-10), 4.
- BOUTIER, A. 2012 Vélocimétrie laser pour la mécanique des fluides. *Hermes Science-Lavoisier* .
- BRAHMS, A. 1757 *Anfangsgründe der Deich-und Wasserbaukunst*, , vol. 1. bey Herman Tapper.
- BREUGEM, W.P., BOERSMA, B.J. & UITTENBOGAARD, R.E. 2006 The influence of wall permeability on turbulent channel flow. *Journal of Fluid Mechanics* **562**, 35–72.
- BRINKMAN, H.C. 1949 A calculation of the viscous force exerted by a flowing fluid on a dense swarm of particles. *Applied Scientific Research* **1** (1), 27–34.

## Bibliography

---

- BROWN, G. O. 2003 The history of the darcy-weisbach equation for pipe flow resistance. In *Environmental and Water Resources History*, pp. 34–43. p.
- BUFFINGTON, J. M. & MONTGOMERY, D. R. 1997 A systematic analysis of eight decades of incipient motion studies, with special reference to gravel-bedded rivers. *Water Resources Research* **33** (8), 1993–2029.
- CAMERON, S. M., NIKORA, V. I. & STEWART, M. T. 2017 Very-large-scale motions in rough-bed open-channel flow. *Journal of Fluid Mechanics* **814**, 416–429.
- CHAPUIS, R. P. 2004 Predicting the saturated hydraulic conductivity of sand and gravel using effective diameter and void ratio. *Canadian geotechnical journal* **41** (5), 787–795.
- CHARRU, F. 2011 *Hydrodynamic instabilities*, , vol. 37. Cambridge University Press.
- CHEN, K., LIN, Y. & TU, C. 2012 Densities, viscosities, refractive indexes, and surface tensions for mixtures of ethanol, benzyl acetate, and benzyl alcohol. *Journal of Chemical & Engineering Data* **57** (4), 1118–1127.
- CHENG, ZHEN, HSU, TIAN-JIAN & CHAUCHAT, JULIEN 2018 An eulerian two-phase model for steady sheet flow using large-eddy simulation methodology. *Advances in Water Resources* **111**, 205–223.
- COLEMAN, N. 1981 Velocity profiles with suspended sediment. *Journal of Hydraulic Research* **19** (3), 211–229.
- COLES, D. 1956 The law of the wake in the turbulent boundary layer. *Journal of Fluid Mechanics* **1** (2), 191–226.
- COLOMBINI, M. & STOCCHINO, A. 2012 Three-dimensional river bed forms. *Journal of Fluid Mechanics* **695**, 63–80.
- DARCY, HENRY PHILIBERT GASPARD 1856 *Les Fontaines publiques de la ville de Dijon. Exposition et application des principes à suivre et des formules à employer dans les questions de distribution d'eau, etc.* V. Dalamont.
- DETERT, M., NIKORA, V. & JIRKA, G. 2010 Synoptic velocity and pressure fields at the water–sediment interface of streambeds. *Journal of Fluid Mechanics* **660**, 55–86.
- DEY, S. & DAS, R. 2012 Gravel-bed hydrodynamics: double-averaging approach. *Journal of Hydraulic Engineering* **138** (8), 707–725.
- DI FELICE, R. 1994 The voidage function for fluid-particle interaction systems. *International Journal of Multiphase Flow* **20** (1), 153–159.
- DRAMAIS, G., LE COZ, J., CAMENEN, B.T & HAUET, A. 2011 Advantages of a mobile lspiv method for measuring flood discharges and improving stage–discharge curves. *Journal of Hydro-Environment Research* **5** (4), 301–312.
- VAN DRIEST, E. R. 1956 On turbulent flow near a wall. *Journal of the Aeronautical Sciences* **23** (11), 1007–1011.
- DURÁN, O., ANDREOTTI, B. & CLAUDIN, P. 2012 Numerical simulation of turbulent sediment transport, from bed load to saltation. *Physics of Fluids* **24** (10), 103306.

- ELLIOTT, A. H. & BROOKS, N. H. 1997 Transfer of nonsorbing solutes to a streambed with bed forms: Theory. *Water Resources Research* **33** (1), 123–136.
- ERGUN, S. 1952 Fluid flow through packed columns. *Chem. Eng. Prog.* **48**, 89–94.
- FANG, H., HAN, X., HE, G. & DEY, S. 2018 Influence of permeable beds on hydraulically macro-rough flow. *Journal of Fluid Mechanics* **847**, 552–590.
- FERGUSON, R. 2007 Flow resistance equations for gravel- and boulder-bed streams. *Water Resources Research* **43** (5), arXiv: <https://agupubs.onlinelibrary.wiley.com/doi/pdf/10.1029/2006WR005422>.
- FERGUSON, R. 2012 River channel slope, flow resistance, and gravel entrainment thresholds. *Water Resources Research* **48** (5).
- FOX, ARYEH, BOANO, FULVIO & ARNON, SHAI 2014 Impact of losing and gaining streamflow conditions on hyporheic exchange fluxes induced by dune-shaped bed forms. *Water Resources Research* **50** (3), 1895–1907.
- GAO, MING, PRADHANA, ANDRE, HAN, XUCHEN, GUO, QI, KOT, GRANT, SIFAKIS, EFTYCHIOS & JIANG, CHENFANFU 2018 Animating fluid sediment mixture in particle-laden flows. *ACM Transactions on Graphics (TOG)* **37** (4), 149.
- GAUDIO, R., MIGLIO, A. & DEY, S. 2010 Non-universality of von kármán’s  $\kappa$  in fluvial streams. *Journal of Hydraulic Research* **48** (5), 658–663.
- GHISALBERTI, M. & NEPF, H. 2004 The limited growth of vegetated shear layers. *Water Resources Research* **40** (7).
- GHISALBERTI, M. & NEPF, H. 2009 Shallow flows over a permeable medium: the hydrodynamics of submerged aquatic canopies. *Transport in porous media* **78** (2), 309.
- GIBILARO, L., DI FELICE, R., WALDRAM, S. P. & FOSCOLO, P. U. 1985 Generalized friction factor and drag coefficient correlations for fluid-particle interactions. *Chemical engineering science* **40** (10), 1817–1823.
- GRIFFITHS, G. A. 1981 Flow resistance in coarse gravel bed rivers. *Journal of the Hydraulics Division* **107** (7), 899–918.
- HEITZ, DOMINIQUE, MÉMIN, ETIENNE & SCHNÖRR, CHRISTOPH 2010 Variational fluid flow measurements from image sequences: synopsis and perspectives. *Experiments in fluids* **48** (3), 369–393.
- HERSCHEL, C. 1897 *115 Experiments on the Carrying Capacity of Large, Riveted, Metal Conduits, Up to Six Feet Per Second of Velocity of Flow*. Wiley.
- HEY, R. 1979 Flow resistance in gravel-bed rivers. *Journal of the Hydraulics Division* **105** (4), 365–379.
- HO, R. T. & GELHAR, L. 1973 Turbulent flow with wavy permeable boundaries. *Journal of Fluid Mechanics* **58** (2), 403–414.
- HOWES, F. & WHITAKER, S. 1985 The spatial averaging theorem revisited. *Chemical engineering science* **40** (8), 1387–1392.

## Bibliography

---

- JACKSON, R. 2000 *The dynamics of fluidized particles*. Cambridge University Press.
- JENKINS, J. & HANES, D. 1998 Collisional sheet flows of sediment driven by a turbulent fluid. *Journal of Fluid Mechanics* **370**, 29–52.
- KÄHLER, C., ASTARITA, T., VLACHOS, P., SAKAKIBARA, J., HAIN, R., DISCETTI, S., LA FOY, R. & CIERPKA, C. 2016 Main results of the 4th international PIV challenge. *Experiments in Fluids* **57** (6), 97.
- KEULEGAN, G. 1938 *Laws of turbulent flow in open channels*, , vol. 21. National Bureau of Standards US.
- KEYLOCK, C. 2015 Flow resistance in natural, turbulent channel flows: The need for a fluvial fluid mechanics. *Water Resources Research* **51** (6), 4374–4390.
- KOLL, K. 2006 Parameterisation of the vertical velocity profile in the wall region over rough surfaces. In *River flow*, pp. 163–172. Taylor & Francis.
- KROGSTAD, P. A. 1991 Modification of the van driest damping function to include the effects of surface roughness. *AIAA journal* **29** (6), 888–894.
- LAMB, M., BRUN, F. & FULLER, B. 2017 Hydrodynamics of steep streams with planar coarse-grained beds: Turbulence, flow resistance, and implications for sediment transport. *Water Resources Research* **53** (3), 2240–2263.
- LAMB, M., DIETRICH, W. & VENDITTI, J. 2008 Is the critical shields stress for incipient sediment motion dependent on channel-bed slope? *Journal of Geophysical Research: Earth Surface* **113** (F2).
- LE COZ, J., HAUET, A., PIERREFEU, G., DRAMAIS, G. & CAMENEN, B. 2010 Performance of image-based velocimetry (LSPIV) applied to flash-flood discharge measurements in mediterranean rivers. *Journal of hydrology* **394** (1-2), 42–52.
- LEAL, L. 2007 *Advanced transport phenomena: fluid mechanics and convective transport processes*, , vol. 7. Cambridge University Press.
- LEVA, M. 1959 *Fluidization*. McGraw-Hill.
- LI, L. & SAWAMOTO, M. 1995 Multi-phase model on sediment transport in sheet-flow regime under oscillatory flow. *Coastal Engineering in Japan* **38** (2), 157–178.
- LIÉBAULT, F. & PIÉGAY, H. 2001 Assessment of channel changes due to long-term bedload supply decrease, roubion river, france. *Geomorphology* **36** (3-4), 167–186.
- LIU, T. & SHEN, L. 2008 Fluid flow and optical flow. *Journal of Fluid Mechanics* **614**, 253–291.
- DE MARSILY, G. 1986 Quantitative hydrogeology. *Tech. Rep.*. Paris School of Mines, Fontainebleau.
- MAURIN, RAPHAËL, CHAUCHAT, JULIEN, CHAREYRE, BRUNO & FREY, PHILIPPE 2015 A minimal coupled fluid-discrete element model for bedload transport. *Physics of Fluids* **27** (11), 113302.
- MAURIN, R., CHAUCHAT, J. & FREY, P. 2016 Dense granular flow rheology in turbulent bedload transport. *Journal of Fluid Mechanics* **804**, 490–512.

- MAURIN, R., CHAUCHAT, J. & FREY, P. 2018 Revisiting slope influence in turbulent bedload transport: consequences for vertical flow structure and transport rate scaling. *Journal of Fluid Mechanics* **839**, 135–156.
- MEI, C. & AURIAULT, J. 1991 The effect of weak inertia on flow through a porous medium. *Journal of Fluid Mechanics* **222**, 647–663.
- MENDOZA, C. & ZHOU, D. 1992 Effects of porous bed on turbulent stream flow above bed. *Journal of Hydraulic Engineering* **118** (9), 1222–1240.
- MIGNOT, E.L., BARTHELEMY, E. & HURTER, D. 2009*a* Double-averaging analysis and local flow characterization of near-bed turbulence in gravel-bed channel flows. *Journal of Fluid Mechanics* **618**, 279–303.
- MIGNOT, E., BARTHÉLEMY, E. & HURTER, D. 2009*b* Double-averaging analysis and local flow characterization of near-bed turbulence in gravel-bed channel flows. *Journal of Fluid Mechanics* **618**, 279–303.
- MIGNOT, E., HURTER, D. & BARTHÉLEMY, E. 2009*c* On the structure of shear stress and turbulent kinetic energy flux across the roughness layer of a gravel-bed channel flow. *Journal of Fluid Mechanics* **638**, 423–452.
- MIOZZI, M., JACOB, B. & OLIVIERI, A. 2008 Performances of feature tracking in turbulent boundary layer investigation. *Experiments in fluids* **45** (4), 765.
- MUNOZ G., ROBERTO J. & GELHAR, L. 1968 Turbulent pipe flow with rough and porous walls. PhD thesis, Massachusetts Institute of Technology, Dept. of Civil Engineering.
- MUSKAT, M. & MERES, M. 1936 The flow of heterogeneous fluids through porous media. *Physics* **7** (9), 346–363.
- NEZU, I. 1977 Turbulent structure in open-channel flows. PhD thesis, Kyoto university.
- NEZU, I. 2005 Open-channel flow turbulence and its research prospect in the 21st century. *Journal of Hydraulic Engineering* **131** (4), 229–246.
- NEZU, I. & NAKAGAWA, H. 1993 Turbulence in open channels. *IAHR/AIRH Monograph. Balkema, Rotterdam, The Netherlands*.
- NEZU, I. & RODI, W. 1986 Open-channel flow measurements with a laser doppler anemometer. *Journal of Hydraulic Engineering* **112** (5), 335–355.
- NI, W.-J. & CAPART, H. 2015 Cross-sectional imaging of refractive-index-matched liquid-granular flows. *Experiments in Fluids* **56** (8), 163.
- NIELD, D. & BEJAN, A. 2006 *Convection in porous media*, , vol. 3. Springer.
- NIKORA, V., GORING, D., MCEWAN, I. & GRIFFITHS, G. 2001 Spatially averaged open-channel flow over rough bed. *Journal of Hydraulic Engineering* **127** (2), 123–133.
- NIKORA, V., MCEWAN, I., MCLEAN, S., COLEMAN, S., POKRAJAC, D. & WALTERS, R. 2007 Double-averaging concept for rough-bed open-channel and overland flows: Theoretical background. *Journal of Hydraulic Engineering* **133** (8), 873–883.

## Bibliography

---

- NIKURADSE, J. 1933 Gesetzmäßigkeiten der turbulenten Strömung in glatten Röhren (nachtrag). *Forschung im Ingenieurwesen* **4** (1), 44–44.
- NIVEN, R. 2002 Physical insight into the Ergün and Wen & Yu equations for fluid flow in packed and fluidised beds. *Chemical Engineering Science* **57** (3), 527–534.
- NOVAK, M., WARLAND, J., ORCHANSKY, A., KETLER, R. & GREEN, S. 2000 Wind tunnel and field measurements of turbulent flow in forests. part i: uniformly thinned stands. *Boundary-Layer Meteorology* **95** (3), 457–495.
- OCHOA-TAPIA, J. & WHITAKER, S. 1995 Momentum transfer at the boundary between a porous medium and a homogeneous fluid—i. theoretical development. *International Journal of Heat and Mass Transfer* **38** (14), 2635–2646.
- OURIEMI, M., AUSSILLOUS, P. & GUZZELLI, E. 2009 Sediment dynamics. part 1. bed-load transport by laminar shearing flows. *Journal of Fluid Mechanics* **636**, 295–319.
- PAINTAL, A. S. 1971 A stochastic model of bed load transport. *Journal of Hydraulic Research* **9** (4), 527–554.
- PETIT, L., HULIN, J.-P. & GUYON, É. 2012 *Hydrodynamique physique 3e édition (2012)*. EDP sciences.
- POKRAJAC, D., FINNIGAN, J. J., MANES, C., MCEWAN, I. & NIKORA, V. 2006 On the definition of the shear velocity in rough bed open channel flows. In *River flow*, , vol. 1, pp. 89–98.
- POKRAJAC, D., MANES, C. & MCEWAN, I. 2007 Peculiar mean velocity profiles within a porous bed of an open channel. *Physics of Fluids* **19** (9), 098109.
- POPE, S. 2001 Turbulent flows.
- PRANCEVIC, J. & LAMB, M. 2015 Unraveling bed slope from relative roughness in initial sediment motion. *Journal of Geophysical Research: Earth Surface* **120** (3), 474–489.
- DE PRONY, R. 1804 *Recherches physico-mathématiques sur la théorie des eaux courantes*. Imprimerie impériale.
- RECKING, A. 2009 Theoretical development on the effects of changing flow hydraulics on incipient bed load motion. *Water Resources Research* **45** (4).
- RECKING, A., FREY, P., PAQUIER, A., BELLEUDY, P. & CHAMPAGNE, J.-Y. 2008 Feedback between bed load transport and flow resistance in gravel and cobble bed rivers. *Water Resources Research* **44** (5).
- REVEL-BAUDARD, T. & CHAUCHAT, J. 2013 A two-phase model for sheet flow regime based on dense granular flow rheology. *Journal of Geophysical Research: Oceans* **118** (2), 619–634.
- REVEL-BAUDARD, T., CHAUCHAT, J., HURTHUR, D. & BARRAUD, P.-A. 2015 Investigation of sheet-flow processes based on novel acoustic high-resolution velocity and concentration measurements. *Journal of Fluid Mechanics* **767**, 1–30.
- RICHARD, G. & GAVRILYUK, S. 2012 A new model of roll waves: comparison with brock’s experiments. *Journal of Fluid Mechanics* **698**, 374–405.

- RICHARDSON, J. F. 1954 Sedimentation and fluidization: Part i. *Trans. Inst. Chem. Engrs.* **32**, 35–52.
- RICKENMANN, D. & RECKING, A. 2011 Evaluation of flow resistance in gravel-bed rivers through a large field data set. *Water Resources Research* **47** (7), arXiv: <https://agupubs.onlinelibrary.wiley.com/doi/pdf/10.1029/2010WR009793>.
- ROSTI, M., CORTELEZZI, L. & QUADRIO, M. 2015 Direct numerical simulation of turbulent channel flow over porous walls. *Journal of Fluid Mechanics* **784**, 396–442.
- ROTH, M. 2000 Review of atmospheric turbulence over cities. *Quarterly Journal of the Royal Meteorological Society* **126** (564), 941–990, arXiv: <https://rmets.onlinelibrary.wiley.com/doi/pdf/10.1002/qj.49712656409>.
- SCARANO, F. & RIETHMULLER, M. 1999 Iterative multigrid approach in piv image processing with discrete window offset. *Experiments in Fluids* **26** (6), 513–523.
- SCHMEECKLE, M. W., NELSON, J. M & SHREVE, R. L. 2007 Forces on stationary particles in near-bed turbulent flows. *Journal of Geophysical Research: Earth Surface* **112** (F2).
- SHI, J. 1994 Good features to track. In *Computer Vision and Pattern Recognition, 1994. Proceedings CVPR'94., 1994 IEEE Computer Society Conference on*, pp. 593–600. IEEE.
- STEVENSON, P. 2003 Comment on “physical insight into the ergun and wen & yu equations for fluid flow in packed and fluidised beds”, by rk niven [chemical engineering science, volume 57, 527–534]. *Chemical engineering science* **58** (23–24), 5379.
- TILTON, N. & CORTELEZZI, L. 2008 Linear stability analysis of pressure-driven flows in channels with porous walls. *Journal of Fluid Mechanics* **604**, 411–445.
- TOMINAGA, A. & NEZU, I. 1992 Velocity profiles in steep open-channel flows. *Journal of hydraulic Engineering* **118** (1), 73–90.
- VAN DER VAART, K., GAJJAR, P., EPELY-CHAUVIN, G., ANDREINI, N., GRAY, J. & ANCEY, C. 2015 Underlying asymmetry within particle size segregation. *Physical review letters* **114** (23), 238001.
- VALLET, J., PANISSOD, F., STRECHA, C. & TRACOL, M. 2011 Photogrammetric performance of an ultra light weight singlet uav. In *UAV-g*.
- VOERMANS, J. J., GHISALBERTI, M. & IVEY, G. N. 2017 The variation of flow and turbulence across the sediment–water interface. *Journal of Fluid Mechanics* **824**, 413–437.
- VOERMANS, J. J., GHISALBERTI, M. & IVEY, G. N. 2018 A model for mass transport across the sediment-water interface. *Water Resources Research* **54** (4), 2799–2812.
- VON CHÉZY, HELMINA 1834 *Catalogue de livres d’une très bonne condition, provenant de la bibliothèque de M.A.L. De Chézy (fils de Antoine Chézy) et précédé d’une notice rédigée par sa Veuve..* néan.
- WELBER, M., LE COZ, J., LARONNE, J., ZOLEZZI, G., ZAMLER, D.L, DRAMAIS, G., HAUET, A. & SALVARO, M. 2016 Field assessment of noncontact stream gauging using portable surface velocity radars (svr). *Water Resources Research* **52** (2), 1108–1126.

## Bibliography

---

- WHITAKER, S. 1986 Flow in porous media i: A theoretical derivation of darcy's law. *Transport in porous media* **1** (1), 3–25.
- WHITAKER, S. 1996 The Forchheimer equation: a theoretical development. *Transport in Porous media* **25** (1), 27–61.
- WILSON, N. R. & SHAW, R. 1977 A higher order closure model for canopy flow. *Journal of Applied Meteorology* **16** (11), 1197–1205, arXiv: [https://doi.org/10.1175/1520-0450\(1977\)016<1197:AHOCMF>2.0.CO;2](https://doi.org/10.1175/1520-0450(1977)016<1197:AHOCMF>2.0.CO;2).
- ZAMPOGNA, G. A. & BOTTARO, A. 2016 Fluid flow over and through a regular bundle of rigid fibres. *Journal of Fluid Mechanics* **792**, 5–35.
- ZHANG, G. & CHANSON, H. 2018 Application of local optical flow methods to high-velocity free-surface flows: Validation and application to stepped chutes. *Experimental Thermal and Fluid Science* **90**, 186–199.
- ZIPPE, H. & GRAF, W. 1983 Turbulent boundary-layer flow over permeable and non-permeable rough surfaces. *Journal of Hydraulic research* **21** (1), 51–65.



# Gauthier ROUSSEAU

Date and place of birth : 9<sup>th</sup> of August 1987 at Château-Thierry

## Curriculum Vitae



rue Maupas, 17, 1004, Lausanne (CH)  
+41 77 456 88 70, +33 6 87 61 66 58  
gauthier.rousseau@gmail.com  
<https://github.com/grousseau>

### PROFESSIONAL EXPERIENCE

OCT 2014 – JAN 2018 (FULL TIME)

EPFL - Ecole Polytechnique Fédérale de Lausanne  
**PhD student / Teaching assistant**

Subject : “**TURBULENT FLOWS OVER ROUGH PERMEABLE BEDS IN MOUNTAIN RIVER: EXPERIMENTAL INSIGHTS AND MODELING**”

SEPT 2013 – JUNE 2014 (PART TIME)

Prépa CPE/La Martinière college - Lyon  
**Teaching assistant**

Teaching assistant for practical courses and oral examiner in scientific preparatory schools (~ 10 hours per week).

SEPT 2011 – AUGUST 2012 (FULL TIME)

Irstea - Lyon  
**Associate engineer**

Engineer position on pesticide transfer problematic in Beaujolais's winegrowing area for 9 months and assistant for fluvial geomorphology field campaigns for 3 months.

SEPT 2010 – JUNE 2011 (FULL TIME)

French student network for a sustainable development  
**Civilian service**

Creation/administration of an association supporting small farming and local food networks.

FEBRUARY 2010 – AUGUST 2010 (FULL TIME)

University of Stockholm  
**Master project**

Subject : Characterization of the 2009/2010 winter with the water stable isotopes and climate models.

### PHD TEACHING

**Teaching assistant:** “Physics”, “Fluid mechanics”, “Waves and dambreaks”, and “Hydrology”.

**6 student projects supervision:**

- Antidunes and sediment transport (2015)
- Sediment transport measurement by imagery (2015)
- Particle tracking with multiple frames (2016)
- Dam break over sediments - Experiments (2016)
- Dam break over sediments - Models (2017)
- Optical flow and velocimetry (2018)

**2 full time internships supervision:**

- Effect of the bed slope on the hyporheic flow (2016)
- Material Point Method (MPM) for granular flows: a comparison with experiments (2017)

### EDUCATION

2012 – 2014 **Master in Education of Physics**  
Department of Physics  
École Normale Supérieure of Lyon

2008 – 2010 **Master in Hydrogeology/Hydrology**  
Department of Science of the Universe  
Sorbonne Université / UPMC

2006 – 2008 **Bachelor in Physics**  
Department of Physics  
Sorbonne Université / UPMC

2005 – 2006 **Scientific « Baccalauréat »**  
Engineering science, spec. mathematics  
Lycée Jules Verne at Château-Thierry

### COMPUTER SKILLS

BEGINNER	R, Cpp
INTERMEDIATE	UNIX and Microsoft Environments Softs: Paraview, ArcGIS, SolidWorks
EXPERT	Matlab, Python (openCV, vtk, Scikit, Keras), L <sup>A</sup> T <sub>E</sub> X

### COMMUNICATIONS

**Rousseau G., Papa D., and Ancy C.** (2016). The role of the hyporheic flow on the stability of an erodible bed: A laboratory approach using particle image velocimetry. *Poster presented at the European Geophysical Union (Vienna) and at Conference on Mathematical Geophysics (Paris)*

**Rousseau G., Sklivaniti A., Papa D., and Ancy C.** (2017). The role of the hyporheic flow on sediment transport processes : an experimental approach using particle image velocimetry. *Talk presented at the European Geophysical Union (Vienna), Vienna*

**Dhont B., Rousseau G., and Ancy C.** (2017). Continuous Monitoring of Bed-Load Transport in a Laboratory Flume Using an Impact Sensor. *Journal of Hydraulic Engineering*, 143(6), p.04017005

**Rousseau G., de Graffenried B. and Ancy C.** (2018). Vélométrie par scan 3D d'écoulements turbulents: application à un écoulement à surface libre sur fond poreux *Article and talk presented at the French Laser Technique Conference, Dourdan*

**Rousseau G. and Ancy C.** (in prep., 2019). Particle image velocimetry for measuring turbulent flow over rough beds using a refractive index matched technique. *Experiments in Fluid*